Gridpix:

TPC development on the right track

Martin Fransen

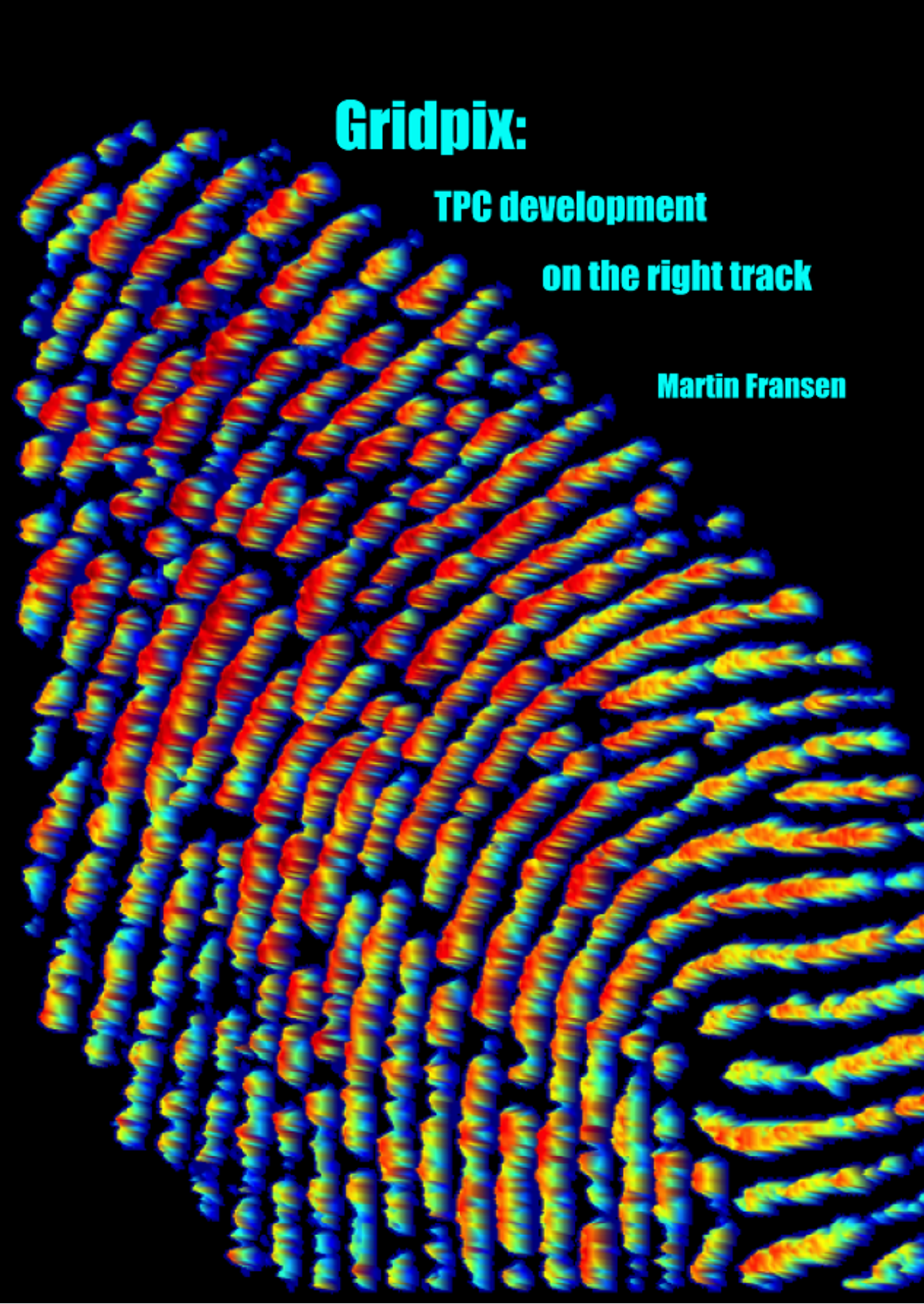

Gridpix: TPC development on the right track

The development and characterisation of a TPC with a CMOS pixel chip read out

ACADEMISCH PROEFSCHRIFT

Ter verkrijging van de graad van doctor
aan de Universiteit van Amsterdam
op gezag van de Rector Magnificus
prof. dr. D.C. van den Boom
ten overstaan van een door het college voor promoties ingestelde
commissie, in het openbaar te verdedigen in de Agnietenkapel
op woensdag 26 september 2012, te 14:00 uur

door

Martin Fransen

geboren te Amsterdam

Promotor :	Prof. dr. F. L. Linde
Co-promotor :	Dr. ir. H. van der Graaf
Overige leden :	Dr. M. Vreeswijk
	Prof. dr. B. van Eijk
	Prof. dr. ir. E. N. Koffeman
	Prof. dr. ir. P. J. de Jong
	Dr. M. P. Decowski
	Dr. P. M. A. Colas
	Prof. dr. S. J. de Jong

Faculteit der Natuurwetenschappen, Wiskunde en Informatica

Dutch title :	*Gridpix: TPC ontwikkeling op het goede spoor* *Het ontwikkelen en karakteriseren van een TPC uitgelezen met een CMOS pixel chip*
Cover design :	*Martin Fransen*
Cover :	*Finger print of the author's right index finger recorded with a Gridpix detector used as an optical imaging device. The modified Gridpix detector was built for the Ph.D. research of J. Melai [85].*

Print: GVO drukkers & vormgevers B.V. | Ponsen & Looijen
ISBN: 978-90-6464-581-5

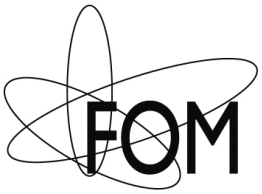

This work is part of the research programme of the Foundation for Fundamental Research on Matter (FOM), which is part of the Netherlands Organisation for Scientific Research (NWO).

Contents

Introduction

In the field of high energy physics, interactions between subatomic particles are studied in the search for the most elementary building blocks of matter and their properties. In the 1960's a model emerged that describes the properties of elementary particles and how they interact according to the fundamental forces. The fundamental forces included in the model are the strong, the weak and the electromagnetic force. This model is called the Standard Model and it has proven to be very accurate. The Standard Model predicts that under the right conditions certain particles can be created. Measurements confirmed the existence of all but one of the predicted particles, for the Standard Model to be consistent the Higgs particle is predicted but still has to be discovered. The Higgs particle is associated with the mechanism responsible for the fact that all matter has mass and discovering it is one of the main goals in high energy physics. Presently there are hints of its existence but these have yet to be confirmed.

In order to measure a specific process (like the creation of a Higgs particle), subatomic particles are collided which results in radiation that can be measured. The radiation is composed of particles that carry information about the processes that formed them. For that reason each individual particle is of interest and therefore one prefers to speak about particle detection rather than radiation detection. Particle collisions can be produced on demand with a particle accelerator that accelerates two beams of particles and collides them head on at a well defined point where a detector can measure the collision products. The higher the energy density in a collision the more processes can occur and the more information we can obtain from it. For that reason particle colliders became more and more powerful over the years. The most powerful particle collider presently is the LHC[1] at CERN[2], brought into service in 2009. The LHC can collide protons and other atomic nuclei and is designed to accelerate protons up to an energy of 7 TeV, resulting in 14 TeV proton-proton collisions. Due to technical difficulties the proton energy currently is limited to 3.5 TeV. The plan is to solve the technical issues in 2013 and to run at design energy from 2014 on. Plans for future particle colliders are still in the concept phase, these will probably collide electrons.

The particles created in a collision may be short lived and exotic and may only travel a fraction of a centimetre before they decay into other particles. It is possible

[1] *L*arge *H*adron *C*ollider.
[2] *C*onseil *E*uropéen pour la *R*écherche *N*ucléaire.

that a whole chain of decays occurs before the detector is reached. To reconstruct a collision precise tracking of the particles is required. Each particle must be identified since it carries information about the underlying process that created it. Another important aspect is how much energy is involved in a collision. In order to determine the energy in a collision the energy of the created particles has to be measured. Briefly put, to reconstruct the processes in a collision three questions have to be answered for each produced particle:

1 What kind of particle was it?

2 What was its track?

   - Where did it originate?
   - What was its direction?

3 How much energy did it have?

The challenge for a particle detector is to measure each of these properties without adversely affecting the particle. For example: Measuring a particle's trajectory should not cause the particle to scatter so tracking should be performed with as little material in the particle's path as possible. A particle can also collide inside the tracking detector such that it is destroyed while creating other particles, making it difficult to identify and track the original particle.

This thesis describes the verification of the performance of a new gaseous detector concept developed to cope with high particle rates. The detector is designed to track particles with a minimal amount of material in the particle's path and to simultaneously measure the amount of energy a particle deposits inside the detector. The latter can be used to help to identify a particle and to improve the momentum measurement.

Chapter 1

High energy physics in a lab

Detection of particles can occur through electromagnetic interactions in which released charge or generated light is detected. The nature of the particles and the required information determines the required concept of how it can be detected i.e. how it can be made to produce an appropriate electrical or optical signal. The way a particle interacts is determined by the forces it is sensitive to. Figure 1.1 shows all known quarks and leptons except for their antimatter counterparts. Quarks and leptons are elementary particles. For antimatter, some of the properties have the same magnitude but opposite sign, i.e. an anti-electron has a positive charge of the same magnitude as the electron's negative charge. The 'normal' matter we observe in daily life is composed of the particles indicated by the rectangle. A bound state of one down and two up quarks form a proton; one up and two down quarks form a neutron. Protons and neutrons form atomic nuclei and electrons are bound in an orbital around a nucleus to form atoms. The other quarks: Charm (c), Strange (s), Bottom (b), and Top (t) are heavier than the up and down quarks and particles composed of those quarks all decay into lighter particles. Particles composed of quarks are called hadrons. The muon (μ) and tau (τ) are heavy, unstable, electron-like particles. In several decay steps neutrinos are produced (the ν_e, ν_μ and ν_τ). Neutrinos are stable particles which are present around us in large numbers but imperceptible in daily life due to a very low interaction probability. Table 1.1 shows the fundamental forces and the associated bosons.

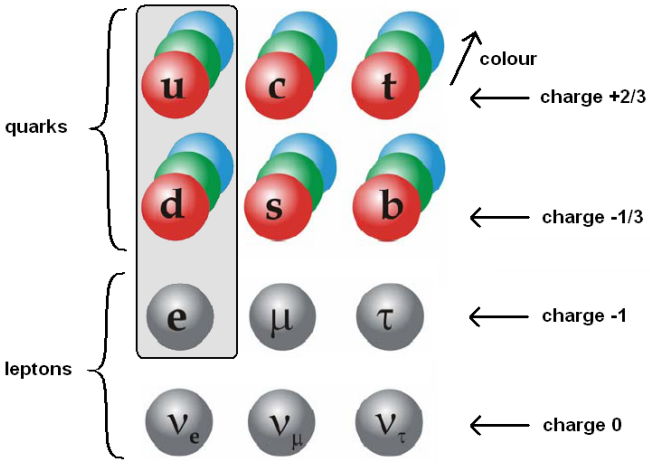

Figure 1.1: *The quarks and leptons we know of presently, all are sensitive to gravity. The quarks are also sensitive to the weak, the electromagnetic and the strong force. The electron (e), muon (μ) and tau (τ) are also sensitive to the weak and the electromagnetic force. The neutrinos are also sensitive to the weak force.*

force	relative strength	mediator	coupling
strong	10	gluon	colour
electromagnetic	10^{-2}	photon	charge
weak	10^{-13}	W and Z boson	flavour
gravity	10^{-42}	graviton?	mass

Table 1.1: *The four known fundamental forces, indication of their relative strength, their mediators and particle properties they couple to [1].*

In particle physics gravity is left out of consideration due to its negligible contribution on a microscopic scale[1].

In the field of particle physics energy is expressed in units of eV. One eV is the amount of energy that corresponds to the work done on a unit charge moved over a potential difference of 1 V. A unit charge is the charge of one electron (1.6×10^{-19} C). Mass is a form of energy and for that reason mass can be expressed in units of energy. The amount of energy (E) represented by a mass (m) is [3]:

$$E = mc^2, \tag{1.1}$$

where c is the speed of light. The amount of energy involved in an interaction, for example a collision in a particle collider, and the type of interaction (a strong, a weak or electromagnetic interaction) determines what particles can be created.

[1] It is even debated whether gravity is a fundamental force at all [2].

In high energy physics velocities are expressed as a fraction of the speed of light, called β:

$$\beta = \frac{v}{c}. \tag{1.2}$$

According to special relativity, as particles approach the speed of light their observed mass starts to increase, the time in the particle's frame appears to slow down and the dimension in the direction of movement contracts (called Lorentz contraction). The magnitude of these relativistic effects scale with a factor γ.

$$\gamma = \frac{1}{\sqrt{1 - \frac{v^2}{c^2}}}. \tag{1.3}$$

The observed mass of a moving particle with a rest mass m_0 is γm_0. One can see that in equation (1.3) γ goes to infinity as v approaches the speed of light c. For that reason a particle's velocity will never be faster than the speed of light. A more thorough overview of relativistic kinematics can be found in [4].

In this chapter, section 1.1 briefly discusses the LHC and future plans for other particle accelerators. Section 1.2 addresses some basic particle detection concepts and how these can be put to use in particle detectors. Based on different concepts required to do different measurements, a detector for experiments at a particle collider has a specific geometry. Section 1.3 describes how different detector concepts are combined into a single detector.

1.1 The Large Hadron Collider and the future

The LHC [6] is a circular accelerator with a circumference of 27 km that collides two beams of hadrons (protons or other atomic nuclei) head on. Hence the name *Large Hadron Collider*. Around the ring there are four interaction (collision) points where particle detectors are placed. The LHC is designed to accelerate protons up to an energy of $7{\times}10^{12}$ eV (7 TeV) and provide up to approximately 10^9 collisions per second in a detector. The LHC will be upgraded to the super-LHC (sLHC)[2] to provide up to 10^{10} collisions per second in the future. Figure 1.2 shows a sketch of how the particle beams are arranged.

[2] Recently renamed to *H*igh *L*uminosity LHC (HL-LHC). At the moment of writing sLHC was a common name for the LHC upgrade.

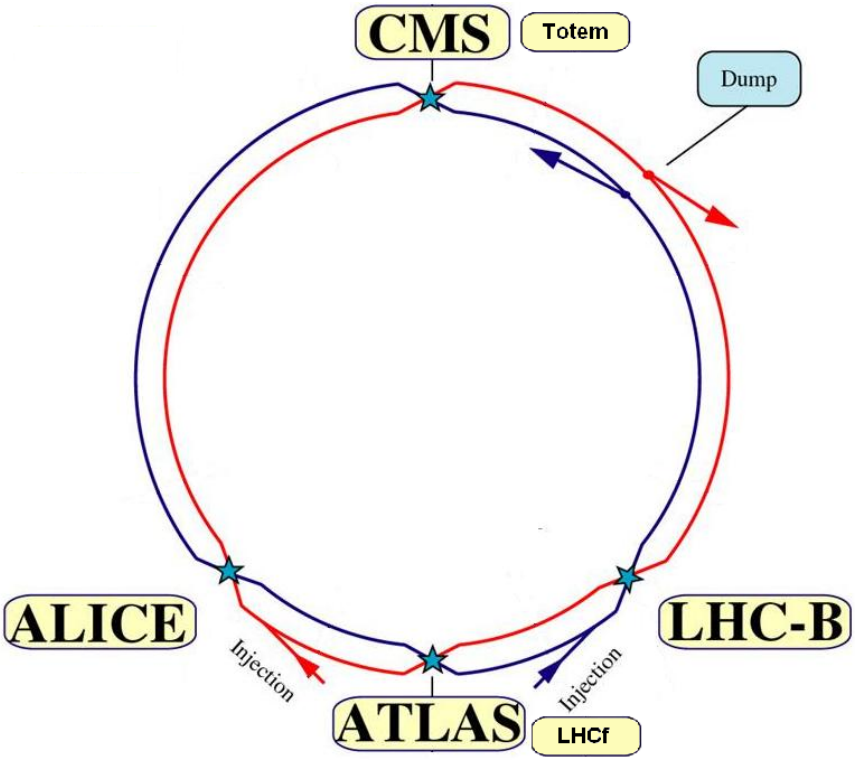

Figure 1.2: *Sketch of the beams in the LHC. There are four interaction (collision) points where detectors are placed. A part of the ATLAS detector will be discussed in section 1.3. After several hours of collisions the intensity of the particle beams will be reduced to such a level that the beams are dumped onto a graphite block and the machine is refilled with fresh beams.*

With a circular accelerator a proton can gain high energy with moderate acceleration fields as it repeatedly passes the acceleration cavity. Another advantage is that for each revolution every proton has a chance of collision, making it power efficient[3]. The disadvantage of a circular accelerator is that charged particles lose energy in the form of synchrotron radiation as they are deflected by magnets to stay on track. The higher the value of γ for a particle the more energy is lost by synchrotron radiation. The kinetic energy of a particle and the value of γ are related according to:

$$E_{kin} = (\gamma - 1)\, m_0 c^2 \rightarrow \gamma = \frac{E_{kin}}{m_0 c^2} - 1. \tag{1.4}$$

According to equation (1.4) for the same energy a light particle is more relativistic than a heavy one.

[3] In the LHC a 7 TeV beam with 3.2×10^{14} protons contains 350 MJ. The protons do $3 \times 10^8 / 2.7 \times 10^4 \approx 1.1 \times 10^4$ rounds per sec. If a beam is dumped it will deliver 3.9 TW for 91 µs, which is 25% of the world's power consumption in 2008 [5] ***per beam***!

The power radiated by a relativistic charged particle as synchrotron radiation is given by:

$$P_{syn} = \frac{cq^2 (\beta\gamma)^4}{6\pi\epsilon_0 r^2}, \tag{1.5}$$

where q is the charge of the particle and r the radius of the curvature. Equation 1.5 shows that synchrotron losses scale with γ^4 and equation (1.4) shows that γ is inversely proportional to the mass for a given energy. For that reason the LHC accelerates and collides protons instead of electrons. Protons are 2000 times more heavy than electrons.

Because protons are composite particles (composed of quarks and gluons) it is not known a priori which parts participate in a collision and also the transferred energy is not known which make proton-proton collisions more difficult to interpret than electron-positron collisions. Interpretation of electron-positron collisions does not have that problem as they are point particles. However, as mentioned, electrons need to be much more relativistic than protons to reach the same collision energies, resulting in insuperable losses by synchrotron radiation in a circular collider. For that reason plans are made for the ILC [7] (*I*nternational *L*inear *C*ollider) and CLIC (*C*ompact *LI*near *C*ollider) [8], positron electron colliders to be build in the future. The requirements for these colliders depend on what will be discovered with the LHC.

1.2 Particle detection

1.2.1 Tracking

A charged particle's trajectory can be determined by measuring the position of its ionisation as it passes through matter. The challenge for tracking detectors is to minimise the scattering of a particle and to minimise the probability to radiate secondary particles and/or to initiate a shower (see section 1.2.3). Tracking often is performed with a stack of thin layers of low Z material or with a gaseous volume. The detector has to be light i.e. should have little mass in the particle's path. The use of gas for particle detection is discussed in chapter 2. Solid state tracking detectors often use a stack of thin silicon slabs [9]. The sensitive part of the detector is the depletion layer of a PN junction. A PN junction is the boundary between two different types of semiconductors and in the depletion layer there are no or very few charge carriers (it is an insulator). A charged particle traversing matter liberates charge along its path (figure 1.3). The charge released in the depletion layer can be measured as it drifts towards a readout electrode. The read-out of a PN junction is patterned in strips or pixels in order to determine where the particle went through (figure 1.4).

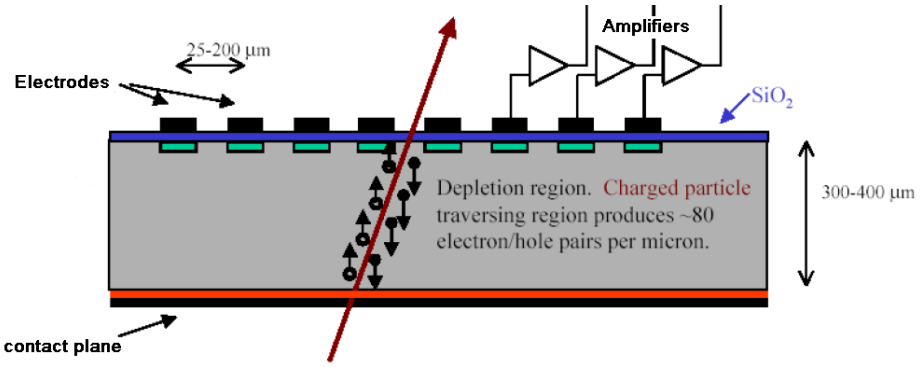

Figure 1.3: *Cross section of a silicon strip detector [10]. The charge released (the electron hole pairs) by a particle is read out with amplifiers connected to the strips.*

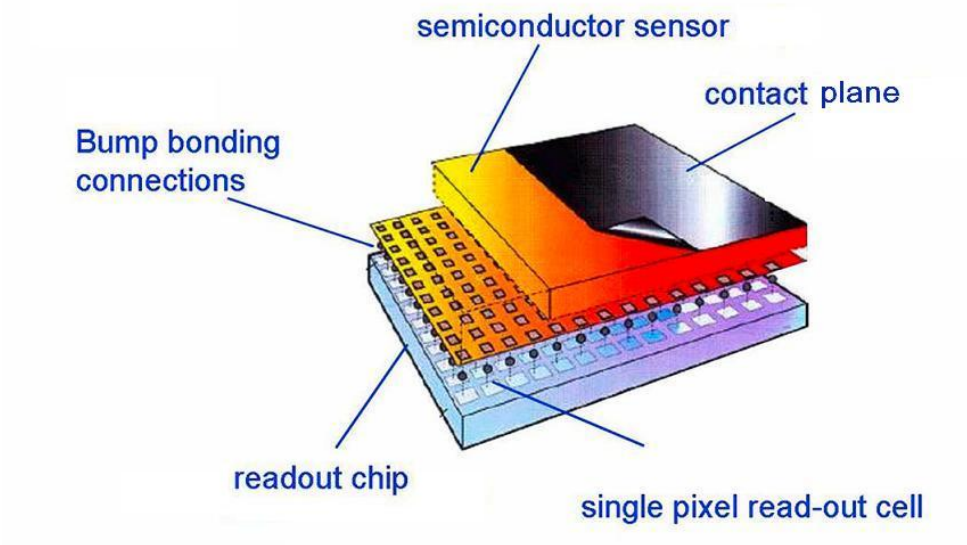

Figure 1.4: *Sketch of a pixel detector [11]. A pixel matrix for readout gives the detector a 2D resolving power to find the point a particle went through.*

The particle's trajectory can be reconstructed by using the points through which the particle traversed the different layers of the stack. By placing a tracking detector in a magnetic field the direction of deflection of a particle shows its polarity (i.e. positive or negative electric charge). In case the magnitude of the charge is known (mostly one unit charge), the momentum can be determined by the radius of curvature.

1.2.2 Particle identification

Finding the mass of a particle is an important aspect for its identification. In case the momentum of a particle is known (by measuring its deflection in a magnetic field) one can find the particle's mass by measuring its velocity. The momentum P of a particle is given by:

$$P = \gamma m_0 v. \tag{1.6}$$

According to equation (1.6) a particle with a given momentum may be a 'slow' heavy particle or a 'fast' light particle. By passing particles with the same momentums through a (transparent) medium a condition may appear in which a light particle moves faster than the speed of light in that medium while a heavier particle doesn't. If a particle moves through a medium faster than the speed of light in that medium, Cherenkov light is generated [12] which can be detected. By choosing a medium with a refractive index n one can discriminate between heavy and light particles for a certain range of momenta. Another way to use Cherenkov light to determine the velocity of a particle is to measure the angle (θ_c) of emission of the Cherenkov light with respect to the particle's trajectory [13]:

$$\cos\theta_c = \frac{1}{\beta n}. \tag{1.7}$$

in which n is the refractive index of the medium. For different velocities the light will be emitted under different angles. By allowing the Cherenkov light to travel some distance after the Cherenkov radiator (such as in the ALICE detector [14]), or by using optics (like in the LHCb detector [15]), this light can be projected as a ring onto an array of light detectors. The diameter of the ring is a measure for the particle's velocity.

Another method to discriminate between the velocities of particles is transition radiation. A particle that traverses the transition between materials with different permittivity will have an increasing probability to create X-rays with increasing γ [16]. In general one needs many transitions (a stack of foils or a foam) to have a sufficiently large probability for a highly relativistic particle to create X-rays. The detection of X-ray photons accompanying the particle indicates a high γ.

For particles with a low relativistic factor γ one can measure the time of flight (TOF) to determine their velocity by measuring the time af passage between two points of a known distance apart. For velocities close to the speed of light the difference in times becomes very small, for that reason this method is not suitable for highly relativistic particles.

1.2.3 Calorimetry

The last measurement that can be performed on a particle is to completely absorb it to measure its kinetic energy. A particle is absorbed by having it initiate a shower in which many more particles are created.

As hadrons traverse matter they can collide with an atomic nucleus and initiate a hadronic shower in which more hadrons are created. The created hadrons, with

sufficient kinetic energy, again can produce more particles as they collide with other nuclei. Such a chain reaction increases the multiplicity of tracks and decreases the average energy per hadron until no more particles can be created. All charged particles lose energy by ionisation of the medium they traverse. The energy content of the particle that initiated the shower can be determined by measuring the charge released by the ionisation caused by all the charged particles in a shower.

In an electromagnetic shower particles are created through the electromagnetic force. A high energy photon can create an electron-positron pair when it interacts with an electrically charged particle. The photon is fully absorbed in the process. An electron can create bremsstrahlung (photons) as it is deflected by a charge. The probability of both processes, pair creation and bremsstrahlung, increases with the square of the charge of the particle the photon or electron interacts with. For that reason these processes are most likely to occur at an atomic nucleus. Photons from bremsstrahlung can again create an electron positron pair. The process pair creation $\rightarrow$ bremsstrahlung $\rightarrow$ pair creation etc. continues until the photon energy drops below 1.022 MeV which is the threshold for electron positron pair creation. The electrons and positrons lose energy by ionisation. The positrons will eventually annihilate with an electron creating two 511 keV photons. Photons with an energy of less than 1.022 MeV will ionise the medium by Compton scattering and by the photo electric effect. The total ionisation caused by an electromagnetic shower is a measure for the energy the initial electron, positron or photon had.

As charged particles traverse a scintillating material atoms are excited and emit light when returning to ground state. The amount of emitted light is proportional to the amount of energy a particle lost in the scintillator. The light can be detected by a sensor that gives an electrical charge proportional to the amount of light. The net result is an electrical signal proportional to the amount of energy lost in the scintillator. A calorimeter can be made up of an interleaved stack of metal slabs and scintillator slabs. The metal slabs are the dominant factor in forming a shower (the absorber) and the scintillator slabs take 'samples' of the shower at different depths. Based on these samples the total energy in a shower is determined.

To initiate a hadronic or an electromagnetic shower it is beneficial to use materials with a high atomic number (Z) that have large nuclei with high electric charge. Since all energy has to be absorbed the material has to be thick. Calorimeters in general are large and heavy structures.

1.2.4 Muons and neutrinos

High energy muons are the only particles with enough penetrating power, a long enough life time *and* enough interaction with a detector to be both 'unstoppable' *and* detectable. This property distinguishes a muon from other particles. The momentum of a muon can be determined by deflecting it with a magnetic field and measure the radius of curvature.

Neutrinos can be 'identified' by missing energy. Neutrinos have a low interaction probability since they are sensitive to the weak force only and for that reason mostly escape detection. In case the conservation of momentum appears to be violated the missing energy often is carried away by neutrinos that escape detection.

1.3 Detectors at the LHC

1.3.1 Detector geometry

Most particle detectors are composed of different sub-detectors in order to perform tracking, particle identification and calorimetry. An example of a general purpose detector at the LHC is the ATLAS[4] detector [17]. The ATLAS detector encloses the interaction point. A sketch of the cross section of a part the detector is shown by figure 1.5.

The layers of the detector that are closest to the interaction point are for tracking the path of particles. The outermost layer of the tracker also measures transition radiation to identify particles. The tracker is embedded in a strong magnetic field to deflect charged particles for measuring charge polarity and momenta. The next stage are the calorimeters which fully absorb most charged particles. As figure 1.5 illustrates, muons are the only measurable particles that are not stopped by the calorimeter and go through the muon spectrometer which is the outermost stage of the ATLAS detector. The momentum of the muons is determined by measuring their deflection in a strong magnetic field that fills the volume of the muon spectrometer. To fully absorb the high energy particles in the calorimeters and to deflect the muons enough to be measured, the ATLAS detector has to be a physically large device. Figure 1.6 shows a sketch of the full ATLAS detector.

[4] *A Toroidal LHC ApparatuS.*

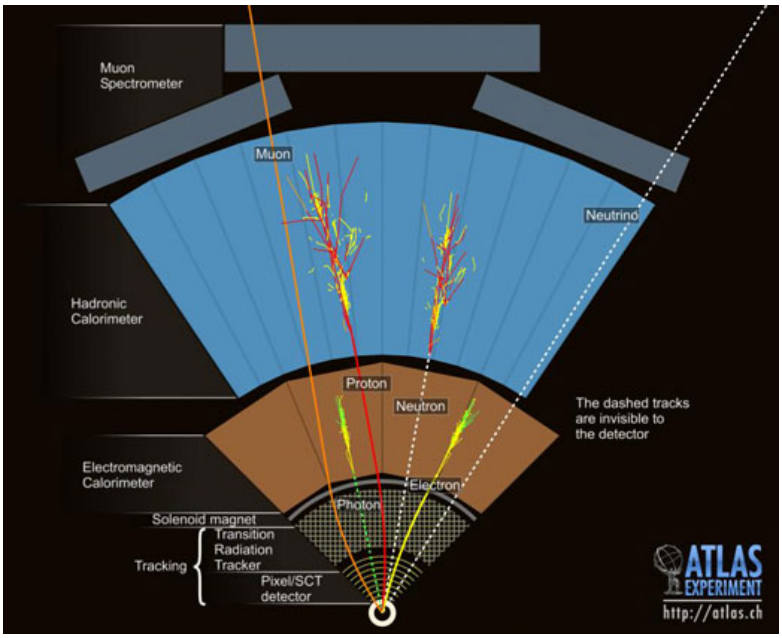

Figure 1.5: *Sketch of the cross section of a part of the ATLAS detector. The tracks shown in the picture illustrate how different parts in the detector respond to different types of particles.*

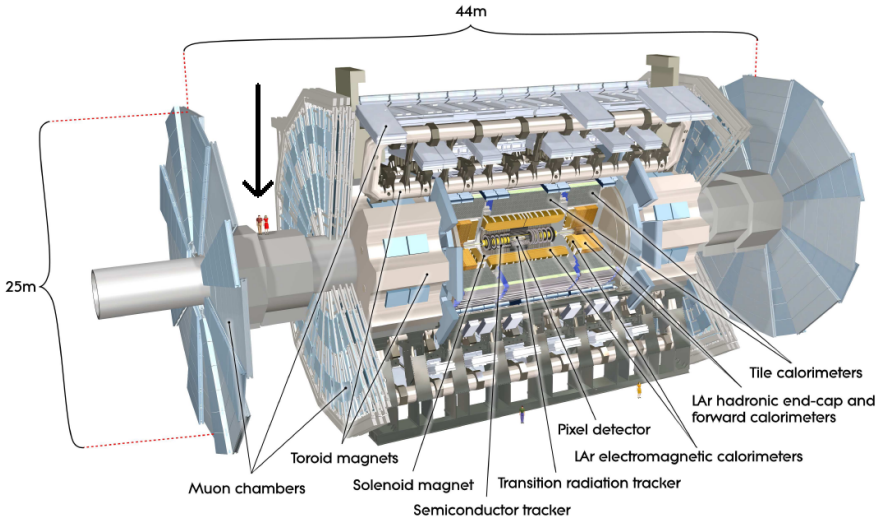

Figure 1.6: *Sketch of the ATLAS detector. Its large physical size is illustrated by the human figures pointed out by the arrow [17].*

1.3.2 Tracking particles in the ATLAS and ALICE detector

The challenges for a tracking detector are accuracy, occupancy and mass budget. The tracking detector should have as little mass in the particle's path as possible to minimise both scattering and the probability to generate background radiation (secondary particles). Since the tracking detector is close to the interaction point it has to cope with a high particle flux, i.e. many tracks per surface area per second. The inner part of the detectors that are closest to the interaction point consist of semiconductor detectors. Semiconductor tracking detectors can be produced with high granularity (many pixels or strips per surface area) and therefore can cope with a high particle flux and have a high position accuracy. In the ATLAS detector the particle flux in the first layer, 5 cm from the interaction point, is a few 10^7 particles per cm^2 per second when the LHC runs at design luminosity. In the future the LHC is planned to be upgraded to provide 10 times more collisions per second. The spatial resolution of the present pixel detectors is 12 μm for a normal incidence particle. Further outwards the pixels are replaced by strips since less granularity is required. The outermost tracking detector is a transition radiation detector composed of small gas filled tubes. Figure 1.7 shows a sketch of the sub detectors in the tracking detector. More details about the ATLAS detector can be found in [17].

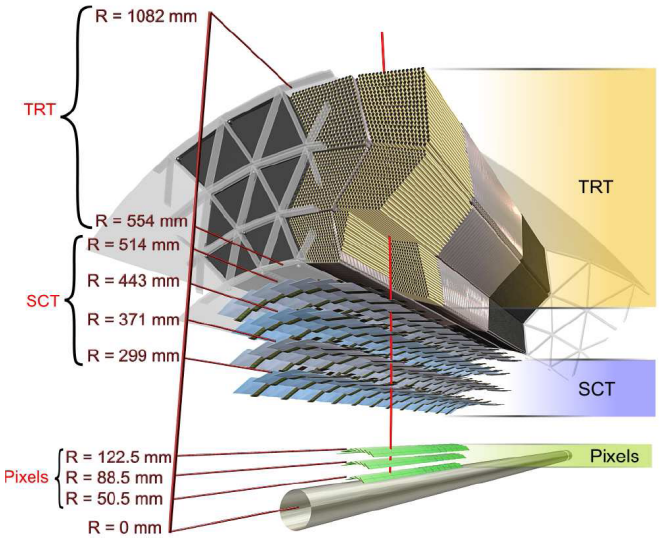

Figure 1.7: *Sketch of the tracking part of the ATLAS detector. The detectors closest to the beam pipe are pixel detectors, the next layer is composed of silicon strips (SCT) and the outer tracking detector is a transition radiation tracker (TRT). The transition radiation tracker helps identifying particles, notably electrons, and has spatial resolving power in the plane perpendicular to the colliding beams.*

In the ALICE[5] [14] detector the outer stage of the tracking system consists of a TPC (*T*ime *P*rojection *C*hamber), which is a large volume (5 m diameter) gaseous detector to reconstruct the trails of ionisations left by charged particles. Figure 1.8 shows a reconstruction of tracks through the ALICE TPC.

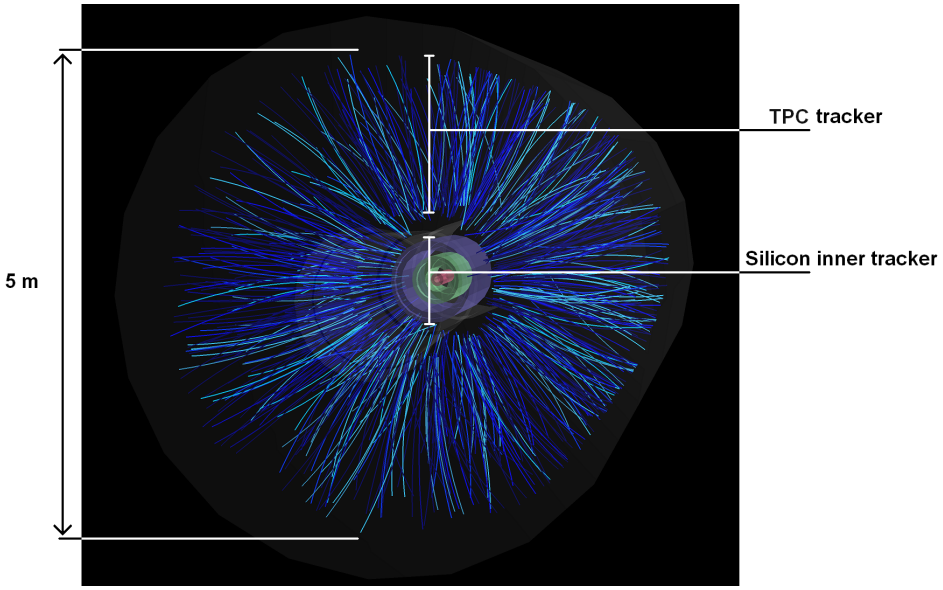

Figure 1.8: *Tracks through the ALICE TPC [18]. The inner part of the tracking system in the ALICE detector consists of silicon detectors.*

The operation principles of gaseous detectors and specifically the TPC are discussed in chapter 2. In a gaseous detector a large track segment can be sampled with only a limited amount of matter in a particle's path. Since the gas can be flushed a gaseous detector will suffer less from radiation damage than a semiconductor based detector. On the other hand, a gaseous detector can suffer from ageing, which is a process related to the amount of charge collected on electrodes and shows up as deposits. Ageing is caused by traces of certain chemicals that may originate from impurity in the used gas and/or from contamination of materials used for the construction of the detector [19]. The larger the volume of a gaseous detector the lower the particle flux in which it can operate due to the time required to extract the liberated charge. Most gaseous detectors are large volume devices which must be operated with a lower particle flux than a silicon detector.

A problem in silicon detectors is that the silicon gets damaged by radiation. The silicon used for detection has to be of high purity with low doping levels in order to be able to create a depletion layer of 300 µm thick with voltages in the order of a few 100 V. Under the influence of radiation the crystal lattice becomes damaged

[5] *A* Large *I*on *C*ollider *E*xperiment

because of displacements of atoms and becomes contaminated with other elements due to transmutations caused by the hadronic interactions. The result of a large irradiation dose eventually leads to a worsening of the signal to noise ratio due to an increase in leakage current. Also the voltage required for the depletion layer will increase. The end of life of a silicon detector is marked by a poor signal to noise ratio or by breakdown. The risk of breakdown increases with increasing depletion voltage. The inner pixel detector in ATLAS is expected to reach its end of life after three years of nominal LHC operation.

The advantages of silicon detectors in general are speed and accuracy, the drawbacks are a relatively high mass and their degradation by radiation. Gaseous detectors in general have a low mass but, due to large volumes, cannot handle a high particle flux. In the search for a low mass tracking detector with high accuracy that can handle a high particle flux a small volume gaseous detector has been developed that uses a pixel chip for readout. The pixel chip has a pitch of 55 μm. With such high granularity the individual electrons from the ionisation trail can be measured. Such a detailed measurement of the ionisations in a gas allows high precision measurements with very small gas volumes, making it possible for this concept to be used in a high flux environment. In this thesis the performance of this detector concept is verified. The general performance is discussed in chapter 6 and a specific set up for operation in a high flux environment is discussed in chapter 7.

Chapter 2

Gaseous detectors

Ionising radiation like X-rays and charged particles can be detected by measuring ionisation in a gas. The first gaseous detector was the Geiger counter [20], invented by E. Rutherford and H. Geiger in 1908. The Geiger counter only detects charge and can be used to measure the amount of radiation by counting hits. The multi wire proportional chamber (MWPC), invented in 1968 by G. Charpak, can also determine the position of a hit [21]. Charpak was awarded the Nobel prize for this invention. By the end of the 1970s the time projection chamber, often denoted as TPC, was developed by D. Nygren [22]. A TPC can measure a particle's trajectory in three dimensions.

The drift volume is the part of the detector from which the primary charge is collected. Primary charge is the charge released by the ionising radiation. By means of an applied electric field the liberated electrons drift towards the anode and the positively charged ions drift towards the cathode. Electrons approaching the anode enter an amplification region. In this region charge is amplified in order to increase the sensitivity for primary charge. Charge amplification will be discussed in section 2.2. The segmentation of the anode of a TPC determines the spatial resolution (in the XY plane) and may be composed of wires, pads, or a pixel chip. Figure 2.1 shows a sketch of the cross section of a TPC. The patterned anode measures the projection of the ionised trail left by a traversing particle. The time electrons need to arrive at the readout is a measure for the distance they had to drift. The drift time is used to reconstruct the third (Z) coordinate. The name *time projection chamber* refers to the fact that a 2D projection of the track, in combination with the drift time, is used to make a full 3D track reconstruction. Figure 2.2 shows reconstructed ionisation trails recorded with a TPC with a pixel chip as anode.

The processes in the drift volume are discussed in section 2.1.1 to 2.1.6. Gas gain and the signals induced in the readout electronics are covered by sections 2.2.1 and 2.2.2.

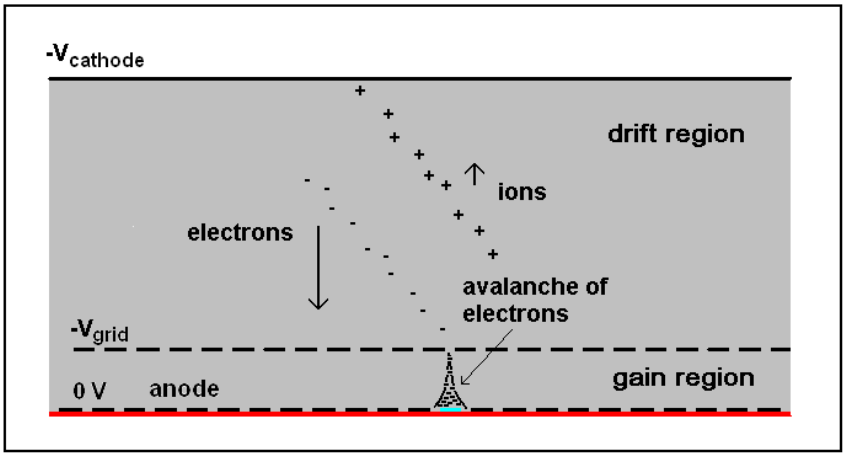

Figure 2.1: *Schematic cross section of a TPC. The height of the drift volume depends on the application and may vary from one mm to more than a meter. Gas amplification occurs in the gain region. A single electron from the drift volume can be detected if it creates a sufficiently large avalanche.*

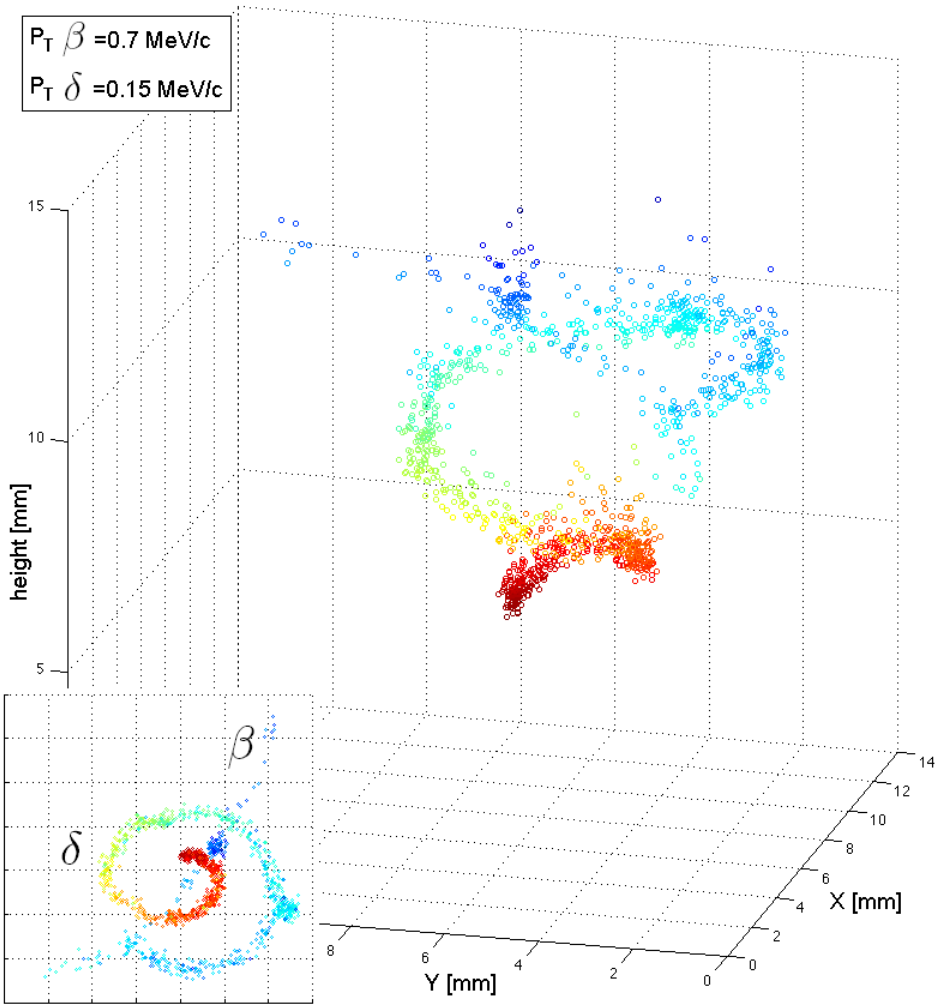

Figure 2.2: *Tracks of a β-ray (an electron emitted by a ^{90}Sr source) and a δ-ray through a TPC placed in a magnetic field of 0.13 T. The β-ray hits an electron hard enough to have it making its own track. Electrons that are released with enough energy such that they make a distinguishable track by their own are called δ-rays. Due to collisions in the gas, low energy electrons tend to follow an irregular trajectory that sometimes give association with the curly letter δ. The inset on the bottom left is the projection on the XY plane. Most of the dots are single electrons. The colour represents the drift time that was used to reconstruct the drift distance. The gas mix was a mixture of He/iC_4H_{10} in a ratio of 80/20. This event was recorded with a TPC that uses a pixel chip to read out. The pixel matrix of the chip has a pitch of 55 μm, making it possible to distinguish single electrons from the ionisation trail. Chapter 3 will focus on the pixel chip.*

2.1 Ionisation and charge transport in gas

2.1.1 Ionisation by particles

The amount of energy a charged particle loses by ionisation per unit of length depends on its velocity, its charge and the gas mix in the detector. For particles much heavier than electrons, the relation of energy loss by ionisation and the particle's velocity is given by the Bethe Bloch equation [23]:

$$-\frac{dE}{dx} = \frac{4\pi N e^4 z^2}{m_e c^2 \beta^2}\left(\ln\frac{2m_e c^2\beta^2\gamma^2}{I} - \beta^2\right). \tag{2.1}$$

N is the number density of the number of electrons in the material that is traversed, e is the electron charge, z^2 is the charge of the ionising particle, m_e is the electron mass and I is the mean ionisation potential. Figure 2.3 shows the Bethe-Bloch curves for several materials and different types of ionising particles.

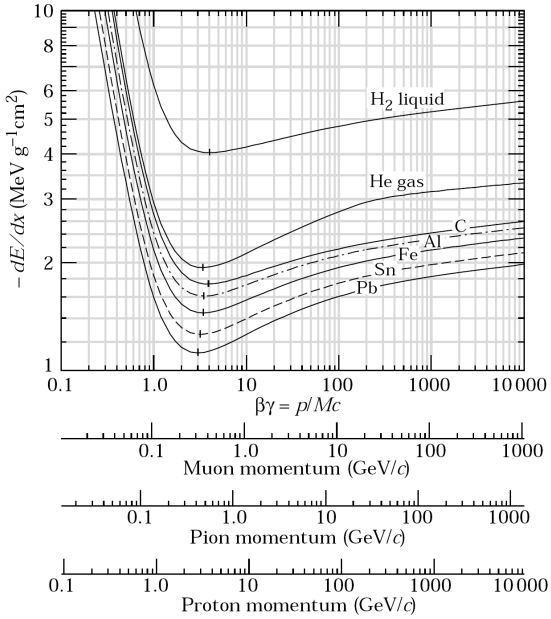

Figure 2.3: *Ionisation loss per gram traversed material [24].*

According classical mechanics, with increasing velocity the particle has less time to transfer momentum by the Coulomb force. The drop in ionisation is proportional with $1/\beta^2$. As the particle approaches the speed of light the velocity will not increase much more with increasing energy, resulting in a slower decrease of ionisation loss per unit length. For increasing particle energies the loss by ionisation will increase again because of the Lorentz contraction of its E field. This is incorporated in the

$ln(\gamma^2/I)$ part. The contracted E field transfers the same momentum in a shorter time interval which makes it more efficient in ionising gas molecules further from the particle's track. The increase of ionisation loss with increasing γ is called relativistic rise. As a result there is a velocity where the ionisation loss has a minimum. A particle at this velocity is called a *minimum ionising particle* or MIP. Since these particles deposit the smallest, and thus the hardest to detect, amount of energy in a detector, the performance of a detector is often characterized by how well it can measure a MIP. This minimum is equal for all particles with the same charge, therefore a material can be characterized by the energy loss per unit of length for a MIP.

The difference in ionisation loss for different velocities is shown by figure 2.2, one can see the difference in ionisation density of the 'fast' β ray and 'slow' δ electron. The original β ray is the horizontal track and has the fewest ionisations per unit length. Because of its lower velocity, the δ ray starts with a much denser ionisation and is deflected more by the magnetic field than the β ray. As the δ electron travels it slows down and the ionisation becomes denser until it is fully stopped. The maximum ionisation density at the end of a track is called the Bragg peak.

Figure 2.2 shows that fluctuations in energy loss can be very large. Creating a δ ray like the one shown takes hundreds of times more energy than what is required to just release an electron. There can be large fluctuations in energy loss per interaction. An interaction can result in one or multiple ionisations. The ionisation(s) as the result of one interaction is called a cluster. The average number of electrons per cluster depends on the gas mixture. Another contribution in fluctuations in energy loss is due to the number of clusters per unit length. The collisions in the gas are purely random with a mean free path λ. As a result the number of clusters N_c per length L will be Poisson distributed with an average of $\overline{N_c}=L/\lambda$ [23]:

$$P\left(N_c, \overline{N_c}\right) = \frac{\overline{N_c}^{N_c} e^{-\overline{N_c}}}{N_c!}. \tag{2.2}$$

Depending on the type of particle the mechanisms for energy loss may be other than ionisation. That energy loss will be in addition to that what is described by the Bethe-Bloch formula but will not be detected as a track in a TPC. It is beyond the scope of this thesis to discuss those other processes. For further reading about energy loss from particles through matter one can read [24] and [25].

2.1.2 Ionisation by photons

Photons can release electrons by the photo electric effect or by Compton scattering. In case of the photoelectric effect the photon will be fully absorbed while in case of Compton scattering the photon loses a certain fraction of its energy and is scattered. In both scenarios the released electron will have the energy of what the photon lost minus the electron binding energy. Photons will start to ionise as soon as the energy is more than the binding energy of the weakest bound electrons which, for common gas mixtures, is in the order of 10 eV. Pair production may occur for photons with more energy than 1.022 MeV. The created electron positron pair can release more

electrons. Figure 2.4 shows the cross sections for different processes as a function of the photon energy. Figure 2.5 shows the absorption of X-rays in different noble gases, which is a sum of the processes shown by figure 2.4. The efficiency of photon absorption of a gas can be changed by more than two orders of magnitude by the selection of the type of gas.

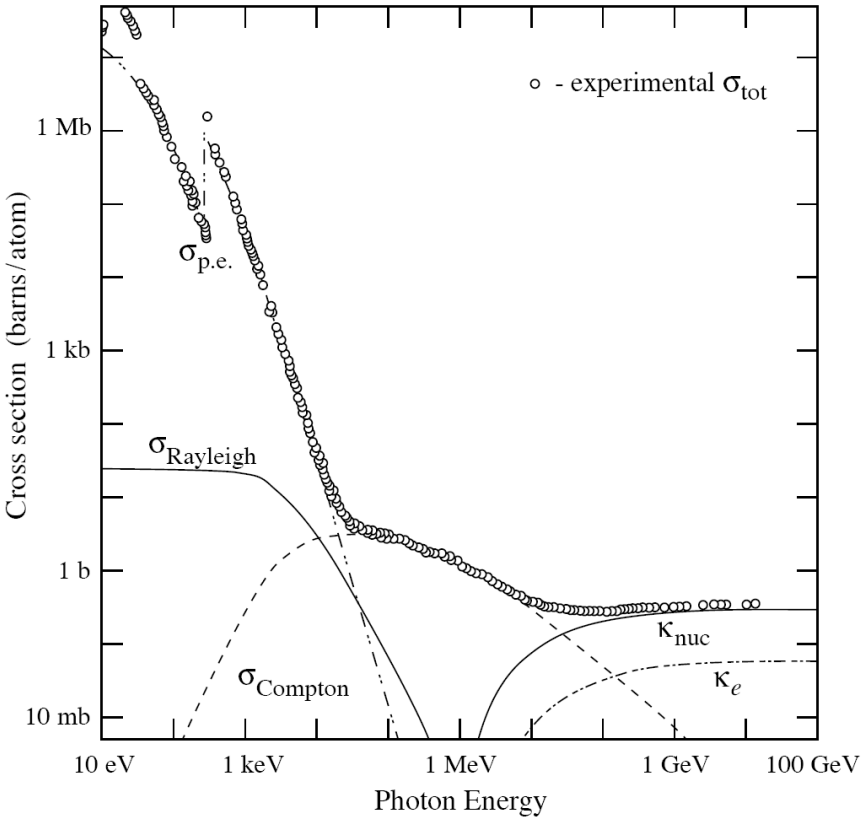

Figure 2.4: *Cross section of carbon for different processes as a function of the photon energy [24].* $\sigma_{p.e.}$ *is the photoelectric effect,* $\sigma_{Rayleigh}$ *is Rayleigh scattering,* $\sigma_{Compton}$ *is Compton scattering, and* κ_{nuc} *and* κ_e *are cross sections for pair creation of the nuclei and the electrons. Carbon is a common element in a gas mix used for TPC since hydrocarbons are commonly used as quencher gas. The importance of a quencher gas is explained in sections 2.1.3 and 2.2.1.*

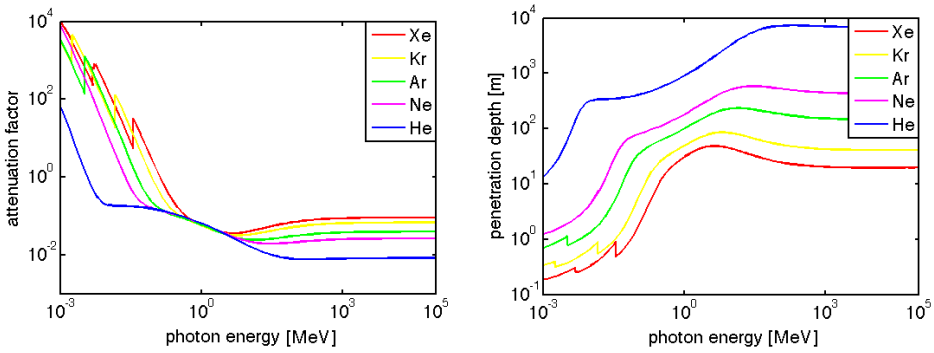

Figure 2.5: *X-ray absorption in different noble gases as a function of the photon energy [26]. Left: Attenuation of X-rays through 1 g/cm^2 of gas. Right: Depth of penetration in gases at one atmosphere (25° C) after which a fraction of 1/e is left.*

2.1.3 Drift

With no electric field applied, the kinetic energy[1] of molecules, atoms, ions and electrons in a gas is determined by the temperature. For each degree of freedom the thermal energy will be $\frac{1}{2}k_bT$ with k_b Boltzmann's constant and T the temperature in Kelvin. For three dimensions the translational thermal kinetic energy will be $\frac{3}{2}k_bT$ and for the velocities we can find:

$$\frac{3}{2}k_bT = \frac{1}{2}mv^2 \Rightarrow v = \sqrt{\frac{3k_bT}{m}}. \tag{2.3}$$

For room temperature the thermal energy will be approximately 0.04 eV which results in an average velocity of 11 cm/µs for electrons and a few 10^{-2} cm/µs for noble gas atoms. The direction of this velocity is randomised by collisions in the gas. By applying an electric field ions and electrons will obtain a net velocity in the direction of the field. P. Langevin [27],[28] formulated an equation of motion of electrons in gas under influence of an electric and magnetic field:

$$m\frac{d\vec{v_e}}{dt} = e\vec{E} + e\left(\vec{v_e} \times \vec{B}\right) - K\vec{v_e}. \tag{2.4}$$

The velocity of an electron (with charge e) is denoted as $\vec{v_e}$. Energy gained by acceleration in the drift field and energy lost by collisions will quickly reach an equilibrium which results in a net and constant drift velocity ($\vec{v_d}$) through the gas volume. The energy lost by collisions is described by the $K\vec{v_e}$ term. For a constant drift velocity the average of the left part of equation (2.4) is zero. K can also be written as m/τ in which τ is a characteristic time and m the electron mass. We can

[1] Vibrational and rotational modes of molecules are left out of consideration, only translational energy, which is measurable as velocity, is taken into account

also write $\frac{e}{m}B$ as ω, which is the cyclotron frequency [23]. The drift velocity can be expressed as:

$$\vec{v_d} = \frac{e}{m}\tau\left|E\right|\frac{1}{1+\omega^2\tau^2}\left(\widehat{E}+\omega\tau\left(\widehat{E}\times\widehat{B}\right)+\omega^2\tau^2\left(\widehat{E}\cdot\widehat{B}\right)\widehat{B}\right). \tag{2.5}$$

In case there is no magnetic field equation 2.5 reduces to:

$$\vec{v_d} = \frac{e}{m}\tau\vec{E} = \mu_e\vec{E}. \tag{2.6}$$

The drift velocity in equation (2.6) is the average net velocity in the drift direction gained between collisions. According $\vec{v} = \frac{\vec{F}}{m}t$, τ is the average time between collisions. μ_e is called the electron mobility. Equation (2.6) holds as long as electrons can be considered thermal. The time between collisions not only depends on $\vec{v_e}$ but also on the cross section of the atoms and molecules in the gas. For the noble gases Ar, Kr and Xe and small molecular gases it happens to be that the "Broglie wavelength" of an electron with an energy of a few tenths of an eV is close to the 'size' of those atoms. As a result of a quantum mechanical effect, the cross section drops and thus the mobility of electrons increases. This effect is called the Ramsauer effect [29].

As electrons drift through the gas they lose energy by collisions. In case of collisions with a noble gas the collisions are elastic up to an electron energy of a few eV. The average fractional energy loss of a particle with mass M_1 in an elastic collision with a particle with mass M_2 is according to:

$$f = \frac{2M_1M_2}{\left(M_1+M_2\right)^2}. \tag{2.7}$$

In case there is a large difference in mass ratio between the particles, M_1 and M_2, there is only very little loss of energy in a collision, as is the case with electron atom collisions. An electron can only lose a significant fraction of its energy on impact by excitation or ionisation of the atom it collides with, which starts at approximately 10 eV for noble gases. As a result electrons will gain energy from the drift field until they reach such energies. Because these electron energies are approximately hundred times more than 'room temperature' such a gas mix is called a 'hot' gas. A molecular gas can be added to reduce the average electron energy. The electrons can excite resonant states of the molecules that are only tenths of an eV, effectively cooling the electrons. Gases often used are CO_2 and hydrocarbons which are called quenchers. Quenchers also have to stabilise the gas gain discussed in section 2.2.1. Gas mixtures that keep electron energies low are called 'cold' gases. By keeping electrons cool one can benefit from the Ramsauer effect.

For ions the situation is different. Due to their mass, which is comparable to what they collide with, ions lose a larger fraction of their energy in a collision. Ion drift velocity is given by:

$$\vec{v_d} = \frac{e}{N\sigma_s}\sqrt{\frac{1}{M_1}+\frac{1}{M_2}}\sqrt{\frac{1}{3k_bT}}\vec{E} = \mu_i\vec{E}. \tag{2.8}$$

In equation (2.8) σ_s is the cross section, μ_i is the ion mobility and N is the number density. Ions remain thermal in much higher electric fields than electrons because ions lose about half the energy gained between collisions. Because of the 'low' velocities (compared to electrons) of ions associated with temperature, the drift velocity also is low.

2.1.4 Diffusion

If a point like cloud of electrons is 'released' in the gas, by diffusion it will form an expanding cloud with a Gaussian density distribution in all three directions with a Gaussian width:

$$\sigma = \sqrt{2t\left(\frac{2\epsilon\mu_e}{3e}\right)}. \tag{2.9}$$

With $\epsilon = 1/2 m_e {v_e}^2$ is the average kinetic energy of the electrons. To see how electron temperature affects diffusion one can rewrite equation (2.9), using (2.6), to see how it scales with electron velocity:

$$\sigma^2 = 2t\left(\frac{2\epsilon\mu_e}{3e}\right) = \frac{4}{3}\frac{\frac{1}{2}m_e {v_e}^2 \frac{e}{m_e}\tau}{e}t = t{v_e}^2\tau. \tag{2.10}$$

The average time between collisions τ can be related to a specific distance λ according to $\tau = \frac{\lambda}{v_e}$ and equation (2.10) can be expressed as:

$$\sigma^2 = t{v_e}^2\tau = t{v_e}^2\frac{\lambda}{v_e} = tv_e\lambda. \tag{2.11}$$

To reduce diffusion according to equation (2.11) electrons should be kept cool (to keep v_e low) and the time t, the drift time, should be kept short. Using equation (2.3), (2.6) and (2.9) the diffusion can be expressed as diffusion per unit length as a function of the drift field:

$$D = \sqrt{\frac{2k_bT}{eE}}. \tag{2.12}$$

Figure 2.2 shows the effect of diffusion. The trails are not sharp defined lines but clouds of points. As the δ ray gets closer to the chip, the electrons have shorter drift times and the diffusion becomes less. This can best be observed in the XY projection of the tracks. For further reading and a more detailed analysis about charge transport in gas one can read [23].

2.1.5 Applying a magnetic field

TPCs often are operated in a magnetic field to deflect charged particles going through. Deflection in a magnetic field makes it possible to determine the momentum and charge sign of a particle. Drifting electrons will also be affected by the magnetic field. A magnetic field not parallel with the drift field will alter the drift direction because of the Lorentz force experienced by the moving charge. For

a constant drift velocity, the Lorentz force and Coulomb force will reach an equilibrium resulting in a drift direction under an angle with the applied electric field. The angle of 'drift deflection' is called the Lorentz angle. This effect needs to be taken into account for track reconstruction. The electron drift velocity is described by equation (2.5). In case the magnetic field is perpendicular to the electric field the expression becomes:

$$\vec{v_d} = \frac{e}{m}\tau\,|E|\,\frac{1}{1+\omega^2\tau^2}\left(\widehat{E} + \omega\tau\left(\widehat{E}\times\widehat{B}\right)\right). \tag{2.13}$$

We can express equation (2.13) as a sum of the drift velocity in the direction of the drift field and the drift velocity in the direction of deflection, the 'Y' direction:

$$\vec{v_d} = \frac{e}{m}\tau\,|E|\,\frac{1}{1+\omega^2\tau^2}\widehat{E} - \frac{e}{m}\tau\,|E|\,\frac{1}{1+\omega^2\tau^2}\omega\tau\widehat{Y}. \tag{2.14}$$

Left of the - sign is the drift velocity in the direction of the electric field ($\vec{v_E}$) and the right part is the component in the direction of deflection ($\vec{v_y}$). For the Lorentz angle we can use:

$$\tan\left(\theta_{Lorentz}\right) = \frac{|v_y|}{|v_E|} = -\frac{\frac{e}{m}\tau\,|E|\,\frac{1}{1+\omega^2\tau^2}\omega\tau}{\frac{e}{m}\tau\,|E|\,\frac{1}{1+\omega^2\tau^2}} = -\omega\tau. \tag{2.15}$$

All electron movements perpendicular to the magnetic field will be deflected, the electrons tend to follow helical trajectories along the magnetic field lines. One can imagine that as long as an electron does not have a collision in the gas this trajectory is undisturbed and well confined around the magnetic field lines. The diffusion reducing effect can be noticed when the revolution time $\left(\frac{1}{\omega}\right)$ of the electrons becomes shorter than the time between consecutive collisions. The factor of reduction in diffusion is according to:

$$\frac{\sigma_{reduced}}{\sigma} = \frac{1}{1+\omega^2\tau^2}. \tag{2.16}$$

Maximizing ω can be achieved by using an as strong as possible magnetic field; τ will be increased if the average free path is increased and if the electrons are kept cool.

In general it is preferred to operate a TPC with the magnetic field parallel to the drift field to eliminate the Lorentz angle and to reduce diffusion.

2.1.6 Rate effects

The positively charged ions inside the drift region will drift towards the cathode. Those ions, however, drift approximately hundred times slower than the electrons and therefore tend to build up a net positive spatial charge. The build up of ions continues until an equilibrium is reached in which as many ions are neutralised as there are created. The electric field caused by the ions is superimposed on the applied drift- and amplification field. In the drift volume the tracks will be deformed and

in the gain region the gain may drop. The magnitude of the superimposed field can be determined by using Gauss Law:

$$\oint \vec{E} \cdot d\vec{A} = \frac{Q_{enc}}{\epsilon_0}. \tag{2.17}$$

The integral is over the surface area that encloses the charge Q_{enc}. Solving this is a very elaborate procedure in case the geometry is not spherical and the charge density distribution is not homogeneous. The effect is however of great importance for TPCs and is the main reason large volume TPCs cannot be used in a high rate environment. To make a TPC fit for a high rate environment the drift volume can be scaled down to reduce the time needed to extract the ions. A prototype of such a TPC is discussed in chapter 7.

Added to ions caused by primary ionisations are ions that come back from the gas amplification region which is called ion back-flow. The ion back-flow is proportional with primary charge and gas gain and is described by:

$$Q_{bf} = \eta_{bf} Q_{prim} G. \tag{2.18}$$

With Q_{bf} is the ion back-flow, η_{bf} is the fraction of ions that drift from the amplification region to the drift volume and depends on detector geometry. Q_{prim} is the primary charge and G is the gas gain. For the TPCs discussed in this thesis the ion back-flow fraction is in the order of 1% [31], [51]. Commonly used gas gains are between 10^3 and 10^5 so even for small back-flow fractions the amplification region is the major source of ions. Considering the ion back-flow the gas gain should be as low as possible. Another option is to use a gating grid. After the collection of the primary charge from the drift region the gating grid is set to a potential such that it collects all ions from the gain region. As long as the gating grid is switched on, charge from the drift volume will be prevented from reaching the gain region and will not be detected. Using a gating grid introduces a dead time as long as needed to collect the ions. This technique was applied in the STAR [33], ALEPH [34], and DELPHI [35] TPCs.

2.2 Gas amplification

2.2.1 The electron multiplication process

Electrons from the drift volume that arrive at the gain region will ionise the gas due to a local high electric field. The released electrons may, independently from the initial electron, release other electrons. The result is an avalanche process in which the number of drifting electrons is multiplied. This process amplifies charge from the drift region to make a measurable signal for the readout electronics. One can define an average distance between ionisations l_i. Starting with one electron the amount of electrons in an avalanche will be:

$$N_e = 2^{\frac{X}{l_i}}. \tag{2.19}$$

It can be said that after each length l_i the amount of electrons doubles. When expressed as a number of ionisations per unit length $a_i = \frac{1}{l_i}$ equation (2.19) becomes:

$$N_e = 2^{X a_i}. \tag{2.20}$$

X is the distance that the avalanche crosses. The parameter a_i depends on the electric field; a higher field results in more ionisations per unit length. In case the electric field also depends on distance, for example around a wire, one has to integrate over this distance for a_i. For that reason it is generally more convenient to solve:

$$dN = N(x)\,\alpha\,(E(x))\,dx. \tag{2.21}$$

The increase in the number of electrons dN is proportional to the number $N(x)$ of electrons already there and the local value of α. α is the Townsend coefficient and is related to the number of ionisations per unit length. In case of a homogeneous electric field the gas amplification will be:

$$G(X) = e^{(\alpha X)}. \tag{2.22}$$

Equation (2.22) is a good approximation for the gas amplification in a detector with a geometry presented in figure 2.1. In practice the amplification is determined by α, which depends on the electric field. The electric field is controlled by setting the voltage on the grid. Raether found that there is an upper limit in the amplification that can be reached. The negative charge that forms the front of an avalanche will increase the field strength between the avalanche and anode. As a result the electrons at the front will undergo a higher gas amplification and a runaway process may occur. Raether found an upper limit of 10^8 electrons for his experiments [36]. Since both the amount, and density, of charge affects this upper limit, the maximum avalanche size will also depend on detector geometry and the rate [37].

De-excitation and neutralisation of ions and atoms result in UV photons being emitted. UV photons are capable of releasing new electrons from the gas or electrodes by the photoelectric effect. The released electrons may also be amplified. This effect is called photon feedback and may result in disturbed proportional operation and even in discharges. To absorb the UV photons a molecular gas, called a quencher, is added. The quencher gas absorbs the photons without emitting an electron [40], [41].

Due to the exponential nature of the avalanche development, small variations at the start of an avalanche have a large effect on the total amount of charge arriving at the anode. If, for example, the first ionisation is one unit (l_i) 'late' the average amplification will be only half as large. Due to fluctuations the charge in avalanches will have a certain spread. In general the gas gain is defined as the average magnitude of the avalanches. A way to describe the spectrum of gas amplification in a uniform field was proposed by Byrne [42], [23] and is known as the Pólya distribution:

$$p(m, N) = \frac{m^m}{\Gamma(m)\,\overline{N}} \left(\frac{N}{\overline{N}}\right)^{m-1} e^{\left(\frac{-mN}{\overline{N}}\right)}. \tag{2.23}$$

In equation (2.23) N is the size of an avalanche, $\overline{N}$ is the average size of an avalanche and m is a dimensionless parameter that depends on field strength and detector geometry. Assumed is that the probability of releasing another electron is not always constant. After each ionisation the original and the released electron can be considered at rest and therefore travel a certain distance in which there is a reduced probability of ionisation [43], [44]. The probability of ionisation increases with drifted distance as the electron gains energy from the amplification field. This effect reduces the spread between avalanches. Figure 2.6 shows distributions for a gas gain of 5000 for three different values of m. For field strengths up to a few tens of kV/cm the value m goes to 1 and the distribution is exponential according to [45], [46]. For higher fields small avalanches become less likely and m increases. The Pólya distribution is a good representation of the gas gain statistics [47], [48].

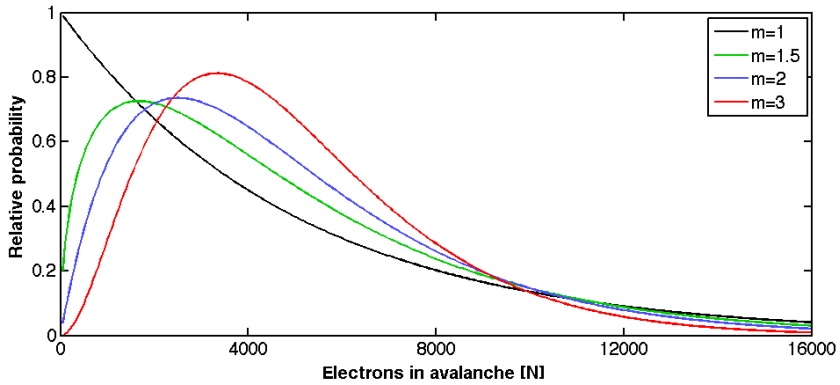

Figure 2.6: *Pólya distributions for a gas gain of 5000 for m=1 ($\sigma = 5.0 \times 10^3$), m=1.5 ($\sigma = 4.1 \times 10^3$), m=2 ($\sigma = 3.5 \times 10^3$) and m=3 ($\sigma = 2.9 \times 10^3$). With increasing m the most likely value approaches the average and the spread reduces.*

2.2.2 Signal induction

An avalanche results in an electric signal on the anode, which is read out by electronics. It is necessary to understand the signal originating from an avalanche in order to be able to optimise the electronics. The avalanche induces a fast, yet small, signal according to the electron drift velocity in the gain region. The ions, which are much slower, are 'left behind', their positive charge keeps most of the electron charge on the anode by induction. As the ions drift away from the anode the electrons will flow from the anode to the readout electronics, inducing the major part of the signal. As a result the signal is composed of two components, a fast and small component related to the avalanche development (collecting the electrons) and a slow and large component related to the drift of the ions.

Consider a potential difference ΔV between two parallel plates in between which an avalanche takes place. The work done on a charge by the electric field is:

$$W = Q\Delta V. \tag{2.24}$$

In order to keep the potential across the gap constant the work done can be expressed as:

$$Q\Delta V = V_{gap}\Delta Q. \tag{2.25}$$

If we call the distance between the plates L_{gap} and the distance of an ionisation to the anode d_i then the electron has to travel d_i and the ion has to travel $(L_{gap} - d_i)$ to the opposite plate. The work done on both the electron and the ion is:

$$W_e + W_{ion} = \left(-e\frac{V_{gap}d_i}{L_{gap}}\right) + \left(e\frac{-V_{gap}\,(L_{gap} - d_i)}{L_{gap}}\right) = -eV_{gap}. \tag{2.26}$$

For the magnitude of the signal it is not important where in the avalanche the ionisation occurs. For the time structure of the signal, however, it is important since the signal induced by the electrons is two orders of magnitude faster. The fraction of the signal induced by an electron is:

$$\frac{W_e}{W_e + W_{ion}} = \frac{d_i}{L_{gap}}. \tag{2.27}$$

Since the avalanche develops exponentially most ionisations occur close to the anode. For that reason most electrons only have to travel a fraction of the gap width (the average d_i is small). The ions must travel almost the entire length L_{gap}. As a result the drifting ions induce most of the signal. For the TPC discussed in the next chapter L_{gap} is 50 µm and the ion signal is in the order of 10-100 ns, depending on how heavy the ions are. For a gas gain of 1000 there are about 10 'steps' in doubling the number of electrons. At 5 µm above the anode the avalanche reaches approximately half its final magnitude. The height where an avalanche reaches half of its final magnitude will shift towards the anode for increasing gas gain.

2.3 Concluding remarks

There is not a single optimal mix of gases that can be chosen in advance. The optimal mixture depends on the application, detector geometry and the operating conditions. In general the fraction of gases with a strong electron affinity (like oxygen) should be kept at a minimum. A drifting electron that is captured by a neutral atom or molecule creates a negatively charged ion that has a drift velocity that is approximately two orders of magnitude less, resulting in a loss of time information. Another problem is that a negatively charged ion cannot be amplified by gas amplification and will therefore not be measured[2]. In case a TPC is operated in a magnetic field it is preferred to have the magnetic and electric drift field parallel to each other.

[2] Drifting ions suffer less from diffusion thus better preserve their position information. Research is performed on stripping electrons from negative ions as they reach the gain region in order to benefit from the lower diffusion [38].

Chapter 3

Pixel chips as TPC anode

Using a pixel chip for TPC readout can increase the spatial granularity with three orders of magnitude compared to common TPC readout structures. Common TPC readout anodes are composed of pads and/or wires spaced millimetres apart while the pixel chips discussed in this thesis have square pixels of 55×55 μm^2. Because of the small physical size of these inputs the capacitance is small and the electronics can be much more sensitive (i.e. have less noise) than electronics required to read out mm^2 sized pads or wires. Due to the high granularity and sensitivity it is possible to detect and distinguish single electrons along a track. One can use all individual primary electrons for track position reconstruction and for a detailed measurement of the energy loss, like displayed in figure 2.2.

In section 3.1 the working principles of a detector are explained. A chip designed to use for initial tests for TPC readout is the Timepix chip [49]. The Timepix chip will be discussed in section 3.2. Applying a gas amplification grid on top of a CMOS[1] chip involves MEMS[2] technology, which will be discussed in section 3.3. All detectors discussed in this thesis use the Timepix chip as anode readout unless otherwise noted.

[1] *C*omplementary *M*etal *O*xide *S*emiconductor
[2] *M*icro *E*lectro *M*echanical *S*ystems

3.1 Gridpix

Gridpix is the general name for the TPCs discussed in this thesis. The cross section of a Gridpix detector is similar to the sketch in figure 2.1. A photo of a partly cut through detector is shown by figure 3.1. From top to bottom the detector consists of a cathode, a drift volume, a grid, a gain region and a pixel chip.

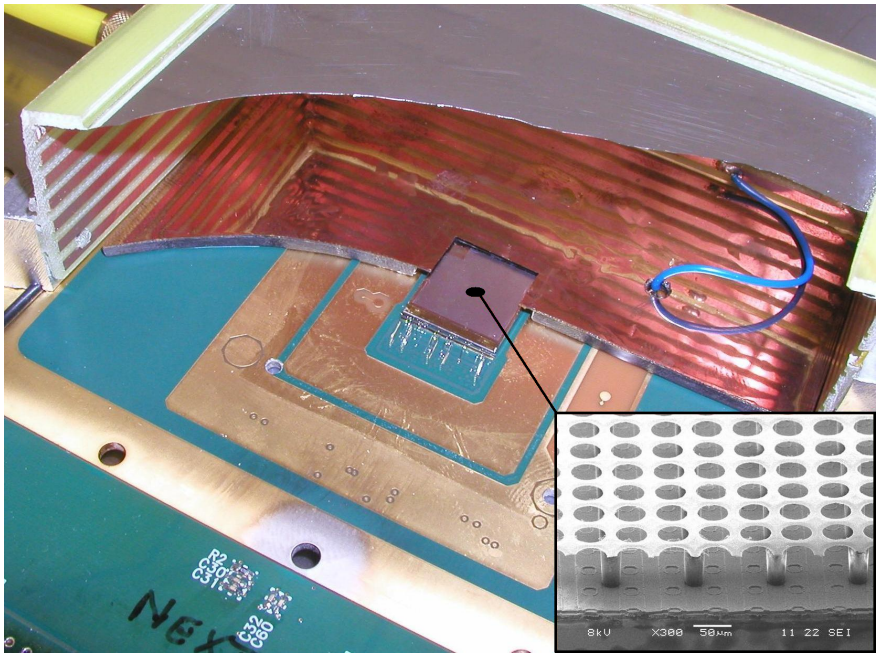

Figure 3.1: *A picture of a partially cut trough Gridpix detector with a Timepix chip. The inset is a SEM (*Scanning Electron Microscopy*) picture of a grid suspended above the chip on 50 µm tall pillars. The copper plane surrounding the chip and the copper strips on the side of the gas volume are electrodes to make the drift field homogeneous throughout the drift volume. The Timepix chip has a pixel matrix of 256 × 256 pixels on an area of 14 × 14 mm^2.*

Depending on the application, the length of the drift volume may be designed from a few meters down to only 1 mm. In a low rate environment, a large drift gap is preferred to capture long track segments at once. In a high rate environment, a small drift gap is required to reduce space charge effects due to ions. Another benefit is that all primary electrons can be extracted in a short time, preventing pile up of events that have to be read out. Below one mm drift gap, the probability that a MIP does not create ionisations becomes no longer negligible (sections 2.1.1 and 7.2.3).

Electron multiplication occurs in the high-field-region between the grid and the surface of the chip. The grid is a one µm thin aluminium sheet with holes, suspended

approximately 50 µm above the chip [50]. The holes are aligned with the pixel input pads and may vary between 10 and 40 µm in diameter. The inset of figure 3.1 shows a SEM (*S*canning *E*lectron *M*icroscopy) picture of a grid on top of a chip. Because of the high ratio between drift field and avalanche field, electrons from the drift region that approach the grid tend to be drawn in the nearest hole [51] and will then be multiplied (figure 3.2). Because of the fine pitch of the pixel chips (55 µm) and the high sensitivity of pixel electronics it is possible to distinguish and measure single primary electrons with a gas amplification of 2000.

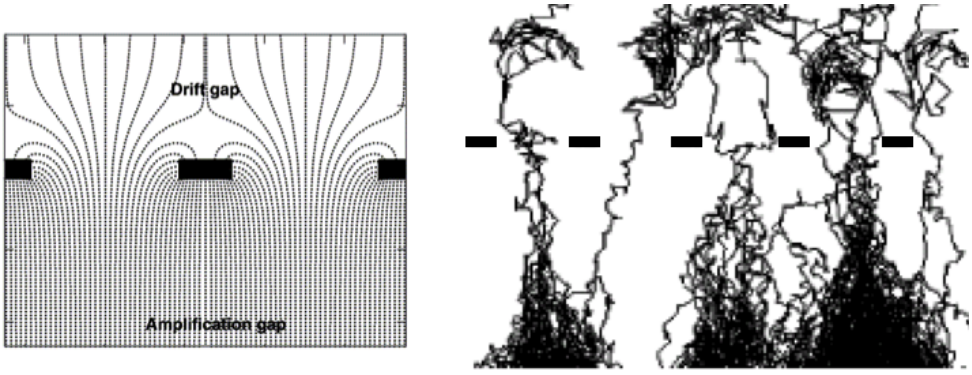

Figure 3.2: *Left: The field lines close to the grid. Electrons from the drift-gap tend be focussed into the holes of the grid. Right: a few simulated avalanches using the GARFIELD code [52]*

The concept to read out a TPC using a pixel chip with a grid directly on top of it was first tested in 2004 [53], [54] using a Medipix2 chip [55]. Figure 3.3 shows an event recorded with a Medipix2 chip. The Medipix2 chip is able to count how often a pixel is hit but cannot measure drift time. For that purpose the Timepix chip has been developed. The Gridpix detectors have been characterised using the Timepix chip. Small detectors with up to 8 chips [56] have been tested. In this thesis most of the detectors discussed use only 1 chip which is sufficient for initial studies.

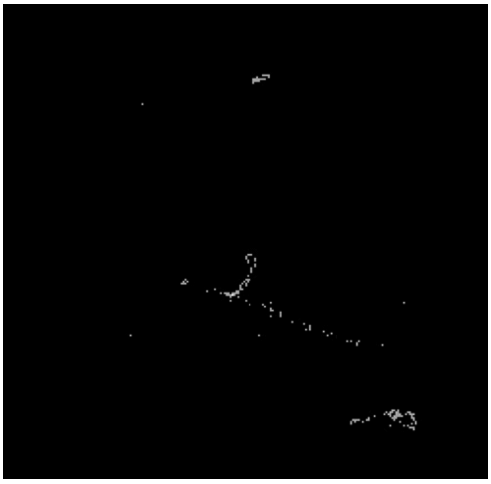

Figure 3.3: *One of the first recorded tracks (in 2004) with a Gridpix detector using a Medipix2 chip. The tracks were made by a cosmic ray and a δ-electron. The gas mix was He/iC_4H_{10} in a 80/20 ratio.*

3.2 The Timepix chip

3.2.1 Front end electronics

After the successful proof of concept by reading out a TPC using a Medipix2 chip, the Timepix chip was developed. To gain time and to save money the Timepix chip was designed using the Medipix2 [55] chip as base design. The chip has a pixel matrix of 256 × 256 pixels of 55 × 55 μm^2. Figure 3.4 shows a sketch of the functional blocks in the analogue part of a pixel.

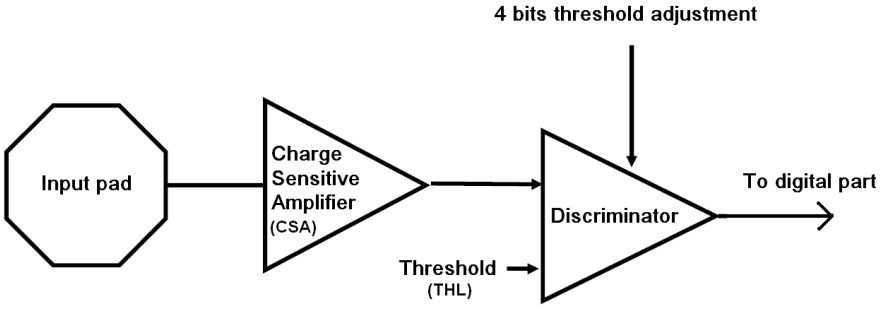

Figure 3.4: *Simplified diagram of the functionalities in the analogue front end of a pixel. Only parts relevant for the readout of the signals are shown.*

The pixel input amplifier is designed to have a sensitivity of 16 mV/ke (a ke is 1000 electrons) with an equivalent noise of approximately 100 electrons. To reduce the spread between pixels the baseline of each pixel can be adjusted. After equalising all pixels one threshold can be applied to set the sensitivity of the chip (THL in figure 3.4). The threshold can be set at approximately 700 electrons for noise free operation. The discriminator gives a signal as long as the output of the charge sensitive amplifier (CSA) is over the threshold. The signal from the discriminator is fed into the digital circuitry of the pixel. The digital circuitry can be set to measure the amount of charge arriving at a pixel by counting how many clock cycles the signal is over threshold, or the time a pixel is hit, or the number of hits [49]. A clock signal is distributed over all pixels. A 100 MHz clock is about the maximum frequency that can be used reliably and is used for all measurements described in this thesis. A detailed description of the development and specifications of the Medipix and Timepix chip can be found in [57].

3.2.2 Improving Timepix

The Timepix chip is not fully optimised for TPC readout yet, the following aspects can be improved:

- Noise. Reducing the noise reduces the required gas gain, effectively making the chip more sensitive.
- Drift time resolution. The time resolution can be reduced from 10 ns down to about 1.5 ns. Below 1.5 ns, diffusion in the drift direction will, in most cases, be the dominant uncertainty in drift time.
- Time walk. A delay, depending on the amount of charge in an avalanche, is added to the measured drift time. Measuring simultaneously the drift time and time over threshold makes it possible to correct for that. Time walk will be discussed in section 4.3.1.
- Power consumption. The power consumption per pixel can be reduced.

To address these issues new pixel electronics have been developed and prototype chips have been produced to test new circuit concepts. Successful designs will be implemented in the successor of the Timepix chip, the Timepix3[3] which will also contain technology applied in the newest Medipix chip, Medipix3 [58].

One of the chips to test new pixel electronics is the Gossipo2 [59], it contains a matrix of 16×16 pixels. The issues addressed are the power consumption, sensitivity and drift time resolution. The sensitivity of the pixel electronics is approximately 50 mV/ke with an equivalent noise of 70 electrons. In anticipation of synchronous operation with the LHC a master clock of 40 MHz is used. The 40 MHz signal is distributed over all pixels. To increase time resolution a fast 560 MHz oscillator is

[3] There is no Timepix2 chip. The newest Medipix chip currently available is the Medipix3. To stay synchronous with the Medipix design, the next Timepix chip to be developed is called the Timepix3 chip.

added to each pixel. When a pixel is hit the fast oscillator starts running and a counter counts the clock cycles of the fast counter (1.8 ns) until the first rising edge of the 40 MHz clock. After the first rising edge of the master clock the fast oscillator and its counter stop. Then another counter starts to count clock cycles of the master clock. When the chip is read out the pixels contain drift time information as the sum of a number of 25 ns (master clock) time bins and 1.8 ns (fast oscillator) time bins. Reduction in power consumption has been achieved by having a fast clock running for only a fraction of the acquisition time and only for the pixels that have been hit. Time walk correction is addressed in the Gossipo3 chip [60]. With the Gossipo3 the time over threshold can be measured simultaneously with the drift time. The Gossipo3 chip contains only one pixel to test the electronic circuitry. Measurements with respect to time walk correction will be discussed in section 4.4.

3.3 Wafer post processing

The first gridpix detectors were made by manually placing a micromegas [50] on top of a chip. Subsequently a method based on photo lithography was developed. This is called wafer post processing; a structure is added on top of the chip. A grid produced in this way is called an InGrid (derived from *In*tegrated *Grid*) [32]. The most mature process at present is the production of an aluminium grid supported by a SU-8 structure. SU-8 is a photo-resist with mechanical and chemical properties such that it can also be used as a part of a permanent structure. A sketch of the steps in the process is shown by figure 3.5.

1 One starts with a wafer (or a part of a wafer) containing multiple chips as they come from the factory.

2 A high resistivity Silicon Rich Nitride (SiRN)[4] layer is deposited, serving as protection against discharges and will be discussed in chapter 5.

3 An approximately 50 μm thick layer of SU-8 photo-resist is applied.

4 The SU-8 is exposed with UV light through a mask. In a later stage the illuminated pattern will form the supporting pillars for the grid.

5 An aluminium layer of approximately one μm is deposited.

6 On top of the aluminium a photo-resist is applied and exposed to UV light through a mask. The pattern will define the holes in the grid and should be precisely aligned with the pixel input pads.

7 The photo-resist on top of the aluminium is developed and the aluminium that has to be etched away is exposed.

8 The holes in the aluminium are etched.

[4] Silicon Rich Nitride is normal Silicon Nitride (Si_3N_4) doped with extra Silicon to make it conductive.

9 Dicing of the wafer or groups of chips to obtain single chips, this has to be done while the structure on top is still mechanically robust.

10 For each individual chip the unexposed SU-8 is dissolved. The remaining structure supports the aluminium grid.

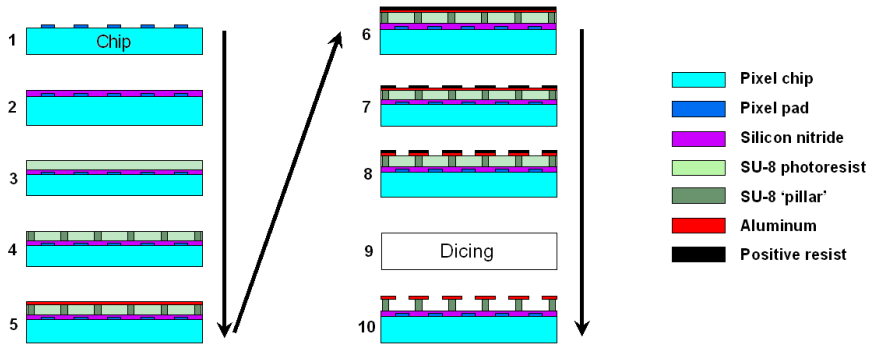

Figure 3.5: *Sketch of the cross-section of a chip in the different phases of grid production.*

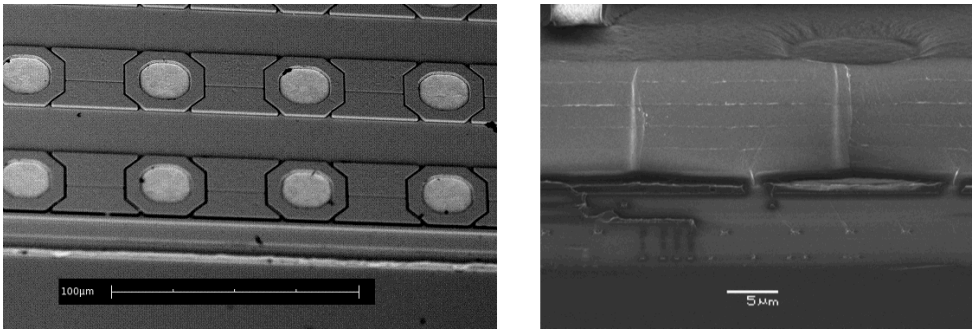

Figure 3.6: *Left: SEM image of the surface of an unprocessed chip, showing exposed pixel input pads. Right: SEM image of a cross section of a chip on top of which 12.5 µm SiRN has been deposited in five runs.*

A SEM image of a finished InGrid is shown by the inset in figure 3.1. A detailed description of the process and material studies can be found in [61]. The detectors presented in this thesis all use Timepix chips that were processed according these steps.

For future Gridpix detectors a process is under development to produce a full ceramic device, a highly resistive grid supported by a SiO_2 (glass) structure. The advantage is that discharges are likely to be quenched better than with an aluminium grid and the detector is potentially mechanically more robust. Applying a sufficient thick layer of the supportive structure without destroying the CMOS chip during the process is challenging. Patterning of both the ceramic grid and its support is difficult because of the chemically inert nature of the used materials. First tests with a glass support and aluminium grid have successfully been performed on a dummy anode (plain silicon with an aluminium anode) and on a Timepix chip [62]. Eventually the aim is to produce a chip with a SiRN protection layer, a glass (or a similar material) grid support and a SiRN grid.

Chapter 4

Signal development

The response of the (analogue) pixel electronics to signals originating from electron avalanches is of great importance for the efficiency of detecting primary electrons and the accuracy of avalanche timing. An accurate avalanche timing is required for an accurate drift time measurement. Signals in pixel electronics have been simulated to study how to improve the accuracy in avalanche timing. Section 4.1 discusses the response of the pixel amplifier to the electron avalanches. The next section (4.2) discusses the method to use the time a signal is over threshold to determine the amount of charge in an avalanche. Variations in avalanche size and the finite response time of the pixel amplifier result in an error in avalanche timing, called time walk. Time walk can be compensated for when the magnitude of the signal is known. Time walk is discussed in section 4.3.

4.1 Gas amplification and amplifier response

4.1.1 Time structure of an avalanche

In a homogeneous electric field, charge in an avalanche develops exponentially according to equation (2.19) in section 2.2. In order to approximate the signal induced on a pad a simulation is performed in which the avalanche develops between parallel plates 50 µm apart and is longitudinally divided in steps in which the number of drifting electrons doubles. The number of amplification steps is varied as a function of the gas amplification. The simulation results shown in figure 4.1 and 4.2 are for a gas mixture of Ar/iC_4H_{10} in a ratio of 80/20 and with a voltage of 410 V across the gap. To obtain the drift velocity of electrons the simulation results from MAGBOLTZ [63] are used. To simplify the simulation it is assumed that the Ar^+ ions carry all charge. Figure 4.1 shows the longitudinal charge distribution in the amplification region at four different times.

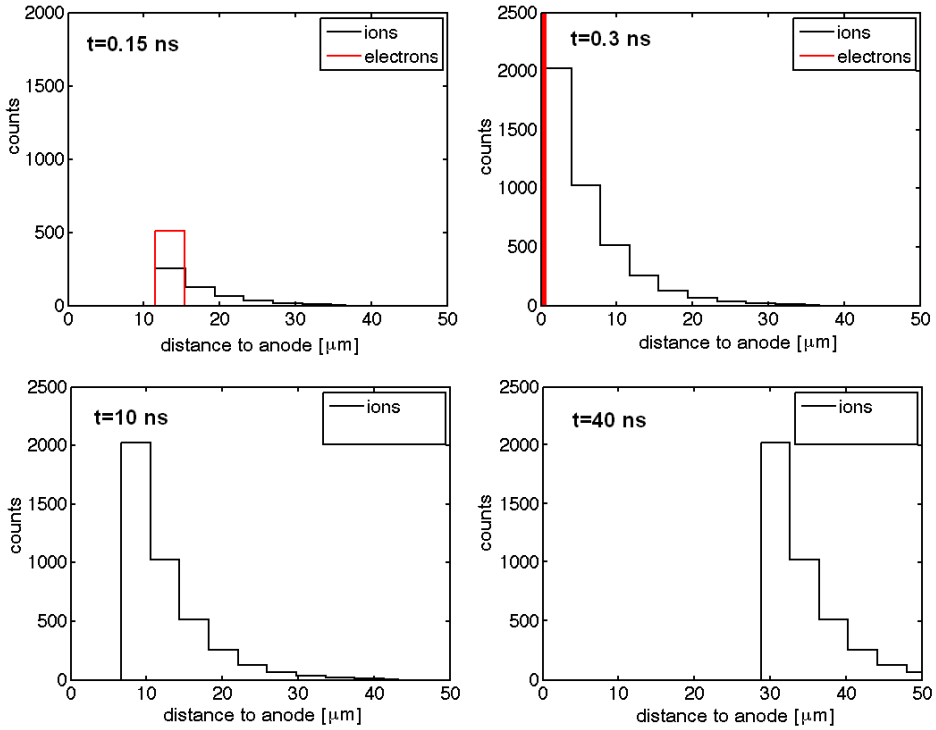

Figure 4.1: *Simulation of an avalanche and ion drift in an Ar/iC_4H_{10} 80/20 gas mixture. The graphs show the amount of charge as a function of the distance to the anode at four different times. At t=0 the avalanche starts with one electron, starting 50 μm from the anode, and ends with approximately 4000 electrons at the anode. The top left graph shows the avalanche after 0.15 ns. After 0.3 ns the avalanche process is finished, the electrons arrived at the anode (top right graph). After the avalanche the much slower drifting ions drift to the cathode, shown by the bottom left (after 10 ns) and bottom right graph (after 40 ns). In the graphs at the bottom the electrons at the anode are not shown. The Y axis is set to 2500 to better show the ion movement. The discrete steps in the graphs are due to the fact that for the electron multiplication the gap is divided in slices of equal thickness in which the number of electrons double. The drift velocity of the ions is 0.07 cm/μs [64] and the drift velocity of electrons is 20 cm/μs. Only the Ar^+ are taken into consideration. The voltage across the gap is 410 V, resulting in an average gas gain of 4000.*

Figure 4.2 shows the current induced by the movement of the charge in the gap. The signal induced by the drifting Ar^+ ions takes approximately 70 ns. Lighter ions like He^+ drift across the gap in 15 ns and heavy ions like Xe^+ need approximately 150 ns. In a gas mix composed of different gases the induced current will be the superposition of the currents induced by the different fractions of ions. For all simulations presented, a signal with a time structure like shown by figure 4.2 is used

unless otherwise noted. Larger or smaller avalanches are approximated by varying the amplitude.

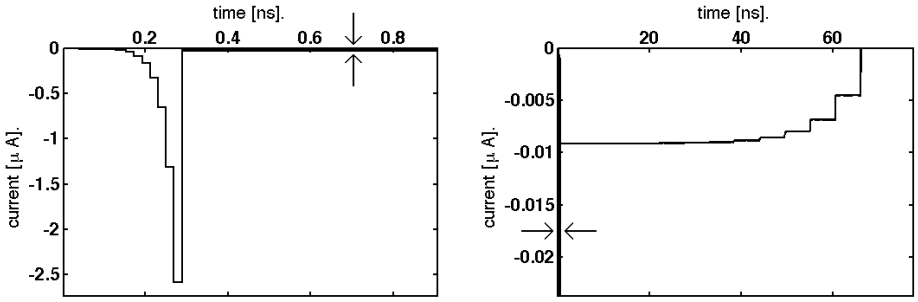

Figure 4.2: *The current induced by the drifting charge shown by figure 4.1. In the left graph the fast electron signal can be seen. The electron signal is completed in approximately 300 ps. The right graph shows the current induced by the drifting ions. In each graph the arrows point out what is shown by the other graph. The integral of the ion current is approximately 3400 e^- and the integral of the electron part is 600 e^-. Only 15 % of the signal is induced by the moving electrons and this fraction becomes smaller for larger avalanches (see section 2.2.2 for the signals induced by an avalanche and drifting ions).*

4.1.2 Pixel amplifier response

Two simplified models of a Charge Sensitive Amplifier (CSA) have been used to simulate signal development. Both are charge integrators, one with an RC network in the feedback line and one that has the resistor replaced by a current source which only conducts current in case there is a voltage across. The feedback with the current source is called a constant current feedback, denoted as CC feedback[1]. Figure 4.3 shows the two (simplified) circuits. In IC technology a current source can be made with one transistor and is physically smaller than a high ohmic value resistor. A current source is also more flexible; the current can be set at a desired value at any time. For that reason, in practice, a current source is preferred. However, the RC network offers some advantages as will be shown in section 4.3.2. In this thesis, the baseline voltage is considered to be zero volt. In practice the baseline will be between zero and the chip supply voltage.

[1] This should not be confused with current feedback, a commonly used concept in which the feedback current is proportional to input voltage.

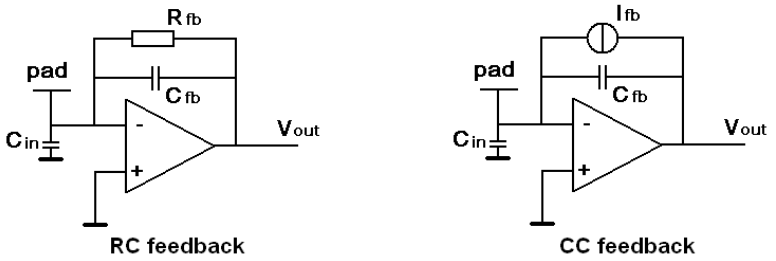

Figure 4.3: *Left: A charge integrator with RC feedback. Right: A charge integrator with a current source in parallel with the feedback capacitor. The current source only conducts current in case there is a potential across. C_{in} is the total capacitance at the input of the amplifier.*

The impulse response of the charge sensitive amplifier is defined by how it responds to a delta pulse, i.e. an instantly deposited amount of charge on the input capacitance (C_{in}). For an amplifier with an RC feedback the impulse response is:

$$U_{out}(t) = \frac{Q_{in}}{C_{fb}} \left(e^{-\frac{t}{\tau_1}} - e^{-\frac{t}{\tau_2}} \right). \tag{4.1}$$

The amplifier response time is τ_1. The relaxation, or integration, time is τ_2. The charge-to-voltage conversion of the amplifier is defined by the feedback capacitor. Charge at the input pad will be integrated onto the feedback capacitor resulting in an output voltage of Q/C_{fb}. An amplifier with a CC feedback has no constant integration time. The integration time is determined by the current and the amount of charge at the input. The impulse response for a circuit with constant current feedback is:

$$U_{out}(t) = \frac{Q_{in}}{C_{fb}} \left(e^{-\frac{t}{\tau_1}} - 1 + \frac{1}{Q_{in}} \int I_{fb}(t) dt \right). \tag{4.2}$$

In equation (4.2) the current (I_{fb}) becomes zero when the output returns to baseline level, giving it an RC like behaviour when the output is close to the base line (figure 4.4). For simulations $1/C_{fb}$ is set to unity since we are only interested in the sensitivity in equivalent charge at the input. Figure 4.4 shows the response of the RC feedback and the CC feedback to a δ pulse with a charge of +5000.

The sensitivity of a pixel is defined by how little charge in a delta pulse can still be detected. In practice however, an input signal has a duration of tens of ns. Due to the current in the feedback loop a fraction of the charge in the feedback capacitor (C_{fb}) will be drained before the signal peaks. As a result an increasingly smaller fraction of the charge will be integrated for increasingly longer signals, effectively reducing the sensitivity for long signals. Figure 4.5 shows the response of the CC feedback circuit and the RC feedback circuit to a charge of 1000 electrons in a delta pulse and avalanches in helium, argon and xenon gas.

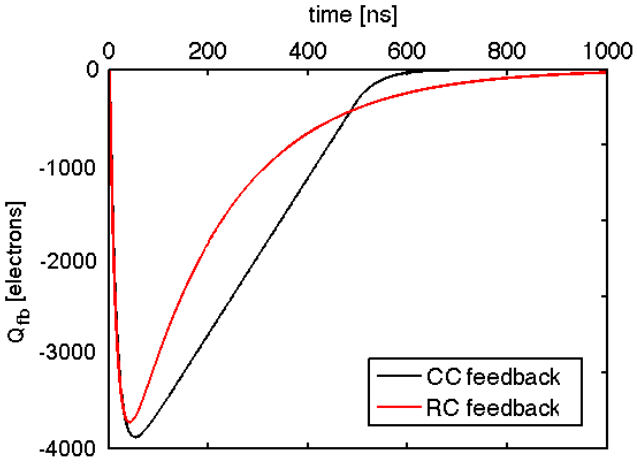

Figure 4.4: *Impulse response of a charge sensitive amplifier with RC feedback (red curve) and CC feedback (black curve). In both cases τ_1 is 15 ns. For the RC feedback, τ_2 is 300 ns. Q_{fb} is the charge in the feedback capacitor.*

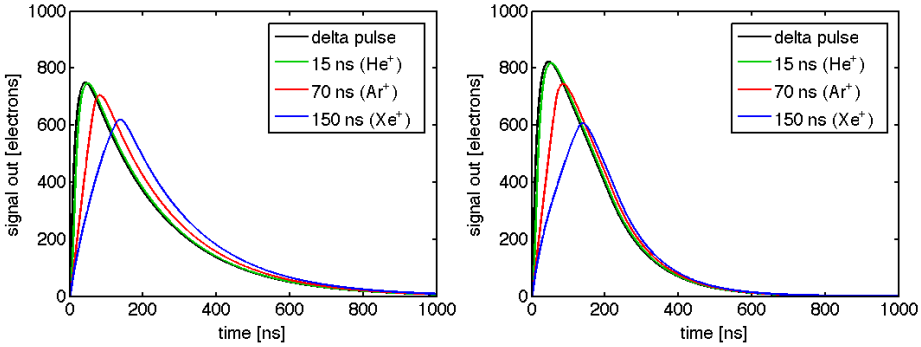

Figure 4.5: *Response to signals of 1000 electrons in a δ pulse and in three different gases that have different ion drift times. Left graph: the response of the RC feedback circuit. Right graph: The response of the CC feedback circuit. The constant current source starts to conduct less current in case less than 300 electrons are stored on the feedback capacitor.*

For the simulations described in this thesis a response time (τ_1) of 15 ns is set. No signals shorter than 15 ns are to be expected, making the amplifier faster will only increase the noise. The ENC (equivalent noise charge) is 70 electrons RMS, which is quite low but expected to be feasible due to the small input capacitance. Noise is discussed in more detail in the section 4.1.3. The current in the CC feedback loop is 1 nA. Those numbers are based on the specifications that near future pixel electronics (Timepix3) are designed to have. For the circuit with RC feedback a

RC time (τ_2) of 300 ns is chosen, which is twice as long as the longest signal to be expected. The time bins in the simulations are 0.2 ns. Due to the low noise level the detection threshold is set at 350 electrons. Those numbers apply for all shown simulation results unless otherwise noted.

4.1.3 Pixel amplifier noise

The output signal from the charge sensitive amplifier (CSA) is generated by convolution of the input signal (electron and ion movement) with the amplifiers δ pulse response. The obtained signal does not yet contain any noise. The noise is added afterwards by superimposing it on the CSA's output signal. The noise must be of the correct magnitude (70 electrons RMS) and should have the proper frequency components corresponding to the amplifier's frequency response. The noise behaviour of the RC feedback circuit is assumed to be a good approximation for the noise behaviour of the CC feedback circuit. Modelling the noise in the RC feedback circuit is less complex than for the CC feedback circuit and for that reason only the RC feedback circuit is used for the simulation of the noise. All noise sources can be represented by sources at the inputs of the CSA. Figure 4.6 shows the noise equivalent circuit for the RC feedback circuit.

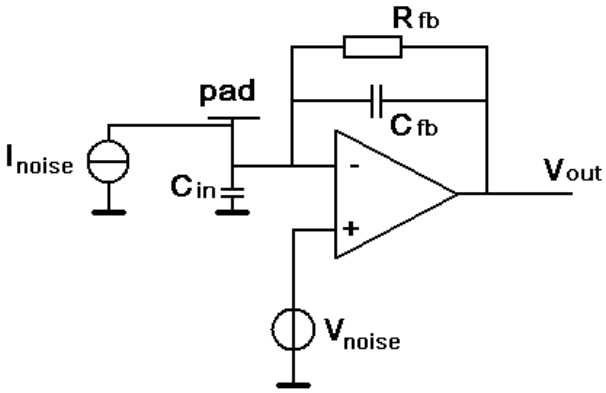

Figure 4.6: *Noise equivalent circuit. A noise current is added to the current input of the amplifier. A noise voltage is represented by the source at the non-inverting input.*

The noise at the output is assumed to be Gaussian. For noise with the correct frequency components one has to observe the frequency depending behaviour of the CSA. The frequency response of the inverting input is:

$$U_{out-}(i\omega) = -I_{in}\frac{R_{fb}}{1+i\omega R_{fb}C_{fb}}\frac{1}{1+i\omega\tau_1}. \tag{4.3}$$

The frequency response of the non inverting input is according to:

$$U_{out+}(i\omega) = V_{in}\left(\frac{i\omega R_{fb}C_{in}}{1+i\omega R_{fb}C_{fb}}+1\right)\frac{1}{1+i\omega\tau_1}. \tag{4.4}$$

In equation (4.4) the input capacitance (C_{in}) is in the numerator and this is why it is so important to minimise input capacitance to minimise noise. The voltage noise (U_{out+}) is the dominant noise component [65]. The amplifiers gain curve (for U_{out+}) is shown by figure 4.7.

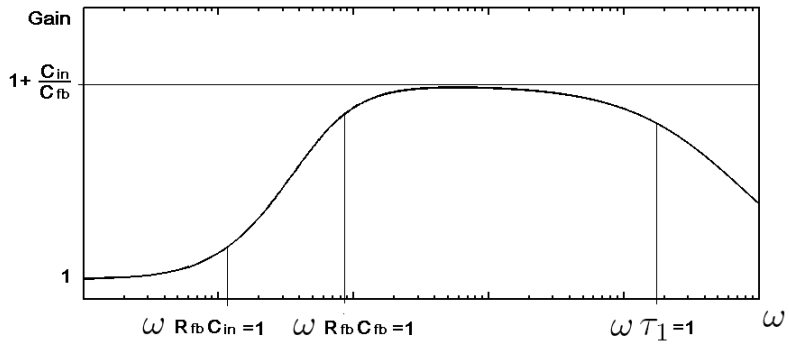

Figure 4.7: *Relative gain of signals on the non inverting input of the CSA. This is the frequency spectrum of the noise that is on the output of the amplifier. At frequencies where the impedance of the input capacitance becomes equal or less than the feedback resistor, the gain increases. At frequencies where the impedance of the feedback capacitor becomes equal or less than the feedback resistor, the gain will be determined by the ratio of the input capacitance and the feedback capacitor. For even higher frequencies the gain drops due to the response time of the amplifier.*

Wide band white noise is generated which is filtered according to equation (4.4). The resulting noise, that now has the correct frequency components, is added to the signal at the output of the CSA. The noise can be scaled in amplitude to match a required RMS value. A signal from an avalanche of 4000 electrons with 70 electrons ENC results in a signal like shown in figure 4.8.

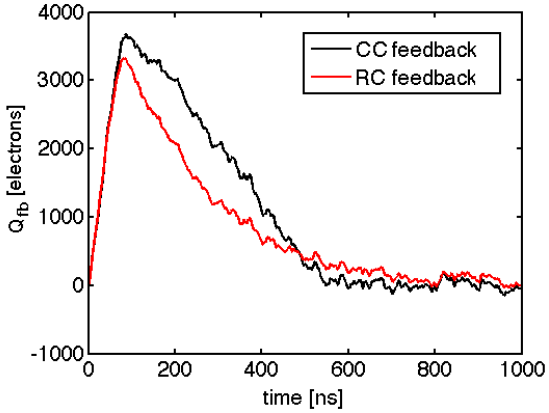

Figure 4.8: *The response of the CC feedback (black curve) and RC feedback (red curve) circuit with 70 electrons ENC to a signal of 4000 electrons with a duration of 70 ns. Due to the current in the feedback loop, not all 4000 electrons are integrated in the feedback capacitor.*

4.2 Electron detection

The signals from the charge sensitive amplifier are fed into a comparator that gives a signal when the input is above the threshold. As mentioned in section 3.2, circuitry in a pixel can register how long a signal is over the threshold. The time a signal is over threshold depends on signal amplitude and therefore can be used to determine the amount of charge in an avalanche. Measuring time over threshold is the most space efficient way to do 'amplitude' measurement on a small 55×55 μm^2 pixel that has only limited space.

4.2.1 Time over threshold

With the threshold set at 350 electrons and no electronic noise, the time over threshold (TOT) as a function of the input charge is shown by figure 4.9. For the CC feedback circuit the relation between TOT and avalanche size is linear over a large range, for the RC feedback circuit the relation has a logarithmic dependency. If, due to noise, a signal crosses the threshold more than two times only the first TOT will be counted. This may result in relatively large signals sometimes having a short TOT.

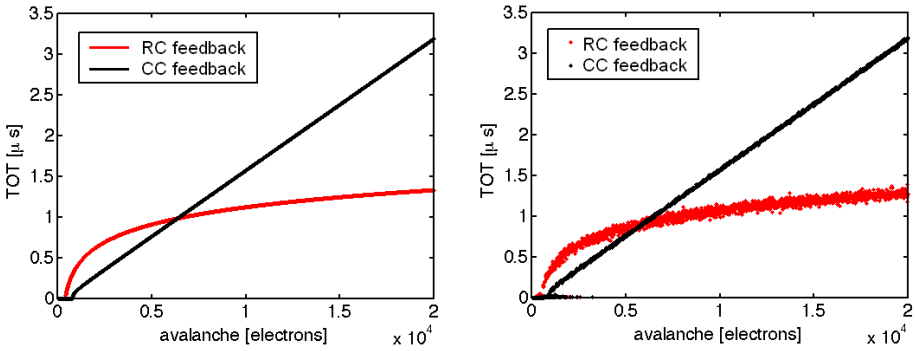

Figure 4.9: *Left: Time over threshold (TOT) as a function of the input charge for RC feedback and CC feedback. The current in the CC feedback loop was set to 1 nA, τ_2 is set to 300 ns. This is due to the fact that, for small signals, the current in de CC feedback is larger than in the RC feedback. The TOT for the RC feedback has a logarithmic dependency. Right: TOT as a function of the input charge for RC feedback and CC feedback with 70 electrons ENC superimposed on the signals. The TOT of the RC feedback appears noisier than the TOT of the CC feedback. This is due to the fact that for the falling slope, when crossing the threshold, the change in voltage over time for the RC feedback is less than for the CC feedback (figure 4.8).*

4.2.2 Single electron detection efficiency

An important aspect in detector performance is the single electron detection efficiency. One would like to detect all primary electrons entering the gain region. However, due to the fluctuations in the magnitude of the avalanches a fraction will be below the threshold (THL) and hence remain undetected. For a certain gas gain the detected fraction (η_{det}) will be, using equation (2.23):

$$\eta_{det} = \frac{\int_{THL}^{\infty} p\,(m,N)\,dN}{\int_{0}^{\infty} p\,(m,N)\,dN}. \tag{4.5}$$

The fraction of electrons that will be detected as a function of the gas gain divided by the threshold is plotted in figure 4.10. It is assumed is that all charge is applied in a time that is shorter than the response time of the amplifier (δ pulse). In case the duration of the signals is longer than the response time of the amplifier the amplitude at the output will decrease with increasing signal length (illustrated by figure 4.5). As a result one will need a higher gain for gases with longer ion drift times. The curves in figure 4.10 will be stretched in the X direction: One needs a higher gain/threshold ratio to obtain the same sensitivity.

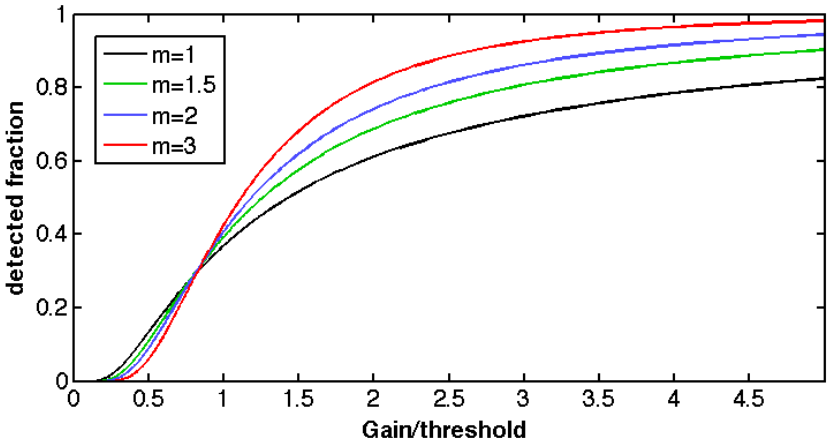

Figure 4.10: *Single electron detection efficiency as a function of the gas gain/threshold for Pólya distributions with different values of the parameter m like shown by figure 2.6 in section 2.2. Note that the detection efficiency for a gain/threshold ratio of approximately 0.8 is independent of the parameter m. This feature is used in chapter 6 (section 6.1.3) to both determine the detection efficiency of a Gridpix detector and the value of parameter m.*

4.3 Time walk

4.3.1 Fluctuations in avalanche timing

Due to the time a signal needs to reach detection threshold an avalanche will be detected with a certain delay. This delay is called Time to Threshold (TtoT) and depends on the signal amplitude and peaking time. The peaking time is determined by the amplifiers response time and the ion drift time. There is no significant difference between the CC feedback and the RC feedback circuit in TtoT as a function of the input charge. Figure 4.8 illustrates that the rising edge of signals for both circuits are equal. The signal amplitude is determined by the avalanche size. The shift in time of detection related to variations in amplitude is called time walk and adds an error to the measured avalanche time. The noise in the electronics adds another error in timing and is referred to as jitter. Figure 4.11 shows the relation between amplitude and TtoT. For all further simulations presented signals with noise superimposed are used unless otherwise noted. In this chapter the CC feedback circuit is the default circuit for simulations and when relevant, the comparison with the RC feedback circuit is made.

Time walk reduces the accuracy of track reconstruction in the drift direction. Figure 4.12 shows two reconstructed tracks in a Gridpix detector for two different gas gains. One can see by eye that the track recorded with a low gas gain is less defined in the drift direction than the one recorded with a high gas gain.

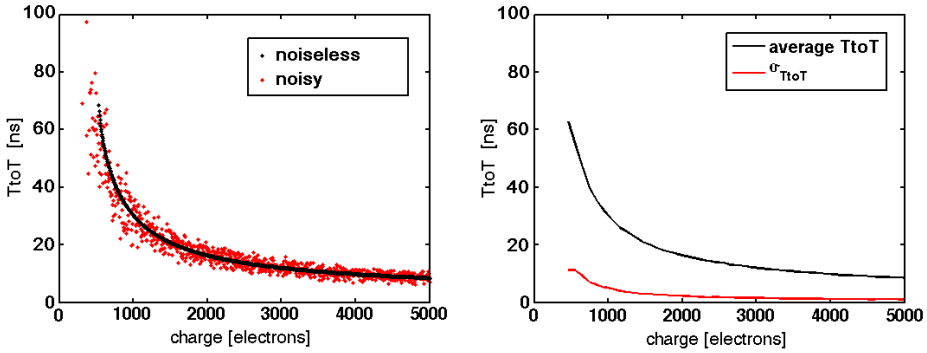

Figure 4.11: *Left: The time to threshold (TtoT) for the CC feedback circuit as a function of the charge in an avalanche. The black dotted line is for a noiseless amplifier. The red dots is with 70 electrons ENC superimposed on the signals. Right: The red line shows the width of the distribution of TtoT (σ_{TtoT}) as a function of the charge at the input (the width of the band of red dots in the left graph). For 400 electrons σ_{TtoT} is 12 ns, for 5000 electrons σ_{TtoT} is one ns. The simulation was performed with 500 samples per bin of 100 electrons. The black line is the reconstructed average TtoT based on averaging over the samples in each bin.*

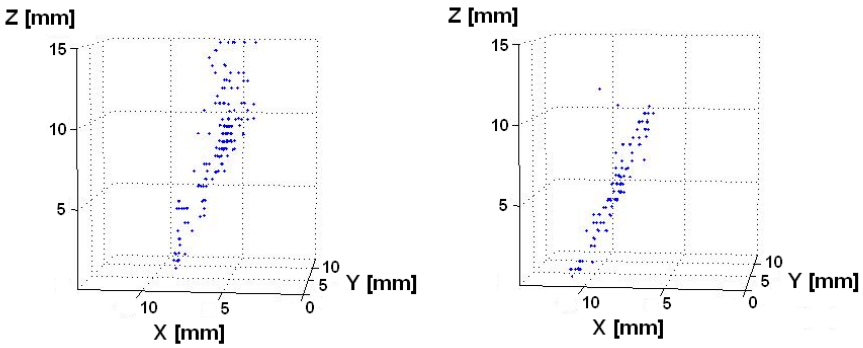

Figure 4.12: *Tracks of 2 GeV/c electrons in a Gridpix detector with a 11 mm drift gap. The pixel amplifiers in the Timepix chip have a response time of 120 ns (opposed to the 15 ns response time used in the simulations). The left track was recorded with a gas gain of 4000, the right track with a gas gain of 13000. Time walk effects can best be observed in the left picture, some electrons even appear to have drifted further than the total length of the drift gap. Due to a higher gas gain, time walk effects in the right picture are notably less i.e. the track appears to be well defined in the drift direction. The drift time is sampled in time bins of 10 ns, resulting in the discrete steps in reconstructed drift distance. The gas mixture was Ar/iC_4H_{10} in a ratio of 80/20. The measurement was performed at DESY in Hamburg.*

Ion drift time may be considered constant since it depends on grid voltage, distance and gas mixture, which are all factors that remain constant during detector operation. However, the magnitude of the avalanches fluctuate according to a Pólya distribution, resulting in a spread of recorded TtoT. As a result of this spread, in addition to jitter, there will be an additional uncertainty in avalanche timing. Figure 4.13 shows the time to threshold spectrum for a gas gain of 3000 for electrons with zero drift time. The average TtoT and the width of this distribution becomes smaller for increasing gas gain.

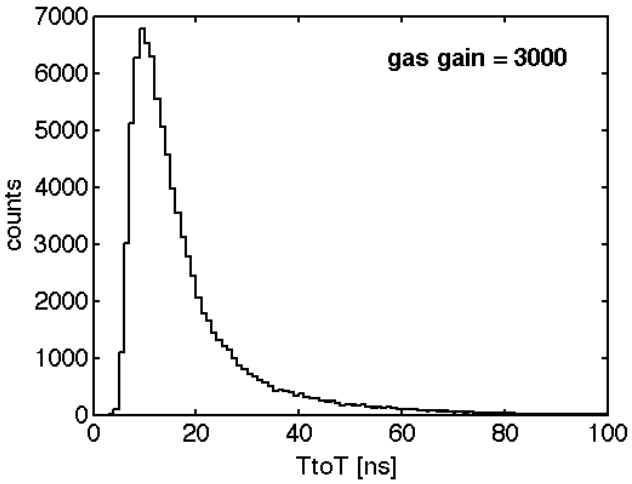

Figure 4.13: *Time to threshold (TtoT) spectrum for a Pólya distributed charge spectrum matching a gas gain of 3000 (CC feedback circuit). The average is 17 ns and the width (σ_{TtoT}) is 12 ns.*

Assuming that the gas gain is a known quantity when operating a detector the average time walk also is assumed to be known. In this thesis the avalanche timing resolution is defined as the width (σ_{TtoT}) of the TtoT spectrum. As figure 4.13 shows this spectrum is not Gaussian, σ_{TtoT} is calculated according to:

$$\sigma_{TtoT} = \sqrt{\frac{1}{N}\sum_{i=1}^{N}(x_i - \overline{x})^2}. \tag{4.6}$$

Figure 4.14 shows the average TtoT and accuracy (σ_{TtoT}) for gas gains between 1000 and 10000. The next section (4.3.2) focuses on how to improve avalanche timing resolution.

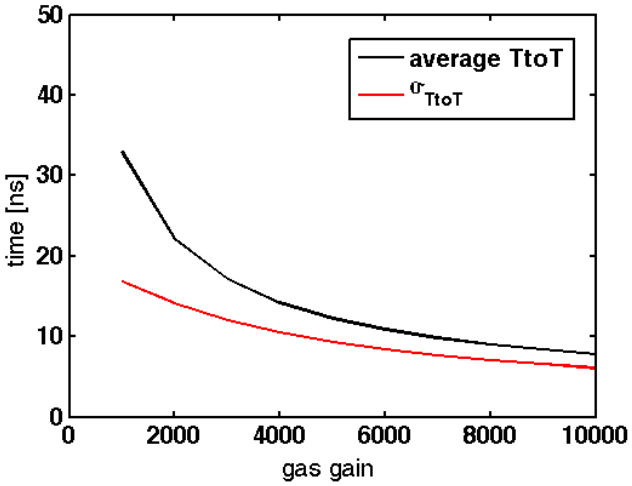

Figure 4.14: *Average time to threshold (TtoT) and TtoT resolution (σ_{TtoT}) for gas gains in a range of 1000 to 10000 (CC feedback circuit). At a gas gain of 10000 σ_{TtoT} is 6 ns, the average time walk is 8 ns.*

4.3.2 Time walk correction

In case fluctuations in drift time due to time walk are equal or larger than fluctuations due to longitudinal diffusion it is beneficial to compensate for time walk effects. The left picture in figure 4.12 is an example for which it would be beneficial to correct for time walk. Time walk can be compensated by using the correlation between time over threshold (TOT) and time to threshold (TtoT). The advantage of this method is that measuring TOT is an already applied and mature technology. The disadvantage of this method is that the TOT is known *after* the signal goes below the threshold again, which makes it a relatively 'slow' method. Time walk correction based on TOT information is discussed in section 4.3.3.

Another option is to measure time between thresholds (TbT). Two thresholds can be applied and the time a signal needs to rise between the first and second threshold is a measure for the steepness of the slope. The steepness of a slope correlates with the time to threshold. The advantage is that it is fast, it takes at most the peaking time of the signal. A disadvantage is that another comparator has to be fit on a pixel. Time walk correction based on TbT is discussed in section 4.3.4.

Yet another way to correct for time walk is to apply a constant fraction discriminator. A constant fraction discriminator gives a signal at a defined fraction of the rise time of a signal (under the condition that the signal shape is the same). This would simplify the required correction procedure to subtracting a constant time from the measured drift times. This is a mature method but at present it is not yet possible to implement a constant fraction discriminator with the required specifications in a pixel. For that reason this option has not been evaluated.

With sufficient gas gain one can also select only the large signals that have a small delay with little spread. However, a high gas gain results in more ion feedback and potentially in ageing of a detector: for that reason gas gain should be kept as low as possible.

Time walk correction can be performed by measuring the charge from each individual signal, then find the corresponding average TtoT (figure 4.11) and subtract that from the measured TtoT. Figure 4.15 shows that avalanche timing resolution improves by correcting each individual measured TtoT based on input charge.

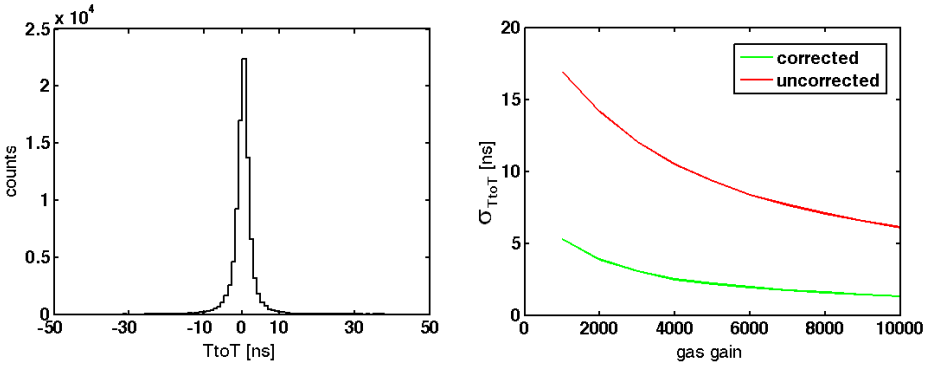

Figure 4.15: *Left: The time to threshold (TtoT) spectrum for the CC feedback circuit for a gas gain of 3000 after time walk correction based on input charge (which is set in the simulation). The uncorrected spectrum is shown by figure 4.13. The avalanche timing resolution (σ_{TtoT}) is improved from 12 ns to 3 ns. Right: The red curve is the avalanche timing resolution without time walk correction, which is the same as the red curve in figure 4.14. After time walk correction the timing resolution is as shown by the green curve. For a gas gain of 1000 the timing resolution is improved from 17 ns to 5.3 ns, for a gas gain of 10000 the avalanche timing resolution is improved from 6 ns to approximately 1.3 ns.*

Figure 4.15 shows that there are negative values for TtoT after time walk correction. This can be interpreted as over-corrected values. In case over-corrected drift times are identified the accuracy can be increased by setting those times to zero.

4.3.3 Time over threshold

A common way to measure charge on a pixel is to measure the time over threshold. The time over threshold as a function of the input charge, for both the CC feedback and RC feedback circuit, is shown by figure 4.9 (right graph). The time over threshold information can be used to correct for time walk. The time to threshold (TtoT) as a function of the time over threshold (TOT) is shown by the left graph in figure 4.16. The right graph in figure 4.16 shows the charge resolution (σ_Q) as a function of the input charge. The charge resolution is calculated according to:

$$\sigma_Q = \frac{\sigma_{TOT}}{\frac{dTOT}{dQ}}. \tag{4.7}$$

In equation (4.7) σ_{TOT} is the spread in TOT for a given charge and $\frac{dTOT}{dQ}$ is the change in TOT as a function of the charge.

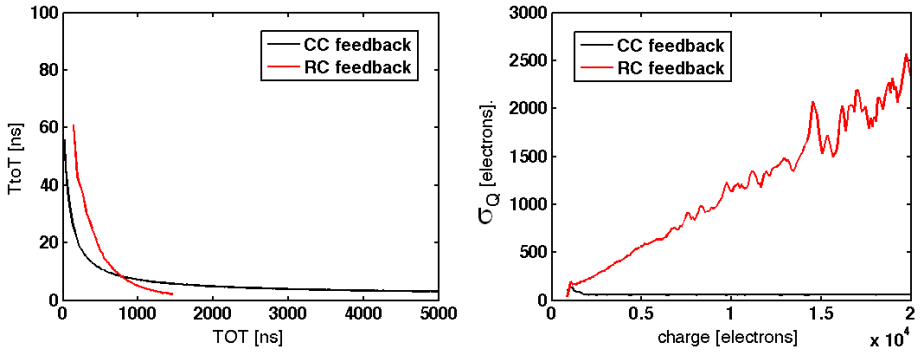

Figure 4.16: *Left: Time to threshold (TtoT) as a function of the time over threshold (TOT) for the RC feedback and CC feedback circuits. For the RC feedback a smaller dynamic range in TOT is required. Right: The charge resolution as a function of the input charge (equation (4.7)). Red is for the RC feedback circuit and black is for the CC feedback circuit. Due to the CC feedback circuit's linear dependency between the input charge and the time over threshold (figure 4.9) the charge resolution (approximately 70 electrons) is constant over a large range. For the RC feedback circuit with logarithmic behaviour the charge resolution becomes worse for increasing charge.*

For large signals, the non-linear relation between charge and time over threshold for the RC feedback circuit results in a shorter time over threshold than for the CC feedback circuit. This means that the time needed for the measurement is less, just as the amount of data to be read out. For large signals the TOT resolution (σ_{TOT}) for the RC feedback is 35 ns and for the current feedback it is 10 ns. This is the one σ width of the bands of points in the vertical direction in the right graph in figure 4.9.

The left graph in figure 4.17 shows the avalanche timing resolution for both circuits after time walk correction using the 0.2 ns time bins of the simulation. In practice the time bins will be 1.6 ns for the time to threshold and 25 ns for the time over threshold (figure 4.17, right graph). For time walk correction based on time over threshold the time binning is precise enough, figure 4.17 shows no significant differences between the use of the different time bins.

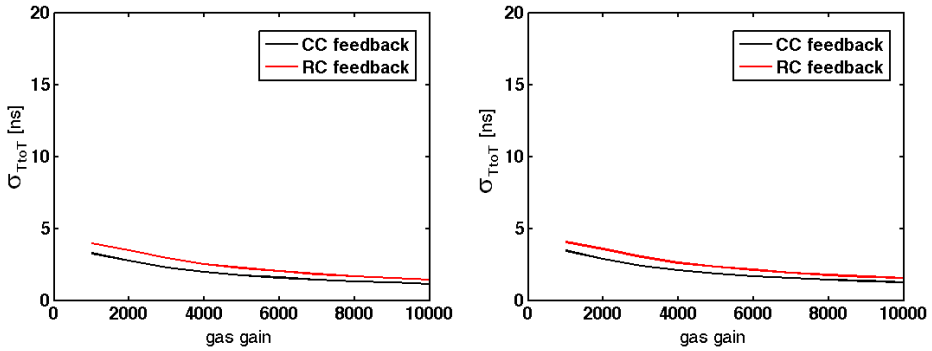

Figure 4.17: *Left: Avalanche timing resolution (σ_{TtoT}) after time walk correction. Right: Avalanche timing resolution after time walk correction but with the TtoT in 1.6 ns time bins and TOT in 25 ns time bins.*

For time walk correction the CC feedback and RC feedback both are sufficient. If charge resolution is not a high priority the RC feedback circuit is preferred for two reasons:

- For large signals the time to return below threshold is shorter than for the CC feedback circuit. This reduces the pile up of data in a high rate environment.
- The logarithmic dependency reduces the required dynamic range of the ADC which reduces the amount of data to be read out.

4.3.4 Time between thresholds

A simulation was run with a threshold set at 350 and at 700 electrons. The time to the 350 electrons threshold is the TtoT as it was before. The time a signal needs to rise from the first to the second threshold is the time between thresholds (TbT). The correlation between TtoT and TbT is used to correct time walk. The response of the circuits with RC feedback and CC feedback are similar because only the rising edge of the signal matters. For the simulation the CC feedback circuit is used. Figure 4.18 (left graph) shows the TtoT as a function of the TbT. To correct time walk, the time between thresholds is measured and the corresponding time to threshold (figure 4.18) is subtracted from the drift time. Measuring TbT can also be used to determine the charge. Figure 4.18 (right graph) shows the charge resolution that can be obtained by using the TbT information. Figure 4.19 shows the avalanche timing resolution for corrected TtoT using TbT information for gas gains from 1000 to 10000.

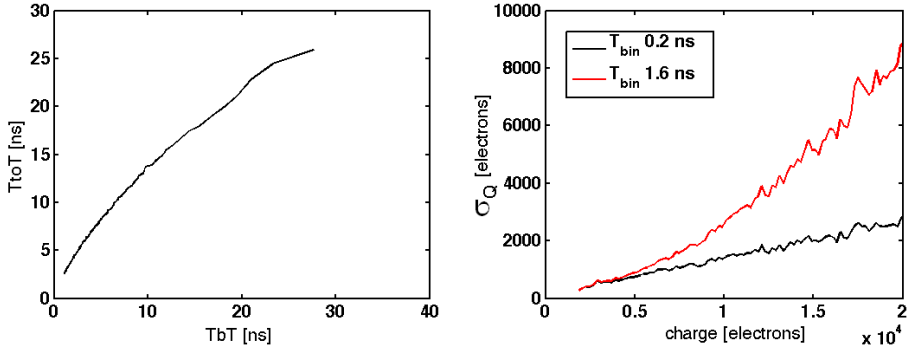

Figure 4.18: *Left: Time to threshold (TtoT) as a function of the time between thresholds (TbT). The maximum time to threshold is reduced to 30 ns since the detected signals now at least have an amplitude of 700 electrons (the second threshold). Right: The charge resolution (Q_{res}) that can be achieved with a TbT time bin of 0.2 ns used in the simulation (black line). In practice the time bins will be approximately 1.6 ns and the charge resolution will be according to the red line.*

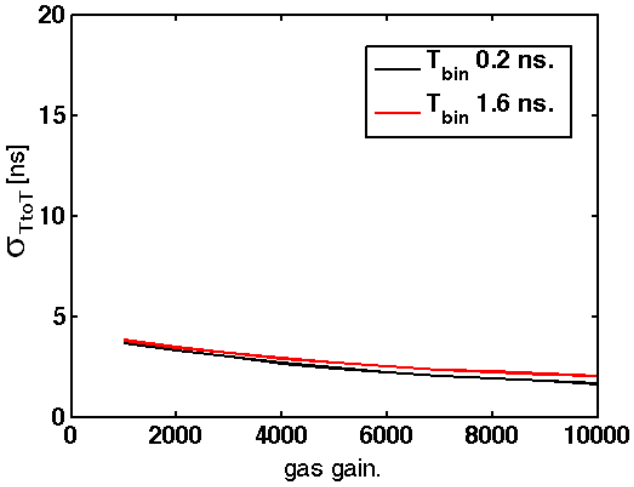

Figure 4.19: *Avalanche timing resolution (σ_{TtoT}) as a function of the gas gain for time bins of 0.2 ns (time bins used in simulation) and time bins of 1.6 ns.*

Due to the need for a second higher threshold the single electron detection efficiency of this method is worse than in case of using the time over threshold method to correct for time walk. This is because signals have to reach the second threshold of 700 electrons instead of the threshold of 350 electrons. The signals that only cross the first threshold can still be used for track reconstruction in the anode plane, it is a measured primary electron with poor time information.

Using the time between threshold is a fast method to correct for time walk: All information is collected within the peaking time of the signal. Figure 4.18 (right graph) illustrates that the charge resolution is poor compared to measuring the time over threshold (figure 4.16). With a maximum time between thresholds of 30 ns and a time bin of 1.6 ns the data is five bits at maximum. Because of the little amount of data *and* the short time required for readout, this method would be preferred rather than a method based on measuring time over threshold. Due to the lack of space on a pixel it is still technically challenging to place two comparators on each pixel.

4.4 Time walk correction in practice: Gossipo3

The Gossipo3 chip is designed to test pixel electronics that measure drift time and time over threshold simultaneously. The time to threshold timer has time bins of 1.7 ns and the time over threshold timer has 25 ns time bins. The response time (τ_1) of the pixel amplifier is 15 ns. It is a CC feedback circuit and the feedback current is set to 1 nA. The ENC in the amplifier appears to be only 25 electrons RMS [66].

To make a signal similar to drifting ions a voltage ramp is applied to a 1.3 fF coupling capacitor. The charge coupled into the amplifiers input is $V_{ramp} \cdot C_{coupling}$ and the current is its derivative. The duration of the ramp was set to 60 ns. After a defined time after the test signal the chip is read out. To determine the dependency between time to threshold (TtoT) and time over threshold (TOT) a total of 3×10^5 measurements have been performed, uniformly distributed between 0 and 7000 electrons.

The Gossipo3 chip still suffers from issues that cause a large spread between chips and sometimes result in the read out of corrupt data. For that reason a successor of Gossipo3 is under development. Despite the problems it is still possible to proof the concept to correct time walk by using the TOT information. Figure 4.20 shows the recorded time over threshold as a function of the input charge. The TOT values are in discrete 25 ns steps which is the time bin size. The threshold was set at 1300 electrons. One would expect the threshold to be set lower with only 25 electrons ENC but that resulted in erratic chip behaviour.

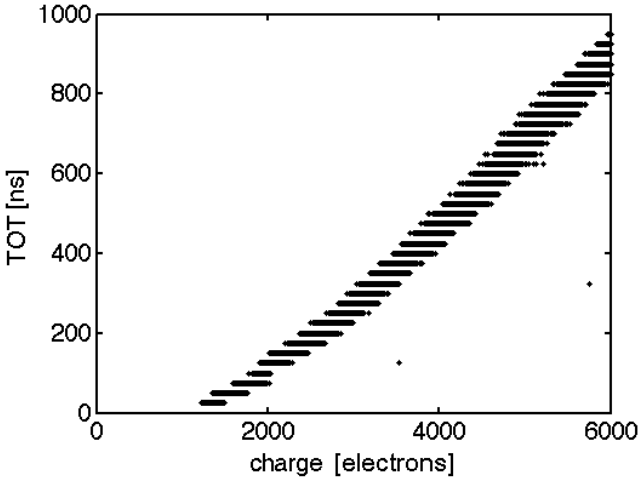

Figure 4.20: *Time over threshold (TOT) as a function of the input charge. The resolution of the time over threshold counter is 25 ns.*

Figure 4.21 shows the recorded time to threshold as a function of the input charge. The curve is not smooth because of problems with the time bins of the time to threshold timer. This is one of the issues addressed in a new chip design. All signals with a TtoT longer than 50 ns are removed from the data set, effectively rejecting all signals with less than 1800 electrons. The TOT and TtoT dependency is shown by figure 4.22. For each TOT bin the average TtoT is determined in order to be used for time walk correction.

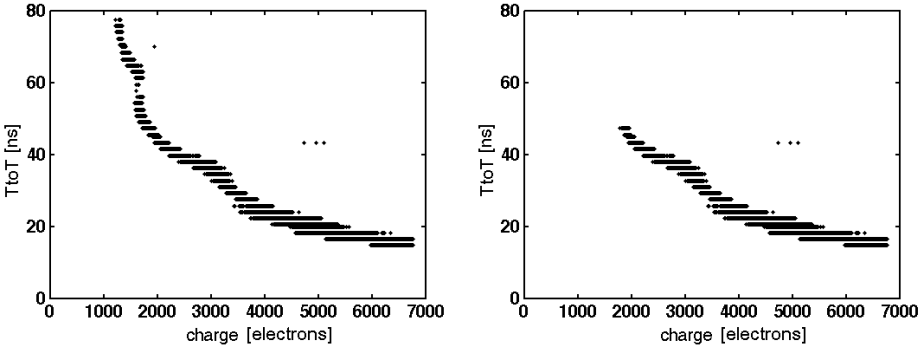

Figure 4.21: *Left: Time to threshold (TtoT) as a function of the input charge. The time bins are 1.7 ns. For small signals with a TtoT longer than 55 ns the chip shows erratic behaviour. Right: All signals with TtoT values longer than 50 ns are cut out. The signals with a TtoT shorter than 50 ns are used for analysis.*

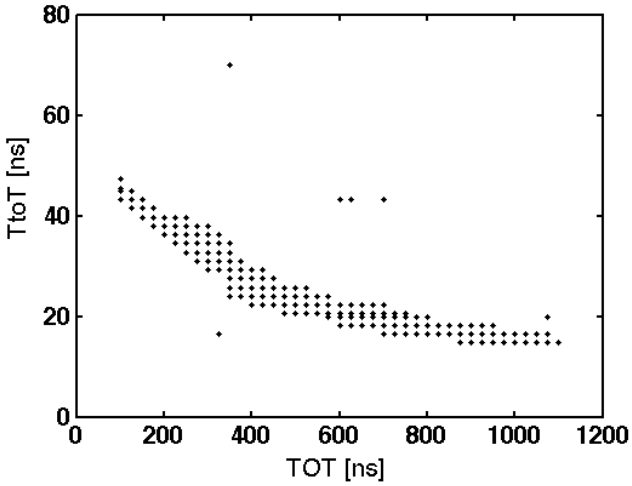

Figure 4.22: *Time to threshold (TtoT) as a function of the time over threshold (TOT).*

A signal spectrum matching a gas gain of 2000 is measured. The fraction of signals detected with a threshold of 1300 electrons is 0.65. After removing the signals with a TtoT longer than 50 ns (effectively selecting signals of more than 1800 electrons) the detected fraction is 0.44. Figure 4.23 shows the TtoT spectrum before and after time walk correction. Before time walk correction the average TtoT is 35 ns with a σ_{TtoT} of 8.5 ns, after time walk correction σ_{TtoT} is reduced to 1.1 ns.

Running a simulation in which the noise is set to 25 electrons RMS and a threshold set at 1300 electrons results in the TtoT spectra shown by figure 4.24. The

average TtoT is 35 ns with a σ_{TtoT} of 10 ns. The σ_{TtoT} becomes 1.1 ns after time walk correction. After removing signals with a TtoT with more than 50 ns the average TtoT is 34 ns with a σ_{TtoT} of 9.2 ns which becomes 1.1 ns after time walk correction.

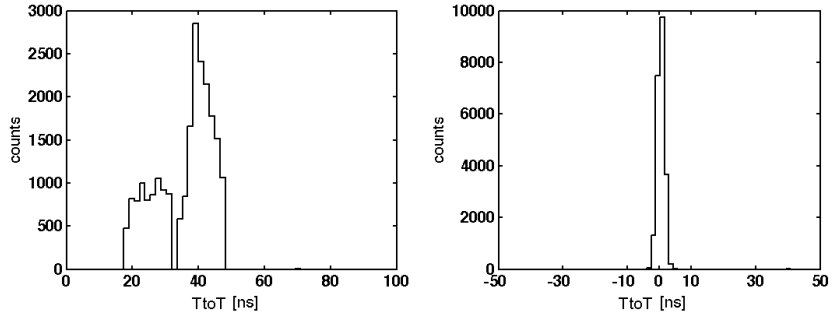

Figure 4.23: *Left: Measured time to threshold (TtoT) spectrum corresponding to a gas gain of 2000 and with the threshold at 1300 electrons. The average is 35 ns, σ_{TtoT} is 8.5 ns. Right: the TtoT spectrum after time walk correction, σ_{TtoT} is 1.1 ns.*

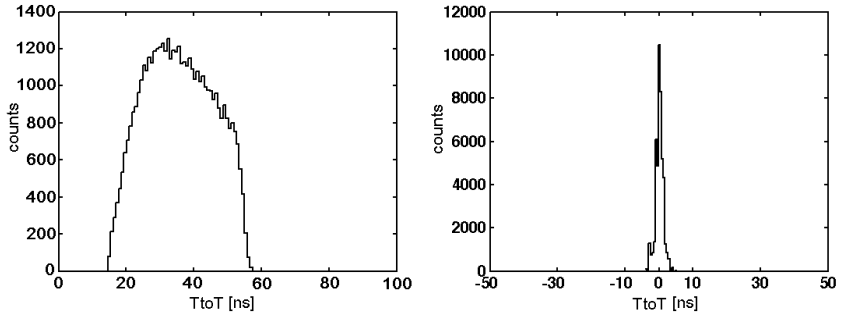

Figure 4.24: *Simulation results for the TtoT spectrum corresponding to a gas gain of 2000. The threshold is 1300 electrons and the ENC is 25 electrons RMS. Left: The average is 35 ns, σ_{TtoT} is 10 ns. Right: the TtoT spectrum after time walk correction, σ_{TtoT} is 1.1 ns.*

According to this test with an existing chip, the avalanche timing resolution can be improved significantly. Due to the bugs in the pixel electronics no other chips have been tested for time walk correction. Time walk correction will be tested more extensively with the successor of Gossipo3.

4.5 Concluding remarks

The models of the electric circuits used in the simulations are simple generalized models and it may be that for small signals circuit behaviour may deviate from the model that is used. For a more accurate simulation it may be required to simulate the physical circuit as it is on the chip.

Noise is assumed to be Gaussian, which is not necessarily the case under all conditions. Effects like crosstalk may add non Gaussian components. Non Gaussian noise may result in systematic errors in time walk correction and is something to be studied with the successor of the Gossipo3 chip.

An additional study is required in order to apply time walk correction for a large system composed of many chips with each chip containing many thousands of pixels. The non-uniformity of pixel response must be minimised since it presently is considered a too large technical challenge to do time walk correction based on a TtoT and TOT dependency for each individual pixel.

A significant improvement in avalanche timing resolution can be achieved by correcting for time walk by using time over threshold and time between thresholds information. Time walk correction based on time between thresholds has not been tested in practice (yet), according to simulations it is the preferred method to correct for time walk. In the case of TOT based time walk correction the RC feedback circuit is preferred since large signals are shorter compared to those from the CC feedback circuit and the least amount of data has to be processed.

Depending on detector application one can decide to use all detected primary electrons for track reconstruction in the plane of the anode (the XY plane) and only a fraction of signals with a large amplitude for track reconstruction in the drift direction. The ratio in which signals are rejected or corrected for time walk depends on the geometry of a detector and how it is operated. Rejecting a signal means that its drift time information is not used, it can still be used for track fitting in the XY plane and analysis of ionisation losses.

The time walk correction is a generic applicable procedure. It can be applied in any situation in which the dependency between time to threshold and time over threshold or time to threshold and time between thresholds is unambiguous.

Chapter 5

Spark protection

In a Gridpix detector a spark in the gain region strikes the pixel chip, damaging the chip. The more charge there is in an avalanche the higher the probability for a spark will be. Due to the statistical fluctuations in charge in an avalanche occasional sparks cannot be prevented, therefore the chip has to be made spark proof. This is achieved by applying a highly resistive layer on the chip [67] that will quench the spark. The spark quenching properties of this layer are discussed in section 5.3. The properties of such a protection layer and how it affects detector performance are discussed in section 5.6.

5.1 Effects of sparks

In case a spark occurs, a significant amount of the charge stored in the grid can be deposited onto the pixel chip. This results in chip damage and in a rising voltage on the grid[1]. The damage of a spark can be physical due to the high temperature plasma where a spark strikes, locally melting the area (figure 5.1). Another form of damage is electric failure of the pixel electronics due to overcharging. A failing pixel may cause a short circuit between electric lines. A pixel causing a short circuit can affect the whole chip since pixels share common electric interconnections. In practice a chip may be destroyed after one spark.

Due to the charge drained by a spark the voltage on the grid rises, reducing the static avalanche field and therefore the gas gain. A spark causes a dead time depending on how quick the grid voltage is restored. For that reason a spark protection should both protect the chip against damage and reduce the amount of charge drained from the grid.

[1] Since the grid voltage is negative, a rise in voltage decreases the gain field.

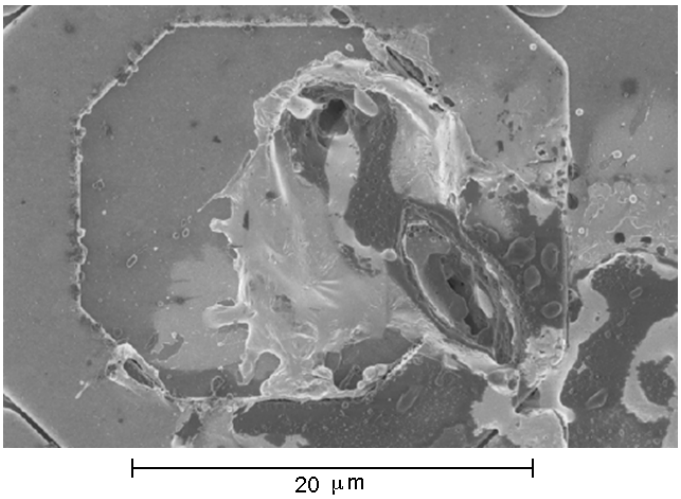

Figure 5.1: *A pixel input pad after it was struck by a spark. Due to the high temperature plasma during a spark the area has partially been molten and evaporated.*

5.2 A SiRN protection layer

To quench sparks a highly resistive layer of Silicon Rich silicon Nitride (SiRN) is deposited directly on top of the pixel matrix. Charge on the surface of the highly resistive layer is drained off much slower than it is deposited by a spark. For a spark the SiRN layer acts as an insulator. As a result a net charge builds up which reduces the electric field between the grid and the charge on the SiRN layer, quenching the spark.

5.2.1 Characteristics of a protection layer

An important aspect of the protection layer is how much charge is coupled into a pixel in case it is struck by a spark. The amount of charge coupled into a pixel by a spark depends on the virtual capacitance[2] of the layer directly above the pixel input pad and the potential build up across the layer. A material with an as low as possible ϵ_r should be used to minimise the required thickness of the protection layer for sufficient spark quenching. In a worst case scenario, the maximum voltage across the layer is assumed to be the grid voltage.

The resistance of the layer is another important aspect. Charge will build up during normal operation and will also cause a potential across the layer. This potential is subtracted from the potential across the gain region. In case the potential across the SiRN layer becomes too large it will significantly reduce the gas gain.

[2] The capacitance is called virtual since there is no real second electrode on top of the SiRN layer in which the charge can move freely.

The capacitance C_{prot} and resistance R_{prot} of a silicon nitride layer with area A and thickness d are:

$$C_{prot} = \frac{A\epsilon_r\epsilon_0}{d} \tag{5.1}$$

$$R_{prot} = \frac{\rho d}{A} \tag{5.2}$$

The characteristic time of the layer is the RC time, called τ_{prot}, and as shown in equation (5.3) it only depends on the specific resistance ρ and ϵ_r. For SiRN the ϵ_r is between 6.5 and 8.7 [61][3]. In this thesis an ϵ_r of 7.5 is used. The excess of silicon can be tuned at will during the deposition of the SiRN layer [67].

$$\tau_{prot} = \frac{\rho d}{A}\frac{A\epsilon_r\epsilon_0}{d} = \rho\epsilon_r\epsilon_0 \tag{5.3}$$

To limit the reduction in gas gain the potential drop across the layer should be limited. In this thesis, 5 V is considered to be the maximum acceptable value. The effect of the SiRN layer on the gas gain is discussed in section 5.6.

5.3 Spark quenching with a 8 μm thick SiRN layer

The spark quenching process is studied in Gridpix detectors with different gases and different grid capacities. These tests have been performed on a broken Timepix chip. The chip was equipped with a 8 thick μm SiRN layer. In all tests described the drift region is 2.3 mm in height and the drift field is approximately 1 kV/cm, unless otherwise noted. Two measurement set-ups are described, one to measure proportional signals and sparks simultaneously (section 5.3.2) and one to measure only sparks (section 5.3.4). The first set-up is used for a reference measurement to verify that the detector works properly and to measure the spectrum of charges deposited by sparks. The second set-up has a high bandwidth (sub ns resolution) to measure the spectrum of currents in sparks. To verify the sensitivity of this set up the charge spectrum of this set up is compared to the spectrum measured with the first set up.

5.3.1 Testing gaseous detectors using ^{55}Fe

A common way to test gaseous detectors is to operate them while irradiating them with X-rays from an ^{55}Fe source. An ^{55}Fe source emits X-rays with energies of 5.9 keV and 6.5 keV in a ratio of 9/1. The X-rays absorbed by the photoelectric effect result in approximately 230 electrons of primary charge (simulation with HEED [68]) in an Ar/iC$_4$H$_{10}$ 80/20 mixture. Such a defined amount of primary charge can be used to characterise the response of a detector. Small detectors like Gridpix detectors always show two peaks in the distribution in the amount of primary electrons when

[3] The amount of excess of silicon determines ρ. The quantitative dependency of ρ with the fraction of silicon has yet to be determined. For the samples tested in section 5.6.2 ρ is in the order of 10^{13} Ωcm.

using an Argon based gas mixture. The photo absorption of a 5.9 keV photon is most likely to eject an electron from the K shell of an Ar atom [69], [51]. These electrons have a binding energy of 3206 eV [70], [71] and as a result, when released, they have only 2694 eV left to ionise. The excited Ar^+ ion that is left can either emit a fluorescence photon or an Auger electron with the probabilities of 0.135 and 0.865 respectively [72]. The Auger electron will deposit its energy by ionisations. In case a fluorescence photon is emitted it may escape the detector volume. In that case the only primary charge released is what was released by the initial photo electron. Figure 5.2 shows the two peaks in the spectrum which was measured in an Ar/CH_4 (90/10) mixture. The small peak at 0.1 pC contains the amplified charge that is released by the photo electron only. The large peak at 0.18 pC contains the amplified charge released by both the photo electron and the Auger electron.

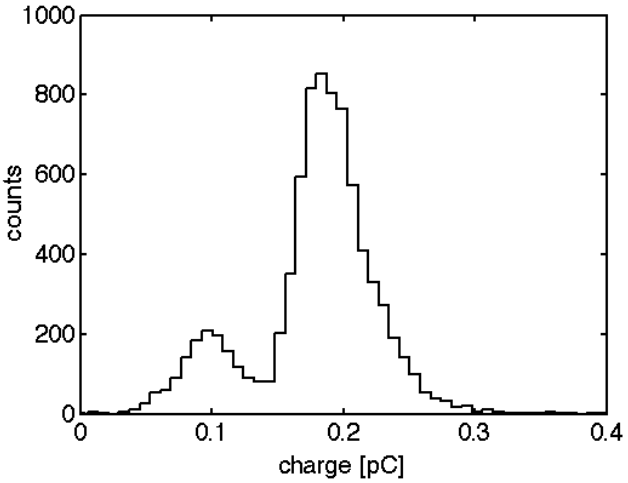

Figure 5.2: *Proportional charge signal spectrum of ^{55}Fe photon conversions in an Ar/CH_4 (90/10) mixture. The peak at 0.1 pC is from the amplified charge from only the photo electron. The peak at 0.18 pC is from the amplified charge from both the photo electron and the Auger electron. Approximately 10 % of the X-ray photons have an energy of 6.5 keV instead of 5.9 keV, causing a slight excess in large signals, i.e. a widening of the distribution to the right. The grid voltage was -380 V, resulting in a gas gain of approximately 5×10^3. This spectrum was measured with the set up described in section 5.3.2.*

5.3.2 Simultaneous measurement of sparks and proportional signals

A Gridpix detector is operated at a gas gain such that occasional sparks occur when irradiated by an ^{55}Fe source. The signals are studied by measuring the charge induced on the grid when the primary electrons are amplified. A set-up is made that is capable to measure charges of less than 0.1 pC up to more than 10 nC, covering

the range of proportional signals and sparks.

Figure 5.3 shows a sketch of the grid readout. Small signals are amplified with the charge sensitive amplifier (CSA) that is decoupled with C_{amp} and is read out with a digital oscilloscope. For signals so large that the amplifier is saturated the RC network R_1, C_1, R_2, C_2 is used. The RC network gives an amplitude as a function of the induced charge on the grid. The output of this RC network is read out with the three remaining channels on the oscilloscope. Each of these three channels is set such that as soon as one channel saturates the signal is in range of a channel with a larger scale setting, effectively increasing the dynamic range that can be covered. The waveforms of all four channels are recorded simultaneously and are analysed afterwards.

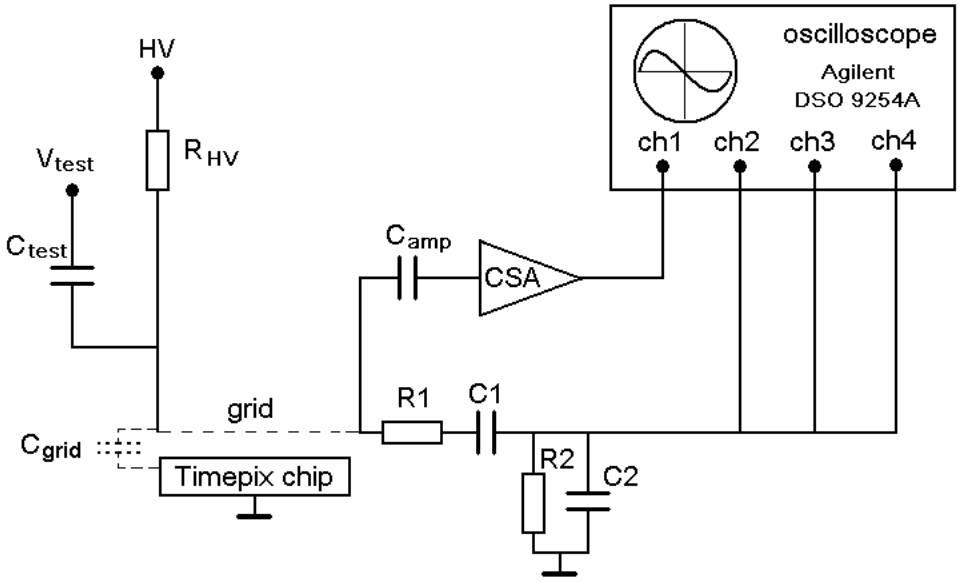

Figure 5.3: *Sketch of the equivalent circuit of the grid readout. The high voltage to the grid is applied through R_{HV} which is 10 MΩ. Test pulses for calibration are fed through C_{test} (4.7 pF). The dashed C_{grid} is the total capacitance measured at the grid. The signals induced on the grid are read out with a charge sensitive amplifier (CSA), decoupled with C_{amp}, and with a RC circuit (R1,C1,R2,C2) that gives a pulse height as a function of the induced charge.*

To calibrate the sensitivity a defined charge (Q_{test}) can be applied to the grid by applying a step voltage at C_{test}:

$$Q_{test} = \Delta V \frac{C_{test} C_{grid}}{C_{test} + C_{grid}} \approx \Delta V C_{test}. \tag{5.4}$$

The approximation is valid in case C_{test} is small compared to C_{grid}. In order to minimise the effect on the behaviour of the grid, the capacities C_{amp} and C1 are

small compared to C_{grid}. In practice C_{grid} is between 60 and 100 pF, for the tested detector it is 80 pF. The capacities C_{amp} and C1 are 4.7 and 10 pF respectively. The high voltage is supplied through a 10 MΩ resistor (R_{HV}). As a result the RC time of the grid and high voltage supply is in the order of one ms. In order not to be sensitive for charge up effects on the grid and to be able to cope with a high rate the RC time of the readout (R2, C2) should be at least one order of magnitude shorter than the RC time of the grid. The RC time of the readout should be much longer than 150 ns which is longest signal to be expected from drifting ions (section 4.1). In practice C2 is 100 pF and is composed of the capacitance of the cables (standard 50 Ω coaxial cables) and oscilloscope inputs. A resistor of 100 kΩ in parallel with the three 1 MΩ oscilloscope inputs results in an RC time of approximately 8 μs.

A spark is a fast process that applies a step voltage to C1. To prevent such a fast signal from reflecting several times at the improperly terminated 50 Ω cables (to prohibit a false amplitude reading) R1 is placed in series with C1 to 'gradually' charge the capacitance (C2) of the cables. A resistance of 4.7 kΩ is chosen for R1, setting the RC (R1, C1) time to 47 ns. The maximum voltage peak that can be produced at the oscilloscope inputs is $\Delta V_{grid} \frac{C1}{C1+C2}$. For a C1 of 10 pF and a C2 of 100 pF the ratio is 1 to 11. A spark causing the grid to drop a few hundred volts only results in tens of volts at the oscilloscope inputs which is a safe value. The sensitivity of the CSA appeared to be 57 mv/pC and the sensitivity of the RC output was 0.41 mV/pC.

Figures 5.2 and 5.4 show two charge distributions in an Ar/CH_4 (90/10) gas mixture: One of proportional signals and one of sparks on a Timepix chip with 8 μm SiRN. The spectra shown in figures 5.2 and 5.4 show that the proportional charges are of the order 0.2 pC while the spark signals range between 100 and 1500 pC. Sparks are defined as signals at least ten times larger than the most probable proportional signals.

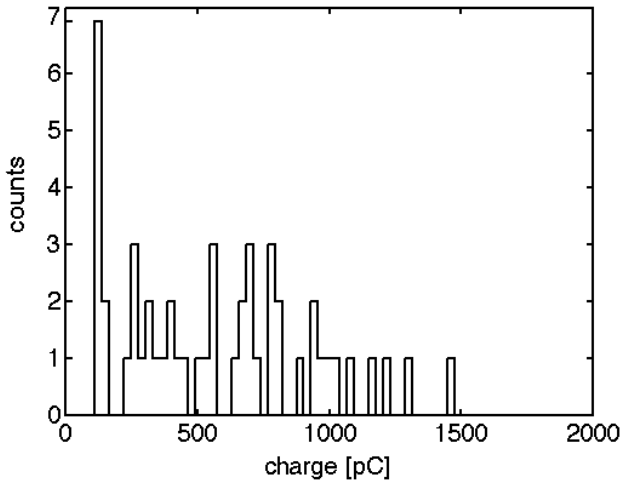

Figure 5.4: *The same measurement as in figure 5.2 but now in a range up to two nC and the proportional signals cut out. The maximum charge observed in a spark was less than 1.5 nC. The total number of entries in figure 5.2 and 5.4 is 8192*

The capacitance of the grid and the connected circuitry is approximately 80 pF. For a grid voltage of -380 V, such as used for these measurements, the charge stored on the grid is 30 nC. The sparks deposit approximately one nC, resulting in a drop in grid voltage of approximately 11 V.

5.3.3 Increasing grid capacitance

We observed that increasing the grid capacitance to one nF, by adding an external capacitor, did not affect the magnitude of the spark signals. That indicates that the spark quenching process does not have a strong dependency on the amount of charge stored on the grid and therefore has to depend on the charge build up on the SiRN layer. With the one nF capacitance the voltage drop on the grid will only be one volt and the gas gain can be considered stable after one spark. The other measurements presented in this chapter have been performed on a grid without the extra capacitance connected in order to be more sensitive to smaller signals.

5.3.4 Grid readout with sub ns time resolution

The quenching properties of different gas mixtures have been measured by recording 1000 sparks for each mixture. A grid readout is made that is capable of recording voltage changes on the grid with sub ns timing resolution. Through a decoupling capacitor the voltage on the grid is measured with an attenuation ratio of 1:480 (figure 5.5). All components are physically small (SMD components) in order to have a reliable high frequency performance. With this set up the only signals that can be measured are sparks; proportional signals are below detection threshold.

The readout circuit is sketched in figure 5.5. The capacitance C1 is 470 pF, which is much larger than the grid capacitance. In case of a voltage change on the grid due to a spark the grid will be recharged from this capacitor through R1 in series with the 50 Ω cable impedance. The voltage on the grid will now have a time constant of $C_{grid}(R_1 + R_{cable})$, which should be much longer than the processes studied. The longest ion drift time to be expected for any gas is 150 ns: choosing R1 to be 24 kΩ results in an RC time of 1.7 μs. This also puts a limit on the attenuation that can be obtained with a 50 Ω readout since R1 cannot be lowered much without affecting the measurement.

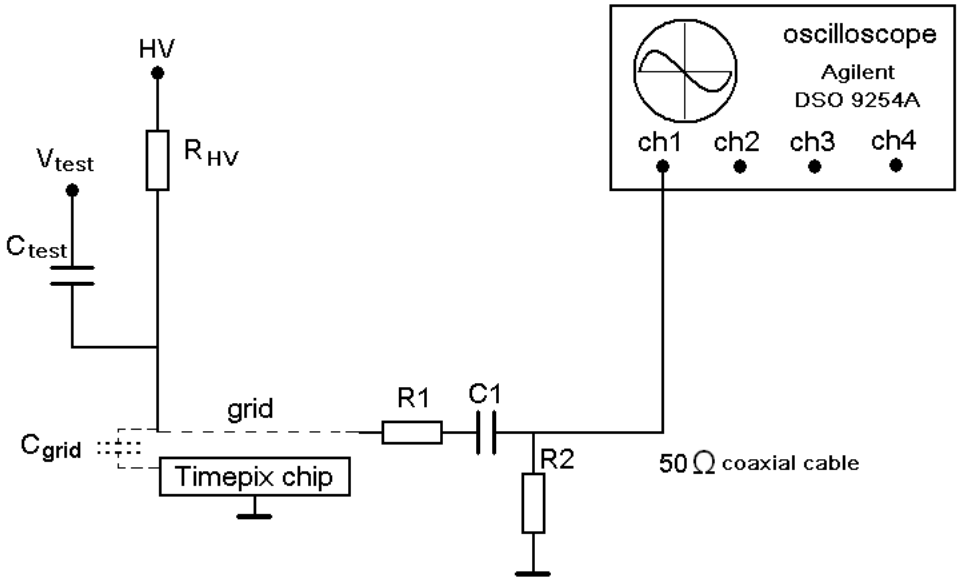

Figure 5.5: *Sketch of the equivalent circuit of the grid readout with sub ns time resolution. The difference with the readout shown in figure 5.3 is that there is only one readout, which is a properly terminated 50 Ω coaxial cable (the oscilloscope input is 50 Ω terminated). To reduce parasitic capacities and inductances that affect high frequency performance all other connections have been removed. The resistor R2 is a 1 MΩ resistor to prevent the cable from charging up in case C1 is slightly conductive and the cable is not connected. R1 is 24 kΩ. C1 is 470 pF.*

The change in charge on the grid (ΔQ_{grid}) is:

$$\Delta Q_{grid} = C_{grid} \Delta V_{osc} \frac{R1 + R_{cable}}{R_{cable}}. \tag{5.5}$$

In equation (5.5) ΔV_{osc} is the voltage at the oscilloscope input. The capacitance at the grid (C_{grid}) is approximately 80 pF. The changes in charge on the grid by current through resistors is neglected, considering that those are small on time scales of 150 ns and less.

This circuitry was tested with the detector operated in the same Ar/CH_4 90/10 mixture as in section 5.3.2. The grid voltage was set at -380 V. The resistor R1 was 24 kΩ. The oscilloscope was set to trigger on signals above 1.8 mV which, according to equation (5.5), corresponds to a ΔQ_{grid} of 70 pC. Figure 5.6 shows a typical spark signal in which the voltage rapidly changes in approximately 200 ps followed by a more 'gradual' change in 10 ns .

The current in a spark (I_{spark}) can be calculated by taking the derivative of the voltage on the grid:

$$I_{spark} = Att \frac{dV}{dt} C_{grid}. \tag{5.6}$$

In equation (5.6) *Att* is the attenuation factor of the readout circuit. Figure 5.7 shows the the current of the spark shown in figure 5.6 which reaches 1.5 A[4]. Due to high bandwidth noise (2.5 GHz) the minimum current that can be measured is 0.7 A.

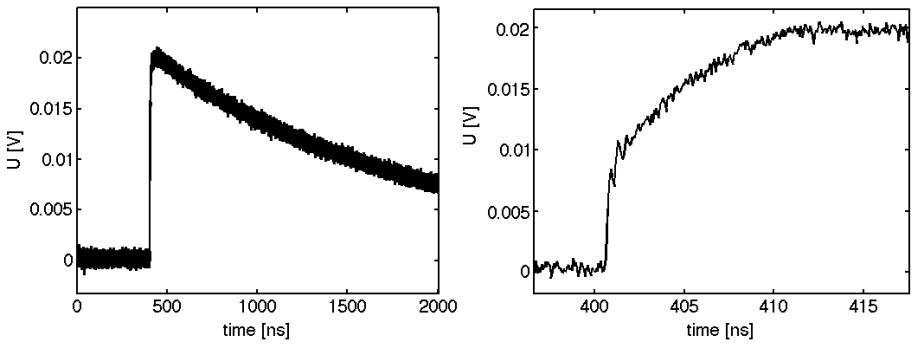

Figure 5.6: *A spark signal recorded by the oscilloscope. On the left picture it can be seen that the RC time is approximately 1.7 μs. The right picture is a zoom on the rising edge of the signal, the full time scale of the X axis is 20 ns. The fastest rising part of the signal, from zero to eight mV is approximately 200 ps. The attenuation factor is 480 which means that the grid voltage changed 3.8 V in 200 ps. With a grid capacitance of 80 pF the change in charge (ΔQ_{grid}) is approximately 300 pC. The maximum current was $3\times10^{-10}/2\times10^{-10}$=1.5 A.*

[4] Yes, that really is 1.5 Amperes! This is in contrast with the nA and μA currents that we are used to with this detector.

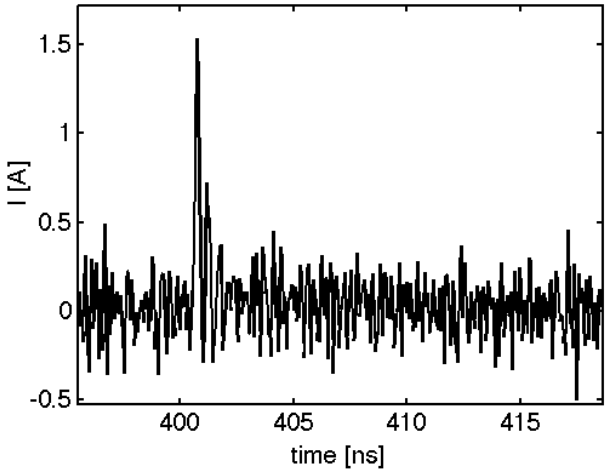

Figure 5.7: *The current in the spark shown by figure 5.6 calculated using equation* (5.6).

Figure 5.8 shows another typical spark signal which is different from the signal shown in figure 5.6 since the spark process is more than one order of magnitude slower (200 ns) than the slowest processes in the 'fast' sparks (10 ns). The spark signal shown in figure 5.8 is called a 'slow' spark. No sparks have been observed (in the Ar/CH_4 90/10 mixture) on intermediate time scales. The ratio of 'slow' and 'fast' sparks is different for gas mixtures with different gases. The fact that there are two distinct time scales in which discharges evolve is not yet understood and is subject for further research. A hypothesis of what may cause this effect is discussed in section 5.3.9.

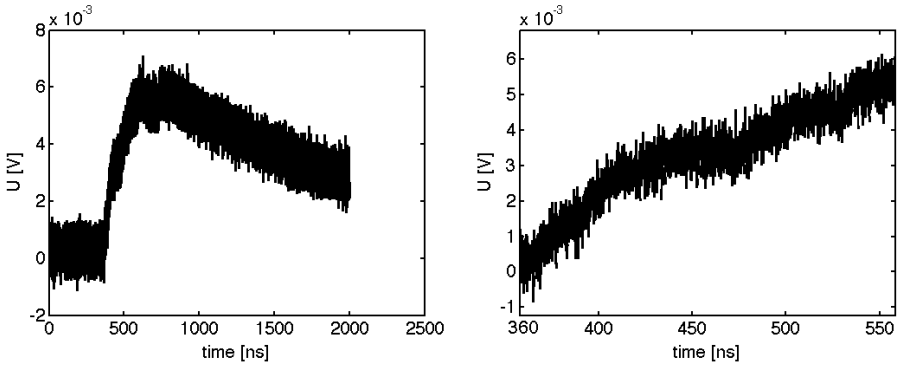

Figure 5.8: *Left: A spark that has 'slow' signal components only. Right: Zoom of the rising edge, the full time scale is 200 ns. The signal rises from 0 to 3 mV in 70 ns. According to equation* (5.6) *the current in the spark was approximately 1.6 mA.*

The 'slow' sparks are processed with a low pass digital filter (a higher order filter with a time constant of 10 ns) to reduce noise. Figure 5.9 shows the current of the spark shown by figure 5.8, after filtering the noise peaks at 1.8 mA.

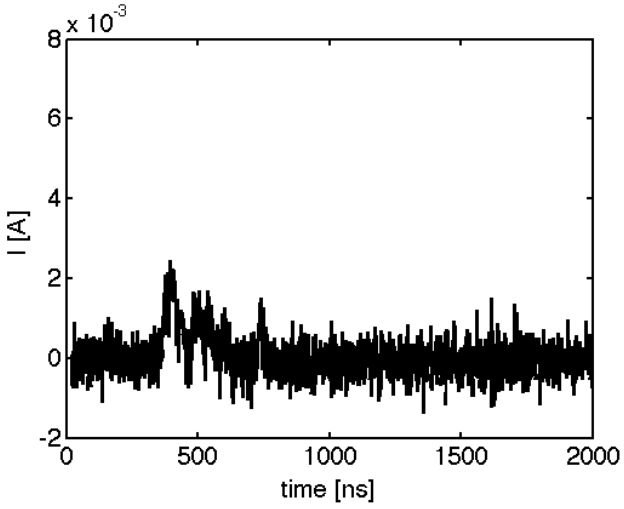

Figure 5.9: *The current in the spark shown by figure 5.8 (after passing through a low pass filter) calculated using equation* (5.6).

5.3.5 Spark quenching in an Ar/CH_4 mixture

Sparks were measured in an Ar/CH_4 90/10 mixure with -380 V on the grid. Figure 5.10 shows the same spectrum as figure 5.4 and is obtained by using the set up sketched in figure 5.5.

In figure 5.10 two distributions can be distinguished: One below 500 pC and one between 500 pC and 1500 pC. The two distributions are not reflected in the currents in the sparks. As figure 5.11 (left graph) illustrates, only a few sparks have been measured with a current of more than 0.9 A, the majority of sparks were 'slow' sparks. After applying the low pass filter to reduce the noise to 1.8 mA it appears that the current in the majority of sparks is between 2 and 10 mA (figure 5.11, right graph).

It is expected that the sparks with high currents and large amount of charge pose the highest thread for the detector.

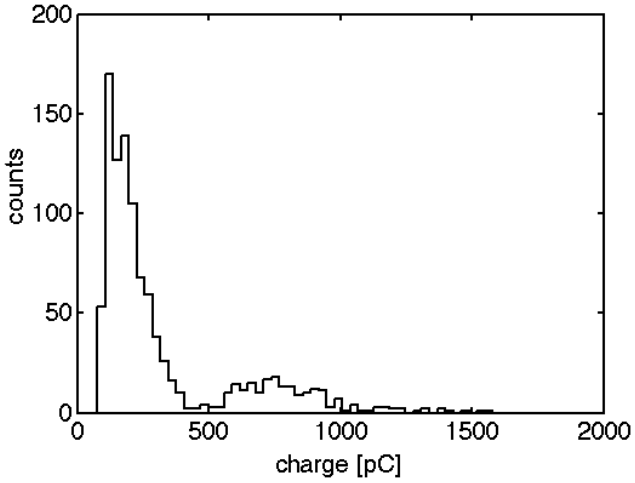

Figure 5.10: *The same measurement as in figure 5.4, now using the circuitry shown by figure 5.5. The upper limit of charge deposited by a spark is approximately 1.5 nC. The large peak below 500 pC are sparks that are quenched in an early stage.*

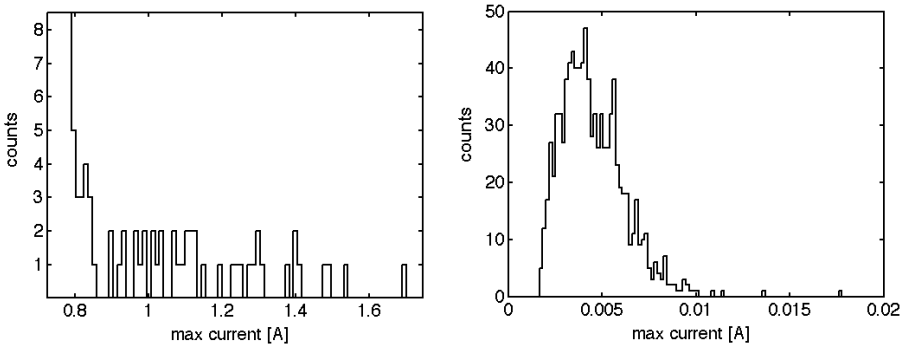

Figure 5.11: *Currents in sparks. Left: Sparks with more than 0.9 A, below 0.9 A most of the signals are noise (out of the Y axis scale). Right: After passing the signals through a low pas filter the currents in the sparks appear to be between 2 and 10 mA.*

5.3.6 Spark quenching in a CO_2/DME mixture

In a CO_2/DME 50/50 mixture sparks behave differently: It appears that there are no sparks that deposit more than 500 pC of charge (figure 5.12, left graph). The average charge deposited at a grid voltage of -580 V is 250 pC. Figure 5.12, right graph, shows that the current in the sparks in this gas mixture extend up to 4 A which is much more than in the Ar/CH_4 mixture (figure 5.11). An example of a

recorded signal (figure 5.13) shows ringing which suggests that the signal is faster than the signals in the Ar/CH_4 mixture and that the readout circuitry has too little dampening for the high frequencies. The oscilloscope has a too low bandwidth to cope with the rise times of less than 150 ps, for that reason the currents may be higher than what is measured.

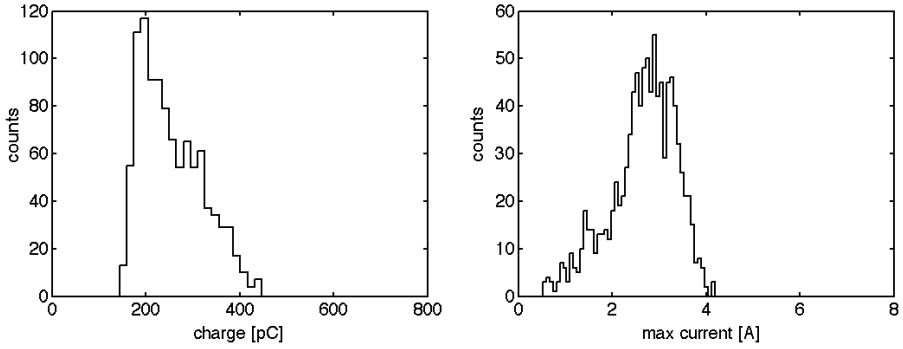

Figure 5.12: *Left: Charge spectrum of sparks in a CO_2/DME (50/50) gas mixture. The grid voltage was -580V. The average charge is 250 pC. Right: Current in sparks.*

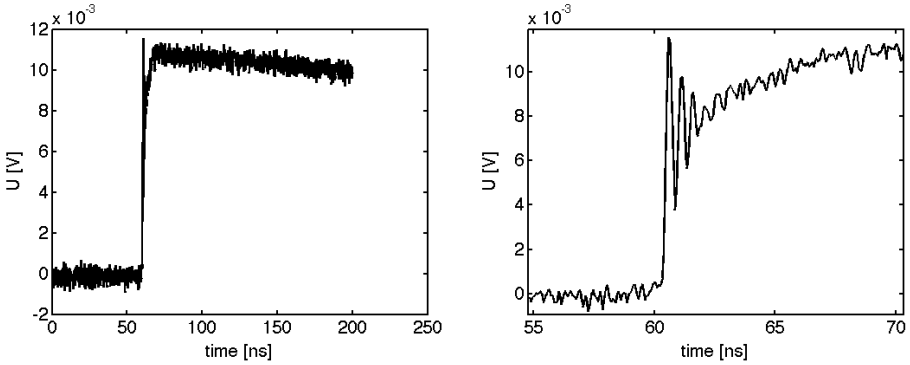

Figure 5.13: *Voltage measured by the oscilloscope. The left graph shows the sample which is 200 ns long. The right graph shows the voltage change in detail. The ringing indicates that the recorded voltage reading is not correct for such short time scales. The fast rise time is limited by the oscilloscope, indicating that the process may be faster.*

5.3.7 Spark quenching in an Ar/iC$_4$H$_{10}$ mixture

In an Ar/iC$_4$H$_{10}$ the average amount of charge is between 280 and 375 pC, for grid voltages between -450 V and -490 V (figure 5.14).

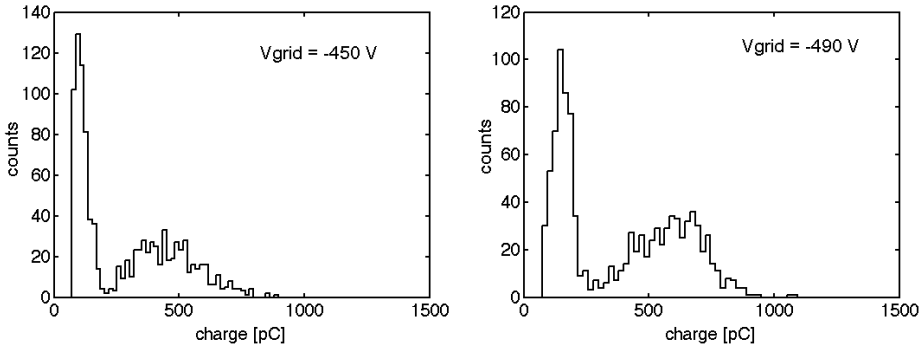

Figure 5.14: *Left: Charge spectrum for a grid voltage of -450 V. The average charge is 280 pC. Right: Charge spectrum for a grid voltage of -490 V. The average is 375 pC. It appears that, like in figure 5.10, there are two different processes.*

The average charge per spark at a grid voltage of -450 V is 280 pC, at -470 V it is 325 pC and at -490 V it is 375 pC, which is an increase of 34% for a change in grid voltage of 9%. Again, like for the Ar/CH$_4$ 90/10 mixture, two different types of sparks appear to occur. The currents in the sparks are estimated to be in the order of a few hundreds of mA.

5.3.8 Spark quenching in a He/iC$_4$H$_{10}$ mixture

Different He/iC$_4$H$_{10}$ mixtures, in the ratios 50/50, 80/20 and 90/10, have been tested to determine the effect of the fraction of iC$_4$H$_{10}$. With decreasing fraction of iC$_4$H$_{10}$ both the current and charge of a spark increases. Sparks with currents of more than 10 A have been measured (figure 5.15 bottom right graph); 10 A even is a low estimation since the rise time of the oscilloscope may be a limiting factor.

The left graphs in figure 5.15 show the charge in sparks and the right graphs show the current. The sparks with a small amount of charge also have a small current. The small currents are below the noise and are cut out in the current graphs. The small currents are in the order of 20 mA.

It appears that sparks in a He/iC$_4$H$_{10}$ gas mixture are quite large compared to the sparks in the other gas mixtures that have been evaluated. Still a He/iC$_4$H$_{10}$ mixture offers the advantage that sparking only occurs for high gas gains. The gas gain in the measurement with the 80/20 mixture is estimated to be approximately 10^5, in contrast to the measurement with the Ar/CH$_4$ mixture in which at a gas gain of 5×10^3 already sparks occurred.

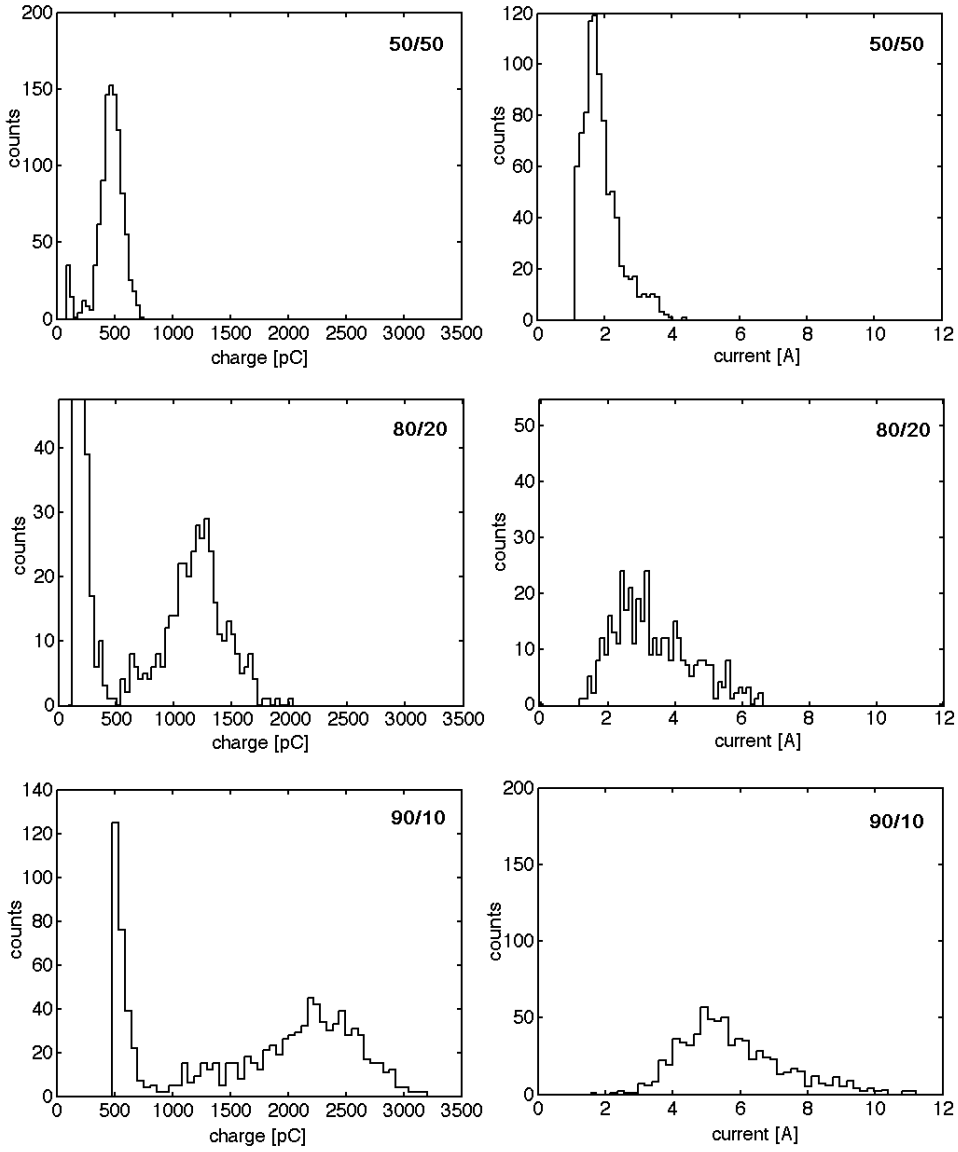

Figure 5.15: *Left: Charge spectrum of sparks in a He/iC_4H_{10} mixture in a 50/50, 80/20 and 90/10 ratio. The grid voltage was -540 V (top graphs), -520 V (middle graphs) and -540 V (bottom graphs) respectively. In the middle left graph the Y axis is scaled to show the charge distribution between 500 and 2000 pC. The majority of the signals had less than 500 pC, the distribution below 500 pC contains 640 out of the 1024 entries. Right: Current spectrum corresponding to the left graphs, the noise is cut out.*

5.3.9 The 'slow' spark hypothesis

The 'slow' spark may not be a spark, it may be the result of a succession of several large avalanches that eventually stop because of the charging up of the SiRN layer. One can imagine that after one (large) avalanche after a few tens of ns the cloud of ions reaches the grid (most ions are created close to the anode, section 2.2.2). A dense cloud of positively charged ions close to the grid locally increases the electric field between the grid and the cloud of ions. This strong field and photons generated by the neutralisation of the positive ions may result in electrons being released from the aluminium of the grid. These electrons in their turn also create an avalanche and the process can happen again.

Using a low pass filter on the 'slow' spark signal shows a substructure in the signal with times in the order of tens of ns (figure 5.16) suggesting that one avalanche in some way initiates another one.

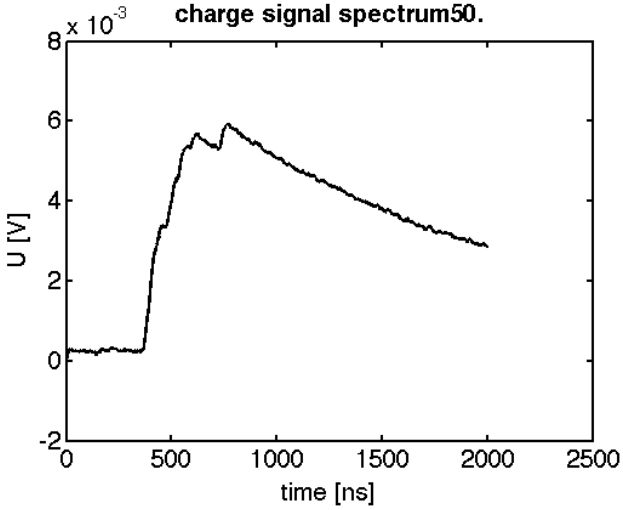

Figure 5.16: *The same 'slow' spark signal as shown by figure 5.8 after it has been passed through a low pass filter showing the sub structure of the signal.*

The assumption that the arrival of the ions at the grid is responsible for another avalanche would imply that the time scale of this process is related to the drift time of the ions. To test this hypothesis one can measure these processes in different gas mixtures with well understood ion drift times. Gases in which the ions have longer drift times should show 'slow' sparks that have a proportionally longer time structures. The ion drift times for the gas mixtures used in the measurements presented in this chapter have not been studied and are therefore not used to investigate this process. One can use an argon based mixture and a xenon based mixture in which the majority of the moving ions are the argon and xenon ions. The factor of two difference in drift velocity between the argon and xenon ions should be clearly distinguishable in the 'slow' sparks. If increasing the amount of quencher gas (increasing

absorption of UV photons) reduces the fraction of 'slow' sparks it is an indication that the electrons are released by the photo electric effect. Photons created in the gas amplification process that release more electrons which in their turn are multiplied effectively increase the gas gain. This process is called photon feedback [51]. If each multiplied electron results in more than one photo electron being multiplied the process is on a runaway and can result in a spark.

5.4 Spark quenching with 4 μm SiRN

A Timepix chip equipped with a 4 μm SiRN layer is tested with a CO_2/DME 50/50 gas mixture, the average amount of charge in a spark was increased from 250 pC (figure 5.12) to 306 pC (figure 5.17). The maximum amount of charge in a spark is increased from 450 pC to 650 pC. The current also increased during the sparks, however it is not precisely known how much the current increased because of the limited readout bandwidth.

It appears that half the thickness of the SiRN layer does not double the amount of charge deposited in a spark. The charge density distribution on the SiRN layer may be different, causing a non-linear relation between SiRN layer thickness and deposited charge.

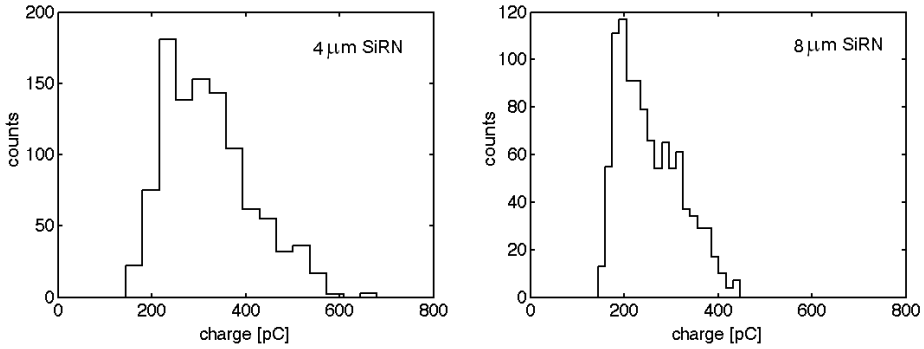

Figure 5.17: *Charge deposition of sparks in a CO_2/DME (50/50) gas mixture for a 4 μm and an 8 μm thick SiRN layer. The grid voltage was -580V. Left: A 4 μm SiRN layer, the average charge is 306 pC. Right: An 8 μm SiRN layer, the average charge is 250 pC.*

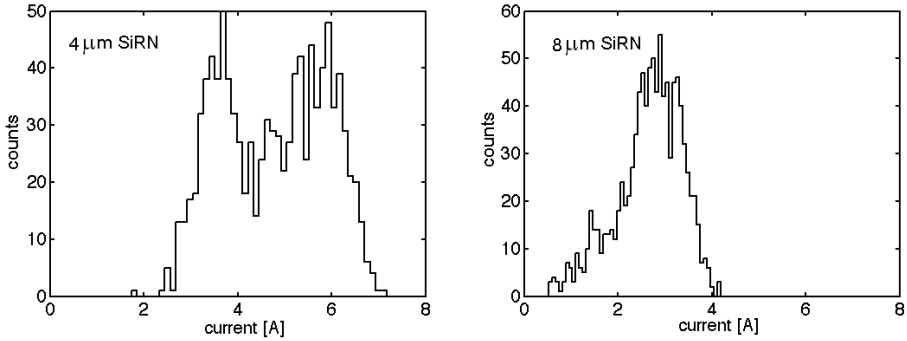

Figure 5.18: *Currents of sparks in a CO_2/DME (50/50) gas mixture for a 4 μm and an 8 μm thick SiRN layer.*

5.5 Spatial structure of charge deposition

One can estimate the maximum amount of charge that will be induced on a pixel input pad in case of a quenched spark. According to equation (5.1) the virtual capacitance of an input pad can be calculated. A pixel input pad is approximately 20 μm in diameter and the SiRN has an ϵ_r of 7.5. In case of an 8 μm thick SiRN layer the capacitance is approximately 2.6×10^{-15}F. In worst case of a spark, this layer becomes charged to the same voltage as the grid. The amount of induced charge on the input pad will be $2.6 \times 10^{-15} V_{grid}$. For a grid voltage of 600 V the induced charge will be in the order of two pC. According to the measurements in previous sections the deposited charge in sparks is in the order of one nC. For that reason one would expect the charge to be spread over an area that extends over many pixels.

In order to see the spatial distribution in a spark a fully operational Gridpix detector is operated in an Ar/iC_4H_{10} (80/20) gas mixture at a gas gain such that, when irradiated with an ^{55}Fe source, occasional sparks occurred. An example of a typical recorded spark is given in figure 5.19. Pixels in the columns struck by a spark record false hits due to the common electrical lines being affected by the spark. The voltage on the grid was -440 V. Figure 5.20 shows the spectrum of charge in the sparks. It appears that on average a charge of approximately 0.6 nC is deposited. Assuming that the full grid potential is on the SiRN layer, the spark should cover a circle of approximately 0.55 mm, 10 pixels in diameter. The 'inner spot' in figure 5.19 is 10 pixels in diameter. The outer circle however, is much larger and it is not yet known what process causes the concentric circle around the central spot.

Due to a defect in the SiRN layer the chip was struck by a spark that damaged the chip and the measurement was terminated. It was not possible to observe correlation between charge measured on the grid and the TOT values recorded by the hit pixels suggesting that the amplifiers in the pixels become saturated when struck by a spark.

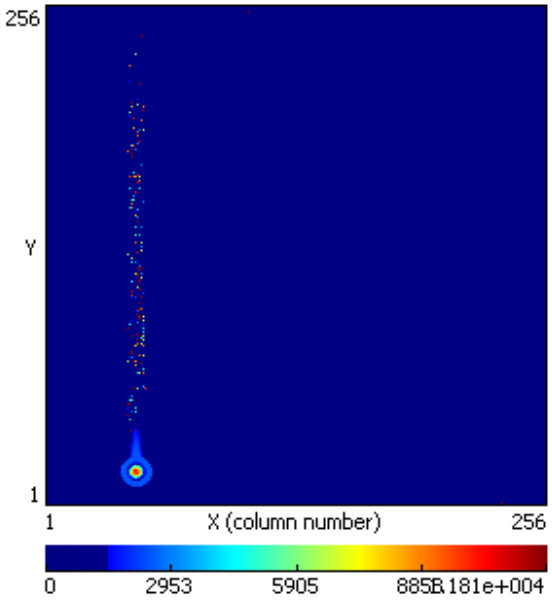

Figure 5.19: *A typical spark in an Ar/iC_4H_{10} (80/20) gas mixture with a grid voltage of -440V. The colour represents the TOT value measured by the pixels. Some other pixels in the same columns that are struck by the spark give false hits due to the shared electric interconnections that are affected by the spark.*

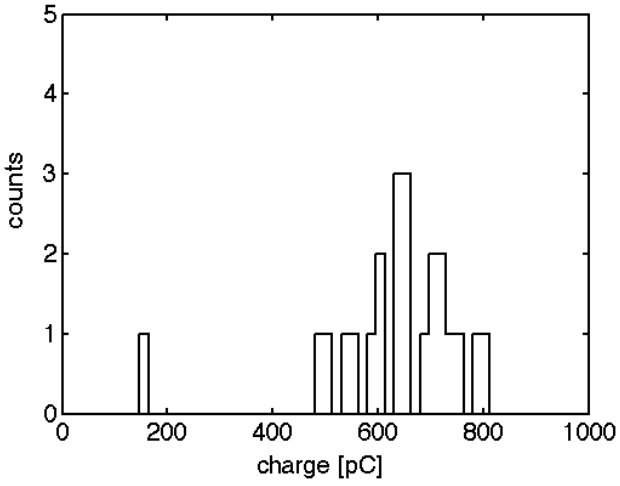

Figure 5.20: *Spectrum of sparks with an Ar/iC_4H_{10} (80/20) gas mixture with a grid voltage of -440V*

Both the spatial structure and processes in the sparks are poorly understood and strongly dependent on the gas mixture. For that reason one should make a spark protection layer such that in worst case condition (instantly full grid potential on top of the protection layer) pixels can cope with the induced charge.

5.6 Charge-up effects of SiRN

After a spark, the charge on the SiRN layer is drained with the characteristic time τ_{prot}, introducing a dead time which is the time needed before the electric field is restored. During normal operation also charge up occurs, causing a potential drop. In case the occupancy is such that the average time between hits on a pixel is more than τ_{prot} the maximum gas gain can be calculated. Assuming an ϵ_r of 7.5, and a layer thickness of 8 µm. A circular pixel input pad has a diameter of 20 µm. According to equation (5.1) the virtual capacitance of the layer above a pixel input pad is approximately 2.6×10^{-15}F. In order to apply a potential of 5 V across this capacitance a charge of 10^5 electrons, evenly distributed above the pad, is needed. This means that with a gas gain of more than 10^5 the average time between hits on a pixel should be more than τ_{prot} to let charge be drained off. With the sensitivity of future pixel electronics a gain of 5000 should be sufficient. In that case the occupancy may be higher, until a steady state current through the layer is reached such that the potential drop is 5 V. The resistance of a SiRN protection layer is measured to determine how it affects gas gain.

5.6.1 Effects of SiRN resistance on gas gain

In order to determine the resistivity of the protection layer a measurement is performed in which is determined how much the gas gain drops with increasing rate. The gas gain depends exponentially on the voltage across the gain gap and can be expressed as [51]:

$$G = ae^{bV} = ae^{b(V_{grid}-\Delta V)}. \tag{5.7}$$

The potential across the SiRN layer is ΔV. The coefficients a and b depend on gas mixture and the width of the gain region and can be obtained by fitting an exponential function through measured gain values. The voltage V_{grid} is the absolute voltage between the anode and the grid. The gas gain is determined by measuring how much charge is induced on the grid after amplification of primary charge released by 5.9 keV photons emitted by an ^{55}Fe source. The gas gain is measured for a constant grid voltage with different intensities of radiation, resulting in different gas gains according to:

$$G_1 = ae^{bV_{grid}}. \tag{5.8}$$

$$G_2 = ae^{b(V_{grid}-\Delta V)}. \tag{5.9}$$

The gain G_1 is measured with a low rate such that ΔV across the SiRN layer is negligible. The ratio of the gains can be used to extract ΔV:

$$\frac{G_1}{G_2} = \frac{ae^{bV_{grid}}}{ae^{b(V_{grid}-\Delta V)}} = \frac{ae^{bV_{grid}}}{ae^{bV_{grid}}e^{-b\Delta V}} = \frac{1}{e^{-b\Delta V}}. \tag{5.10}$$

$$\ln\left(\frac{G_2}{G_1}\right) = -b\Delta V \rightarrow \Delta V = \frac{\ln\left(\frac{G_2}{G_1}\right)}{-b}. \tag{5.11}$$

The specific resistance can be obtained by:

$$\rho = \frac{\Delta V}{Jd} = \frac{A\Delta V}{Id}. \tag{5.12}$$

In equation (5.12) J is the current density, d is the thickness of the SiRN layer, I is the total current between the grid and the chip and A is the surface area where the current flows through. For I can be written:

$$I = G_2 N_e N_\gamma. \tag{5.13}$$

The number of primary electrons released by one photon that arrive in the gain region is N_e and the number of photon absorptions per second is N_γ. Combining equation (5.11) and (5.13) in (5.12) results in:

$$\rho = \frac{A\ln\left(\frac{G_2}{G_1}\right)}{-bdG_2 N_e N_\gamma}. \tag{5.14}$$

The found value for ρ is only an approximation since it is hard to make an accurate estimation of the area A through which the current flows. Areas not beneath a grid hole will receive less charge than the pixel input pads. As a result ΔV also is not constant across the SiRN surface which introduces another uncertainty. For the calculations the total irradiated surface area of the chip is taken. The factor of reduction in gain as a function of the rate and gain can be calculated by using equation (5.12), (5.13) and (5.10):

$$G_r = e^{-b\Delta V} = e^{\frac{-b\rho G N_r d}{A}}. \tag{5.15}$$

In which $N_r = N_e N_\gamma$ is the rate, the total number of primary electrons per second that arrive in the gain region and G_r the factor of reduction in gain.

5.6.2 Measuring the specific resistance of SiRN

The resistance of the SiRN layer is measured using an Ar/iC_4H_{10} gas mixture in a ratio of 80/20. In this mixture the number of primary electrons (N_e) that arrive in the gain region is 226 (section 6.1). The gain for three different photon absorption rates (N_γ) is shown by figure 5.21. The irradiated area is one cm^2.

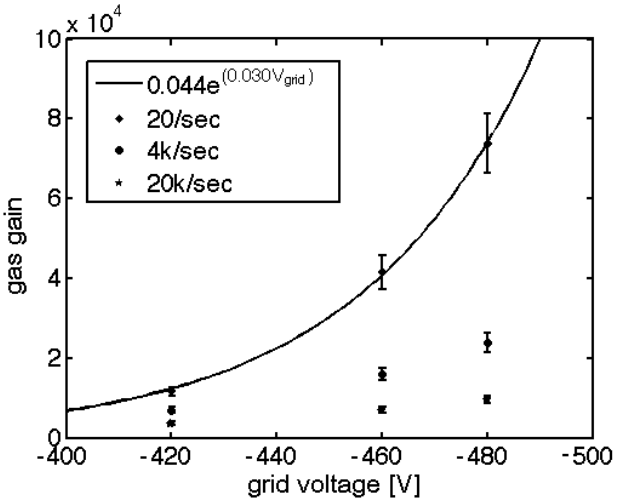

Figure 5.21: *Gas gains for three different photon absorption rates for three different grid voltages (absolute volts) in an Ar/iC_4H_{10} (80/20) gas mixture. The low rate measurement is used to find the gas gain as a function of the voltage across the avalanche gap.*

With an exponential fit the gain as a function of the voltage is obtained. Then, at the same grid voltages N_γ is increased. After ten minutes, when the gain is stable, the gain is measured. Table 5.1 shows the gas gains for the different grid voltages and rates.

V_{grid}	20/sec	4k/sec	20k/sec
-420 V	11.6×10^3	6.96×10^3	3.64×10^3
-460 V	41.5×10^3	15.9×10^3	6.96×10^3
-480 V	73.9×10^3	23.9×10^3	9.66×10^3

Table 5.1: *The different gas amplifications for different grid voltages and photon absorption rates.*

The thickness of the SiRN layer is 8 µm. Filling in those numbers in equation (5.14) result in values varying between 2×10^{13} Ωcm and 3×10^{13} Ωcm which indicates that the specific resistance is a few 10^{13} Ωcm. For the SiRN layer to be compatible to be used in conditions that are expected at the sLHC this value should be as low as 10^9 Ωcm [73] for a gas gain of 5000. The drop in gas gain with 5 V across the SiRN layer will be 0.86, according to equation (5.15). The gain will be reduced to 86% of its original value.

5.6.3 The dependency of the spark probability on the gas gain

For increasing gas gains the probability of an ^{55}Fe photon absorption to result in a spark increases. The measurement described in section 5.6.2 contained enough data to measure the spark rate as a function of the gas gain for the lowest rate of 20/sec. The gas was an Ar/iC$_4$H$_{10}$ 80/20 mixture. Table 5.2 shows the fraction in % of photon absorptions that developed into a spark. For each gas gain setting 8192 samples have been taken.

gas gain	fraction of sparks
11.6×10^3	0%
41.5×10^3	0.1%
73.9×10^3	1.1%
113.6×10^3	9.2%

Table 5.2: *Spark probability for different gas gains for an ^{55}Fe photon absorption rate of 20/sec.*

5.7 SiRN layer defects

To test the robustness of the SiRN protection layer, two detectors with a 4 µm SiRN layer were set to spark at a rate of one spark per second for more than 12 hours. Both detectors survived. One of the detectors failed later during normal operation [67]. The other detector is still operational. Detectors with an 8 µm SiRN layer also sometimes break down. To see where a poorly quenched spark struck, a 1 nF capacitance is connected to the grid. With 1 nF capacitance, poorly or non-quenched sparks result in visible damage, i.e. parts of the grid evaporate and holes are blown in the SiRN layer and chip surface (figure 5.22). After pacifying these spots with UV curing resin (often required consecutively on different spots), these sparks could not be reproduced, even at higher grid voltages. Such behaviour is only possible if the SiRN layer gives sufficient protection. Therefore it have to be defects in the SiRN layer that are responsible for the occasional breakdowns. This explains the occasional break down of a chip with 8 µm SiRN while a chip with only 4 µm can sustain discharges.

The fact that a Timepix chip does not survive one unquenched spark implies that the SiRN layer must be perfect to be adequate. In case the layer is perfect, a 4 µm SiRN layer offers sufficient protection. With a 4 µm SiRN layer, for a grid voltage of -600 V, a maximum charge of 4 pC can be expected on a pixel. The combination of a pixel that can resist an instant charge of a few pC and a perfect SiRN layer of 4 µm or thicker makes a pixel chip spark proof.

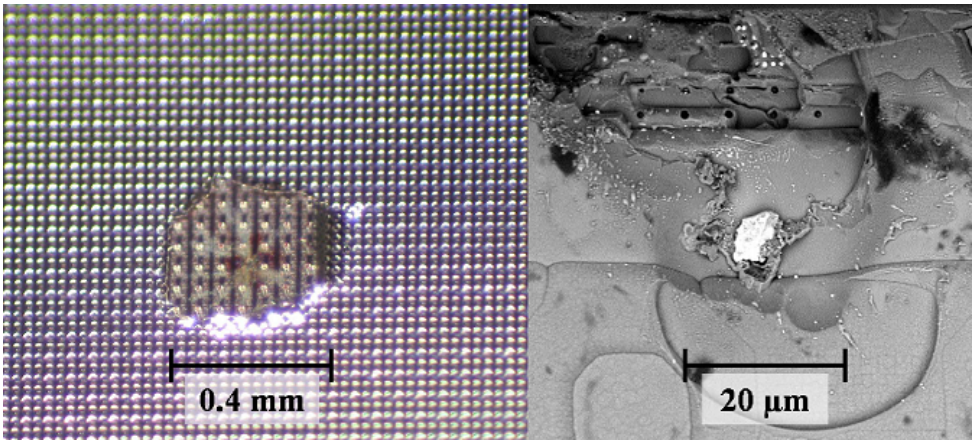

Figure 5.22: *Damage after an unquenched spark from a grid with 1 nF capacitance. Left: a part of the grid is blown away. Right: Damage on the SiRN layer and the chip.*

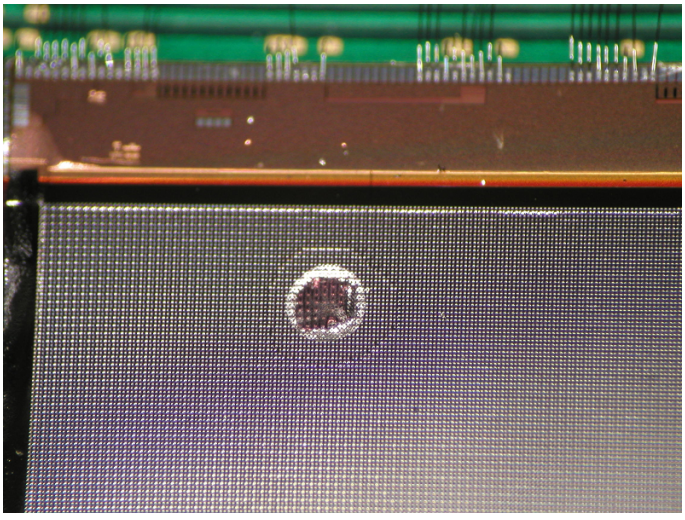

Figure 5.23: *Passivated spot where an unquenched spark struck. At the top, slightly out of focus, the wire bonds of the chip can be recognised.*

5.8 Concluding remarks

The capacitance of the grid does not affect the amount of charge in a quenched spark. The grid capacitance may even be increased to ensure a more stable voltage (and thus gas gain) in case a spark occurs.

It appears that the used gas mixture strongly affects the amount of charge deposited in a quenched spark as well as the current in a spark. In the He/iC$_4$H$_{10}$ the current and charge in a spark reduces with an increase of the quencher gas iC$_4$H$_{10}$. The currents in sparks may have been higher than measured since the bandwidth of the measurement set up may have been insufficient.

The charge in a quenched spark is extended over many pixels, as opposed to a non quenched spark that deposits all energy locally (figure 5.1 and 5.22). For a quenched spark the load per pixel is reduced to a maximum of a few pC. A more extensive study is required to explain the time structure of sparks and the concentric ring structure of the charge deposited on the chip.

The specific resistance of a SiRN layer can be determined by measuring how the gas gain is reduced with increasing rate due to the net charge build-up on the layer.

A chip covered with a perfect 4 μm SiRN layer with pixel amplifiers that can resist an instant charge of 10 pC should be spark proof.

Spark quenching works for layers down to 4 μm SiRN. It is of absolute importance that the SiRN layers do not have any defects since that introduces the risk of total chip failure. The fact that chips still become damaged is an indication that the spark protection requires further study. A long term test (months as opposed to days) still has to be performed with many samples in order to prove long term reliability. To further increase the spark quenching power, research is performed on fabricating highly resistive (SiRN) grids (as mentioned in chapter 3).

Chapter 6

Gridpix characterisation

The Gridpix detector concept has been verified by testing several detectors with different drift gaps and spark protection layers. The detectors have been irradiated with an ^{55}Fe source and 2 GeV/c electrons at DESY[1]. Section 6.1 shows a study on the basic detector performance like measuring the single electron detection efficiency and gas gain as a function of the grid voltage, the effective threshold, the shape of the Pólya distribution (section 2.2.1 and 4.2.2) and the probability of inducing false hits on adjacent pixels in case of very large avalanches. Section 6.2 focuses on the measurements at DESY. Four Gridpix detectors with a drift gap of 11.5 mm and Timepix chips covered with 2, 4, 6 and 8 µm SiRN are tested to determine the effect of different spark protection layers on detector performance. In section 6.3 the track reconstruction accuracy of the Gridpix detectors is determined and the diffusion is measured. With the measured diffusion the quality of the applied track fitting procedure is tested.

6.1 Basic detector performance with ^{55}Fe

To determine the sensitivity of a Gridpix detector both the gas gain as a function of the grid voltage and the single electron detection efficiency as a function of the gas gain has to be determined. Photo absorption of 5.9 keV photons from an ^{55}Fe source is used to release a defined amount of primary charge. In this section (6.1) the SiRN spark protection layer is 8 µm thick unless otherwise noted.

6.1.1 Single electron detection efficiency

The cluster of primary electrons created with a 5.9 keV photon will diffuse as it drifts to the readout chip. With sufficient transversal diffusion almost all primary electrons each arrive at a different pixel. With increasing gas gain the number of

[1] *D*eutsches *E*lectronen *SY*nchrotron

pixels that detect an avalanche will asymptotically approach the total number of electrons arriving in the gain region.

When the number of electrons arriving in the gain region is known, the charge induced on the grid by the amplification process is measured. The amplitudes of individual avalanches follow a Pólya distribution. The charge induced on the grid is the sum of all the avalanches and for large numbers it can be considered to be the sum of the average of the Pólya distribution. The gas gain is the average amount of charge induced on the grid divided by the average number of electrons arriving in the gain region.

To measure the single electron efficiency and the gas gain, a Gridpix detector with a 10 cm drift gap (figure 6.1) has been used. The X-ray source was placed near a hole in the field cage 8 cm above the readout chip. Along the 8 cm drift distance the primary charge clusters diffuse sufficiently to have each electron arriving at a different pixel.

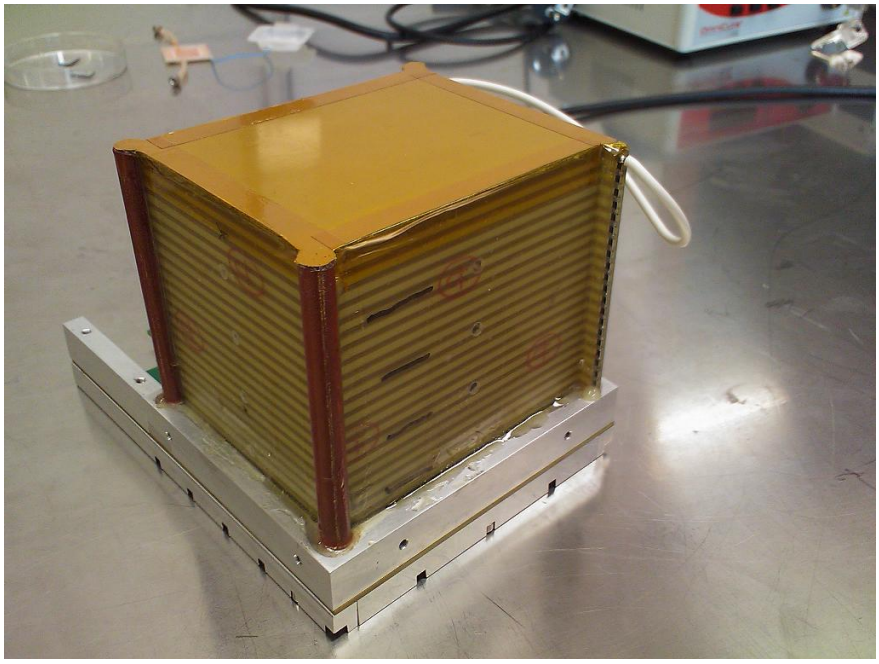

Figure 6.1: *A Gridpix detector equipped with a 10 cm drift gap. A pattern of four holes has been drilled in each side of the field cage to make 'transparent' spots for irradiation with a source. To make the volume gas tight the holes are covered with a 25 μm mylar foil.*

The Timepix chip is set in TOT mode (see section 3.2 and 4.2) to measure the amplitude of the signals induced on the pixels. The chip is read out using a MUROS [74] readout system that sends the data to a computer. On the computer the data is processed and stored by Pixelman software [75]. A sketch of the readout is shown by figure 6.2.

Using a gas mixture of He/iC$_4$H$_{10}$ 80/20 a scan was made of grid voltages between -340 V and -480 V. Figure 6.3 shows events at two different grid voltages. Figure 6.4 shows the histogram of the number of hit pixels for 10^3 photon conversions at a grid voltage of -440 V.

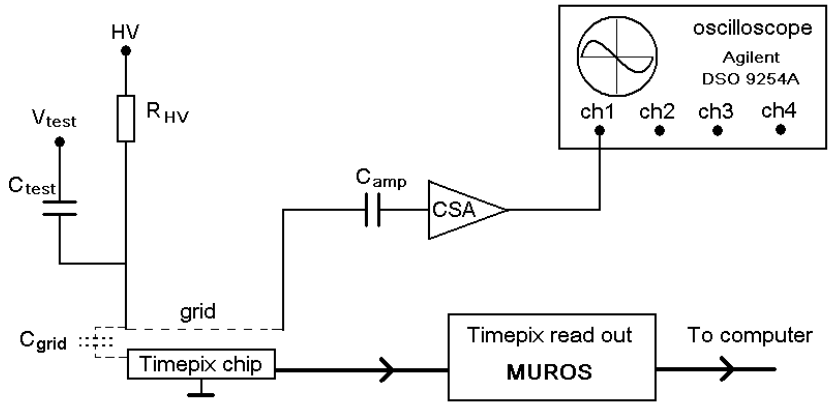

Figure 6.2: *Set-up to count primary electrons and to measure signals induced on the grid. The grid is read out with a charge sensitive amplifier (CSA) and the Timepix chip is read out using a MUROS readout system that sends data to a computer. The drift region (not drawn) is 10 cm in height.*

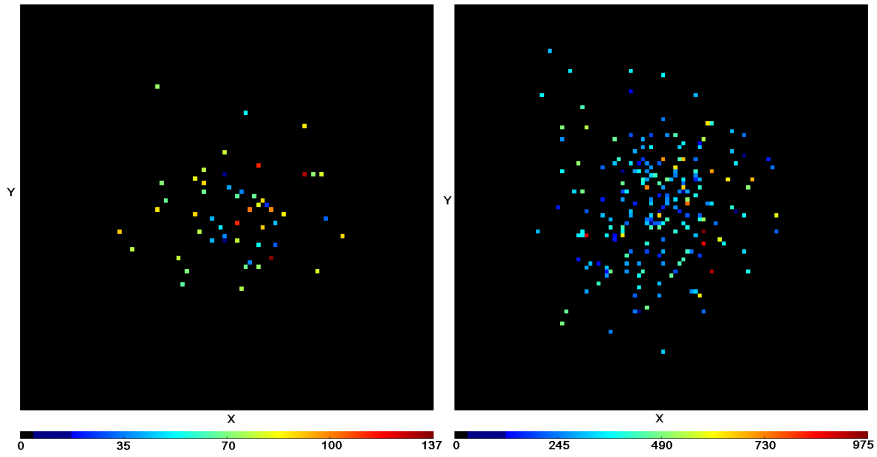

Figure 6.3: *Two typical ^{55}Fe events, on the left picture the grid voltage was -340 V, on the right it was -440 V. The colour indicates the TOT value. The plots show that with increasing grid voltage the number of detected avalanches increases as well as the charge in an avalanche. In the left picture the maximum TOT value is 137 clock counts, in the right picture it is 975 counts.*

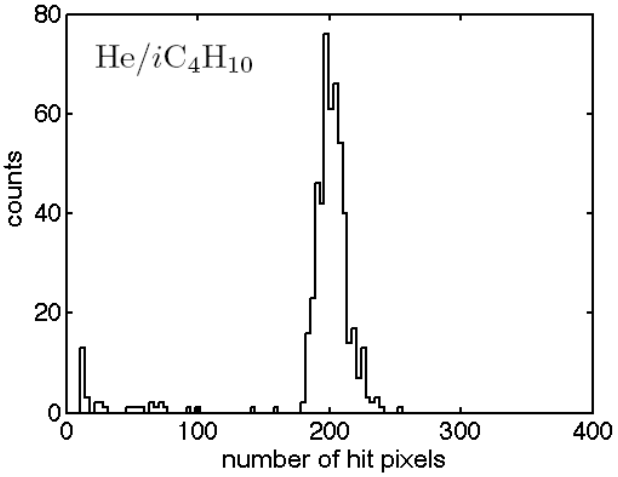

Figure 6.4: *Histogram of the number of pixels being hit for a grid voltage of -440 V. The average number of hit pixels is 210. The asymmetry on the right side of the distribution (the hump at approximately 230 pixels) may be caused by the second 10% energy band of the ^{55}Fe at 6.4 keV.*

Figure 6.5 shows that the increase in number of hit pixels as a function of the grid voltage first tends to saturate but starts to increase again at -480 V. This phenomenon is supposed to originate from the fact that some avalanches become large enough to be detected by neighbouring pixels. This effect is illustrated in the TOT spectra for these grid voltages. Figure 6.6 (red line) shows the TOT spectra for -440 V and -480 V on the grid. While at -440 V the distribution still has a normal shape, at -480 V unexpectedly an additional peak from small charge signals has appeared. This is in contradiction with the fact that for an increasing gas gain the fraction of small signals should decrease. According to this assumption a large avalanche causes an adjacent pixel to detect a 'false hit', i.e. a hit that does not represent primary charge from the drift region. Figure 6.7 shows that small signals always are accompanied by a large signal on one or more adjacent pixels. This phenomenon enables identification and removal of false hits from the dataset.

To identify a hit pixel as a false hit, the pixel should have detected a small signal (low TOT count) *and* the sum of the charge on neighbouring pixels should be large (high TOT count). For the helium mixture, based on the TOT spectrum shown by figure 6.6, a threshold of 180 clock counts is set. The minimum required TOT count for a single adjacent pixel must be 600, or the sum of TOT values for multiple adjacent pixels must be at least 900. After applying these criteria to remove the false hits the TOT spectra shown by the red line in figure 6.6 becomes as shown by the black line. This method does not affect TOT distribution for a lower gas gain as is illustrated by figure 6.6 in the left graph.

After cleaning the dataset from false hits, the curve of the number of hit pixels as a function of the grid voltage now shows the expected behaviour (figure 6.8).

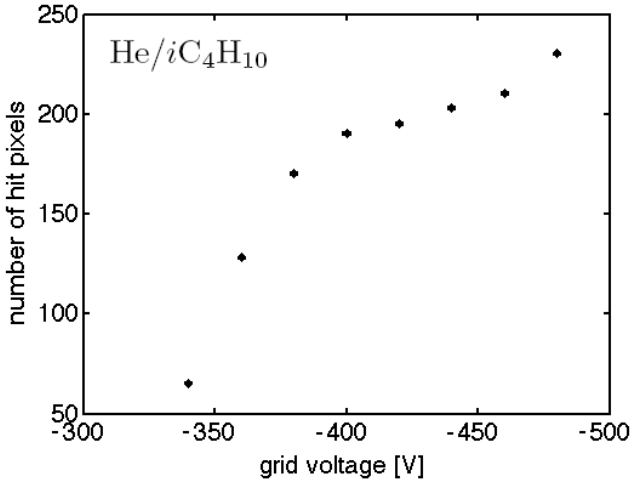

Figure 6.5: *Average number of hit pixels as a function of the grid voltage.*

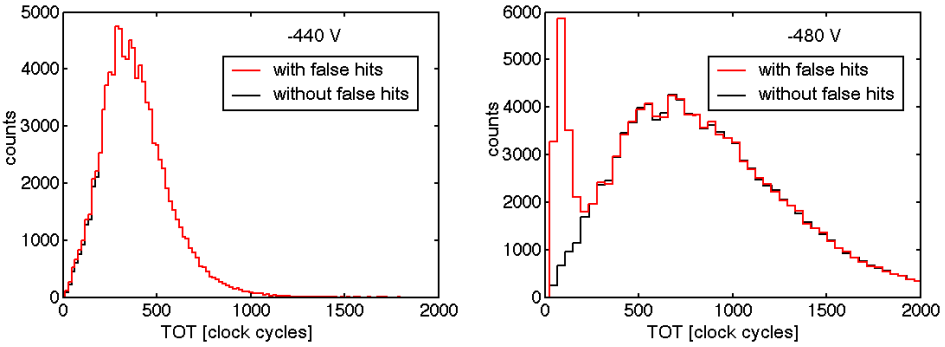

Figure 6.6: *Time over threshold (TOT) spectra for a grid voltage of -440 V (left) and -480 V (right). The red line shows the TOT spectra without the removal of false hits. In the right graph a second peak appears at low TOT values due to charge induced on neighbouring pixels. The black line shows the TOT spectra after removal of the false hits, the peak at low TOT values in the right graph has disappeared.*

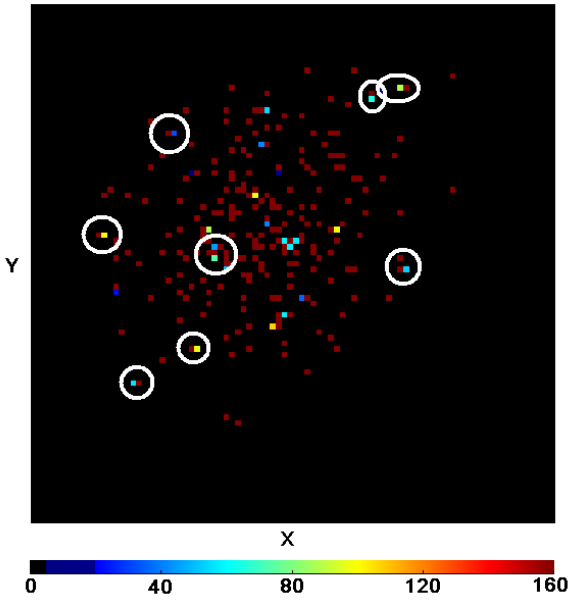

Figure 6.7: *A typical event recorded in a He/iC_4H_{10} 80/20 mixture with a grid voltage of -480 V. The red pixels have a TOT value of 160 or more. The pixels with a TOT value lower than 160 are all accompanied by an adjacent pixel having a high TOT value. A few are highlighted by white circles.*

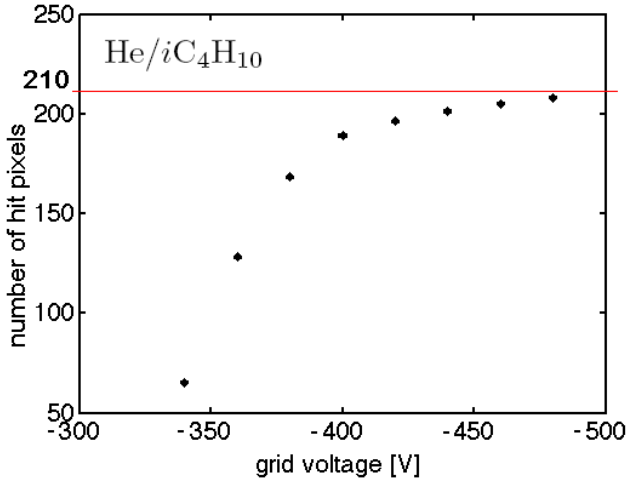

Figure 6.8: *Average number of hit pixels as a function of the grid voltage after removing the false hits. The maximum counted number of pixels was 208 at a grid voltage of -480 V.*

The number of primary electrons has also been measured for an Ar/iC_4H_{10} 80/20 gas mixture. The spectrum of the number of hit pixels for a grid voltage of -430 V is shown by figure 6.9. The small peak at 110 pixels, the 'escape peak', (see section 5.3.1) originates from fluorescence photons escaping detection. The main photo peak at 200 pixels originates from the ionisation caused by an auger electron in addition to the photo electron. To calibrate the gas gain the average number of hit pixels in the photo peak is used. Figure 6.10 (left graph) shows the number of hit pixels as a function of the grid voltage without removing false hits. The right graph in figure 6.10 shows the number of hit pixels after correction.

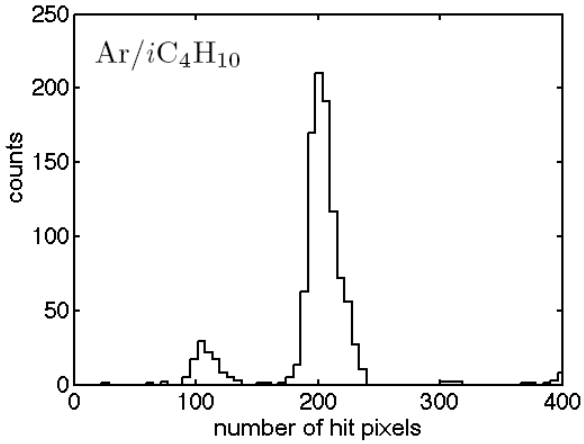

Figure 6.9: *The number of hit pixels for a grid voltage of -430 V. In this graph the average is 210. Again, like in figure 6.4, due to the 10% of 6.4 keV photons the photo peak is broadened on the right side.*

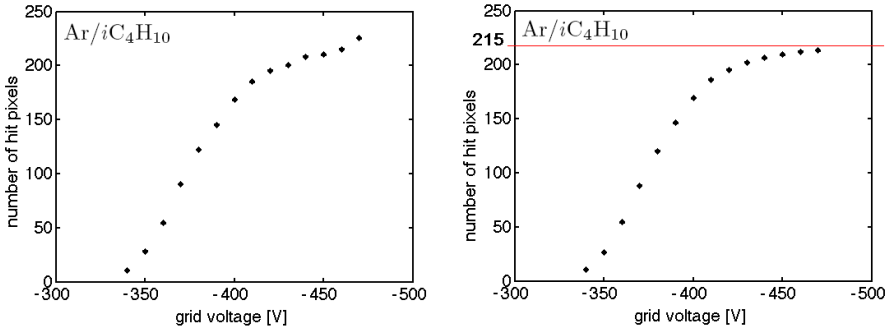

Figure 6.10: *Left: Average number of hit pixels as a function of the grid voltage without removal of false hits. Right: After removal of false hits. The maximum counted number of hit pixels is 213 at a grid voltage of -470 V.*

Sometimes a pixel is hit by more than one primary electron, resulting in less pixels being hit than the number of primary electrons entering the gain region. To account for the number of electrons that do not arrive at separate pixels the TOT spectrum of all hit pixels is compared to the TOT spectrum of pixels that are likely to be hit by only one primary electron. A pixel is likely to be hit by only one electron if the nearest hit pixel is at least 3 pixels away, being the only pixel hit in a square that contains at least 49 pixels. Two electrons arriving randomly at 49 pixels have probability of 2% to end up on the same pixel. The probability that the hit is caused by 3 electrons is 0.04%. The probability that the solitary pixel is hit by more than one electron is 2% + 0.04% + etc.≈ 2.1%. Such a hit pixel is called a solitary pixel. The average TOT of the solitary pixels corresponds to the average amplification of 1 primary electron per pixel. The TOT of pixels hit by more than one primary electron will on average have an accordingly longer TOT. Figure 6.11 shows the distributions of TOT values for all pixels and for solitary pixels. The graphs are scaled such that they cover the same area to show the difference. In both an Ar/iC$_4$H$_{10}$ 80/20 and a He/iC$_4$H$_{10}$ 80/20 gas mixture the TOT for all hits is on average 5% higher than the TOT for solitary pixels, indicating that the average primary charge per hit pixel is 1.05 electrons.

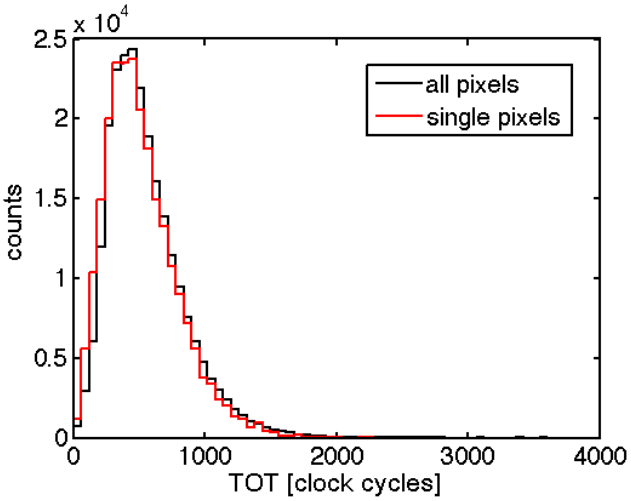

Figure 6.11: *Time over threshold (TOT) spectra for all pixels in all events (black line) and solitary pixels (red line) for an Ar/iC_4H_{10} 80/20 gas mixture with a grid voltage of -470 V. The graphs are scaled such that they cover the same area to show the difference between the distributions. One can observe a lack of low TOT values and an excess of high TOT values in the spectrum of all hits compared to that of the solitary pixels. The average TOT of all hits is 526 counts, which is approximately 5% more than the average TOT of the solitary pixels (500 counts).*

For the highest grid voltages the number of hit pixels is 208 and 213 for the He/iC$_4$H$_{10}$ 80/20 and the Ar/iC$_4$H$_{10}$ 80/20 mixtures respectively. By eye fit the

number of hit pixels as a function of the grid voltage asymptotically approaches 210 and 215. With approximately 1.05 primary electrons per pixel, the total number of primary electrons arriving in the gain region is approximately $1.05 \cdot 210 \approx 221$ for the helium mixture and $1.05 \cdot 215 \approx 226$ for the argon mixture.

One can estimate the expected number of primary electrons in a gas mixture by dividing the photon energy (E_γ) through the average amount of energy required (E_i) to create one ionisation. The value of E_i for a gas mixture with a fraction η_A of gas A and a fraction η_B of gas B can be calculated by:

$$E_i = \frac{\eta_A N_A E_{iA} + \eta_B N_B E_{iB}}{\eta_A N_A + \eta_B N_B}. \tag{6.1}$$

In equation (6.1) N_A and N_B are the average numbers of released electrons[2] per cm track of a MIP traversing gas A and B. The average ionisation energies for those gases are E_{iA} and E_{iB}. The values of E_i for several gases can be found in appendix A in table A.3 [76]. For the Ar/iC$_4$H$_{10}$ 80/20 mixture E_i is 25.0 eV, for the He/iC$_4$H$_{10}$ 80/20 mixture E_i is 25.5 eV. With these values a 5.9 keV photon results in 236 electrons in the argon mixture and in 231 electrons in the helium mixture.

According to simulations with HEED [68] the number of primary electrons to be expected are 230 and 160 for the argon and the helium mixture respectively. For the argon mixture the results are close, for helium based mixtures HEED does not return correct results. This may be due to some wrong settings in the simulation or a bug in the HEED software and has been reported to the authors.

In case one uses the number of hit pixels to estimate the number of primary electrons released in the drift volume, the estimation will be too low. A fraction of primary electrons will end up on the grid instead of entering the gain region. The fraction of electrons that ends up on the grid is in the order of a few %, which depends on the ratio between drift field and amplification field, the diffusion properties of the gas mixture and the grid geometry [51].

6.1.2 The gas gain

The gas gain is determined by measuring the amount of charge induced on the grid divided by the amount of primary charge that enters the gain region. The gain can be calculated by:

$$G = \frac{Q}{1.6 \times 10^{-19} N_e}. \tag{6.2}$$

Q is the charge after amplification, N_e is the number of electrons arriving in the gain region which is 221 for the He/iC$_4$H$_{10}$ 80/20 gas mixture and 226 for the Ar/iC$_4$H$_{10}$ 80/20 gas mixture. For measuring the charge on the grid, the set-up sketched in figure 6.2 is used. Figure 6.12 shows the measured gain for the Ar/iC$_4$H$_{10}$ 80/20 and the He/iC$_4$H$_{10}$ 80/20 mixtures and the fitted exponentials.

[2] Not to be confused with the number of clusters.

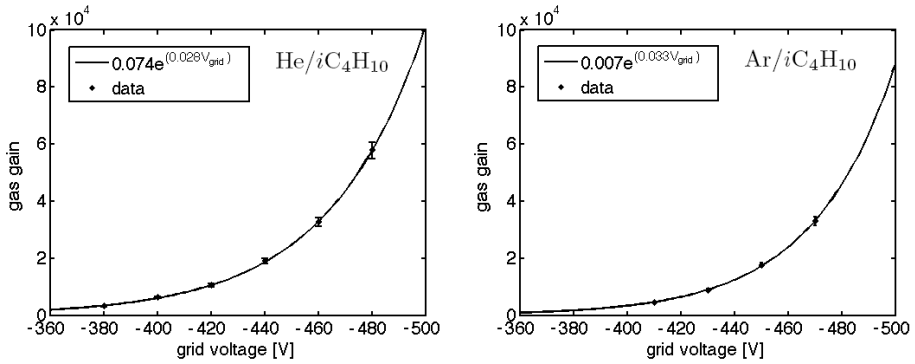

Figure 6.12: *Gas gain as a function of the grid voltage for a He/iC_4H_{10} 80/20 and Ar/iC_4H_{10} 80/20 gas mixture.*

The gas gain can be calculated for intermediate grid voltages by fitting an exponential function through the measured gain values.

Knowing the gas gain as a function of the grid voltage, the number of hit pixels as a function of the gas gain can be determined. Dividing the number of hit pixels by 210 for the helium based mixture and by 215 for the argon based mixture gives the single electron detection efficiency (figure 6.13).

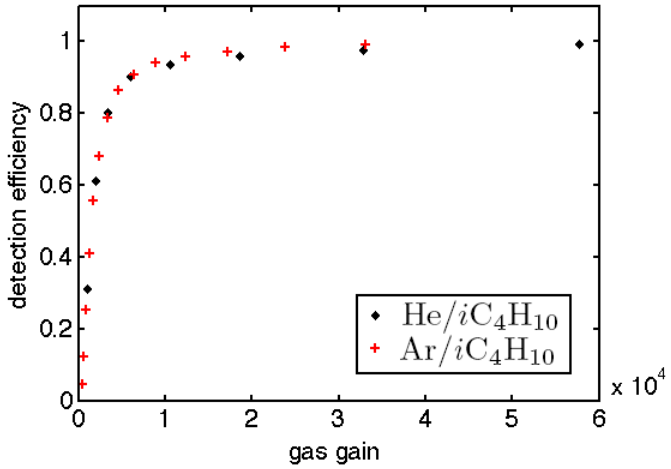

Figure 6.13: *Single electron detection efficiency as a function of the gas gain for an Ar/iC_4H_{10} 80/20 and He/iC_4H_{10} 80/20 gas mixture.*

6.1.3 The effective threshold and the parameter m

The amount of charge in an avalanche is Pólya distributed. The shape of the Pólya distribution is determined by the value of the parameter m (see section 2.2, figure 2.6). The value of the parameter m and the threshold determine how the single electron detection efficiency depends on gas gain (see section 4.2.2, figure 4.10). The parameter m can be determined by using the measured relation between single electron detection efficiency and the gain/threshold ratio. To find the gain/threshold ratio the threshold has to be determined. The measured threshold will be higher than the threshold set in the pixel electronics since less than 100% of the charge in an avalanche is induced in a pixel input pad. The avalanche occurs above an 8 µm SiRN layer and may also occur at the edge of a pixel input pad. On average an avalanche must contain more charge than the minimum amount of charge that can be detected by a pixel.

Figure 4.10 shows that for a gain/threshold ratio of 0.84 the single electron detection efficiency is approximately 0.31 for values of the parameter m between 1 and 4. Figure 6.14 shows the detection efficiencies for m varying between 1 an 4 in 500 steps. The threshold can be found by fitting the measurement results (figure 6.13) through the point (0.84,0.31) by varying the value through which the gas gain is divided. The value for which the curve goes through the point (0.84,0.31) is the threshold. For a detection efficiency of 0.31 the gain/threshold is 0.84 ±0.01 for values of the parameter m between 1 and 4. In that case the maximum deviation of the threshold because of an unknown value of m is ±1.2%.

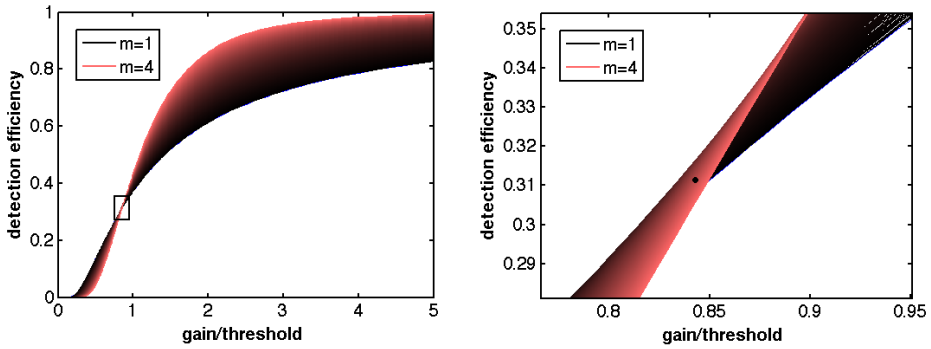

Figure 6.14: *Single electron detection efficiency for m in a range of 1 to 4 as a function of gain/threshold. The black rectangle in the left graph shows what is shown by the graph on the right. For a gain/threshold ratio of 0.84 the single electron detection efficiency is approximately 0.31 independent of m (the black dot in the right graph).*

Figure 6.15, the left graph, shows the result for the He/iC$_4$H$_{10}$ mixture, the measured threshold is 1230 (±15) electrons. The measured value of m is 2 for a gas gain of 1800 (gain/threshold ratio of 1.5) and approaches 1.5 for larger gas gains. For the Ar/iC$_4$H$_{10}$ mixture the results are shown in the right graph, the value of parameter m appears to be 1.5.

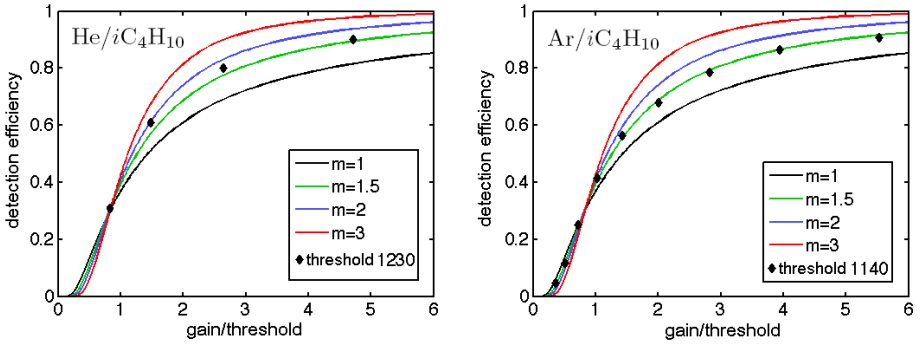

Figure 6.15: *Left: Single electron detection efficiency for a He/iC_4H_{10} 80/20 gas mixture (diamonds). The threshold is 1230 (±15) electrons. The value of parameter m is 2 for a gas gain of 1800 and approaches 1.5 for a gain of 6000. Right: Single electron detection efficiency for an Ar/iC_4H_{10} 80/20 gas mixture (diamonds). The threshold is 1140 (±14) electrons. The curve for a value of parameter m of 1.5 fits the data.*

The threshold set in the Timepix chip is approximately 700 electrons [57] and according to the measured thresholds, on average approximately 60% of the charge in an avalanche is detected.

6.1.4 Probability of false hits

As shown by figure 6.7 large avalanches may create enough charge to be detected by adjacent pixels. The probability of a false hit as a function of the charge on an adjacent pixel has been estimated by using solitary pixels. If a solitary pixel has an adjacent pixel with a non zero value lower than 180 counts the adjacent pixel is considered to be a false hit. By dividing the total number of false hits by the total number of pixels adjacent to pixels with a high TOT count the fraction of false hits is obtained. This fraction represents the probability of inducing a false hit. Only the vertically and horizontally adjacent pixels are counted. The diagonal pixels are $\sqrt{2}$ further away and have less than halve the charge induced on them and are neglected. Figure 6.16 shows the probability of a false hit as a function of the charge in an adjacent pixel for a chip with 8 µm SiRN and a chip with 4 µm SiRN. The amount of charge in an avalanche is approximately 45 electrons per clock count.

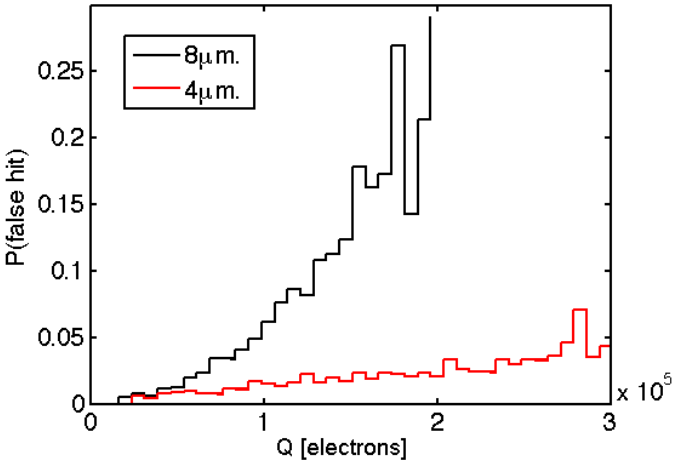

Figure 6.16: *Probability of a false hit as a function of the charge (Q) in an avalanche. The gas mixture was He/iC_4H_{10} (80/20). For a Timepix chip with an 8 μm SiRN layer (black line) the probability of a false hit is much higher than for a chip with only 4 μm SiRN (red line). The chip with 8 μm SiRN was operated at a lower gas gain (5.8×10^4) than the chip with 4 μm SiRN (9.4×10^4), resulting in more statistics for large charges for the chip with 4 μm SiRN. The irregularities in the graphs for large charges is due to less statistics for increasingly large signals. The small but non zero probability for small Q is because there is a change that a pixel with low TOT value is adjacent to a pixel with high TOT value without being a false hit.*

The probability of inducing a false hit with a 4 μm SiRN layer appears to be significantly lower than for an 8 μm SiRN layer. The distance between the charge and an adjacent pixel is approximately constant for different layer thickness while, for a given charge, the potential on top of the layer reduces with reducing thickness. As a result less charge will be induced on an adjacent pixel for a thinner SiRN layer. The smaller angle with respect to the plane of the adjacent pixel pad further reduces charge induction. For half the SiRN layer thickness the charge induced on an adjacent pixel will be less than half.

With respect to false hits, the 4 μm SiRN layer is preferred above the 8 μm SiRN layer.

6.2 Basic detector performance at DESY

At DESY four Gridpix detectors with a drift gap of 11.5 mm were tested with 2 GeV/c electrons. The difference between the detectors is the thickness of the SiRN spark protection layer on the Timepix chips, 2, 4, 6, and 8 µm.

6.2.1 Gridpix trigger set up

In order to reconstruct drift distance the drift time has to be measured which requires a t_0, which is the moment when a particle passed through the detector. The time after t_0 at which the electrons are detected is the drift time. When a pixel is hit, a counter starts to count clock cycles until the acquisition is stopped. In this case pixels do not count TOT but time of arrival. The time that is measured is the time between a hit and the stop of data acquisition. This demands that the stop time (T_{stop}) of the data acquisition should be well defined with respect to t_0. The drift time (T_{drift}) is:

$$T_{drift} = T_{clk} \left(N_{max} - N \right). \tag{6.3}$$

The drift distance (L_{drift}) is:

$$L_{drift} = v_d T_{clk} \left(N_{max} - N \right). \tag{6.4}$$

T_{clk} is the length of one time bin, v_d is the drift velocity, N_{max} is the maximum number of counts according to T_{stop}/T_{clk} and N is the number of counts when the pixel is read out.

A trigger is generated using two scintillators[3], this defines t_0. The projected area of the two scintillators defines the volume particles have to traverse in order to be detected. Figure 6.17 shows a sketch of the detector position in the test beam at DESY. Figure 6.18 shows a sketch of the trigger circuit.

[3] Scintillators are materials that produce light when a charged particle goes through. The amount of light is small and has to be detected by a photo multiplier tube (often referred to as PMT) which is capable of detecting single photons. PMTs give an electric signal ≈10 ns after light hits the photo-cathode.

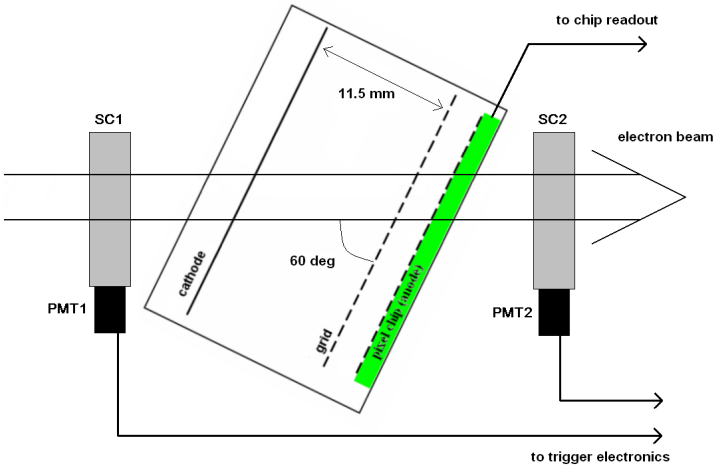

Figure 6.17: *Sketch of the geometry of the set up in the DESY beam line. SC1 and SC2 are the scintillators and PMT1 and PMT2 are the photomultiplier tubes.*

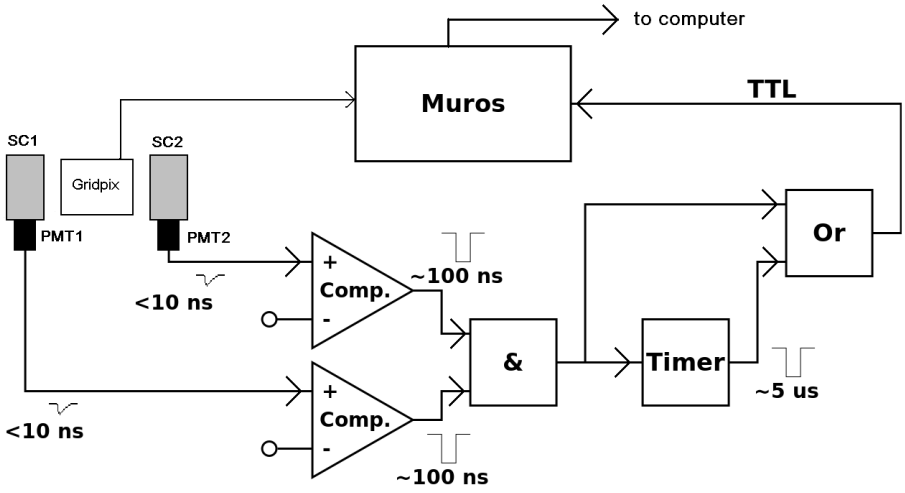

Figure 6.18: *Sketch of the trigger circuit. The photo multiplier tubes (PMT1 and PMT2) each give a signal after a particle passes through the scintillators SC1 and SC2. To trigger on a particle and not on noise the signal must have an amplitude larger than a set threshold. If a signal is large enough the comparator (Comp.) gives a digital pulse. In case both comparators simultaneously give a pulse the AND gate gives a pulse to the OR gate and a timer. The OR gate immediately feeds the pulse to the MUROS, wich starts the acquisition. By the time the pulse from the AND gate ends the Timer has started to apply signal to the OR gate. The MUROS is the electronics used to read out the Timepix chip and to transfer the data to a computer.*

The four detectors were placed such that the plane of the chip had an angle of approximately 60° with respect to the beam. In this orientation the beam entered the drift region through the cathode foil and left through the Timepix chip (figure 6.17). The whole length of the track is projected on the chip (figure 6.19). The drift gap is 11.5 mm and with an angle of 60° the total track length through the drift volume is 13 mm.

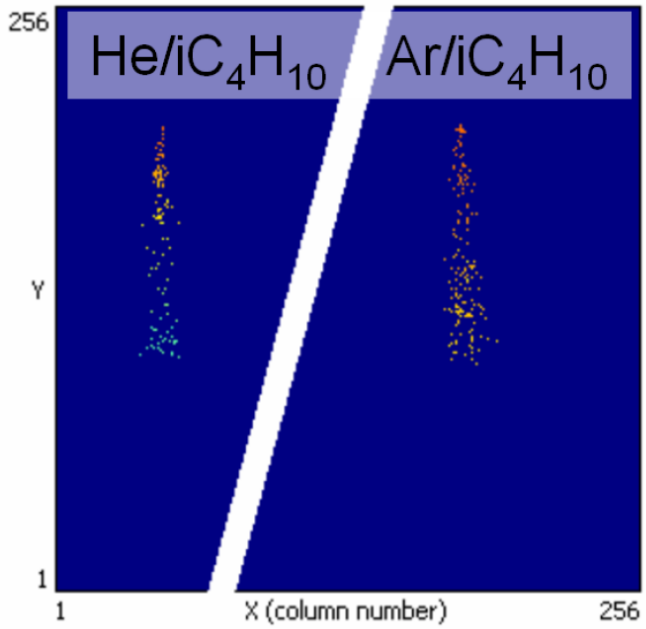

Figure 6.19: *Two tracks recorded with a Gridpix detector. The left track has been recorded in a He/iC_4H_{10} (80/20) mixture with -440V on the grid. The right track has been recorded in a Ar/iC_4H_{10} (80/20) mixture with -460V on the grid. The colour indicates the time a pixel recorded a hit, red represents short drift times and blue long drift times. It can be observed that diffusion increases with increasing distance from the chip. Also the time range in the helium mixture is larger than in the argon mixture, which shows that in the latter case the drift velocity is higher. In the argon mixture the ionization density is higher than in helium mixture.*

For an optimal data acquisition the Timepix chip should be enabled while waiting for a particle and be stopped a defined time after a trigger. Due to practical reasons that was not possible for the measurements discussed in this thesis. Instead, an acquisition of a well defined time was started by a trigger, introducing a dead time of the delay between trigger and the start of an acquisition.

6.2.2 Single electron detection efficiency in He/iC$_4$H$_{10}$

The single electron detection efficiency has been determined for the detectors with a 2, 4, 6, and 8 μm thick layer of SiRN in a He/iC$_4$H$_{10}$ 80/20 mixture to observe how this may be affected by the thickness of the SiRN layer. The detection efficiency is determined by counting the average number of pixels being hit in a recorded track for different voltages on the grid (figures 6.20 and 6.21). For each grid voltage a few thousand tracks have been recorded. Only tracks in the centre of the chip are selected to ensure that the full length of a track is recorded and to minimise distortions in drift field near the edge of the chip. Tracks with distinguishable delta rays are rejected by rejecting all tracks with more than 10 times the most likely number of electrons.

Taking the average number of hit pixels for different grid voltages for the four different detectors result in the curves in figure 6.21.

Figure 6.21 shows that for all four Gridpix detectors a plateau is reached. In case a chip would be less sensitive due to a thicker SiRN layer it is expected that the curve shifts to the right. If because of charge spread more pixels are being hit due to false hits, a higher maximum amount of hits is expected. This appears to be the case for the chip with 8 μm SiRN for a grid voltage of -450V. In this test no correlations in sensitivity have been observed with SiRN layer thickness, i.e. all curves appear to be at approximately 90% of their maximum at a grid voltage of -400 V. The differences in the plateaus may be caused by differences in drift gap width, variations in angle and poor areas on the grids (some grids showed visible wrinkles). The maximum number of hit pixels is approximately 60. With a track length of 13 mm this means that there are at least on average 46 electrons per cm along the tracks.

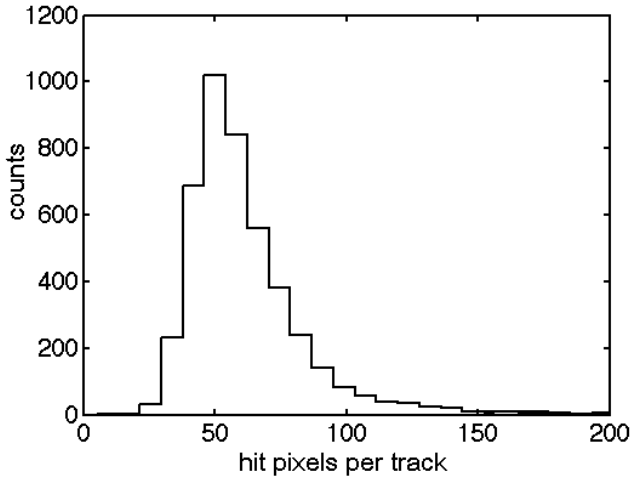

Figure 6.20: *Number of hit pixels per track in He/iC$_4$H$_{10}$. Grid voltage was set at -440 V. The average of this distribution defines the number of hits per track.*

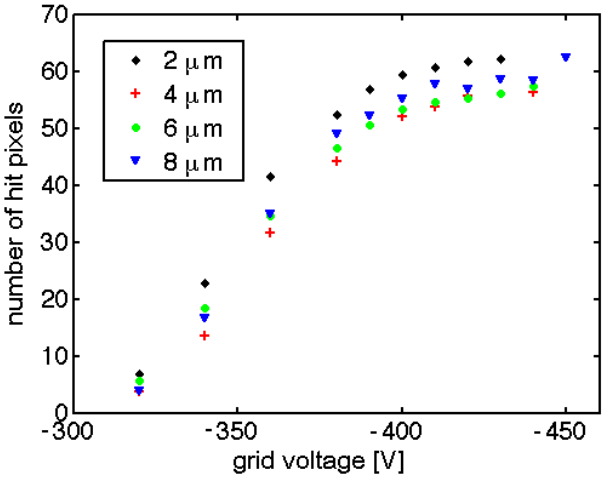

Figure 6.21: *Average number of hit pixels per track in He/iC_4H_{10} for different grid voltages.*

6.2.3 Single electron detection efficiency in Ar/iC_4H_{10}

The number of hit pixels as a function of the grid voltage also has been measured for an Ar/iC_4H_{10} 80/20 gas mixture (figure 6.22). The detector with 4 µm SiRN was used. The two curves are from measurements done 11 days apart.

The maximum number of hits (eye fit) is approximately 145, with a track length of approximately 13 mm the ionisation density is at least 111 electrons per cm.

The absolute gas gain has been calibrated using ^{55}Fe and by reading out the signals induced on the grid. The estimated accuracy of the gain measurements is 20% due to poor statistics and poor readout equipment. The signals induced on the grid have been measured with an oscilloscope in a noisy environment and were read out by eye, in total 100 signals have been measured. In figure 6.23 the counted hits are plotted as a function of the gain. For a gain of more than 5000 the single electron efficiency is 90% or better.

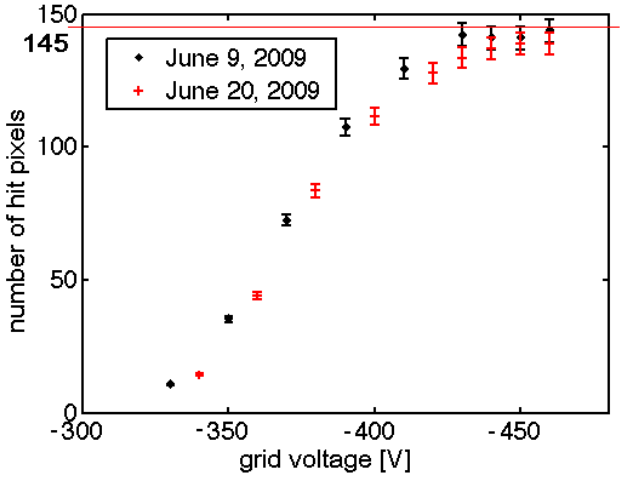

Figure 6.22: *Average number of hit pixels per track in Ar/iC_4H_{10} for different grid voltages. By eye fit the number of hit pixels asymptotically approaches 145. The detector with a 4 μm protection layer was used. Discharges have been measured for voltages exceeding -430 V. These do not affect detector performance. The slightly lower gas gain on June 20th may be due to a difference in atmospheric pressure. The gas gain decreases with increasing pressure. The atmospheric pressure on June 9th was 1007 hPa and on June 20th it was 1017 hPa.*

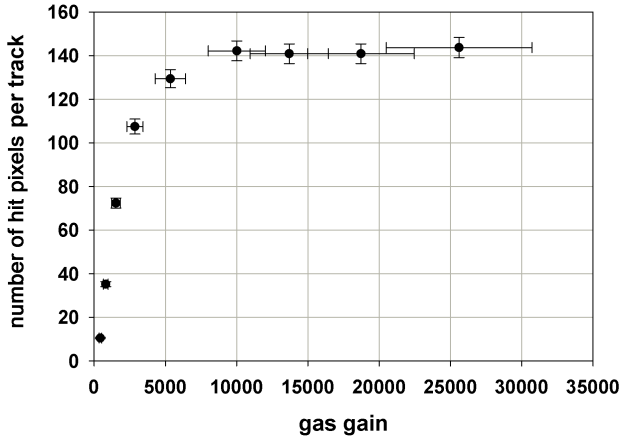

Figure 6.23: *Average number of hit pixels in Ar/iC_4H_{10} (80/20) as a function of the gas gain.*

6.2.4 Robustness of the detectors

To test the robustness of the SiRN layer the detector with 4 µm SiRN was operated for approximately 24 hours with a grid voltage of -460 V in an Ar/iC$_4$H$_{10}$ gas mixture such that it sparks about once or twice per second. After 24 hours no effects of deterioration were measured. However, when continuing to do measurements in other gas mixtures the detectors with 6 µm, 2 µm and the one with 4 µm SiRN broke down [67]. No correlation with SiRN layer thickness is noticed. Probably defects in the SiRN layer are responsible for the breakdown of the detectors, which is a problem that still has to be solved (section 5.7).

6.2.5 Drift time spectrum He/iC$_4$H$_{10}$

To measure the drift time spectrum in a He/iC$_4$H$_{10}$ gas mixture (80/20) the drift field is set to 450 V/cm and a scan is made with the grid voltage. Changes in the drift time spectrum have to be caused by the change in gas gain. The delay between a trigger and the start of a measurement is 60 ns. Averaged over many tracks the drift time distribution should be uniform across the full drift length since on average the ionisation across the drift gap is uniform. The drift time information as it comes from the chip is shown by figure 6.24 in the left graph. The grid voltage was -320 V and the gas gain was approximately 500. The time is in units of clock counts, one clock count is 10 ns.

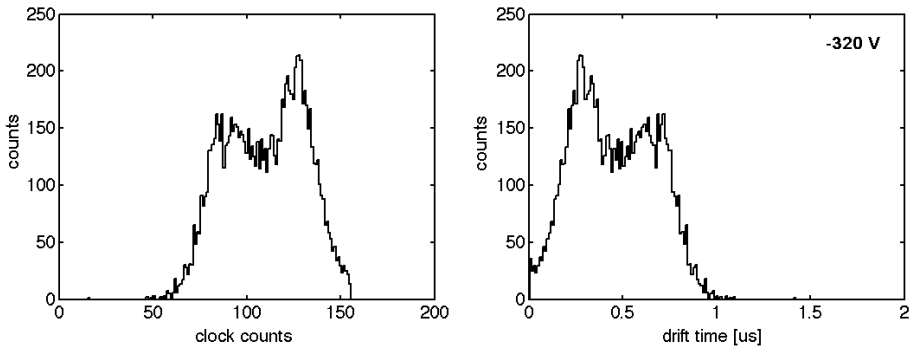

Figure 6.24: *Left: Clock count spectrum as it comes from a chip for a grid voltage of -320V (the gas gain is approximately 500). Since the time between hit and stop of acquisition is measured the spectrum is inverted. The first hit pixels that represent the shortest drift times have the highest number of counts. Right: Drift time spectrum (in µs) obtained by using equation* (6.3) *to calculate the drift time based on the number of clock counts.*

As mentioned in section 6.2.1 the time between hit and end of acquisition is measured. The highest counts come from the primary electrons closest to the chip. The drift time can be calculated by using equation (6.3) which results in the distribution shown by the right graph in figure 6.24. The drift time spectrum in figure 6.24 is not uniform as it should be. Due to time walk only very few electrons are detected

early. The large peak at approximately 0.25 µs is due to primary electrons close to the chip that because of little diffusion often arrive with more than one electron per pixel. For low gas gains multiple electrons per pixel have a significantly higher probability of being detected. Figure 6.25 shows the drift time spectra for a grid voltage of -400 and -440 V. The gas gain was approximately 5×10^3 and 1.6×10^4 respectively. It appears that there is a lack of charge from close to the chip. This effect is caused by multiple primary electrons arriving at the same pixel in which case they will be counted as only one primary electron. Due to a decreasing diffusion with decreasing distance to the chip it is more likely to have multiple electrons per pixel close to the chip. The peak at zero drift time for -440 V on the grid is due to the 60 ns delay: Some pixels are already hit when the measurement starts and those pixels start to count immediately.

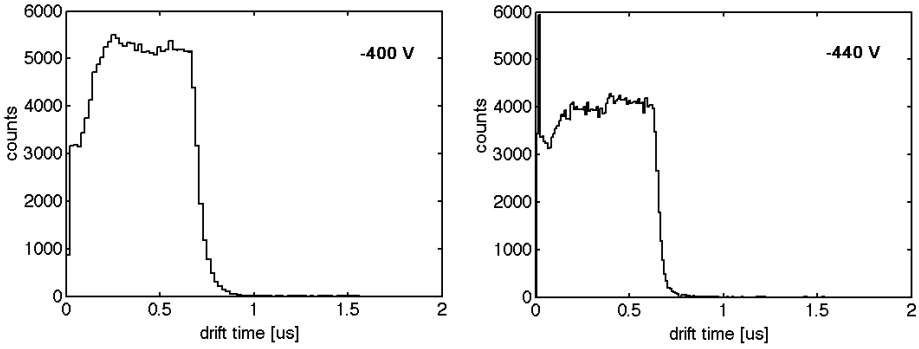

Figure 6.25: *Drift time spectra for a grid voltage of -400 and -440 V. The peak at zero time in the right picture is due to the 60 ns delay between the particle passing through and the start of data acquisition. Some pixel amplifiers already give a signal above threshold as soon as the measurement starts and then the counter start to count immediately. It appears that for short drift times less charge is detected. Primary charge with short drift distance more often arrives with multiple electrons per pixel which are counted as one. As a result fewer hits with short drift times are detected.*

According to simulation with MAGBOLTZ the drift velocity should be 1.9 cm/µs for a drift field of 450 V/cm. The width of the drift time distribution for a grid voltage of -440 V is approximately 0.65 µs. The physical height of the drift gap is 11.5 mm, resulting in a reconstructed drift velocity of 1.77 cm/µs. The slightly lower drift velocity may be due to time walk that widens the drift time distribution. Time walk effects are best illustrated by the drift time spectrum shown by figure 6.24 (right graph) that has widened to approximately 0.8 µs instead of the 0.65 µs for higher gas gains. The average recorded drift time as a function of the gas gain is shown by figure 6.26.

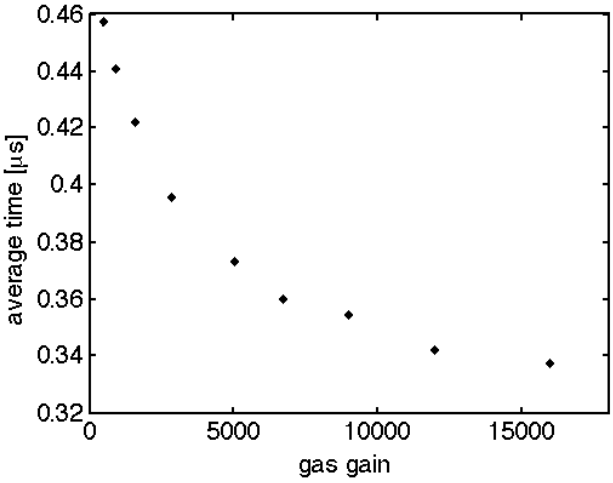

Figure 6.26: *Average recorded drift time as a function of the gas gain. With increasing gas gain the average time recorded decreases due to a decrease in time walk.*

6.2.6 Drift time spectrum Ar/iC$_4$H$_{10}$

In Ar/iC$_4$H$_{10}$ (80/20) the drift field is set to 900 V/cm and, according to GARFIELD, the drift velocity is 5 cm/μs. Figure 6.27 shows the drift time spectra for a grid voltage of -340 and -440 V. The width of the distribution is 0.24 μs for a grid voltage of -460 V which corresponds to a drift velocity of 4.8 cm/μs.

For both the argon and helium based mixture the average drift time decreases with approximately 120 ns with increasing gas gain. Based on figure 6.28 a gas gain of more than 1.5×10^4 is needed to reduce the average time walk to less than one or two time bins.

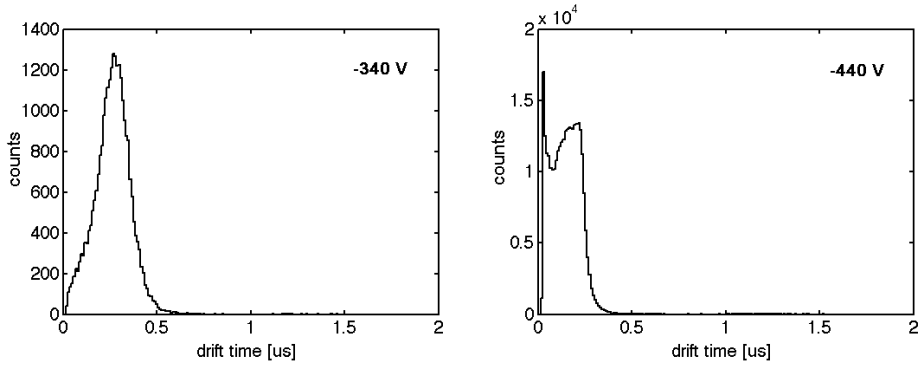

Figure 6.27: *Drift time spectra for a grid voltage of -340 and -440 V.*

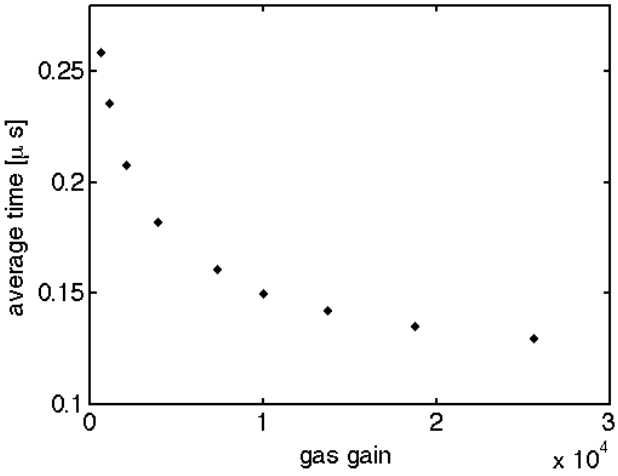

Figure 6.28: *Average recorded drift time as a function of the gas gain.*

6.3 Track reconstruction

To estimate the accuracy of track reconstruction an event is split into two parts by dividing the chip into a chess board pattern with 'A' pixels and 'B' pixels. Each selection (fraction A and fraction B) has approximately half the number of hits and is used to determine a regression line, resulting in two regression lines for each recorded track. The differences between the two regression lines is a measure for the accuracy of the track reconstruction. Tracks in the middle region of the chip have been selected to be sure that the full length of the track is projected onto the chip.

6.3.1 Determining a regression line

A regression line is determined by means of minimisation of the sum of squared errors. The points of the track are projected onto a plane called H (figure 6.29) [79]. The centre of gravity (x_{cog},y_{cog},z_{cog}) of the projections in plane H is determined, then the sum of the squared errors of the projections to this point is calculated. The time information of the points is used to assign a weight to each point, inversely proportional to the drift time. By assigning weight to the points the more diffused electrons far from the chip have less influence on the regression line than the electrons close to the chip that have less diffusion and thus better spatial information. The inclinations of plane H in the XZ and YZ planes are adjusted until the sum of squared errors is minimised. The line perpendicular to this plane going through the point (x_{cog},y_{cog},z_{cog}) is the regression line, shown in figure 6.29. This method requires that the track is a straight line.

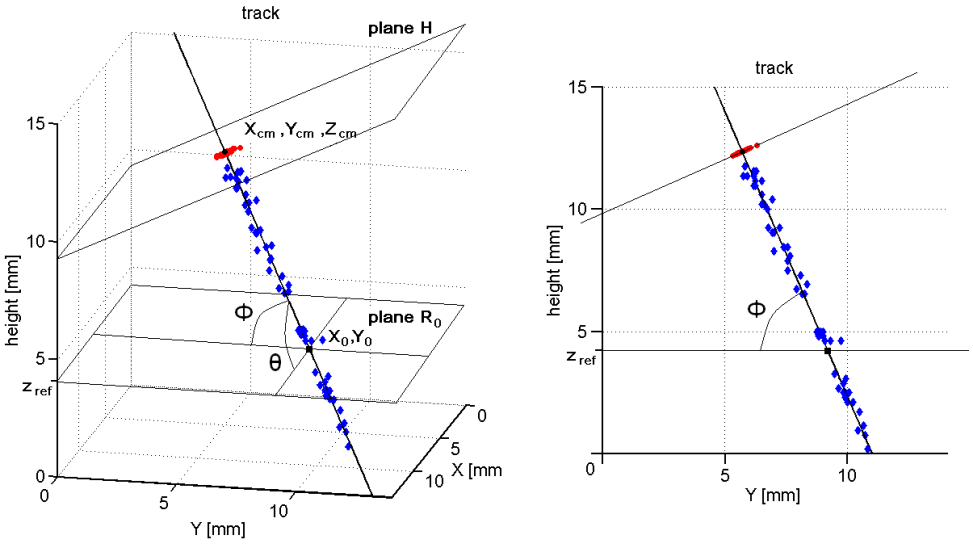

Figure 6.29: *A reconstructed ionisation trail (blue diamond dots) in a He/iC_4H_{10} (80/20) mixture and the found regression line (black line). The red round dots are the projections of the hits onto the plane H. The angle θ is the angle of the regression line with respect to the X axis, ϕ is the angle with respect to the Y axis. The right picture is the projection on the YZ plane. The plane R_0 is the plane in which the spatial resolution is determined.*

A plane is defined by:

$$aX + bY + cZ + d = 0. \tag{6.5}$$

The vector (a,b,c) is perpendicular to this plane and a line L in parallel with this vector is described by the following set of equations:

$$\begin{aligned} X &= u + at \\ Y &= v + bt \\ Z &= w + ct \end{aligned} \tag{6.6}$$

Each point P_i in the track with coordinate (x_i,y_i,z_i) has a projection P_{Hi} (x_{Hi},y_{Hi},z_{Hi}) onto the plane H which has to be determined by finding a line L such that it goes through (x_i,y_i,z_i):

$$\begin{aligned} X &= x_i + at \\ Y &= y_i + bt \\ Z &= z_i + ct \end{aligned} \tag{6.7}$$

The line will intersect the plane H for t=t_H and t_H can be determined by solving:

$$a\,(x_i + at_H) + b\,(y_i + bt_H) + c\,(z_i + ct_H) + d = 0 \Rightarrow \tag{6.8}$$

$$t_H = -\frac{ax_i + by_i + cz_i + d}{a^2 + b^2 + c^2}. \tag{6.9}$$

With t_H solved, the coordinates (x_{Hi},y_{Hi},z_{Hi}) can be calculated according to:

$$\begin{aligned} x_{Hi} &= xi + at_H \\ y_{Hi} &= yi + bt_H \\ z_{Hi} &= zi + ct_H \end{aligned} \tag{6.10}$$

After calculating the projected points for all the points in the track the centre of gravity P_{cog} (x_{cog},y_{cog},z_{cog}) can be calculated by:

$$x, y, z_{cog} = \frac{1}{N_w} \cdot \sum_{i=1}^{N} (W_i \cdot x, y, z_{Hi}) \,. \tag{6.11}$$

In which N_w is the sum of all weights of all points and W_i is the weight of the point P_i. After this the sum of the errors squared is calculated according to:

$$E^2 = \sum_{i=1}^{N} W_i \left((x_{Hi} - x_{cog})^2 + (y_{Hi} - y_{cog})^2 + (z_{Hi} - z_{cog})^2 \right). \tag{6.12}$$

Since the projections of the points on the plane are used it is not important where this plane lies, only the angles with the XY plane are relevant. For that reason c can be set to any non zero convenient value and d can be set to any value. Parameters a and b are the only parameters to be optimised.

The procedure is started with both a and b set to zero, defining a plane parallel to the XY plane intersecting the Z axis at $-d/c$. Then this plane is rotated around an axis parallel to the y axis by optimising a. In that case the minimum of errors squared is when the projection of the track is parallel to the y axis. Then the plane has to be rotated perpendicular to the last rotation axis, which is done by rotating around the intersection line in the XZ plane by optimising b. In this manner only two orthogonal parameters have to be optimised. The projection of the track on the H plane after each step is shown by figure 6.30. To make a more clear example the track in figure 6.30 is inclined in both the X and Y direction, it is taken from a different data set (cosmic ray).

After finding P_{cog} the regression line is according to:

$$\begin{aligned} X &= x_{cog} + at \\ Y &= y_{cog} + bt \\ Z &= z_{cog} + ct \end{aligned} \tag{6.13}$$

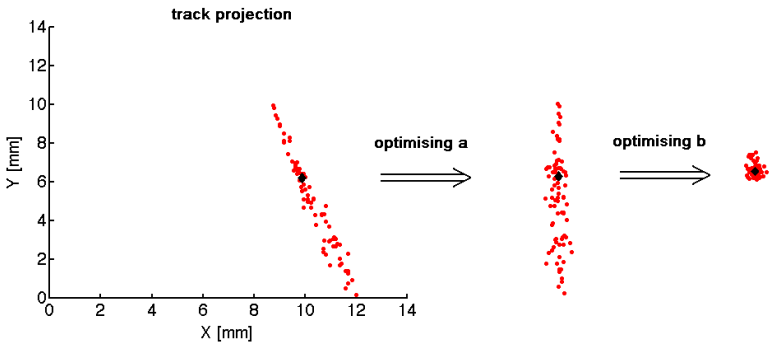

Figure 6.30: *The projection of a track on the H plane. The black diamond dot is the centre of gravity. The left figure shows the projection on the H plane as it initially is parallel to the XY plane. After optimising a (rotation around an axis parallel to the Y axis) the projection is as shown by the middle figure. The right figure shows the projection after optimising b.*

To remove hits that suffered much from time walk all hits further than 1 mm from this regression line are removed and the procedure is repeated again with the cleaned up track. Figure 6.31 shows a track before and after removing the late hits.

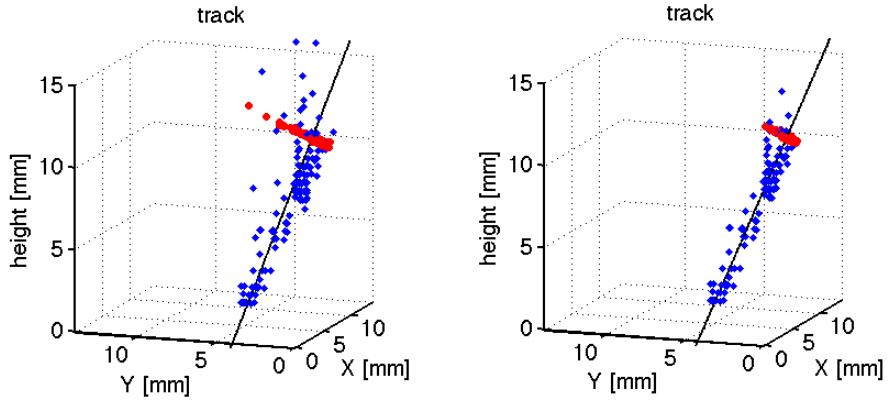

Figure 6.31: *A reconstructed ionisation trail (blue diamond dots) and its projection onto the H plane (red dots) in an Ar/iC_4H_{10} (80/20) mixture and the regression line (black line). In the left picture all points in the track have been used to determine a regression line. Hits further than 1 mm from this line have been removed and the regression line is determined again (right picture). In this way the poorest hits that reduce accuracy are removed.*

The procedure to find a regression line is applied on each of the two track fractions obtained from one single track. Fraction F_a is obtained by selecting all 'A' pixels and fraction F_b is obtained by selecting all 'B' pixels. The best position resolution can be found in a reference plane R_0 parallel with the chip that intersects the centre

of gravity of a track in the Z direction. Determining this reference plane for each individual track makes a consistent interpretation of the resolution difficult. For that reason the height (z_{ref}) of R_0 is chosen at Z=4 mm which is close to the average height of the centre of gravity of the tracks.

After finding the two regression lines the track parameters $(P_{0a})=(x_{0a}, y_{0a})$ and $(P_{0b})=(x_{0b}, y_{0b})$ where they intersect R_0 and the angles ϕ_a, ϕ_b and θ_a, θ_b have to be calculated. For each track fraction, in order to find P_0 the value t_0 has to be calculated for which $Z=z_{ref}=4$ by solving:

$$Z = z_{cog} + ct_0 = z_{ref} \rightarrow t_0 = \frac{z_{ref} - z_{cog}}{c}. \tag{6.14}$$

Using t_0 the point (x_0, y_0) for each track fraction can be calculated using equation (6.15):

$$\begin{aligned} X &= x_{cog} + at_0 = x_0 \\ Y &= y_{cog} + bt_0 = y_0 \\ Z &= z_{cog} + ct_0 = z_{ref} \end{aligned} \tag{6.15}$$

The angles ϕ and θ of each track fraction can be found according to:

$$\begin{aligned} \phi &= \arctan\left(\frac{c}{b}\right) \\ \theta &= \arctan\left(\frac{c}{a}\right) \end{aligned} \tag{6.16}$$

The differences (residuals) of the track parameters are x_{0err}, y_{0err}, θ_{err} and ϕ_{err} and are obtained according to:

$$\begin{aligned} x_{0err} &= x_{0a} - x_{0b} \\ y_{0err} &= y_{0a} - y_{0b} \\ \phi_{err} &= \phi_a - \phi_b \\ \theta_{err} &= \theta_a - \theta_b \end{aligned} \tag{6.17}$$

Assume the resolution for an angle or position of the detector to be σ_{det}. A random selection of half the number of points of a track will result in a worse accuracy of $\sqrt{2}\sigma_{det}$. The accuracies (σ_a and σ_b) of the two track fractions F_a and F_b are assumed to be equal. The accuracy of a track fraction will be:

$$\sigma_a = \sigma_b = \sqrt{2}\sigma_{det}. \tag{6.18}$$

The accuracy of both track fractions is not correlated and the width of the distribution of the residuals (σ_{err}) will be according to:

$$\sigma_{err}^2 = \sigma_a^2 + \sigma_b^2 \rightarrow \sigma_{err} = \sqrt{2}\sigma_a. \tag{6.19}$$

To find the resolution of the detector (σ_{det}) based on a distribution of the residuals equation (6.18) can be used to substitute σ_a in equation (6.19), resulting in:

$$\sigma_{err} = \sqrt{2}\sigma_a = 2\sigma_{det} \rightarrow \sigma_{det} = \frac{\sigma_{err}}{2}. \tag{6.20}$$

A practical problem that occurs in all tracks in the data set obtained at DESY is that the hits in the first drift time bin have to be rejected. Due to the 60 ns late trigger some pixels are already hit and do not contain any drift time information. This significantly worsens the position accuracy (x_0 and y_0). The position accuracy that can be expected with N points with each an uncertainty of σ_i is according to:

$$\frac{1}{\sigma^2} = \sum_{i=1}^{N} \frac{1}{\sigma_i^2} \rightarrow \sigma = \sqrt{\left(\sum_{i=1}^{N} \frac{1}{\sigma_i^2}\right)^{-1}}. \tag{6.21}$$

In equation (6.21) σ_i is the error of each detected primary electron which is composed of the error due to the pixel size (σ_{pixel}) and the error due to diffusion (σ_{diff}) which depends on drift distance. For each hit pixel σ_i^2 is according to:

$$\sigma_i^2 = \sigma_{pixel}^2 + \sigma_{diff}^2. \tag{6.22}$$

With pixels of 55×55 μm^2 the error of the pixels is 16 μm causing the diffusion to be the dominant error for drift distances more than a few tenths of a mm. One can also observe in equation (6.21) that the primary electrons with little diffusion (with a small σ_i) are very important for the position resolution.

Figure 6.32 shows a typical track in an Ar/iC$_4$H$_{10}$ (80/20) mixture and what hits are rejected. The hits in the second time bin already suffer from a lot of diffusion compared to the the hits in the first time bin.

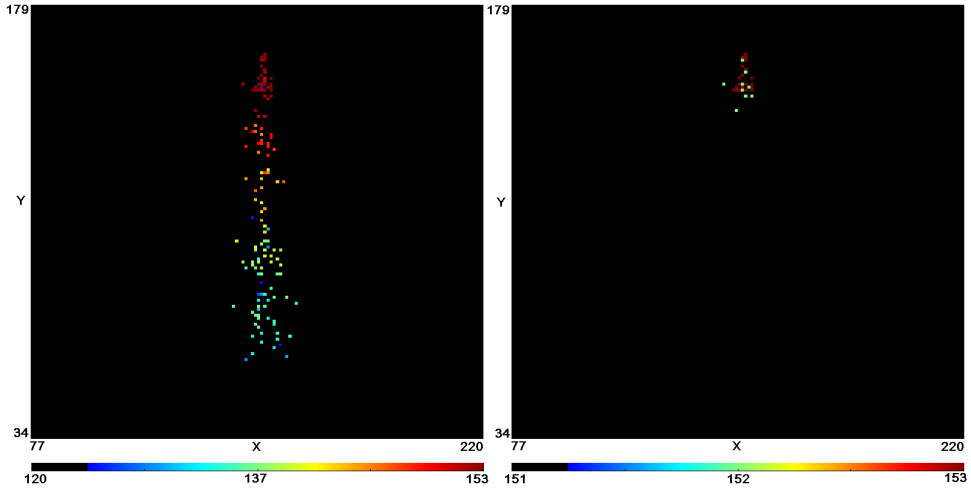

Figure 6.32: *Recorded track in an Ar/iC_4H_{10} (80/20) mixture, the drift field was 900 V/cm and the grid voltage was -460 V. The colour represents drift time. The right picture shows the hits in the first (red dots) and second (light dots) time bin. The hits in the first time bin with the best position information are discarded due to the lack of timing information.*

6.3.2 Angular accuracy

Figures 6.33 and 6.34 show the distributions of θ_{err} and ϕ_{err} for the Ar/iC_4H_{10} 80/20 and He/iC_4H_{10} 80/20 mixtures.

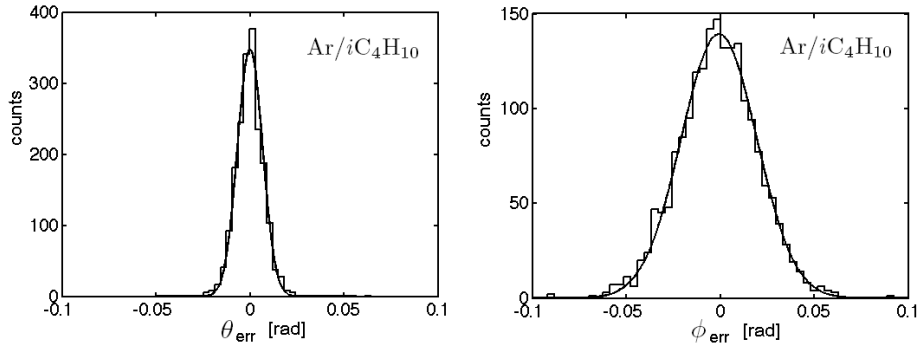

Figure 6.33: *Left: Distribution of θ_{err}. The fitted Gauss curve has a σ of 6.4 mrad. Right: Distribution of ϕ_{err} for which σ is 21 mrad. The gas mixture was Ar/iC_4H_{10} (80/20), the drift field was 900 V/cm and the grid voltage was -460 V, the number of tracks was 1912.*

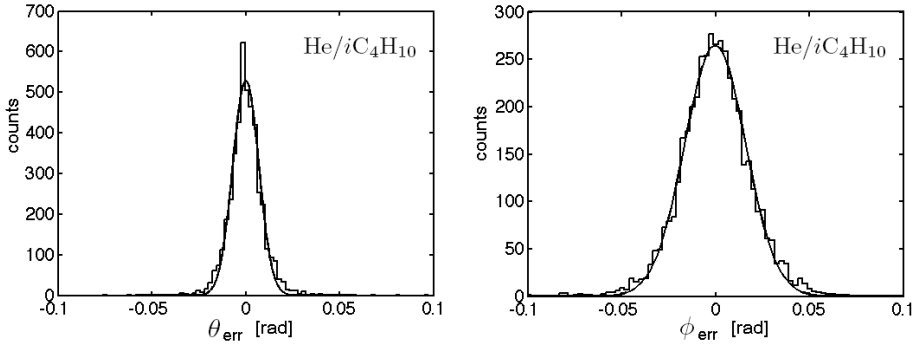

Figure 6.34: *Left: Distribution of θ_{err}. The fitted Gauss curve has a σ of 6.7 mrad. Right: Distribution of ϕ_{err} for which σ is 16 mrad. The gas mixture was He/iC_4H_{10} (80/20), the drift field was 450 V/cm and the grid voltage was -440 V, the number of tracks was 4452.*

For the He/iC$_4$H$_{10}$ 80/20 mixture σ for θ_{err} and $\phi_{err}$is 6.7 mrad and 16 mrad respectively. According to equation (6.20) the angular resolution is 3.4 mrad for θ and 8 mrad for ϕ. For the Ar/iC$_4$H$_{10}$ 80/20 mixture σ for θ_{err} and $\phi_{err}$is 6.4 mrad and 21 mrad respectively. According to equation (6.20) the angular resolution is 3.2 mrad for θ and 11 mrad for ϕ.

6.3.3 Position accuracy

Figure 6.35 shows the distribution for x_{0err} and y_{0err} for the Ar/iC$_4$H$_{10}$ (80/20) gas mixture and figure 6.36 for the He/iC$_4$H$_{10}$ (80/20) mixture.

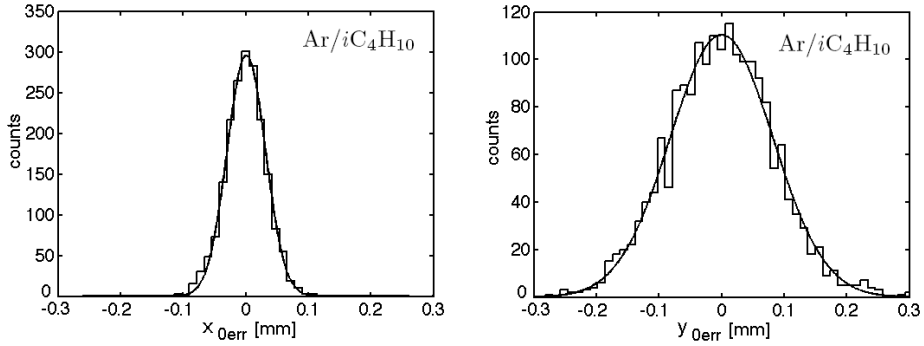

Figure 6.35: *Left: Distribution of x_{0err}. The fitted Gauss curve has a σ of 31 μm. Right: The distribution in the Y direction, the σ is 82 μm. The gas mixture was Ar/iC_4H_{10} (80/20), the drift field was 900 V/cm and the grid voltage was -460 V, the number of tracks was 1912.*

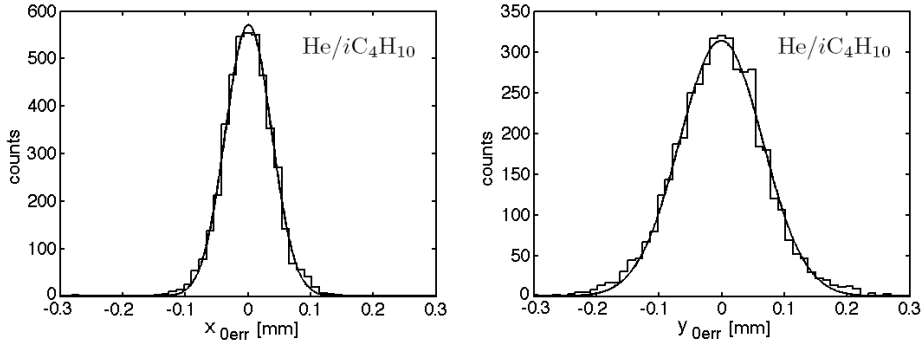

Figure 6.36: *Left: Distribution of x_{0err}. The fitted Gauss curve has a σ of 37 μm. Right: The distribution in the Y direction, the σ is 67 μm. The gas mixture was He/iC$_4$H$_{10}$ (80/20), the drift field was 450 V/cm and the grid voltage was -440 V, the number of tracks was 4452.*

Due to the track inclination in the Y direction the precision in the Y direction is worse, diffusion in the Z direction and time walk add an error in Y. For the He/iC$_4$H$_{10}$ 80/20 mixture σ for x_{0err} and $y_{0err}$is 37 and 67 µm respectively. According to equation (6.20) the spatial resolution is 19 µm for x and 34 µm for y. For the Ar/iC$_4$H$_{10}$ 80/20 mixture σ for x_{0err} and $y_{0err}$is 31 and 82 µm respectively. According to equation (6.20) the spatial resolution is 16 µm for x and 41 µm for y.

6.3.4 Remarks on detector accuracy

Systematic errors have not been taken into account in the reconstructed tracks. To measure systematic errors the detector can best be compared with a reference detector with well known properties.

Due to time walk, a hit can be recorded later but not earlier, resulting in an average net delay according to a non-Gaussian distribution (figure 4.13 in section 4.3.1) causing a track to be too high. The delay between trigger and start of acquisition causes the drift time to be measured too short, causing the track to be too low. Close to the chip the avalanches on average are a bit larger due to more 'multiple electrons per pixel' hits. As a result the average time walk effects are less for primary electrons close to the chip than for electrons far from the chip. The net effect is that the angle between track and the plane of the chip appears to be too large.

Due to the delay between trigger and the start of measurement there may be pixels already hit when the measurement starts. Those hits carry no information in the Z direction. For that reason all hits in the first time bin have been discarded, severely affecting the accuracy for the x_0 and y_0 coordinates since those electrons suffered the least from diffusion. In order to use the hits in the first time bin the trigger should arrive within 30 ns.

6.3.5 Diffusion

Due to time walk effects the only diffusion to be measured is the transversal diffusion (perpendicular to the drift direction). Figure 6.37, left picture, shows the distances between the hits and the regression line projected on the XY plane as a function of the drift length in an Ar/iC_4H_{10} (80/20) mixture. The value of σ of the distribution of distances to the regression line is the diffusion. The diffusion shown by figure 6.37 (right picture) is for a drift length of 9 mm.

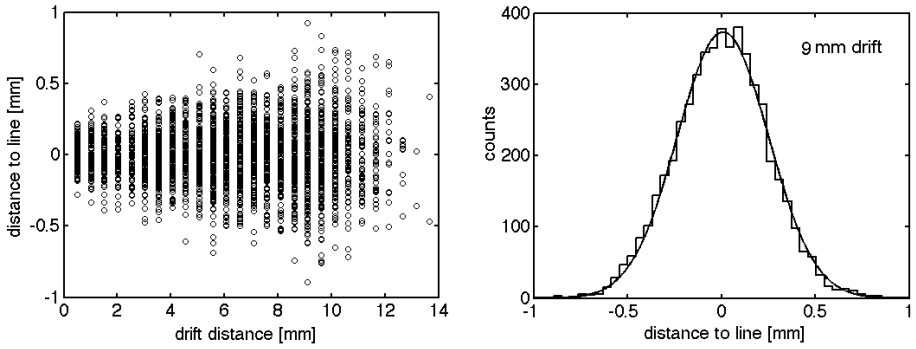

Figure 6.37: *Left: Distance of hits to the regression line as a function of the drift distance for 30 tracks. Right: The distribution for distance to the regression line for a drift distance of 9 mm. The sample consisted of 1000 tracks. The σ is 245 μm. The gas mixture was Ar/iC_4H_{10} (80/20), the drift field was 900 V/cm and the grid voltage was -460 V.*

According to equation (2.12) in section 2.1.4 the diffusion is proportional with the square root of drift distance. In practice it is more convenient to plot the σ^2 as a function of the drift length to obtain a linear dependency. Figure 6.38 shows the measured diffusion as a function of the drift length for an Ar/iC_4H_{10} (80/20) gas mixture and figure 6.39 for a He/iC_4H_{10} (80/20) mixture. For the argon mixture (drift field of 900 V/cm) a diffusion of 230 $\mu m/\sqrt{cm}$ is measured. According to simulation with MAGBOLTZ a diffusion of approximately 250 $\mu m/\sqrt{cm}$ is to be expected. The helium mixture shows a diffusion of 190 $\mu m/\sqrt{cm}$ which should be 215 according to simulation for a drift field of 450 V/cm.

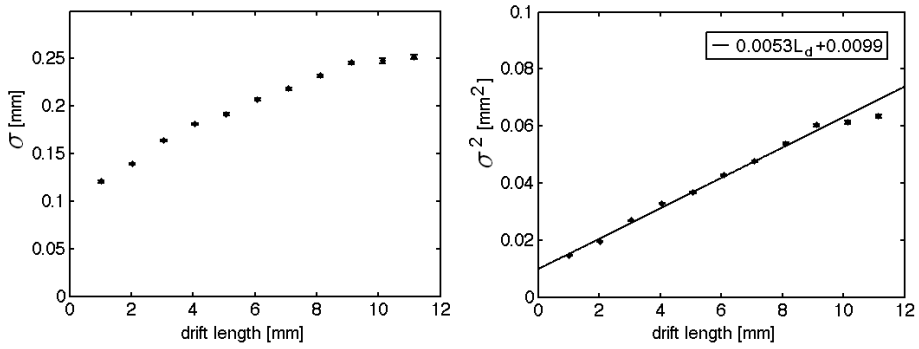

Figure 6.38: *Left: Diffusion (σ) as a function of the drift length. Right: σ^2 as a function of the drift length. The equation of the fitted line is: σ^2=0.0053L_{drift}+0.0099. The gas mixture was Ar/iC_4H_{10} (80/20), the drift field was 900 V/cm and the grid voltage was -460 V.*

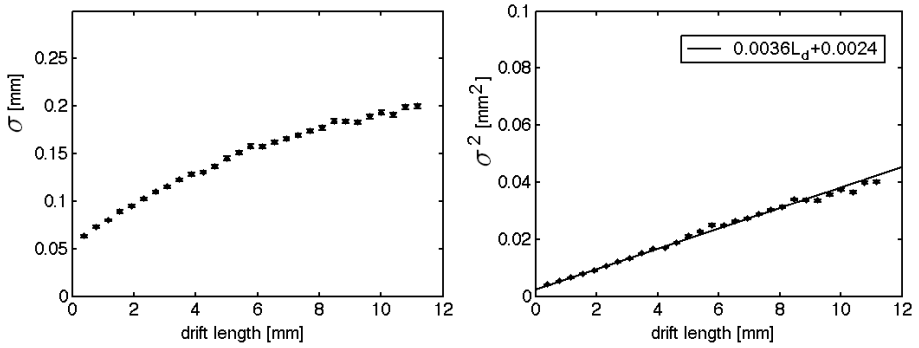

Figure 6.39: *Left: Diffusion (σ) as a function of the drift length. Right: σ^2 as a function of the drift length. The equation of the fitted line is: σ^2=0.0036L_{drift}+0.0024. The gas mixture was He/iC_4H_{10} (80/20), the drift field was 450 V/cm and the grid voltage was -440 V.*

A non-zero diffusion for zero drift length can be noticed, 49 µm for the helium mixture and 99 µm for the argon mixture. The expected 'diffusion' for zero drift ($\sigma_{zerodrift}$) length is composed of the errors due to the finite pixel size, error in position and an error due to the angular uncertainty (σ_{angle}) that is added when extrapolating from the reference plane (where the position is measured) to the chip surface.

$$\sigma_{zerodrift} = \sqrt{\sigma_{pixel}^2 + \sigma_{det}^2 + (z_{ref}\sigma_{angle})^2}. \tag{6.23}$$

For the He/iC_4H_{10} (80/20) mixture σ_{pixel} is 16 µm, σ_{det} is 19 µm and $z_{ref}\sigma_{angle}$ is 14 µm. According to equation (6.23) this results in an expected zero drift diffusion

of 30 μm. Due to the late trigger the found 'zero drift diffusion' is actually the diffusion corresponding to a drift distance that is drifted in a few tens of ns and for that reason the zero drift diffusion will be larger. For the Ar/iC_4H_{10} (80/20) mixture this effect is worse due to the higher drift velocity. Figure 6.32 illustrates that for the argon mixture a significant number of hits are in the first time bin.

6.3.6 Goodness-of-fit

After measuring the diffusion, the goodness-of-fit can be tested by means of the pull. The pull is determined for each point in each track and is found according to:

$$pull_x = \frac{x_i - x_{ri}}{\sigma_i} \tag{6.24}$$

Equation (6.24) is the same for the Y and Z coordinate. The value x_i is the X coordinate of the data point, x_{ri} is where the point 'should be' i.e. its projection on the regression line and σ_i is the expected error in the position of the corresponding x_i, which should be dominated by diffusion and is a function of drift length. The distribution of all the values for the pull should be Gaussian with a mean of zero and a σ of one. A non zero mean or asymmetric shape implies that a systematic error has been made. A σ of more than one is an indication that the estimated error (σ_i) is too low. A too low estimated error may be due to another error contribution in addition to the one accounted for.

Figure 6.40 shows the distribution (for the argon mixture) of the pull for the X coordinate before and after the removal of the by time walk delayed hits. The values for σ_i have been obtained by the measured diffusion (figure 6.38). The sigma is approximately one and the mean is zero which implies that the found diffusion indeed is by far the most dominant error source on the points. Figure 6.41 shows the distribution for the Y coordinate, the sigma before hit selection is 1.26 and after selection it is 1.19. This implies that there is another error in the Y direction in addition to diffusion. This is caused by the inclination of the track in the YZ plane: An error in Z direction is partly added in the Y direction and in the Z direction time walk is an error in addition to diffusion. The mean of the pull in the Y direction is not zero, before hit selection the mean is -0.34 and after hit selection it is -0.14. This can be interpreted as more than half the points lying 'below' the regression line, i.e. have a lower Y value than the its projection on the regression line. This can be explained by the regression line being too high due to the hits that are late due to time walk. Those hits are too far above the regression line and form the tail of the distribution on the right side. After removing those late hits the mean of the pull is closer to zero and the tail on the right side is reduced as is illustrated by figure 6.41 in the right picture.

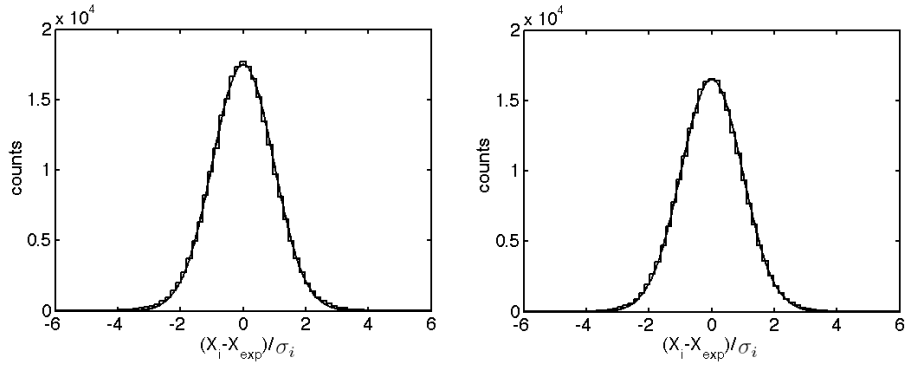

Figure 6.40: *Left: Pull in the X direction before removing late hits, σ is 0.97 and the mean is 0.00. Right: Pull in the X direction after removing the late hits, σ is 0.98 and the mean is 0.00. The gas mixture was Ar/iC_4H_{10} (80/20), the drift field was 900 V/cm and the grid voltage was -460 V.*

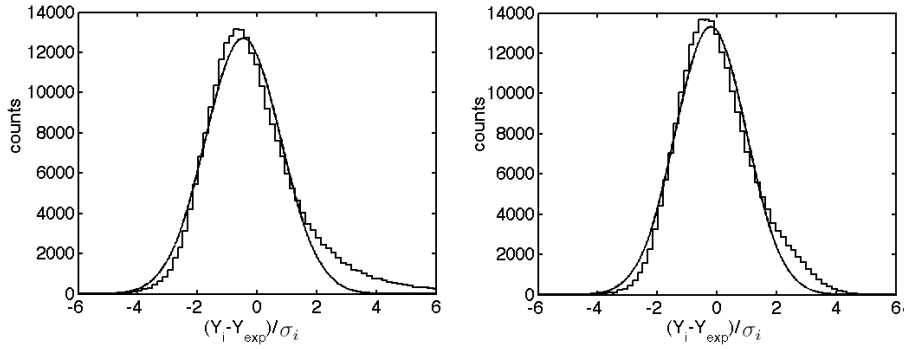

Figure 6.41: *Left: Pull in the Y direction before removing late hits, σ is 1.26 and the mean is -0.47. Right: Pull in the Y direction after removing the late hits, σ is 1.19 and the mean is -0.21. The gas mixture was Ar/iC_4H_{10} (80/20), the drift field was 900 V/cm and the grid voltage was -460 V.*

6.4 Concluding remarks

The present Gridpix detectors with Timepix chips can best be equipped with a 4 μm SiRN protection layer to keep false hits to a minimum for high gas gains. A gas gain of more than 3×10^4 is preferred to minimise time walk effects. In case time information is not required, a gas gain of 5×10^3 is sufficient to detect approximately 90 % of the primary electrons.

Time walk significantly affects detector performance, especially for high drift velocities. In order to reduce time walk effects a gas mixture and drift field should be chosen with an as low as possible drift velocity as can be tolerated.

The precision of a Gridpix detector will be improved if the chip always is enabled and ready to measure and is stopped a defined time after a trigger. In that way also the primary electrons close to the chip, which are the most important for position resolution, can be used for track fitting.

Chapter 7

GOSSIP: a 1 mm drift gap TPC for vertex detection

*G*as *O*n *S*limmed *SI*licon *P*ixels, GOSSIP, is a Gridpix detector under development which has a drift gap of approximately one mm. The aim is to make a low mass radiation hard vertex detector that can be applied in a high particle flux environment, like close to an interaction point of the (s)LHC. With a drift gap of only one mm the charge can be extracted quickly. Present vertex detectors use silicon strips or pixels to determine a point a particle passed through. A GOSSIP detector can measure a track segment (figure 7.4) which facilitates track reconstruction. The silicon used for detection deteriorates with increasing dose. Gas can be flushed and will not suffer from degradation by radiation. Another advantage is that gas has a low density and therefore reduces unwanted interactions of the particles inside the detector, i.e. less scattering and production of other particles (showering). One of the possible applications of GOSSIP is as the replacement of the inner tracker of the ATLAS detector when the present vertex detector needs to be replaced.

GOSSIP detectors were tested in a beam of 150 GeV/c muons at the H4 test beam facility at CERN. The set-up is described in section 7.1. Single electron detection efficiency, track detection efficiency and time walk effects are discussed in section 7.2. In section 7.3, based on simulations and the measurements performed at CERN, the spatial resolution of a GOSSIP detector is estimated. All detectors described in this chapter are equipped with Timepix chips.

7.1 Requirements and test set-up

7.1.1 Requirements

The high rate close to an interaction point of the (s)LHC makes it necessary to quickly extract the charge from a TPC to limit the pile up of events and the build up of space charge (section 2.1.6). Both problems can be reduced by having the

drift gap just thick enough to have a probability of 99% or more to have at least one cluster (an interaction in which at least one electron is released) when a MIP passes through. A good compromise can be achieved by using a CO_2/DME 50/50 mixture, which (according to simulations with MAGBOLTZ) has on average 45 clusters per cm, a low diffusion and a small Lorentz angle. With 45 clusters per cm and a 1 mm drift gap the probability of having at least one cluster from a normal incident MIP is 98.9% (equation (2.2) in section 2.1.1). With a drift field of 6 kV/cm the electrons can be extracted from the drift gap in 20 ns. Applying a drift field of 6 kV/cm over 1 mm only requires 600 V and therefore such a high drift field is not a large challenge in this system. For a drift field of 6 kV/cm the transversal diffusion is approximately 110 $\mu m/\sqrt{cm}$. A lower diffusion is obtained with a drift field of 2 kV/cm which is 70 $\mu m/\sqrt{cm}$. More details of the GOSSIP requirements are discussed in [73]. Diffusion and drift properties of the CO_2/DME 50/50 gas mixture can be found in appendix B.3.

7.1.2 GOSSIP test set-up at CERN

A telescope composed of three GOSSIP detectors and one general purpose Gridpix detector has been constructed (Figure 7.1 and figure 7.2). The GOSSIP detectors each have a drift gap of 0.95 mm and the general purpose Gridpix detector has a drift gap of 19.3 mm. The detectors were placed 155 mm apart. The set up was placed in the H4 test beam at CERN providing 150 GeV/c muons. The test beam first traversed the three GOSSIP detectors and finally the general purpose Gridpix. The set up was placed on an XY stage to move the set up horizontally (X direction) and vertically (Y direction) to align with the particle beam. Services like the high voltages, gas flow and the XY stage were remotely controlled during the experiment. Two scintillators, one in the front and one behind the detectors, defined a 15×15 mm^2 triggering area. The trigger set up is similar to the one used for the test at DESY described in section 6.2.1 but with a faster trigger due to newer electronics developed for this test. The time between a signal from a PMT and the start of data acquisition is less than 20 ns. The use of the trigger electronics is described in appendix C.

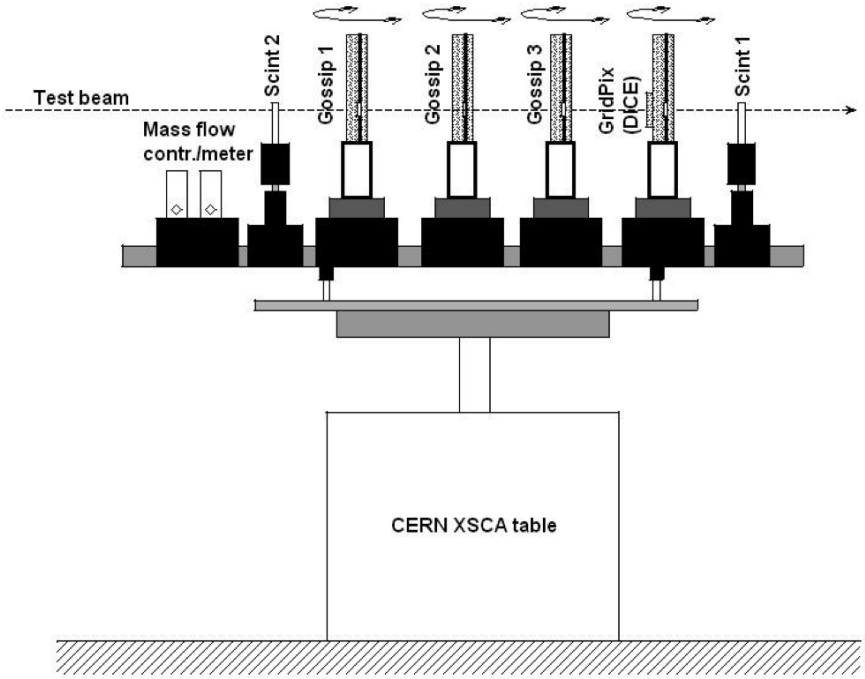

Figure 7.1: *Sketch of the side view of the Gossip telescope mounted on an optical bench.*

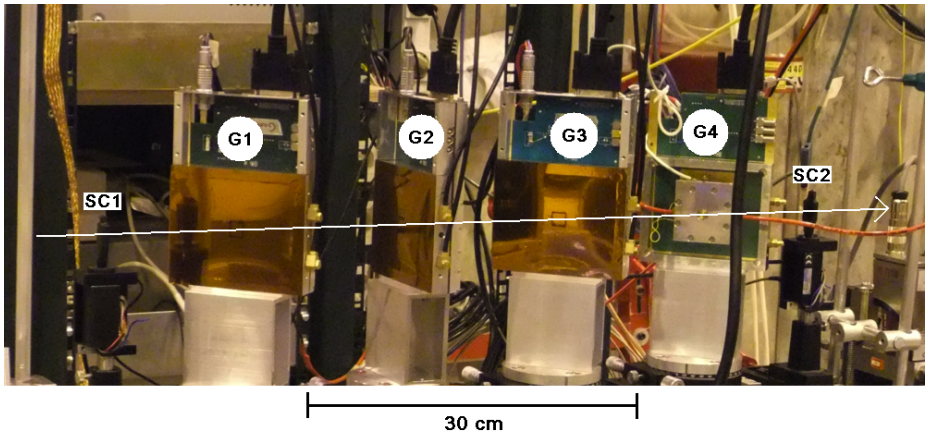

Figure 7.2: *GOSSIP test set-up in the H4 beam line at CERN. The Gridpix detectors G1, G2 and G3 are the 3 GOSSIP detectors, G4 is the general purpose detector. The particles used for this test were 150 GeV/c muons (arrow). SC1 and SC2 are two scintillators that both have to be hit by a muon to generate a trigger.*

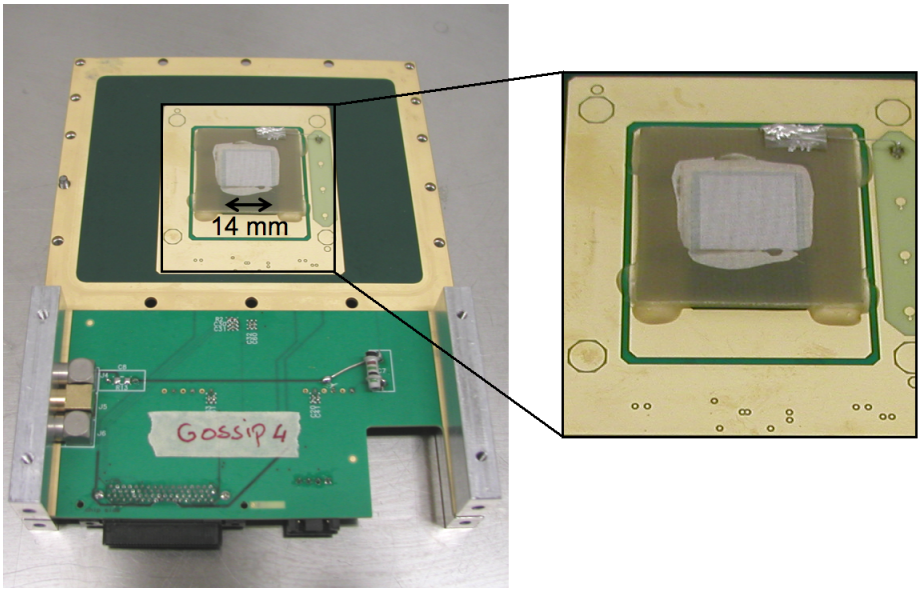

Figure 7.3: *Left: A GOSSIP detector without the gas seal. The cathode is a fine mesh 1 mm above the grid. Right: The Timepix chip with grid can be recognised through the cathode mesh.*

7.2 Detector efficiency

7.2.1 Single electron detection efficiency

To measure the single electron detection efficiency the GOSSIP detectors were placed at an angle of 45 ° to the beam to reduce the number of electrons collected by the same pixel. An example of a track segment recorded by a GOSSIP detector is shown by figure 7.4.

The grid voltage was scanned between -450 and -620 V and for each voltage the number of hit pixels was counted (figure 7.5). According to simulations with MAGBOLTZ for tracks at 45 °, approximately 8 pixels should be hit. For grid voltages of more than -600 V a sudden increase in the number of hit pixels appears due to false hits. For the same grid voltages un-triggered data was taken in TOT mode, containing multiple tracks per stored frame. For grid voltages of more than -600 V the TOT spectrum shows an increase in TOT values below 200 counts, indicating false hits (figure 7.6). Since the single tracks are in time mode it is not possible to remove the false hits based on TOT information. For that reason the average number of hit pixels per track have not been corrected. The differences between the curves from the different GOSSIP detectors are due to large areas suffering from non functional pixels and small differences in drift gap widths between detectors.

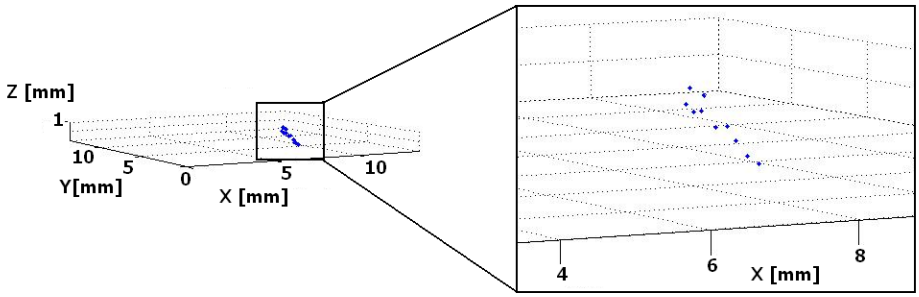

Figure 7.4: *A typical track recorded with a GOSSIP detector placed 45° with respect to the beam. The gas mixture was CO_2/DME 50/50 and the grid voltage was -620 V.*

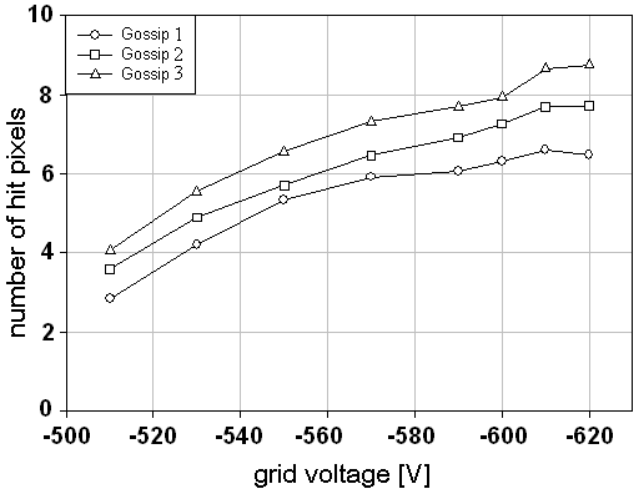

Figure 7.5: *Number of hit pixels as a function of the grid voltage. The sudden increase in the number of hit pixels for grid voltages of more than -600 V is due to false hits. In the TOT spectrum a peak appears for TOT counts below 200 (figure 7.6).*

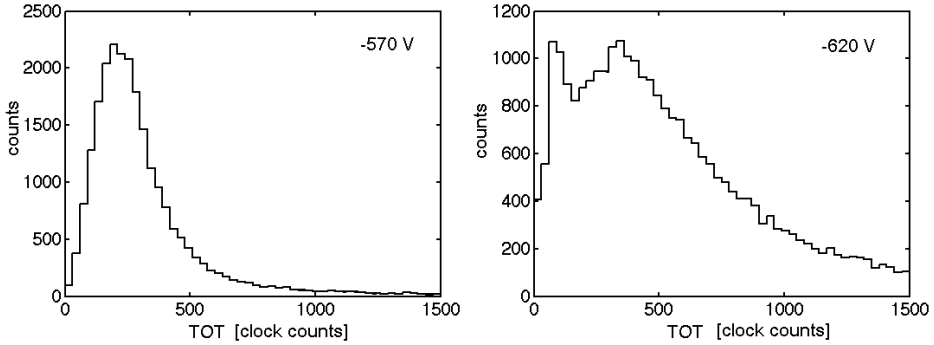

Figure 7.6: *The time over threshold (TOT) spectra (in clock counts) for the GOSSIP detectors in the test beam for a grid voltage of -570 V and -620 V. In the right graph the peak at low TOT values indicates false hits.*

7.2.2 Gas gain

Section 6.1 explained how the gas gain is determined by measuring the charge induced on the grid when an electron cloud released by an ^{55}Fe photon is amplified. For the GOSSIP detectors placed in the test beam this was not possible, there was no ^{55}Fe available for irradiation and the charge on the grid could not be read out.

The gain measurements in section 6.1 were used to find the average TOT as a function of the gas gain, shown by figure 7.7 for the Ar/iC$_4$H$_{10}$ 80/20 and He/iC$_4$H$_{10}$ 80/20 gas mixtures.

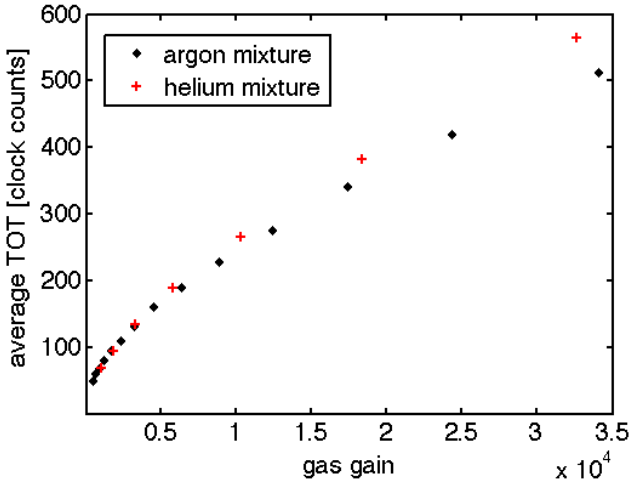

Figure 7.7: *The average TOT count per pixel as a function of the gas gain for Ar/iC_4H_{10} (black diamonds) and He/iC_4H_{10} (red crosses) 80/20 gas mixtures.*

The average TOT can be measured for the GOSSIP detectors when the muon tracks are recorded with the Timepix chips set in TOT mode. In this way, by using the TOT information, the gas gain in a GOSSIP detector can be estimated. The assumption is made that different Timepix chips have equal sensitivity and that, due to an amplifier response time longer than ion drift times in the gain gap, the response to the CO_2/DME 50/50 mixture is the same as to the helium and argon mixture (section 4.1). Due to little diffusion of the primary electrons the pixels often are hit by more than one electron and as a result the average TOT value will be larger than in the case of only single primary electrons hitting the pixels (section 6.1). For that reason the gas gain estimation based on the average TOT may be systematically too high. Figure 7.8 shows the average TOT for the CO_2/DME 50/50 mixture for the different grid voltages.

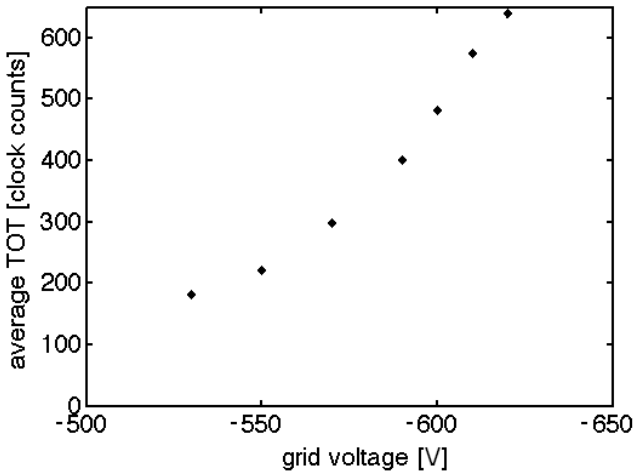

Figure 7.8: *Average TOT (in clock counts) for the CO_2/DME mixture as a function of the grid voltage.*

The data from the argon mixture is used to find the gas gain in the CO_2/DME 50/50 mixture, assuming that for the TOT measurements the CO_2/DME 50/50 mixture can best be compared to the argon mixture (ionised molecules vs. high Z ions). The TOT values from the argon mixture are interpolated to find the gas gain in the CO_2/DME 50/50 mixture. Figure 7.9 shows the TOT (for the CO_2/DME 50/50) as a function of the gas gain based on the data from the argon mixture.

Based on the interpolation shown in figure 7.9 and the TOT as a function of the grid voltage (figure 7.8) the gas gain as a function of the grid voltage can be determined (figure 7.10). In the argon based mixture the average TOT does not linearly increase with the gas gain, the increase becomes less for increasing gain. For that reason the last two points in figure 7.9 for the CO_2/DME 50/50 mixture have a too high estimated TOT count since these are based on a linear extrapolation

of the last two points of the argon mixture. As a result the gain estimated for these TOT values may be too low. The last point for which the extrapolation error is the largest is not used for the exponential fit in figure 7.10 that shows the gain as a function of the grid voltage.

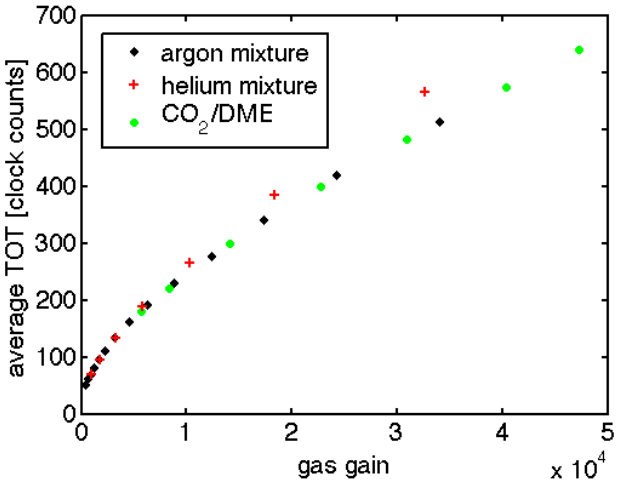

Figure 7.9: *The average time over threshold (TOT) count per pixel for the CO_2/DME 50/50 mixture (green dots) as a function of the gas gain based on the interpolation of the points from the measurement of the Ar/iC_4H_{10} 80/20 gas mixture (black diamonds).*

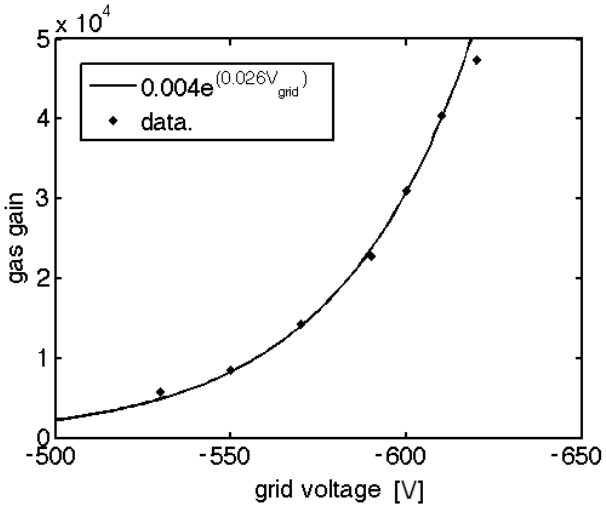

Figure 7.10: *Gas gain as a function of the grid voltage for a CO_2/DME 50/50 mixture.*

7.2.3 Track detection efficiency

To determine how often a track is detected by the GOSSIP detector, the general purpose Gridpix detector is used as a reference. Tracks detected by the general purpose Gridpix should also have been detected by the three GOSSIP detectors. Figure 7.11 shows the track efficiency of the GOSSIP detectors as a function of the grid voltage.

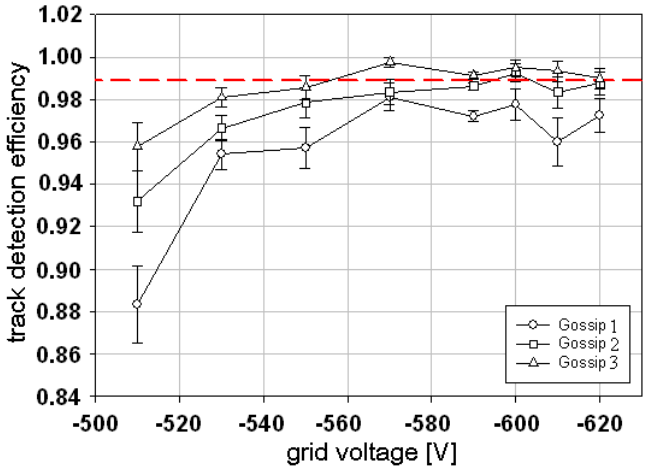

Figure 7.11: *Track detection efficiency as a function of the grid voltage. The dashed line is the expected maximum detection efficiency of normal incident MIPs. The efficiency of the detector with the highest efficiency is more than this because the muons are not minimum ionising (150 GeV/c) and the tracks are under an angle of 45 °, resulting in a 1.4 mm track length instead of 1 mm. The GOSSIP detector that has the lowest detection efficiency suffered from 10% inactive pixels.*

7.2.4 Drift time spectrum

For grid voltages less than -610 V the resolution in the drift direction is deteriorated by time walk. The effect of this time walk is illustrated by the drift time spectrum of the Gossip detectors. The ionisation is expected to be uniform over the entire drift gap and for an applied drift field of 2 kV/cm a square drift time spectrum between 0 and 90 ns is expected. At a less negative grid voltage, i.e. a low gas gain, the drift time spectrum extends to many hundreds of ns beyond the expected drift time domain (figure 7.12, left picture). At a more negative grid voltage, the majority of the signals is detected within 110 ns resulting in a reasonable square drift time distribution (figure 7.12, right picture). The tail of the distribution beyond 120 ns may be caused by false hits. False hits are small signals and are therefore detected late, contaminating the recorded track with late hits that do not represent primary charge.

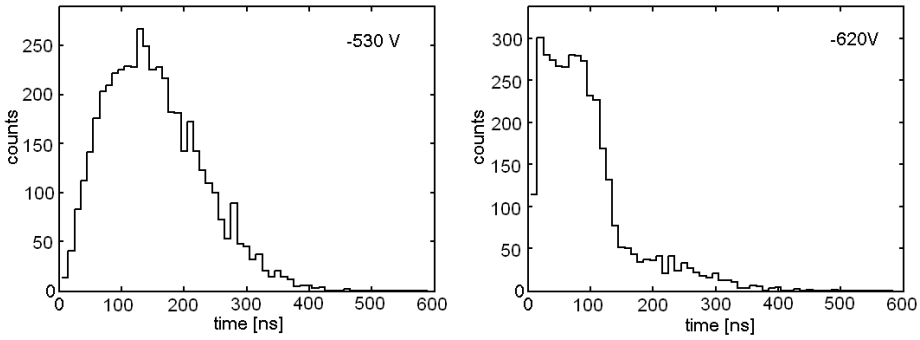

Figure 7.12: *Left: Gossip drift time spectrum for a grid voltage of -530 V. Right: Gossip drift time spectrum for a grid voltage of -620 V.*

For the short drift times in the GOSSIP detectors and because of the lack of time walk compensation with the used Timepix chip it is not possible to find an adequate working point. For low gas gains time walk dominates the error in drift time and with increasing gas gain false hits appear before time walk is reduced below a point at which it is no longer dominant. The Timepix chips used for all detectors in the test set-up have a 8 µm thick spark protection layer. According to the measurement presented in section 6.1.4 (figure 6.16) it is preferred to use chips with a 4 µm spark protection layer and operate them with a high gas gain to reduce time walk without suffering from false hits.

7.3 GOSSIP resolution

An estimation of the spatial resolution of the detectors has been made for tracks perpendicular to the chip plane. For perpendicular tracks it is sufficient to determine the centre of gravity (cog) of the hit pixels and the poorly defined drift time (due to time walk) is left out of consideration, i.e. only the projection of the track on the chip plane is used. A line is drawn through the two centres of gravity of the two outer GOSSIP detectors. After that, the distance between the centre of gravity of the middle GOSSIP detector to this line is measured, which is called the residual. In a simulation the same procedure is performed on a 'detector' with a defined resolution of 100 µm in order to know how the distribution of residuals scales with detector resolution. The residuals are assumed to be according to a Gaussian distribution. Multiple scattering (2.4 µm) of the 150 GeV/c muons through the three detectors is not taken into account.

7.3.1 GOSSIP simulation

Simulations have been performed by W. Koppert [73] to estimate the spatial resolution (σ_G) that can be obtained with a GOSSIP detector. The simulations have

been performed by simulating 10 GeV/c muons through 1 mm of CO_2/DME 50/50 gas with a drift field of 7 kV/cm (MAGBOLTZ). For a drift field of 7 kV/cm the diffusion is 110 $\mu m/\sqrt{cm}$. The XY plane is binned in units of 55 $\times$ 55 μm that represent the pixels. A gas gain is chosen and a time is added to the drift time according to a time walk spectrum corresponding to that particular gas gain and a 120 ns amplifier response time (see section 4.3.1 for time walk). The drift times with time walk error are divided into time bins corresponding to the clock frequency. Resulting data: binX, binY, binT. Figure 7.13 shows a simulated track and how the projection of the track is binned in the XY plane.

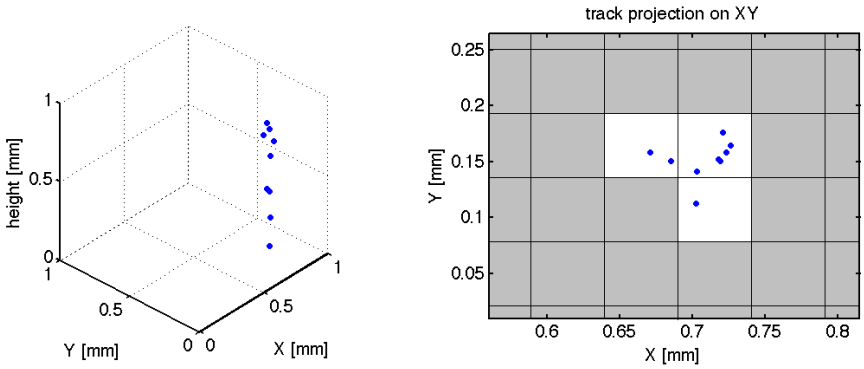

Figure 7.13: *Left: A simulated track in 1 mm of a CO_2/DME 50/50 gas mixture. Right: The projection of the track on the XY plane divided into 'pixels' of $55\times55\mu m^2$. The blue dots are the original positions of the primary electrons. On a chip with a pixel pitch of 55 μm the event would appear as the three light pixels.*

The resolution (σ_G) that can be obtained by using only the centre of gravity of the projected track is equal to the sigma of the distribution of the residuals (σ_r) of the centre of gravity and the track intersection with the 'chip'. The position where the particle's trajectory intersects the chip is set in the simulation. Figure 7.14 shows the distribution of residuals. The value of σ_r for both X and Y is 16 μm. To reject events with delta rays, events with more than 9 hit pixels are rejected (approximately 0.4 %).

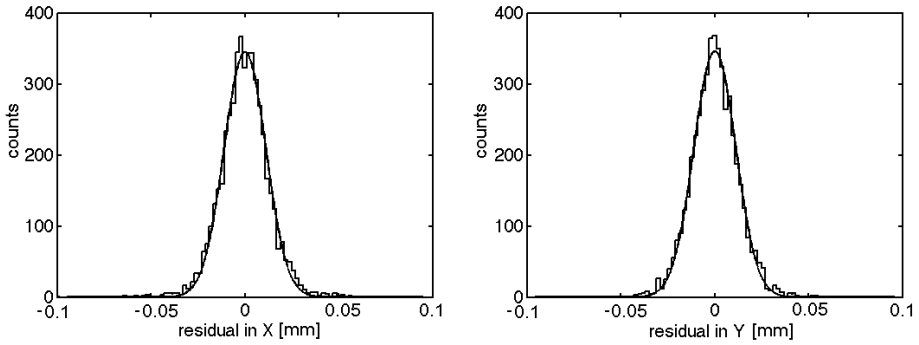

Figure 7.14: *Distributions of the residuals of the centre of gravity of the hit pixels and the position of the simulated muon track. Left: residuals in X, the value of σ_r is 16 μm. Right: residuals in Y, the value of σ_r is 16 μm.*

7.3.2 Position resolution with CO_2/DME

For the measurements the GOSSIP detectors were operated with a drift field of 2 kV/cm for which de diffusion is 70 $\mu m/\sqrt{cm}$. For that reason a better position resolution can be expected than what was found for the simulation in the previous section (7.3.1). For the measurements with the 150 GeV/c muons the information of the position of the track is not present. For that reason the two outer GOSSIP detectors are used to determine the track. The track will intersect the middle gossip at point P. The distance of point P to the centre of gravity of the hits in the middle GOSSIP detector is the residual. Figure 7.15 shows a sketch of how the residual is defined. The three GOSSIP detectors are assumed to be identical.

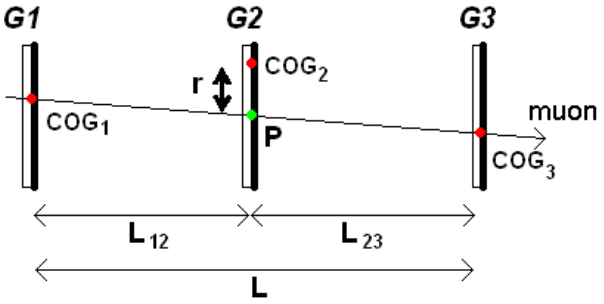

Figure 7.15: *Sketch of how the residual is defined. The centre of gravity (cog_1 and cog_3) from the two outermost GOSSIP detectors (G1 and G3) determine the track. The track goes through G2 at point P. The distance of P to cog_2 is the residual.*

The distance between the first and the second GOSSIP detector is L_{12}, the distance between the second and third detector is L_{23} and the distance between the

first and third detector is L. In the used set-up both L_{12} and L_{23} are 155 mm. The residual (r=cog_2-P) is calculated for each track according to:

$$r = cog_2 - \left(cog_1 \frac{L_{23}}{L} + cog_3 \frac{L_{12}}{L} \right). \tag{7.1}$$

Equation (7.1) is used to determine the residual in both the X and Y coordinate. The residuals also contain an error from the two outer GOSSIP detectors. The second GOSSIP detector is in the middle between GOSSIP1 and GOSSIP3, resulting in addition of half the error in GOSSIP1 and half the error in GOSSIP3. As a result the width of the distribution (σ_r) will be larger than the resolution (σ_G) of the detector according to:

$$\sigma_r = \sqrt{(0.5\sigma_G)^2 + \sigma_G^2 + (0.5\sigma_G)^2} = \sqrt{1.5}\sigma_G. \tag{7.2}$$

Equation (7.2) was verified with a Monte Carlo simulation in which the procedure is performed on a 'detector' with a defined resolution of 100 µm. The found value for σ_r is 122 µm. For the Monte Carlo simulation the distribution of the residuals is assumed to be Gaussian, which is a reasonable assumption according to figure 7.14. The position resolution of the GOSSIP detector is according to:

$$\sigma_G = \frac{\sigma_r}{\sqrt{1.5}}. \tag{7.3}$$

The accuracy of the assembly of the three GOSSIP detectors affects the measured resolution. Misalignment of the detectors create an offset in the detected track position. Rotation of the detectors around the Z axis (beam direction) causes the columns of the three Timepix chips to have different orientations resulting in a different offset depending on track position. A different offset as a function of the position on the chip results in a widening of the distribution of the residuals. Also the planes of the chips may not be perfectly aligned. To reduce position depended errors a small area of 30 × 30 pixels is used for data analysis. Figure 7.16 shows the selected areas in the three GOSSIP detectors, note the different positions of the areas due to misalignment. In total 302 tracks have been recorded in the selected area. The condition that has to be met by the tracks is that each of the three GOSSIP detectors should have at least one pixel hit. Figure 7.17 shows the residuals in the X and Y direction with offsets due to misalignment. Figure 7.18 shows the distributions after correcting for the offset.

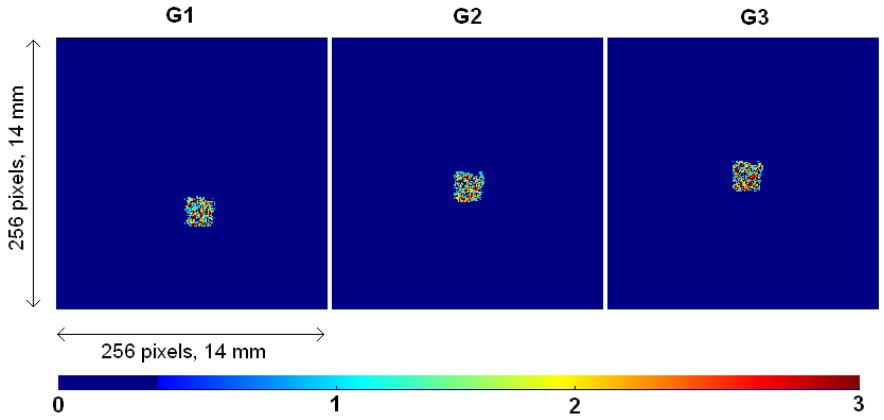

Figure 7.16: *The areas in the GOSSIP detectors that are used to find the resolution. The areas are 30 × 30 pixels. The colour indicates the total number of hits counted by a pixel during the data acquisition. In total 302 tracks have been recorded with the areas shown.*

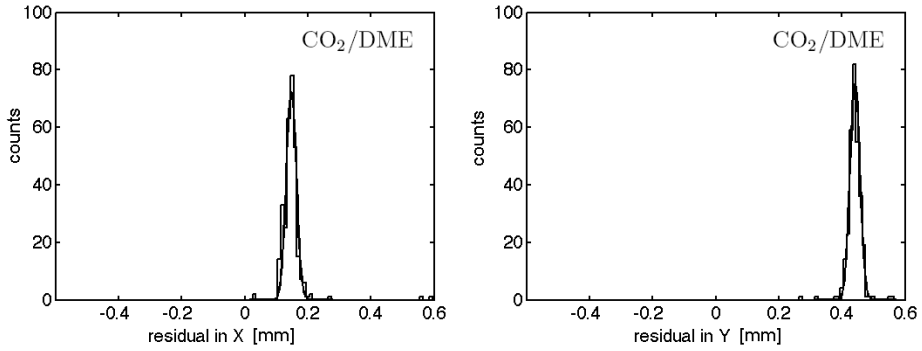

Figure 7.17: *The residuals in X and Y direction in pixels. The offset is due to misalignment of the detectors.*

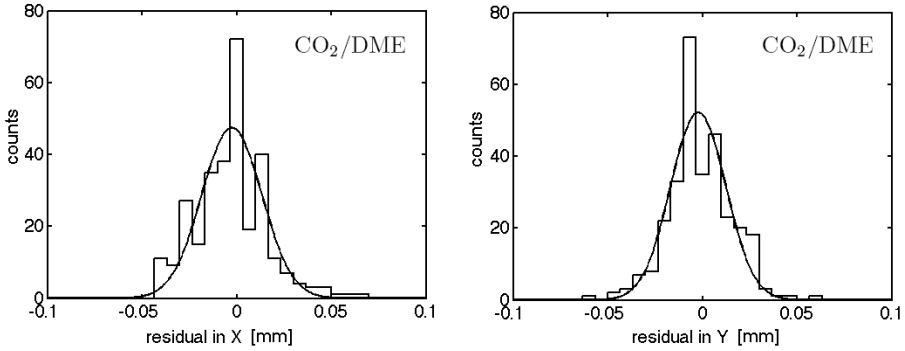

Figure 7.18: *The residuals in X and Y direction after correction for offset. The values of σ_r are 0.016 mm for the X direction and 0.015 mm for the Y direction.*

The values for σ_r are 16 and 15 μm in the x and y direction. The resolution, σ_G, is 13 μm (equation (7.3)).

7.3.3 Position resolution with Ar/iC_4H_{10}

The same measurements have been performed with an Ar/iC_4H_{10} (80/20) mixture in a drift field of 1.5 kV/cm. The diffusion is 250 $\mu m/\sqrt{cm}$. After correction for the offset the distributions are as shown by figure 7.19. The value of σ_r is 35 μm for x and 36 μm for y. The resolution (σ_G) is 30 μm.

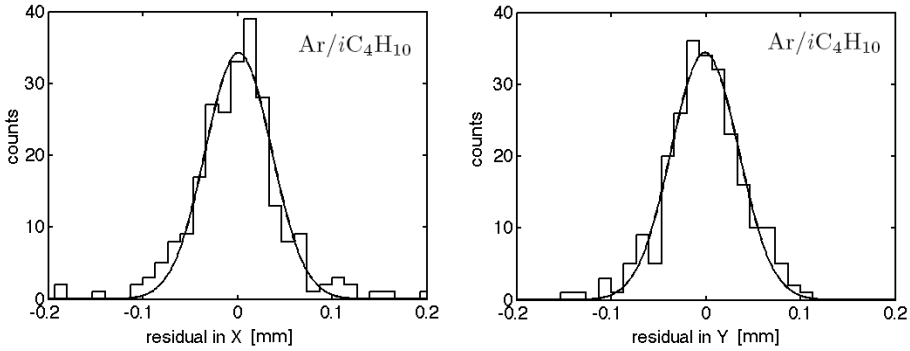

Figure 7.19: *The residuals in X and Y direction for an Ar/iC_4H_{10} (80/20) gas mixture. The value of σ_r is 0.035 mm for x and 0.036 mm for y.*

7.4 Performance of the general purpose Gridpix detector

The general purpose Gridpix detector was tested with the muon beam under an angle of 80 ° with the chip plane. Figure 7.20 shows a typical track in the Gridpix detector. The muons enter through the cathode and leave through the chip. The gas was CO_2/DME in a 50/50 ratio. The grid voltage was -540 V which, based on the measurement presented in section 7.2.2, results in a gas gain of at most 5×10^3. The single electron detection efficiency is expected to be less than 90 %. The drift field was 2 kV/cm, resulting in a drift velocity of 1 cm/µs. The trigger arrived within 20 ns. No excess of hits are found in the first time bin (which was a problem encountered in section 6.3) which is due to the fast trigger in combination with the moderate gas gain and low drift velocity.

Due to an error in a voltage setting the detector suffered from a poor uniformity of the drift field causing the direction of the reconstructed trail to vary as a function of the position on the chip. For that reason this detector is not used as part of the beam telescope in combination with the three GOSSIP detectors in front of it. Despite this effect an estimation of accuracy can be obtained by applying the analysis method performed in section 6.3. The events are split into two fractions each containing approximately half the number of hits. The chip is divided in a chess board pattern to select the hits for each of the two fractions. A regression line is fit through both track fractions and the differences between those lines, the angles and the intersection with the reference plane are the residuals. The reference plane is placed at 5 mm above the chip. Based on the width of a distribution of a residual the detector accuracy can be calculated according to equation (6.20) in section 6.3.

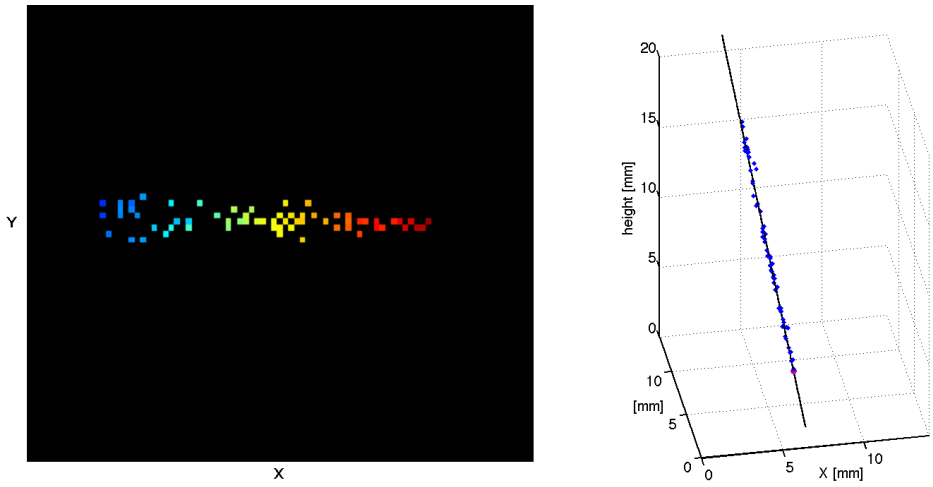

Figure 7.20: *A typical track in the general purpose Gridpix detector in a CO_2/DME 50/50 gas mixture. Left: Recorded track, the colours reflect recorded drift time. Red represents short and blue long drift times. Right: The reconstructed track and regression line.*

Figure 7.21 shows the distribution of the residuals for x_0 and y_0. The sigmas are 25 µm for x_0 and 13 µm for y_0. According to equation (6.20) in section 6.3 the accuracy is 13 and 6.5 µm in the X and Y direction. The accuracy in X direction is worse due to the inclination of the track in this direction. Due to this inclination errors in the Z direction (time walk and diffusion) contribute to errors in the X direction.

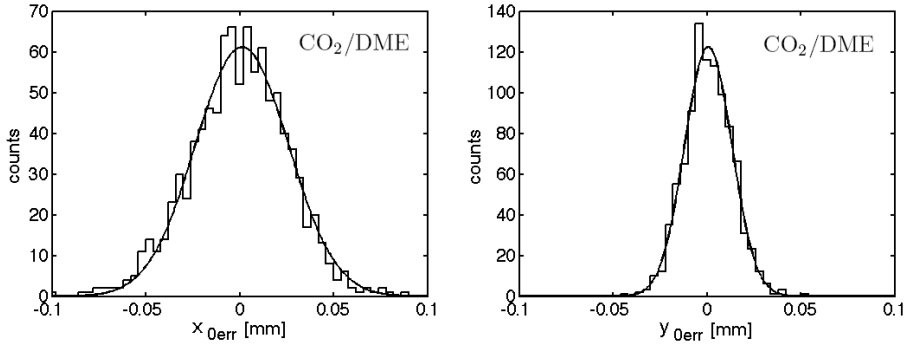

Figure 7.21: *Left: Distribution for x_{0err}. The σ has a value of 25 μm. Right: Distribution for y_{0err}. The σ has a value of 13 μm.*

Figure 7.22 shows the distributions for the angles ϕ and θ which have a σ of 4.6 and 2.7 mrad respectively. According to equation (6.20) this results in an angular accuracy of 2.3 and 1.4 mrad respectively.

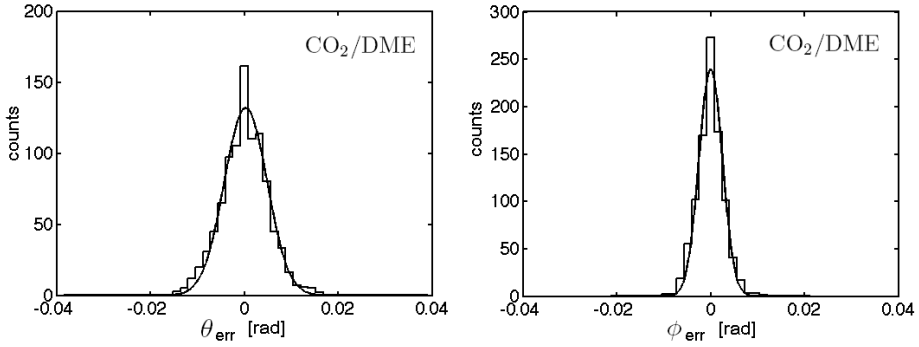

Figure 7.22: *Left: Distribution of θ_{err}. The fitted Gauss curve has a σ of 4.6 mrad. Right: Distribution of ϕ_{err} for which σ is 2.7 mrad.*

Since there are only very few pixels hit with electrons that drifted a short distance there is a large probability that one of the track fractions ends up with none or few of those hits. Such poor track samples may cause the residual to be found too large. This effect has not been taken into account. In the future the measurement should be repeated by comparing the general purpose Gridpix detector with a well characterised reference detector. Also the Gridpix detector should have a proper drift field.

The diffusion in the CO_2/DME 50/50 mixture also is determined (figure 7.23) which is 70 $\mu m/\sqrt{cm}$ and matches the result from GARFIELD.

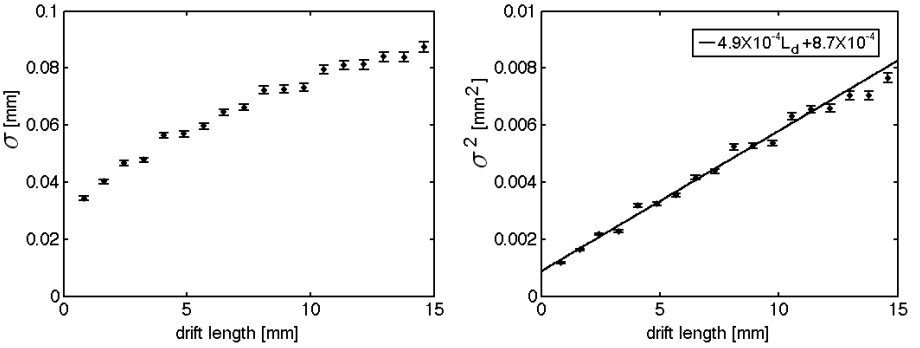

Figure 7.23: *Left: Diffusion (σ) as a function of the drift length. Right: σ^2 as a function of the drift length. The equation of the fitted line is: $\sigma^2 = 4.9 \times 10^{-4} L_{drift} + 8.7 \times 10^{-4}$.*

7.5 Ageing

A topic not yet discussed but relevant for the long term reliability of GOSSIP detectors is ageing. Ageing is a process in which deposits are formed on the electrodes. Insulating deposits may locally reduce gas gain and conductive deposits may increase the risk of discharges. These deposits are formed due to decomposition and chemical reactions of trace components in the gases. The electrode material may be involved in the chemical reactions. To reduce ageing the used gases must be as pure as possible and the materials used in the detector should be clean and not contain out-gassing compounds. For GOSSIP a study must be performed to identify and minimise the sources of ageing. Ageing depends on the amount of integrated charge through an electrode area and for that reason the gas gain should be kept as low as can be tolerated. A study on ageing can be found in [81].

7.6 Concluding remarks

As mentioned in section 7.3.2 not all parameters, like the rotation of the chips around the beam axis, are accounted for. Taking these parameters into account may improve the position resolution. Also, because of time walk effects, the resolution for inclined tracks is not yet determined. An improved analysis, in which more parameters will be taken into account, will be possible with the Gridpix tracking framework in the near future [78], which is being developed by W. Koppert. Also the GOSSIP detectors are treated as if they are identical, however, based on figure 7.5 and 7.11 it can be observed they are slightly different and the measured resolution is probably not the best that can be obtained. According to the measurements presented, a position resolution of at least 13 μm can be achieved for normal incident tracks and may be improved in the future.

For the tested GOSSIP detectors time walk or false hits compromises the accuracy. With no simultaneous TOT and drift time measurement available in the present Timepix chip, the gas gain must be high (more than $2{\cdot}10^4$, see figure 6.28 in section 6.2.6) to reduce time walk effects. In order to reduce the effects of false hits the chips must have a 4 μm SiRN protection layer instead of 8 μm used for the tests (figure 6.16 in section 6.1.4). In the near future, time walk compensation should be possible with the Timepix-3 chip which is currently under development. The pixels in the Timepix-3 chip can simultaneously measure drift time and TOT.

As mentioned in section 5.6.2, a SiRN spark protection layer should have a specific resistance in the order of 10^9 Ωcm or less to be able to cope with the high rate at the (s)LHC.

Chapter 8

Concluding remarks and outlook

8.1 Concluding remarks

The aim of the research presented in this thesis is to give a generic performance characterisation of Gridpix detectors. Based on this information, further research can focus on more specific aspects, which may depend on the application.

Drift time measurements that suffer from time walk can be improved significantly when the drift time is measured simultaneously with the signal amplitude. Simulations based on the specifications of a prototype chip, the Gossipo-3, and measurements with this chip proved that this concept works (chapter 4). GOSSIP detectors probably will benefit most from time walk correction. In GOSSIP detectors drift times are short and the diffusion is low, which makes time walk quickly the dominant error in drift time measurement. The gas gain in a GOSSIP detector should be low in order to minimise ion feedback and ageing effects. However, the lower the gas gain the more the error in drift time due to time walk. Presently a pixel chip (the Timepix-3) is under development that can measure the drift time and signal amplitude simultaneously. With this chip time walk correction should be possible. The Timepix-3 chip can measure the drift time in bins of 1.7 ns.

To protect the pixel chips against sparks a highly resistive protection layer of silicon rich silicon nitride (SiRN) is applied. Layers of 4 and 8 μm thickness were tested. Both appear to offer protection under the condition that there are no defects in the layer (chapter 5). However, occasionally chips still break down and therefore the robustness of the spark protection layer is not yet sufficient and must be improved. The resistance of the tested layers are in the order of 10^{13} Ωcm. The high resistance of the SiRN layer causes the gas gain to drop as the rate increases. In order for Gridpix detectors like GOSSIP to be used in a high particle flux environment the specific resistance should be 10^{9} Ωcm or less.

For gas gains of more than $2{\times}10^{4}$ a chip covered with a 8 μm SiRN starts to

suffer from false hits (chapter 6). For a SiRN layer of 4 µm the number of false hits is significantly less. It is not possible to correct time walk in Gridpix detectors with the currently used Timepix chips. For that reason it is best to equip the chips with a 4 µm thick protection layer and operate them at a high gas gain.

A set up with GOSSIP detectors was tested in a beam of 150 GeV/c muons at CERN (chapter 7). The presented results look promising and appear to be in agreement with expectations. However, due to the limitations of the Timepix chip the full performance of the concept cannot be tested yet. The limitations are caused by the 10 ns drift time bins and the lack of time walk correction. This will be improved with the Timepix-3 chip.

An important aspect still to be tested is the long term stability/reliability of Gridpix detectors. As soon as the means are available a set up with a large number of Gridpix detectors should be left running for a long time (in the order of a year). Also ageing is not covered in this thesis. An ageing study on Gridpix detectors still has to be performed, which may be part of the long term test.

8.2 Outlook and other applications

In a tracking detector the thin gas layers of the GOSSIP detectors can be used to reconstruct track segments that can reduce the complexity for track finding algorithms. The search for hits can be limited to within a certain cone in the direction in which a reconstructed track segment points. Detectors, like the one with a 19 mm drift gap presented in chapter 7, can be used further outwards in a tracking layer where the lower rate allows longer charge collection times. By placing a transition radiator in front of it and by using a Xe based (high Z) gas mixture, X rays from transition radiation can be detected [73]. Like for the GOSSIP detectors its directional information can be used for track finding algorithms to reconstruct tracks in the inner part of the tracking detector. With the tracks coming from the collision point, the angle of the recorded track gives direct information on how much it was deflected by the magnetic field. With that information a Gridpix can provide an estimation of transversal momentum and based on that information an event can be considered worth recording, i.e. the detector can be used as a trigger for high P_T events.

The development of Gridpix detectors initially was driven by the need for improvement of tracking detectors at particle collider experiments. During the development of Gridpix detectors it became clear that it may also be interesting for other applications. Currently an experiment with a Gridpix detector to measure the polarisation of X-rays is running [82]. If successful, it may find use in astrophysical research to investigate cosmic X-ray sources. The Gridpix concept is adopted as one of the possible concepts to be used in a liquid Xenon TPC for dark matter searches [83], [84]. A specially prepared Gridpix detector can even be used as a sensitive optical imaging device where single photoelectrons are multiplied by means of gas amplification [85]. The fingerprint on the cover (which is from my right index finger) was recorded using such a device. Yet another study is to use a Gridpix

detector, similar to the general purpose Gridpix detector presented in chapter 7, for proton tracking in proton therapy [86]. With proton therapy tumours are irradiated with protons (or other nuclei) such that the Bragg peak ends up inside the tumour [87]. Even more applications may emerge as the development of Gridpix detectors continues.

Appendices

Appendix A

Commonly used constants and values

constant	name	value	units
e	unit charge	$1.602177{\cdot}10^{-19}$	C
eV	electron volt	$1.602177{\cdot}10^{-19}$	J
c	speed of light in vacuum	$2.99792458{\cdot}10^{8}$	m/s
ϵ_0	permittivity of vacuum	$8.854{\cdot}10^{-12}$	F/m
μ_0	permeability of vacuum	$1.2566{\cdot}10^{-12}$	N/A^2
m_e	rest mass electron	$9.10939{\cdot}10^{-31}$	kg
m_p	rest mass proton	$1.67262{\cdot}10^{-27}$	kg
m_n	rest mass neutron	$1.67492{\cdot}10^{-27}$	kg
N_A	Avogadro's number	$6.0220{\cdot}10^{23}$	$mole^{-1}$

Table A.1: *The value of some commonly used constants taken from [25] and [88].*

Material	relative permittivity (ϵ_r)
SU-8	3
Si	11.9
Si_3N_4	7.5
SiO_2	3.9

Table A.2: *The relative permittivity of commonly used insulating materials in CMOS post processing [89], [90].*

Gas	Z	A	E_i [eV]	$(dE/dx)_{MIP}$ [keV cm^{-}1]	N_c [cm^{-1}]	N_e [cm^{-1}]
He	2	4	41	0.32	4.2	8
Ar	18	39.9	26	2.44	23	94
Xe	54	131.3	22	6.76	44	307
DME	26	46	23.9	3.9	55	160
CO_2	22	44	33	3.01	35.5	91
iC_4H_{10}	34	58	23	5.93	84	195

Table A.3: *Physical properties of commonly used gases [76]. The average energy loss for one ionisation is E_i. N_c is the average number of clusters per cm (i.e. interactions of the MIP that each result in one or more ionisations), N_e is the average number of ionisations (on average a cluster contains more than one electron).*

Appendix B

Drift and diffusion properties of gas mixtures

This appendix contains graphs to look up electron drift and diffusion in the most commonly used gas mixtures in this thesis. The graphs are the outputs of simulations performed with MAGBOLTZ by W. Koppert for Ar/iC$_4$H$_{10}$ and He/iC$_4$H$_{10}$ in a ratio of 80/20 and CO_2/DME in a ratio of 50/50.

B.1 Ar/iC$_4$H$_{10}$ 80/20

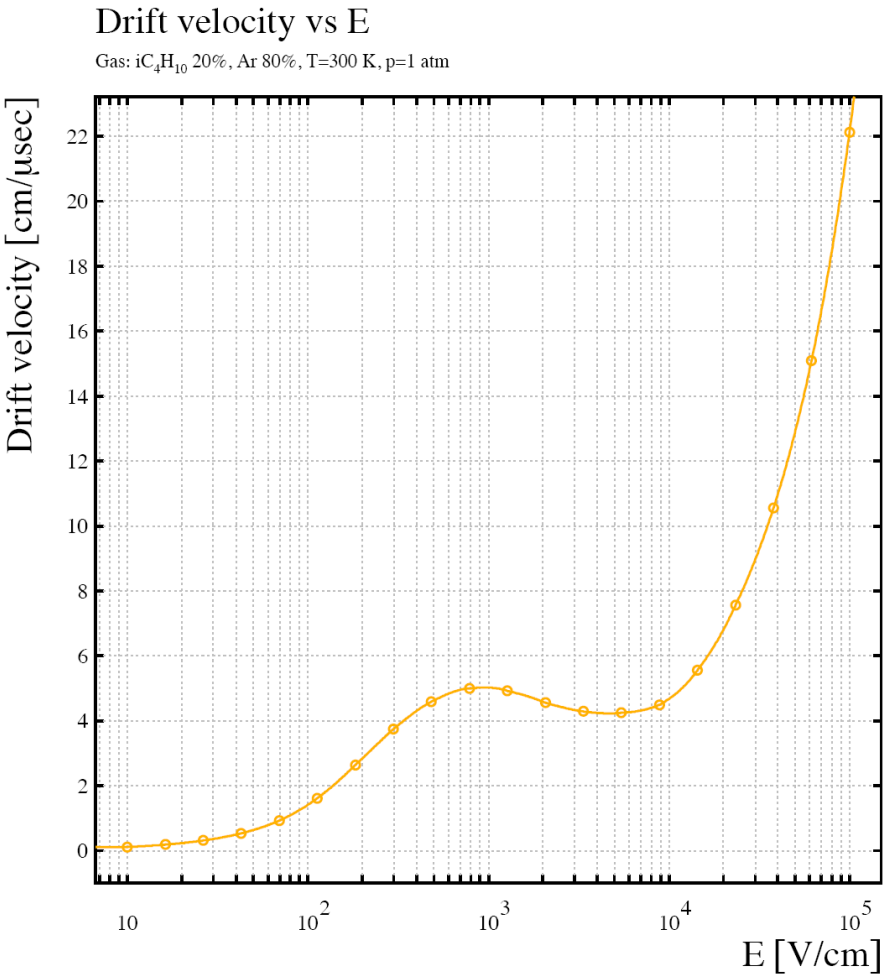

Figure B.1: *MAGBOLTZ simulation of the electron drift velocity as a function of the drift field.*

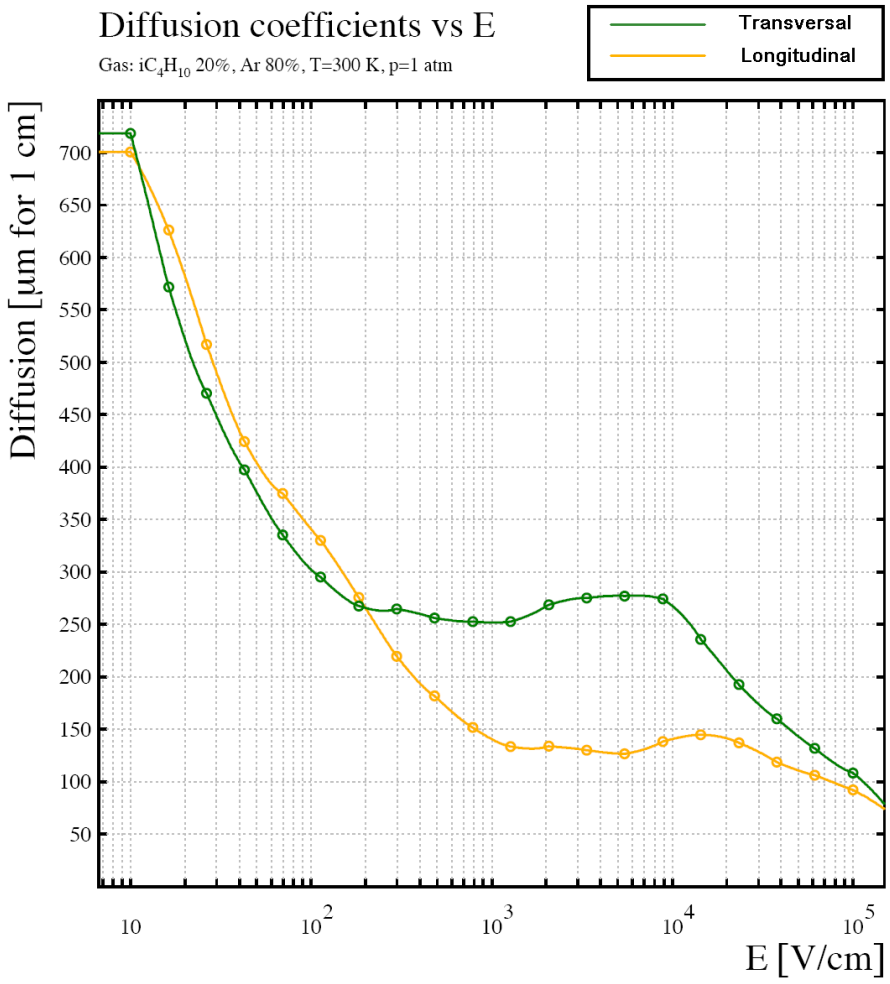

Figure B.2: *MAGBOLTZ simulation of the diffusion as a function of the drift field. Transversal diffusion is the diffusion perpendicular to the drift direction and longitudinal diffusion is the diffusion in the drift direction.*

B.2 He/iC$_4$H$_{10}$ 80/20

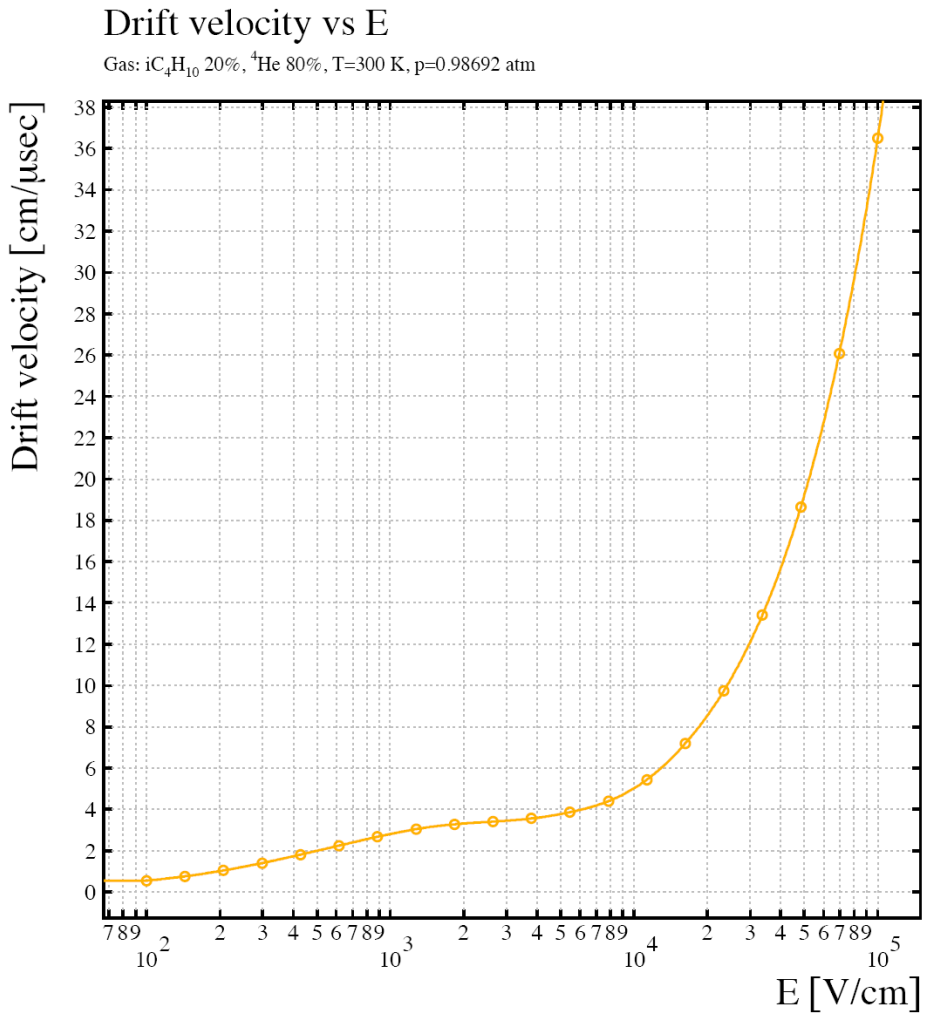

Figure B.3: *MAGBOLTZ simulation of the electron drift velocity as function of drift field.*

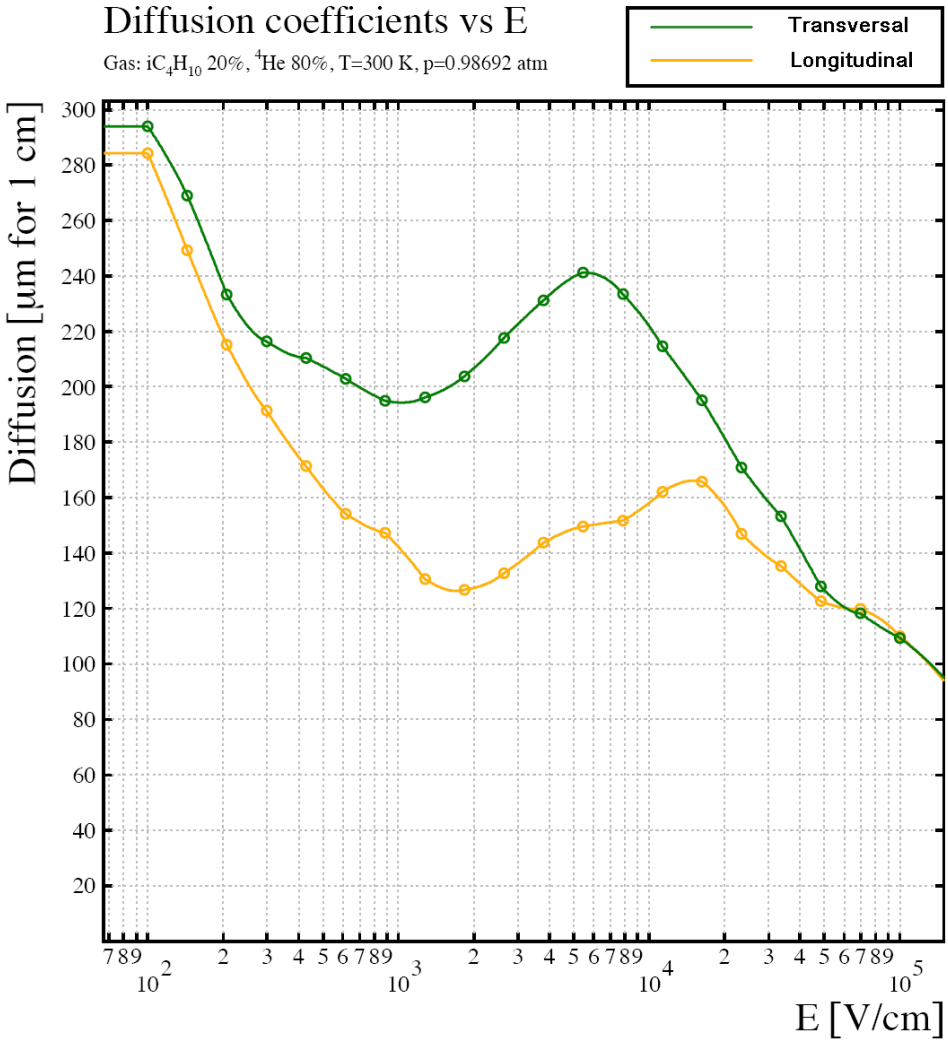

Figure B.4: *MAGBOLTZ simulation of the diffusion as a function of the drift field. Transversal diffusion is the diffusion perpendicular to the drift direction and longitudinal diffusion is the diffusion in the drift direction.*

B.3 CO_2/DME 50/50

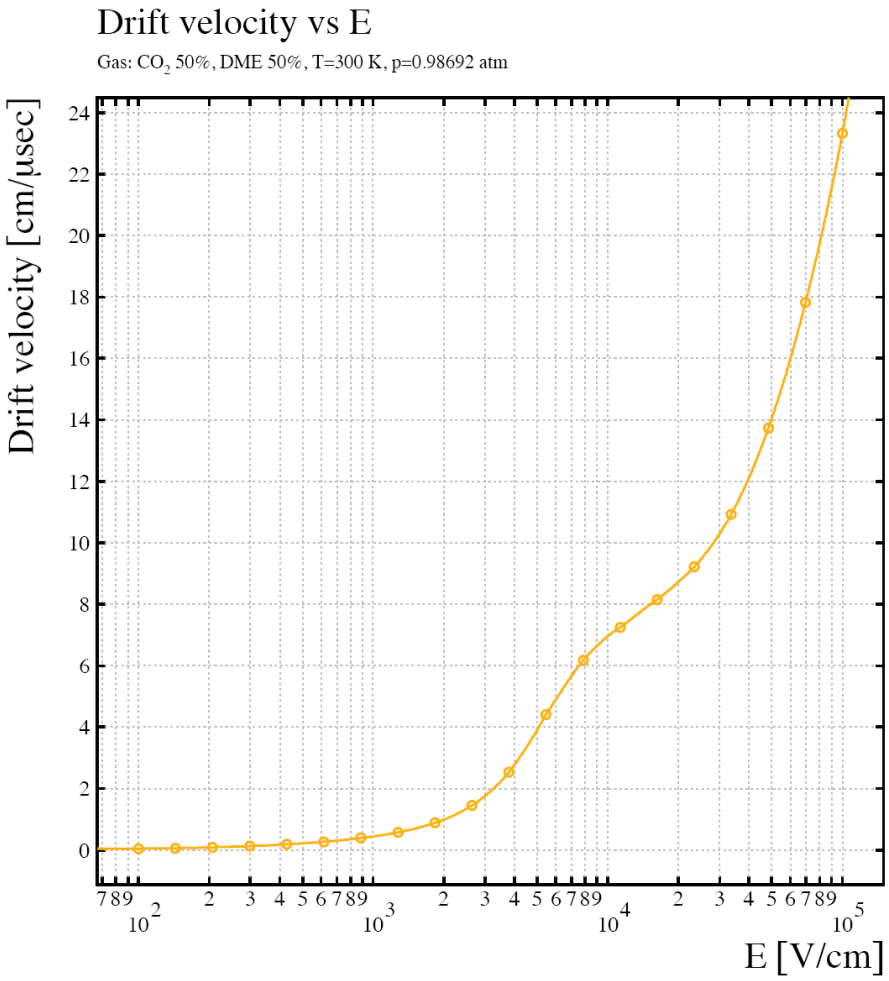

Figure B.5: *MAGBOLTZ simulation of the electron drift velocity as function of drift field.*

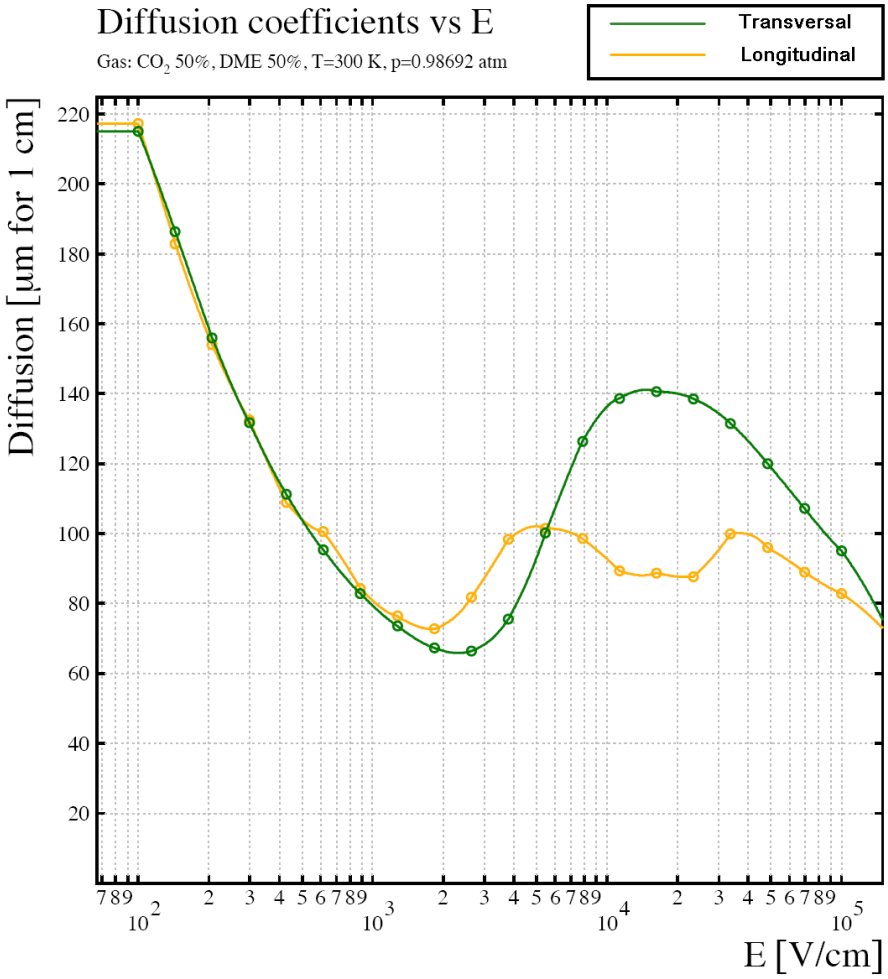

Figure B.6: *MAGBOLTZ simulation of the diffusion as a function of the drift field. Transversal diffusion is the diffusion perpendicular to the drift direction and longitudinal diffusion is the diffusion in the drift direction.*

Appendix C

Trigger box

Due to the limitations of the used trigger set-up presented in section 6.2.1 the start of an acquisition by definition is late. An acquisition was started as quick as possible after a particle was detected (the trigger) and was ended a precisely set time after the trigger. No alternative set up was possible at the time and the available electronics had a latency of approximately 60 ns, which compromised track reconstruction accuracy (section 6.3.1). In order to reduce the latency a new trigger system (the 'trigger box') was built which has a latency of approximately 15 ns. With this trigger good drift time measurements have been performed (section 7.4). The trigger box was built to be used with the MUROS [74] chip readout system. The MUROS readout system now becomes obsolete due to newer readout electronics being developed [91]. In case the trigger box may be of use in the future a description is given of how the trigger box was applied in the set up described in chapter 7.

C.1 Trigger set up

The trigger box requires -12 V, 0 and +12 V for powering, which can be supplied by the 'trigger power' NIM module (figure C.3). The trigger box has two comparator inputs (labelled 'SC1' and 'SC2') that accept a signal from a PMT. The thresholds are set at approximately -15 mV. Each comparator has 4 outputs: NIM, $\overline{\text{NIM}}$, TTL and $\overline{\text{TTL}}$. If a signal is detected the outputs give a digital signal of approximately 200 ns. For NIM a logic '0' is 0 V and a logic '1' is -0.7 V. For the TTL a logic '0' is 0 V and a logic '1' is 3.3 V. The latency between a signal at SC1 or SC2 crossing the threshold and the response of NIM1 or NIM2 is approximately 15 ns. The latency to the TTL, $\overline{\text{TTL}}$ and $\overline{\text{NIM}}$ outputs is approximately 10 ns.

In case of a coincidence the output $\overline{\text{out}}$ goes low for 200 ns. The $\overline{\text{out}}$ output is a $\overline{\text{TTL}}$ signal. The duration of an acquisition is as long as the time $\overline{\text{out}}$ is low. In this context one can consider this signal as a 'shutter', the time $\overline{\text{out}}$ is low defines the 'exposure' time. The latency from a coincidence at the two inputs SC1 and SC2 and the output $\overline{\text{out}}$ going low is 15 ns.

The $\overline{\text{out}}$ signal also is controlled with a NIM signal at the input marked 'in', which is beneath the $\overline{\text{out}}$ connector. By using this input the acquisition time can be set. The NIM outputs of the SC1 and SC2 channels can be used to start an external timer. This external timer is connected to 'in', which will define when the signal at $\overline{\text{out}}$ will go high again. Figure C.1 shows a schematic of the trigger set up of how it was used for the measurement discussed in chapter 7. The cables between the trigger box and the PMTs and the MUROS (or other device) to be controlled should be as short as possible to minimise latency due to cables. Figure C.2 shows the front side of the trigger box with the connectors.

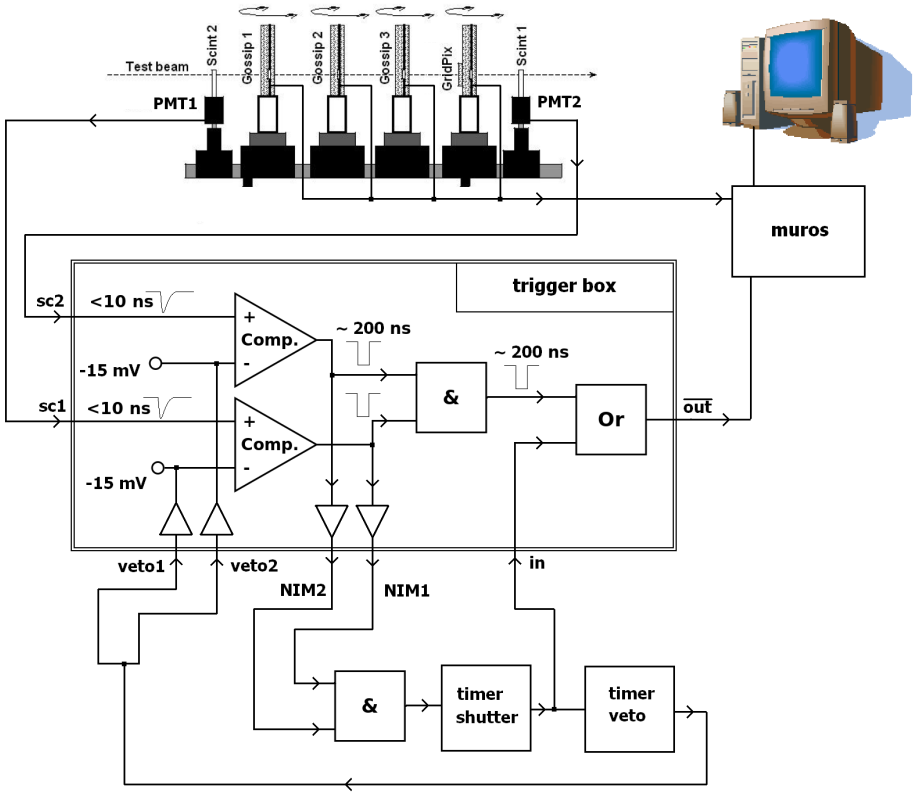

Figure C.1: *Block schematic of the trigger set up. This set up actually does not supply a trigger signal but a shutter signal. If both PMTs simultaneously give a signal the 'AND' gate inside the trigger box passes it trough to the 'OR' gate which directly feeds the signal to the MUROS. In the mean time the NIM1 and NIM2 outputs are used to detect the coincidence with an external 'AND' gate which starts a timer that defines the acquisition time. The output of this timer (NIM level signal) is fed to another timer to make a veto signal and to the input labelled 'in', which feeds the signal to the 'OR' gate in the trigger box. The veto signal 'disables' the comparators to ensure that only one measurement can be performed until after the acquisition the readout is completed by the computer.*

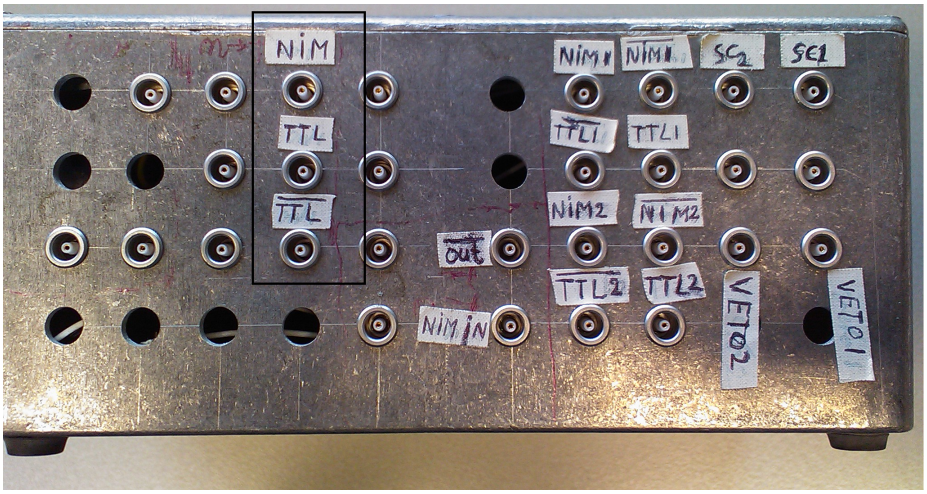

Figure C.2: *Front side of the trigger box. The connectors inside the rectangle are connected to a NIM to TTL converter, which is spare feature. The connectors without label are not used.*

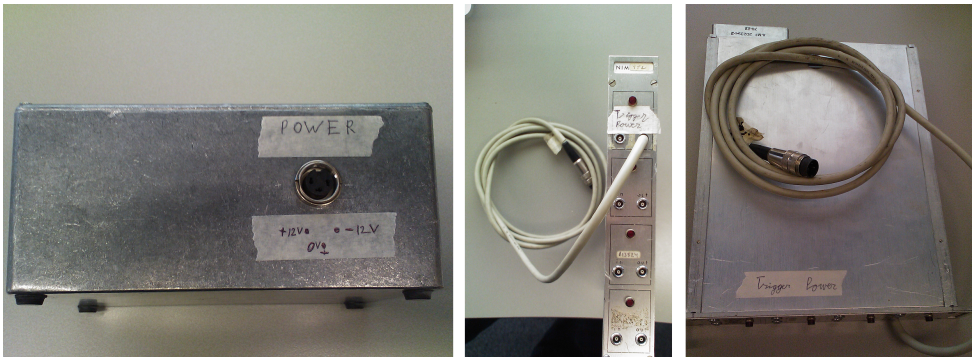

Figure C.3: *Left: Backside of the trigger box with power connector. Middle and right: The Modified NIM module to power the trigger box.*

It is important that the length of the shutter time has a stability of better than half the drift time resolution in order not to affect drift time accuracy. The timing device used for this purpose was a Stanford Research Systems model DG535 delay and timing generator.

The NIM signals should be 50 Ω terminated. The $\overline{\text{TTL}}$ level signal to the MUROS has to be treated in a different way since the signal goes through a 50 Ω coaxial cable without having a 50 Ω termination at the MUROS. The end of the coaxial cable is terminated with a diode (figure C.4) to prevent a negative voltage due to undershoot at the falling edge of the signal. No measures have been taken to reduce overshoot at

the rising edge of the signal. If a different device than the MUROS is connected one should check that the overshoot from the rising edge of the signal does not damage the device.

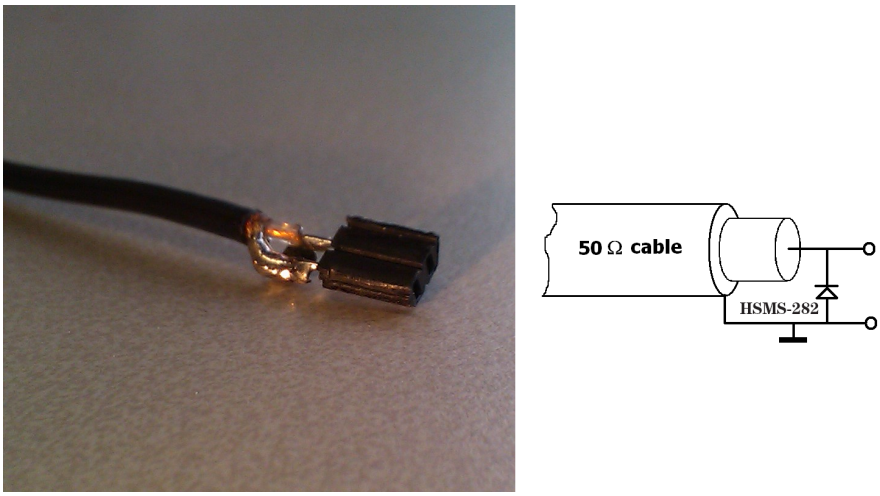

Figure C.4: *The diode termination that is required for the MUROS. The diode is soldered to the connector that is mated with the connector on the MUROS circuit board. The used diode is the HSMS-282 from Agilent but any type with a response time of less than 1 ns is sufficient.*

Applying a veto signal effectively increases the corresponding threshold to -0.7 V which does not fully disable the comparator. A pulse larger than -0.7 V will still be detected. For that reason the connected PMT should be operated at an as low as possible high voltage that still allows a reliable detection with a low (-15 mV) threshold.

Bibliography

[1] D. Griffiths *Introduction to elementary particles.* second revised edition, ISBN 978-3-527-40601-2, 2009

[2] E. P. Verlinde, *On the Origin of Gravity and the Laws of Newton.* arXiv:1001.0785v1, 2010.

[3] A. Einstein, *Ist die Trägheit eines Körpers von seinem Energieinhalt abhängig?* Annalen der Physik 18, 639-641, 1905.

[4] A.P.French, *Special relativity.* M.I.T., ISBN 0-393-09793-5, 1968.

[5] wikipedia, *http://en.wikipedia.org/wiki/World_energy_consumption.* 2011.

[6] L. Evans, P. Bryant *LHC machine.* JINST 3 S08001, 2008.

[7] N. Phinney, N. Toge, N. Walker *ILC reference design report.* Volume 3, 2007.

[8] The CLIC study team *A 3 TeV e+e- LINEAR COLLIDER BASED ON CLIC TECHNOLOGY.* CERN 2000-008, 2000.

[9] G. Hall, *Semiconductor particle tracking detectors.* Rep. Prog. Phys. 57, 481-531, 1994.

[10] J. Wray, *Silicon Strip Detector Efficiency Using a Purpose Built Particle Telescope.* Univ. of California, Santa Cruz, 2004.

[11] Medipix collaboration, *http://medipix.web.cern.ch/medipix/.*

[12] J. V. Jelley, *Cherenkov Radiation and its Applications.* Pergamon Press, 1958.

[13] B. N. Ratcliff, *Imaging rings in Ring Imaging Cherenkov counters.* Nuclear Instruments & Methods, A502 211-221, 2003.

[14] ALICE Collaboration, *The ALICE experiment at the CERN LHC.* JINST 3 S08002, 2008.

[15] LHCb Collaboration, *The LHCb Detector at the LHC.* JINST 3 S08005, 2008.

[16] A. Andronic, J. P. Wessels *Transition Radiation Detectors.* arXiv:1111.4188v1, 2011.

[17] ATLAS Collaboration, *The ATLAS Experiment at the CERN Large Hadron Collider.* JINST 3 S08003, 2008.

[18] ALICE collaboration, *http://aliceinfo.cern.ch.*

[19] M. Capeans, *Aging of Gaseous Detectors: assembly materials and procedures.* ICFA Instrum. Bull. 24, 85 2002

[20] E. Rutherford and H. Geiger, *An electrical method of counting the number of particles from radioactive substances.* Proceedings of the royal society (London). Ser.A, vol.81, 141-161, 1908.

[21] G. Charpak et al, *The use of multiwire proportional counters to select and localize charged particles.* Nuclear Instruments & Methods, 62, 262, 1968.

[22] D.R. Nygren & J.N. Marx, Physics Today 31N10, 46, 1978.

[23] W. Blum and L. Rolandi, *Particle detection with drift chambers.* Springer Verlag, ISBN 0-387-58322-X, 1994.

[24] Particle Data Group, *Review of particle physics, Passage of particles through matter.* Chapter 27, 285-299, 2010.

[25] R.Fernow, *Introduction to experimental particle physics.* Cambridge university press, ISBN 0521379407, 1986.

[26] NIST, *XCOM: Photon Cross Sections Database.* http://www.nist.gov/pml/data/xcom/index.cfm, 2010.

[27] P. Langevin, *C. R. Acad. Sci.* 146, 530, 1908.

[28] D. S. Lemons and A. Gythiel, *Am. J. Phys.* 65 no. 11, 1079, 1997.

[29] C. Ramsauer, *Ann. Phys.* 66, 546, 1921.

[30] E. Fermi, *The ionization loss of energy in gases and in condensed materials.* Phys. Rev. Vol. 57 , 485-493, 1940.

[31] P. Colas et al., *The readout of a GEM or Micromegas-equipped TPC by means of the Medipix2 CMOS sensor as direct anode.* Nuclear Instruments & Methods, A 535, 226, 2004.

[32] M. Chefdeville et al., *An electron multiplying Micromegas grid made in silicon wafer post-processing technology.* Nuclear Instruments & Methods, A 556, 490-494, 2006.

[33] J. H. Thomas et al., Nuclear Instruments & Methods, A 499, 659, 2003.

[34] D. F. Cowen et al., Nuclear Instruments & Methods, A 252, 403, 1986.

[35] D. Delikaris et al., Nuclear Instruments & Methods, A 283, 567, 1989.

[36] H. Raether, *Electron avalanches and breakdown in gases.* Butterworths, London, 1964.

[37] Yu. Ivaniouchenkov et al., *Breakdown limit studies in high-rate gaseous detectors.* Nuclear Instruments & Methods, A 422, 300-304, 1999.

[38] C. J. Martoff et al, *Suppressing drift chamber diffusion without magnetic field.* Nuclear Instruments & Methods, 44, Issue 2, 355-359, 2000.

[39] F. Sauli, *Principles of operation of multiwire proportional and drift chambers.* CERN Report 77-09, 1977.

[40] R.I. Schoen, *J. Chem. Phys. 17.* 2032, 1962

[41] Yu.N. Pestov et al., Nuclear Instruments & Methods, A 456, 11, 2000.

[42] J. Byrne, *Proc. R. Soc. Edinburgh XVI A 33.* 1962.

[43] W. Legler, *Z. Naturforschung*, 16a 253 1961.

[44] W. Legler, *Br. J. Applied Physics*, 18 1275 1967.

[45] R.A. Wijsman, *Phys. Rev. 75.* 833, 1949.

[46] W. Legler, *Z. Phys. 140.* 221, 1955.

[47] P. Fonte et al., Nuclear Instruments & Methods, A 433, 513, 1999.

[48] J. Derré and I. Giomataris, Nuclear Instruments & Methods, A 477, 23, 2002.

[49] X. Llopart et al., *Timepix, a 65-k programmable pixel readout chip for arrival time, energy and/or photon counting measurements.* Nuclear Instruments & Methods, A 581, 485-494, 2007, Erratum, ibid A585, 106-108, 2008.

[50] Y. Giomataris et al., *MICROMEGAS: a high-granularity position-sensitive gaseous detector for high particle-flux environments.* Nuclear Instruments & Methods, A 376, 29-35, 1996.

[51] M. Chefdeville, *Development of micromegas-like gaseous detectors using a pixel readout chip as collecting anode.* Ph.D. Thesis, University of Amsterdam, Amsterdam, 2009.

[52] J. Martin, *Study of a micromegas TPC for the future linear collider.* Master Thesis, IRFU/CEA/SPP, Saclay, 2002.

[53] P. Colas et al., *The readout of a GEM or Micromegas-equipped TPC by means of the Medipix2 CMOS sensor as direct anode.* Nuclear Instruments & Methods, A 535, 506-510, 2004.

[54] M. Campbell et al., *Detection of single electrons by means of a micromegas covered Medipix2 pixel CMOS readout circuit.* Nuclear Instruments & Methods, A 540, 295-304, 2005.

[55] X. Llopart et al., *Medipix2: a 64-k pixel readout chip with 55-μm square elements working in single photon counting mode.* IEEE transactions on nuclear science, vol.49, no 5, 2002.

[56] LCTPC collaboration, *The Linear Collider Time Projection Chamber of the International Large Detector.* Report to the DESY PRC 2010, 2010.

[57] X. Llopart Cudie, *Design and characterization of 64K pixels chips working in single photon processing mode.* Mid Sweden university, Sundvall, ISBN 978-91-85317-56-1, 2007.

[58] R. Ballabriga et al., *Medipix3: A 64 k pixel detector readout chip working in single photon counting mode with improved spectrometric performance.* Nuclear Instruments & Methods, In Press, Corrected Proof, 2010

[59] V. Gromov R. Kluit, H. van der Graaf, *Development of a Front-end Pixel Chip for Readout of Micro-Pattern Gas Detectors.* TWEPP, Naxos, Greece, 2008.

[60] C. Brezina et al., *Gossipo-3: A prototype of a Front-End Pixel Chip for Read-Out of Micro-Pattern Gas Detectors.* TWEPP, Paris, France, 2009.

[61] V.M. Blanco Carballo, *Radiation imaging detectors made by wafer post-processing of CMOS chips.* Ph.D. Thesis, University of Twente, Enschede, 2009.

[62] V.M. Blanco Carballo et al., *A CMOS compatible Microbulk Micromegas-like detector using silicon oxide as spacer material.* Nuclear Instruments & Methods, A 629, 118-122, 2011.

[63] S.Biagi *MAGBOLTZ: Transport of electrons in gas mixtures.* http://consult.cern.ch/writeup/magboltz/

[64] W. L. Harries, *The effect of charge transfer on ion drift velocity in electromagnetic fields.* J. Phys. Appl. Phys, Vol. 11, Great Britain, 1978.

[65] *Communication with V. Gromov.* 2008.

[66] A. Kruth et al., *GOSSIPO-3: measurements on the prototype of a read-out pixel chip for Micro-Pattern Gaseous Detectors.* TWEPP, Aachen, Germany, 2010.

[67] Y. Bilevych et al., *Spark protection layers for CMOS pixel anode chips in MPGDs.* Nuclear Instruments & Methods, A 629, 66-73, 2011.

[68] I. Smirnov *HEED: Interactions of particles with gases.* W5060, http://consult.cern.ch/writeup/heed/

[69] J. Yeh and I. Lindau, *At. Data Nucl. Data Tables.* 32, 1, 1985.

[70] M. Cardona and L. Ley, *Photoemission in Solids I: General Principles.* Springer-Verlag, Berlin, 1978.

[71] J.C. Fuggle and N. Martensson, *J. Electron Spectrosc. Relat. Phenom.* 21, 275, 1980.

[72] K. Ueda et al., *Photoemission in Solids I: General Principles.* J. Phys., B 24, 605, 1991.

[73] Atlas coll., *Performance and prospects of GridPix and Gossip detectors.* ATLAS Note No: ATL-P-MN-0016, 2009.

[74] D. San Segundo Bello et al., *An interface board for the control and data acquisition of the Medipix2 chip.* Nuclear Instruments & Methods, A509, 164-170, 2003.

[75] Pixelman software from IEAP., Czech Technical University in Prague, http://www.utef.cvut.cz/en/index.php

[76] A. Sharma, *Properties of some gas mixtures used in tracking detectors.* GSI-Darmstadt, Germany

[77] *Communication with W. Koppert*

[78] W.J.C. Koppert, *PhD thesis, in preparation.* University of Amsterdam, Amsterdam

[79] *http://www.9math.com/book/projection-point-plane* 2008

[80] Particle Data Group *Particle Physics Booklet* 2004

[81] M. Titov *Radiation damage and long-term aging in gas detectors.* ICFA Instrum. Bull. 26, 002 2004

[82] S. Nauta *PolaPix.* Master thesis, Delft Univ. of technology, 2010

[83] G. Hemink *A pixel sensor for noble liquid dark matter searches.* Master thesis, Univ. of Twente, 2011

[84] M. Alfonsi *Development of the GridPix Detector for Dual Phase Noble Gas Time Projection Chambers.* Conference proceeding NSS-IEEE, 2011

[85] J. Melai *Photon imaging using post-processed CMOS chips.* Univ. of Twente, ISBN: 978-90-365-3132-0, 2010

[86] P. C. Tsopelas *Applying Gridpix as a 3D particle tracker for proton radiography.* Master thesis, Univ. of Utrecht, 2011

[87] S. Braccini *Scientific and Technological Development of Hadron Therapy.* arXiv:1001.0860v1, 2010

[88] *http://chemistry.about.com/od/chartstables/a/constanttable.htm*

[89] *http://www.mit.edu/ 6.777/matprops/su-8.htm*

[90] Virginia Semiconductor *The General Properties of Si, Ge, SiGe, SiO2 and Si3N4.* 2002

[91] J. Visser et. al. *A Gigabit per second read-out system for Medipix Quads.* Nuclear Instruments & Methods, A633, 22-25, 2011

Summary

In the field of high energy physics research is focusing on finding elementary particles and their properties in order to get insight in how nature works. Research can be performed by colliding subatomic particles with almost the speed of light. In a collision new (subatomic) particles are formed which contain information about the fundamental processes that played a role in the collision. In order to understand these processes the collision has to be reconstructed by measuring what particles were created, with what energy, and where the particles originate from. In order to find a particle's point of origin a detector that tracks charged particles is required. Charged particles can be measured by detecting the ionisation they cause when they traverse matter. However, if a charged particle traverses matter it will be scattered off track. It is important that the tracking detector has a low enough mass in the particles path. The less material the less scattering and the lower the probability of 'showering' i.e. of producing other particles that contaminate the measurement. Two commonly used concepts to electronically measure the path of a charged particle are semiconductor detectors and gaseous detectors.

The semiconductor detectors are composed of a stack of thin layers of silicon. These silicon layers are read out by strips or pixels in order to determine the location where charge is released by a charged particle that went through. By using the positions where charge is detected in the different slabs of silicon the particle's trajectory can be reconstructed.

In a gaseous detector the trail of ionisations left by a particle is reconstructed and based on this reconstructed ionisation trail the particle's trajectory is determined. The TPC (Time Projection Chamber) is a gaseous detector in which the ionisation trail can be reconstructed in 3 dimensions. Under the influence of an applied electric field the released electrons will drift towards the anode and the positively charged ions drift towards the cathode. The anode is segmented in order to measure where the electrons arrive, resulting in a two dimensional projection of the trail. The third dimension is reconstructed by using the drift velocity and drift time required for the electrons to arrive at the anode, hence the name Time Projection Chamber.

Both concepts, the silicon and gaseous detectors, have different advantages and disadvantages. The silicon detectors have the advantage that they can be used in an environment with a high particle flux due to their fast response and highly segmented readout (pixels and strip in the order of 50-500 μm). Silicon detectors have a good spatial resolution. The disadvantage of silicon detectors is that they bring relatively

much material in the particles trajectory and the detector material degrades under irradiation. Gaseous detectors require only a little amount of material (gas) in order to detect a charged particle. The gas can be flushed and therefore deterioration of the detecting material does not occur. Due to the time required to extract the charge (the electrons and the ions) from the drift volume a large volume detector cannot be used in a high particle flux environment.

In a study to have better tracking detectors 'Gridpix' is being developed. Gridpix is the general name for a TPC that is read out with a pixel chip with a pixel pitch that is the same as for silicon detectors. With such a fine segmented anode the individual electrons in the ionisation trail can be distinguished. With such a detailed measurement of the ionisation trail one can achieve a high track reconstruction accuracy with only a small volume of gas, which can be read out quickly. This thesis describes developments and tests on this TPC concept. The used pixel chips have a 14×14 mm pixel matrix of 256×256 pixels (55 μm pitch).

As the primary electrons (the electrons from the drift region) drift towards the chip they pass the grid electrode. The grid is a mesh suspended 50 μm above the chip and has holes aligned above the pixel input pads. A negative potential of a few hundred volt is applied to the grid in order to create a strong electric field between the chip and the grid. The electric field is strong enough to give free electrons sufficient energy to release other electrons from the gas, creating an avalanche of electrons. If an avalanche is large enough it can be detected by the pixel circuitry. In this way single primary electrons can be detected. This electron multiplication process is called gas amplification or gas gain. An avalanche of approximately 1200 electrons and more can detected (chapter 6). Figure I.1 shows a sketch of the cross section of a Gridpix detector, Figure I.2 shows a picture of the cross section of a detector with the grid and figure I.3 shows the projection of an ion trail on the pixel chip and its 3 dimensional reconstruction. The line running through the ion trail is the reconstructed particle track.

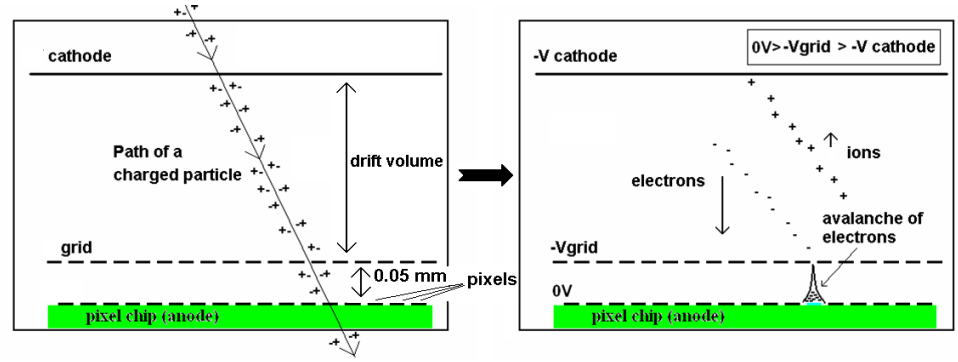

Figure I.1: *Sketch of the cross section of a Gridpix detector. Left: A charged particle leaves a trail of ions and electrons. Right: Due to the electric field the electrons drift towards the chip and the ions towards the cathode. When the electrons enter the gain region between the grid and the chip they cause an avalanche of electrons. A large enough avalanche can be detected by a pixel.*

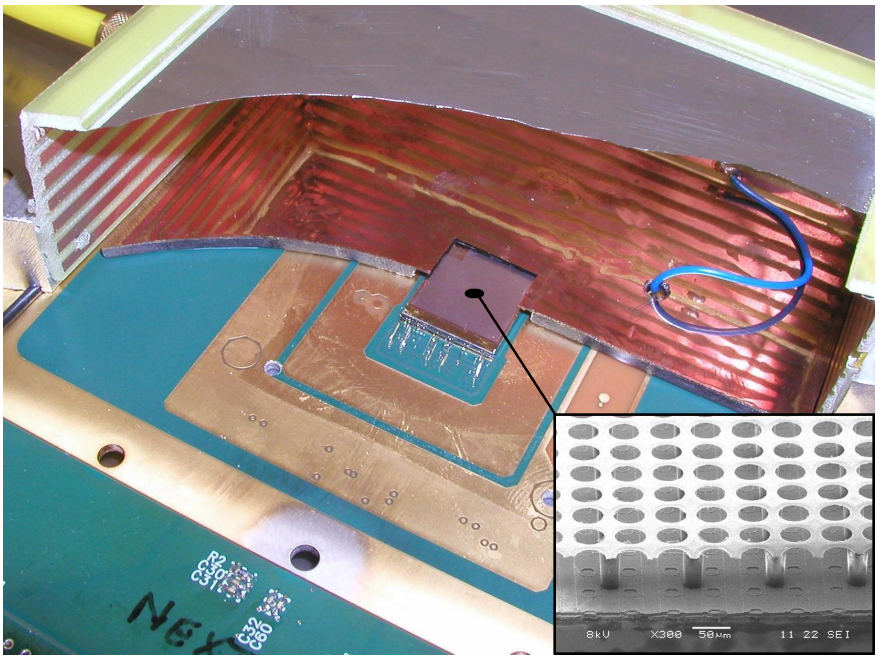

Figure I.2: *The inside of a Gridpix detector. The aluminium sheet at the top is the cathode, the copper strips on the sides and the copper plane surrounding the chip are electrodes to help to make a uniform drift field. The chip has a pixel matrix of 256 × 256 pixels. The pixel matrix is 14 × 14 mm. The inset on the bottom right is a detail of the grid that is supported by 50 µm tall insulating pillars.*

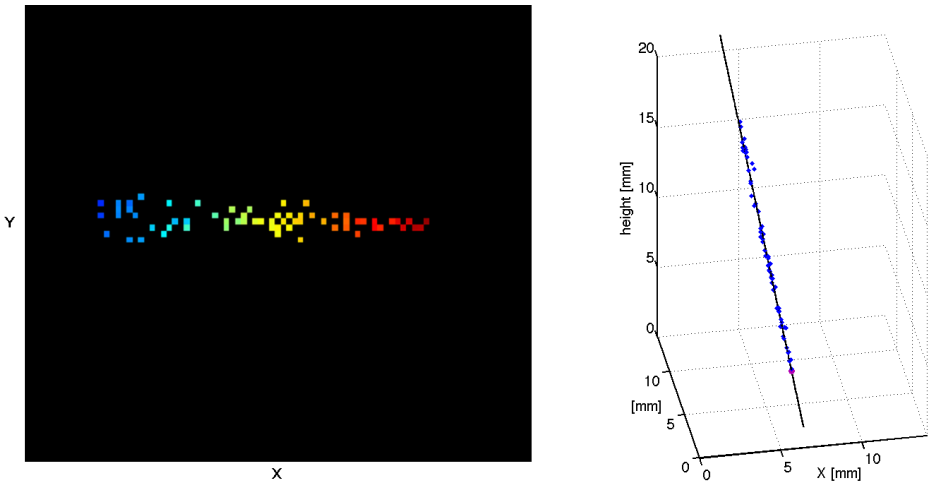

Figure I.3: *A muon track through a Gridpix detector with a 19 mm drift gap. The muon entered through the cathode and left through the chip. The left figure shows the projection of an ionisation trail on the chip plane. The colour reflects the drift time, red is a short drift time and blue is a long drift time. The right figure shows the 3 dimensional ion trail with a line that represents the reconstructed muon track.*

The signal induced on a pixel is composed of a fast and a slow component. The fast component is less than one ns and is due to the drift of the increasing number of electrons towards the pixel input pad, leaving positively charged ions between the chip and the grid. The slow component is in the order of tens of ns and is caused by the ions drifting towards the grid (Chapter 2 and 4). Each pixel has an amplifier that amplifies the signal from an avalanche and the drifting ions. An avalanche is detected if the signal crosses a threshold. Due to the duration of the signal (drifting ions) and the response time of the amplifier the moment of detection is delayed depending on signal magnitude. Due to the statistical nature of the gas amplification process the magnitude of the avalanches will vary according to a Pólya distribution (chapter 2). The varying delay caused by variations in signal amplitude is added to the measured drift time, called time walk. Time walk can be corrected in case the amplitude of the signal is known. Chapter 4 describes how much drift time measurements can be improved according to simulations. The simulations have been verified with a measurement on a prototype chip that simultaneously measures drift time and signal amplitude. In this test the drift time resolution has been improved from approximately 10 ns down to approximately 1 ns.

Due to the high potential applied on the grid sometimes a spark will occur. The charge stored on the grid is in the order of tens of nC and will destroy a chip in case of a spark. In order to quench sparks a silicon enriched silicon nitride (SiRN) layer is applied on top of the chip. The excess of silicon makes the layer slightly conductive. In case of a spark this layer will charge up until the deposited charge reduces the electric field between the chip and the grid such that the spark is quenched. The

deposited charge gradually drains away. Measurements on sparks and the (SiRN) layer show that with a layer thickness of 4 or 8 μm the total amount of charge in a quenched spark is reduced to maximum of a few nC, which is only a few % of the charge stored on the grid. The chip remains operational after suffering quenched sparks. According calculations the deposited charge per pixel will not exceed 5 pC, which would imply that a quenched spark deposits its charge extended over many pixels. This indeed has been observed, the quenched discharges deposit charge over a group of pixels that all simultaneously measure a large signal.

The (multiplied) primary electrons that arrive at the chip will cause a potential drop across the SiRN layer. This potential reduces the amplification field between the grid and the chip, resulting in a reduction of gas gain. Each 20 V reduction in potential across the gap will reduce de gas gain by approximately a factor of 2. The specific resistance of the SiRN layer appears to be in the order of 10^{13} Ωcm.

Chapter 6 describes measurements on general Gridpix performance. Various detectors with drift gaps varying between 1 and 10 cm have been tested. A gas gain of 5000 is sufficient to detect approximately 90% of the primary electrons. For high gas gains chips covered with 8 μm suffer from false hits. False hits are caused by pixels that detect an avalanche above an adjacent pixel, such a hit does not represent a primary electron and contaminates the measurement of the ionisation trail. Using a 4 μm thick SiRN layer significantly reduces the number of false hits due to the smaller distance between the charge and the pixel input pad, i.e. a smaller fraction of the charge is induced on neighbouring pixels. Based on average drift times one can conclude that for gas gains below $2{\cdot}10^4$ time walk significantly affects the drift time measurements. In case time walk can not be corrected (as is presently the case) the gas gain should be set as high as possible. To reduce the number of false hits a 4 μm SiRN layer should be used.

Chapter 7 describes a test of a Gridpix detector with a drift gap of only 1 mm. This concept in mend to be applied in an environment with a high particle flux like close to an interaction point of the (s)LHC. A 1 mm drift gap is thin enough to quickly extract the charge from the drift gap while still have a sufficiently large probability to detect a charged particle going through. A telescope containing 3 thin drift gap Gridpix detectors and one 19 mm Gridpix detector has been tested with 150 GeV/c muons at CERN. According the measurements a first estimation of the position resolution (where the particle track intersects the chip) of the thin detectors is 13 μm for normal incident tracks. The 19 mm detector has a position resolution between 7 and 13 μm for tracks under and angle of 80 °. The angular accuracy of the 19 mm detector is between 1.4 and 2.3 mrad.

Presently a pixel chip is under development that can simultaneously measure drift time and signal amplitude, making time walk correction possible. A test that still has to be performed with a Gridpix detector is a long term test to verify reliable operation for a long period of time. As the development of Gridpix detectors makes progress other fields start to show interest in the detectors. An ongoing investigation is to see if such a detector can be used in a set up to search for dark matter. A test has been performed to use the detector as an optical sensor (I used it to make the image of the fingerprint on the cover, which is from my right index finger). In a

current project it is investigated if a Gridpix detector can be used to track protons in proton therapy treatments.

Samenvatting

Om meer inzicht te krijgen in het functioneren van de natuur, zoekt en onderzoekt men in de hoge energie fysica de meest elementaire bouwstenen van materie en hun eigenschappen. Voor het onderzoek hiernaar worden subatomaire deeltjes met bijna de lichtsnelheid op elkaar geschoten. Bij de botsing tussen twee deeltjes ontstaan nieuwe (subatomaire) deeltjes die informatie geven over de fundamentele processen die plaatsvonden bij de botsing. Die processen wil men begrijpen. Om de botsing te reconstrueren, moet er dus gemeten worden welke deeltjes er vrijgekomen zijn, hoeveel energie ze hadden, waar ze precies gecreëerd werden en de richting waarin ze gegaan zijn. Om dat laatst genoemde te kunnen meten is er vraag naar positiegevoelige detectoren die het traject van geladen subatomaire deeltjes kunnen bepalen. Geladen deeltjes kunnen worden gemeten aan de hand van het spoor van ionisatie dat ze achterlaten als ze door een materiaal schieten. Echter, als een deeltje door een materiaal heen schiet verstoort dit ook de baan van het deeltje. Het is belangrijk dat het meten van de baan van deze deeltjes gebeurt met voldoende weinig materiaal op het pad van een deeltje. Hoe minder botsingen in het materiaal des te kleiner is de kans dat het te meten deeltje van de oorspronkelijke baan afketst of in botsingen andere deeltjes creëerd die de meting vervuilen. Twee veel gebruikte concepten om elektronisch het pad van een geladen deeltje te meten, is met halfgeleider-detectoren en gas-detectoren.

De halfgeleider detectoren bestaan uit meerdere dunne lagen silicium achter elkaar. Hierin kan men met behulp van uitlees strips of pixels de plek meten waar lading is vrijgemaakt door het geladen deeltje dat er doorheen is gegaan. Het traject van een deeltje kan worden gereconstrueerd door op de juiste manier de posities, waar in de verschillende lagen de lading is gemeten, met elkaar te verbinden.

Bij gas gevulde detectoren wordt het ionisatie-spoor, dat door een geladen deeltje in een gas volume wordt gemaakt, gereconstrueerd. Aan de hand van dìt gereconstrueerde spoor wordt het traject van het deeltje gereconstrueerd. De TPC (*T*ime *P*rojection *C*hamber, in het Nederlands: Tijd Projectie Kamer) is een gas detector waarmee het ionisatie spoor in 3 dimensies kan worden gereconstrueerd. Onder invloed van een in het gas volume aangelegd elektrisch veld, zullen de vrijgemaakte elektronen naar de anode drijven en de positief geladen ionen naar de kathode. De anode is gesegmenteerd zodat gemeten kan worden waar de elektronen terecht komen. Het ionisatie spoor wordt zo 'geprojecteerd' op de anode en kan zo in 2 dimensies gereconstrueerd worden. De derde dimensie, de drift afstand, wordt gere-

construeerd op basis van de snelheid waarmee de elektronen naar de anode drijven en de tijd die de elektronen nodig hebben om daar te arriveren. Vandaar de naam *T*ime *P*rojection *C*hamber.

De twee concepten, silicium en gas detectoren, hebben ieder hun voor- en nadelen. Silicium detectoren hebben als voordeel dat ze een snelle response hebben. Zij zijn dankzij een fijne segmentatie (pixels en strips in de orde van 50-500 μm) in een omgeving met hoge deeltjes flux te gebruiken. Ook hebben ze een goede ruimtelijke resolutie. Nadelen van silicium detectoren zijn dat ze relatief veel materiaal in het deeltjes pad nodig hebben en dat het detector materiaal degradeert onder invloed van de bestraling. Gas gevulde detectoren hebben weinig materiaal nodig om een deeltje te detecteren en het gas kan continu ververst worden, hierdoor degradeert het detector materiaal niet. Door de benodigde tijd om de lading (de elektronen en de ionen) uit het gas volume te krijgen kunnen detectoren met een groot volume geen hoge deeltjes flux aan.

In een onderzoek om betere positiegevoelige detectoren te maken is 'Gridpix' in ontwikkeling: Een TPC die wordt uitgelezen met een pixel chip met een pixel afstand vergelijkbaar met die van silicium detectoren. Met een zo fijn gesegmenteerde uitlezing is het mogelijk om de afzonderlijke elektronen van een ionisatie spoor in het gas te meten. Met een zo gedetailleerde uitlezing is het mogelijk om met een klein gas volume een hoge precisie én een hoge uitlees snelheid te halen. In dit proefschrift worden ontwikkelingen aan en het testen van dit type TPC beschreven. De gebruikte pixel chips hebben een 14 × 14 mm pixel matrix van 256 × 256 pixels (55 μm pixel afstand).

Op hun weg naar de uitlees chip passeren de primaire elektronen (de elektronen uit het drift volume) het 'grid'. Het grid is een plaatvormige elektrode die 50 μm boven de chip is geplaatst, met gaatjes boven de pixel input elektrodes. Op dit grid staat een negatieve potentiaal van enkele honderden volts. Dit heeft een elektrisch veld tussen het grid en de chip tot resultaat dat sterk genoeg is om vrije elektronen voldoende energie te geven om andere elektronen los te maken uit het gas. Dit lawine effect maakt dat één primair elektron vermenigvuldigd kan worden. Als de lawine groot genoeg is komt dit als een detecteerbare lading op een pixel aan. Dit proces heet gas versterking en is noodzakelijk omdat één enkel elektron te weinig lading is om gemeten te kunnen worden. Lawines met meer dan ongeveer 1200 elektronen kunnen gedetecteerd worden (hoofdstuk 6). De werking wordt verduidelijkt in figuur J.1, figuur J.2 toont een opengewerkte detector met een detail opname van de chip met het grid en figuur J.3 toont de projectie van een ionisatie spoor op de pixel chip en de 3 dimensionale reconstructie. De lijn door het ionisatie spoor is de gereconstrueerde track.

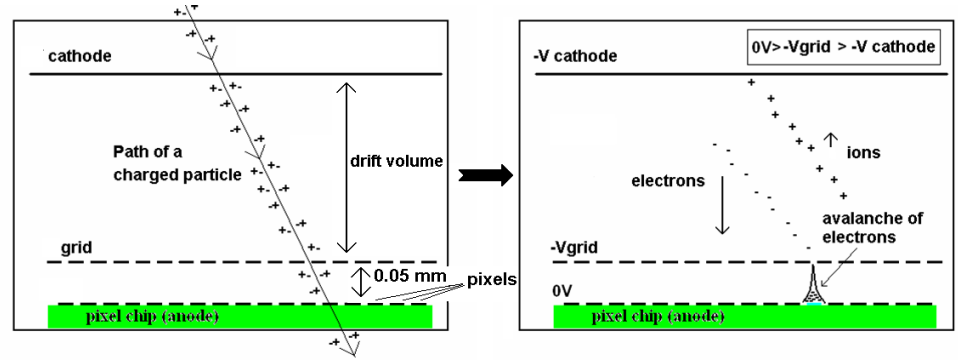

Figuur J.1: *Schets van de doorsnede van een Gridpix detector. Links: Een geladen deeltje laat een geïoniseerd spoor achter. Rechts: De elektronen zullen door het elektrische veld naar de chip met grid drijven. Op het grid, dat 50 µm boven de chip geplaatst is, staat een paar honderd volt. Het elektrische veld is zo hoog, dat een arriverend elektron een lawine van elektronen los maakt. Een lawine die groot genoeg is kan gedetecteerd worden.*

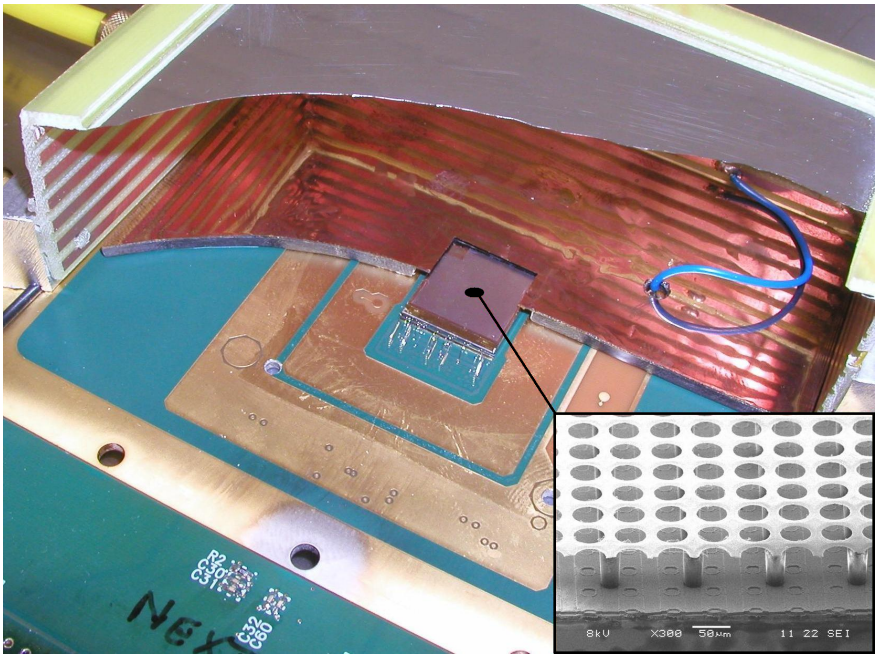

Figuur J.2: *Foto van een opengewerkte Gridpix detector. Het aluminium kleurig vlak is de kathode, de koperstrips aan de wanden en het kopervlak aangrenzend aan de chip zorgen voor een homogeen drift veld. De chip heeft een pixel matrix van 256 × 256 pixels. De pixel matrix is 14 × 14 mm. Rechtsonder is een detail opname van het grid dat op isolerende 50 µm hoge pilaartjes op de chip rust.*

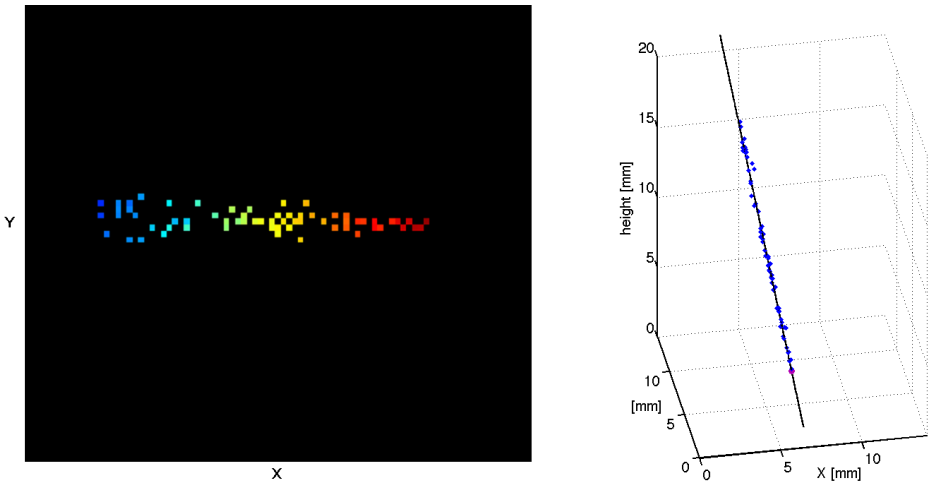

Figuur J.3: *Een track van een muon door een 19 mm hoge Gridpix detector. Het muon kwam de detector binnen door de kathode en ging er uit door de chip. De figuur links is de projectie van het ionisatie spoor op de chip, de kleur geeft de drift tijd aan. Rood is een korte drift tijd en blauw een lange drift tijd. De afbeelding rechts toont het 3D gereconstrueerde ionisatie spoor en de gereconstrueerde track.*

Het signaal dat op een pixel wordt geïnduceerd bestaat uit een snel en een traag component. De snelle component duurt minder dan een nanoseconde en komt van het toenemende aantal elektronen dat naar de chip beweegt, hierbij worden positieve ionen achtergelaten. De trage component duurt tientallen nanoseconden en wordt veroorzaakt door de ionen die naar het grid drijven (zie hoofdstuk 2 en 4). In iedere pixel zit een versterkertje dat het signaal van een lawine en de driftende ionen versterkt. Als dit signaal boven een bepaalde drempelwaarde komt dan wordt de lawine gedetecteerd. Door de traagheid van de versterker en de tijdsduur van het signaal van de gas versterking varieert het moment waarop het signaal gedetecteerd wordt afhankelijk van de signaalsterkte. Door het statistische karakter van gasversterking zal de grootte van de lawine per keer variëren volgens een Pólya verdeling (zie hoofdstuk 2). De variërende vertraging tengevolge van variërende signaalsterktes komt als fout bij de gemeten drifttijd: Dit effect heet ?time walk?. Als de amplitude van het signaal bekend is, kan hiervoor gecorrigeerd worden. In hoofdstuk 4 wordt beschreven met behulp van simulaties, op welke manier en hoeveel winst in nauwkeurigheid in de drift tijd meting te winnen is. De simulatie resultaten zijn geverifieerd met een meting aan een prototype chip die tegelijkertijd zowel de signaalsterkte als de drift tijd meet. Bij deze test is de drift tijd resolutie van ongeveer 10 ns teruggebracht tot 1 ns.

Door de hoge potentiaal op het grid zal er af en toe een vonk tussen het grid en de chip overslaan. De lading opgeslagen in het grid - in de orde van enkele tientallen nC - is zodanig veel, dat als er een vonk ontstaat, de chip stuk gaat. Om vonken in een vroeg stadium te smoren, is er een met silicium verrijkte silicium nitride (SiRN)

laag op de chip aangebracht. De verrijking met silicium geeft enige geleiding van de laag. Als er een vonk overslaat, dan laadt dit laagje op totdat het veld tussen de chip en het grid zodanig is gereduceerd dat de vonk stopt. De gedeponeerde lading vloeit geleidelijk weer af. Metingen aan vonken en aan de SiRN laag (hoofdstuk 5) wijzen uit dat met een laagdikte van 4 of 8 μm de totale lading in een gesmoorde vonk is gereduceerd tot een maximum van enkele nC. Dit is slechts een paar procent van de lading die op het grid zit. De chip blijft functioneren bij deze gesmoorde vonken. Volgens berekening blijft bij een gesmoorde vonk de hoeveelheid lading per pixel beperkt tot onder de 5 pC. Dit betekent dat een gesmoorde vonk dus over vele pixels lading deponeert. Dit wordt ook waargenomen. De gesmoorde ontladingen worden als een groot signaal op een groep van meerdere pixels tegelijkertijd gemeten.

Zodra er lading van de (vermenigvuldigde) elektronen uit het drift volume arriveert, komt er over de SiRN laag een potentiaal te staan. Deze potentiaal zal het veld tussen het grid en de chip reduceren met als gevolg dat de gas versterking minder wordt. Voor elke 20 V reductie zal de gas versterking ongeveer halveren. De specifieke weerstand van de gebruikte SiRN blijkt in de orde van 10^{13} Ωcm te zijn.

In hoofdstuk 6 staat beschreven hoe de algemene eigenschappen van Gridpix detectoren zijn gemeten. De drift lengte bij de verschillende detectoren lag tussen de 1 en 10 cm. Bij een gasversterking van 5000 wordt ongeveer 90% van de primaire elektronen gedetecteerd. Het blijkt dat een pixel chip met een 8 μm dikke laag silicium nitride bij een hoge gasversterking last krijgt van 'valse hits', veroorzaakt doordat pixels soms een lawine detecteren boven een aangrenzende pixel. Ze vertegenwoordigen dus geen primaire lading waardoor er vervuiling van de meting optreed. Met een 4 μm dikke laag is dit effect significant minder omdat de lading zich dichter bij de chip bevind, de verhouding tussen de lading geïnduceerd op de onderliggende pixel en een naburig pixel is groter. Op basis van de gemiddelde drift tijd kan men concluderen dat voor een gasversterking van minder dan $2{\cdot}10^4$ time walk een significante rol speelt. Als er niet voor time walk gecompenseerd kan worden, dan kan men het beste de detector op een zo hoog mogelijke gasversterking laten werken. Om het aantal valse hits te minimaliseren wordt geadviseerd om een 4 μm silicium nitride laag te gebruiken.

In hoofdstuk 7 wordt een test beschreven van een Gridpix detector met een driftlengte van slechts 1 mm. Dit concept is bedoeld om toe te passen in een omgeving met een hoge deeltjes flux zoals op een paar cm van een interactiepunt bij de experimenten bij de (s)LHC. Een drift ruimte van 1 mm is dun genoeg om voldoende snel de lading te onttrekken en dik genoeg om voldoende zekerheid te hebben om een passerend deeltje te detecteren. Een telescoop met drie van deze dunne detectoren en één Gridpix detector met 19 mm drift ruimte is op het CERN getest met 150 GeV/c muonen. Uit de meting blijkt, volgens een eerste inschatting, dat de positie resolutie van de dunne detectors ongeveer 13 μm is voor loodrechte sporen. Voor de 19 mm Gridpix detector ligt de positie resolutie tussen de 7 en 13 μm voor sporen onder een hoek van 80°. De hoekresolutie van de 19 mm detector is ongeveer 1.4 tot 2.3 mrad.

Momenteel is de Timepix-3 chip in ontwikkeling, die de drift tijd en signaalsterkte gelijktijdig kan meten. Met deze chip kan dus time walk correctie worden uitgevoerd.

Verder moet er nog een duurtest worden gedaan om de betrouwbaarheid van Gridpix detectors op lange termijn te bepalen. Naarmate de ontwikkeling van deze detectoren vordert, ontstaat er vanuit andere vakgebieden ook interesse in deze detectoren. Zo wordt er onderzocht of dit type detector in een bepaalde opstelling gebruikt kan worden bij de zoektocht naar donkere materie. Er is ook een test gedaan waarin een detector als optische sensor is gebruikt (op deze manier heb ik de vingerafdruk van mijn rechter wijsvinger op de kaft van dit proefschrift gemaakt). Verder loopt er nog een onderzoek of een Gridpix detector gebruikt kan worden om protonen te traceren bij proton therapie.

Acknowledgements

Finally, the last and the most read chapter! Completing a Ph.D. research is not something one can complete solely (the same counts for the thesis that follows) and I owe a lot of thanks to a lot of people. Sadly there is not enough room to thank all of you explicitly and I apologise to those of you who I cannot mention here.

I would like to thank Frank, my promotor, and Harry, my co-promotor, for giving me a lot of freedom to define the topic of my Ph.D. research. Harry, you always have many inspiring ideas I can learn from and you were always encouraging me to work on new ideas I had. In spite of your high occupation your door is always open and I could walk in any time when I had questions and ideas. Thanks for helping me out and giving me some slack when I needed it. Frank, thanks for being supportive and open to my initiatives and ideas that I wanted to go after (even the non-Ph.D. related projects). This freedom really made me enjoy doing my Ph.D. and is as important to me as the content of the research itself. At the moment of writing I still owe you that 3D movie (and I need an interview with you to finish that).

Fred, no matter what you were doing at the moment, you always had time for me when I had a question or a problem. You also always had the answer or the solution too. Thanks for your time and for teaching me in how to 'do' a test beam.

Els, in spite of that you are not my promoter or co-promoter and your high occupation you were available every time when I had questions. Thanks for your time and for proof reading some chapters I was working on.

Bob, After being my supervisor for my master thesis, you luckily were still there with an objective point of view as a member of the C3 committee. It was good to know that in case of 'issues' I could have turned to you. 'Issues' did not occur, instead, you helped me (again) to get on track when I started writing my thesis (the Ph.D. one this time). So, Bob, thanks again.

I thank the electronic and mechanical engineers since, without you, none of the detectors that we used would have existed at all. I would like to mention the people who I had to bother most often. Joop, thanks for doing the impossible many times, even for the miracles I didn't have to wait long. You helped me a lot by often 'fixing a job' in between other jobs you were already occupied with. Peter and Bas, thanks for helping me many times with electronic related subjects. Peter, I can still remember a 'four fold cable' we had to get going, you somehow made time for that in spite of that you were busy with other (probably more interesting) projects at that time. Wim, thanks a lot for both helping with building detectors and for thinking of

my interest for electronics when old equipment was removed. Ruud and Vladimir, thanks for your input for the chapter on signal development.

On a regular base administrative 'stuff' for travelling, Ph.D. procedure, etc. had to be 'done' and I want to thank Johan, Fred, Katja, Eveline and Joan for taking care of those things.

At the detector R&D group, people were not safe for me either. I really appreciate the 'open door' atmosphere in the group (I hope no one regrets that now). Jan Timmermans, thanks for helping me a lot in getting me introduced in gaseous detectors. Martin v. B., thanks for proof reading some chapters. Yevgen and Max, thanks for the nice evenings with good dinners and a good Vodka. Max, thanks to you I know how it is to 'live' in a monastery near Paris. Victor and Yevgen, great work on the Ingrids. Victor, I remember 'our' first test beam as a great adventure. Lucie, thanks for being the always cheerful (how did you do that?) office mate and for your work on Gridpix detectors. I really enjoyed working on that 3D movie with you. Sander, Maarten, Thijs and Sjoerd, thanks for your work on Gridpix detectors in the test beams. It was a nice time working with you. I also would like to thank the other members of the detector R&D group: Niels, Jan Visser, Jan Visschers, Marten, Enrico, Panagiotis and Matteo. Joost, your search for and development of 'photosensitive post processed CMOS chips' resulted in a nice detector that could be used to take fingerprints. Thanks.

I would like to thank my office mates at the R&D group for the good atmosphere, which often was a reason to be writing my thesis at Nikhef (which I otherwise would have done at home even more). Wilco, with you I could discuss into very detail the technical issues in my research and, in addition to that, we almost found out how to control the rabbit population in the Science Park. Francesco, thanks for some nice parties at your place and for testing the right chip at the right time. Rolf, thanks for your help with the tests at CERN, for helping me to find accommodation, for being a nice house mate, and for helping me to categorise the whiskeys we have.

And of course this could not have been achieved without my friends, with whom I share both the hard and the good times. Guido, Roland and Jana, thanks for being the mental support team. Meike, our situation now is different from when I started my Ph.D. but that doesn't take away the good time we had together, thanks. Arno, Octo, Stefan, Martijn, and Mike, the evenings with cigars and whiskey often did cost me the day after but kept me going for the weeks following (a good investment returns more than it costs). Alex, I really like the relaxed evenings when we went to the Bimhuis for a moment of relaxation during the week.

Alexandra, I am happy that during the last few months of the Stressful Writing I could spend my time with you. In return you got me: A guy who was busy all the time and who was sometimes a bit grumpy and tense too. In spite of the two demanding jobs you had at that time, you had time to support me. From now on both of us can spend more time on you.

Until now, I did not yet mention my parents, my sister and her boyfriend who I probably don't need to thank explicitly and, more important, who shouldn't need to read in a booklet that I am thankful. But nevertheless: Mum, Dad, Saskia and Erik, thanks for your unconditional support over the years.

Propositions accompanying the Ph.D. thesis: 'Gridpix: TPC development on the right track'

- Increasing the capacitance of the grid will improve the performance of a Gridpix detector. (chapter 5)

- The Raether limit does not take the charge density in an avalanche into account, and therefore it cannot be used for studies of the maximum gas amplification and sparks at a microscopic scale like in Gridpix detectors.

- A reduced gas gain caused by charge build-up on the spark protection layer (chapter 5) is a convenience under certain circumstances.

- It appears to be surprisingly simple to determine both the charge sensitivity of a pixel and the value of the parameter m of the Pólya distribution (even for different gas gains) by fitting only one parameter. (chapter 6)

- Concerning the 'false hits' (chapter 6), with a decreasing pixel pitch in Gridpix detectors the maximum thickness of the spark protection layer should also decrease.

- If a trigger with a very low latency is required for the read out of a Gridpix detector one is doing something wrong. (chapter 3)

- Doing something wrong does not necessarily imply that one fails to achieve the main objective.

- Though there may be a correlation between the rabbit population at the Science Park and the performance of the Gridpix detectors in the lab, I do not expect a causal relation between those two.

- It is possible to make a piece of art entitled 'almost = absolutely not' composed of the Timepix chips that broke down during this research.

- Getting drunk can be a good investment.

- The number of conflicts would be less and the level of development would be higher if ignorance would lead to curiosity and not to a lack of understanding.